The American University in Cairo
School of Sciences and Engineering
Engineering Department

ELASTIC-PLASTIC BEHAVIOR AND LIMIT LOAD ANALYSIS OF PIPE BENDS UNDER OUT-OF-PLANE MOMENT LOADING AND INTERNAL PRESSURE

BY

Hashem Mohamed Mourad

A Thesis Submitted in partial fulfillment of the requirements for the degree of

Master of Science in Engineering

with concentration in

Design

under the supervision of

Dr. Maher Y. A. Younan
Professor of Mechanics and Design
The American University in Cairo

December 1999

Acknowledgments

Mere words fail to express my immense gratitude to my professor and advisor Dr. Maher Younan, for his precious guidance and help, and for the endless generosity and kindness with which those were offered.

I would like to thank my parents and my fiancée for their encouragement and patience.

Special thanks to my friends Yasser Hassan and Ihab Naguib for their help and support.

I would also like to thank the CAD-lab. administrator, Mrs. Nabawia Khalil, for keeping all needed resources accessible.

Abstract

When an external load is applied to one of its ends, a pipe bend's cross-section tends to deform significantly both in and out of its own plane. This shell-type behavior, characteristic of pipe bends and mainly due to their curved geometry, accounts for their greater flexibility. This added flexibility is also accompanied by stresses and strains that are much higher than those present in a straight pipe of the same size and material, under the same loading conditions. For this reason, pipe bends are considered the critical components of a piping system. Hence, for the purpose of designing and/or qualifying a pipeline structurally, it is useful to have a reliable estimate of their load-carrying capacity, along with a deep understanding of their structural behavior until instability, under different and combined loading conditions.

The primary goal of this research is to study the elastic-plastic behavior of pipe bends, under out-of-plane moment loading. It is also required to study the effects of changing the value of the pipe bend factor, and the value of internal pressure, on that behavior; and to determine the value of the limit moments in each case.

The finite element method is used, throughout the present work, to model and analyze a standalone, long-radius pipe bend with a 16-in. nominal diameter, and a 24-in. bend radius. A parametric study is performed in which the bend factor takes ten different values between 0.0632 and 0.4417. Internal pressure is incremented by 100 psi for each model, until a value of the pressure is reached, where the bend undergoes plastic instability due solely to pressure.

The results of these analyses are presented in the form of load-deflection plots, for each load case belonging to each model. From the load-deflection curves, the limit moments of each case are obtained. The limit loads are then compared to those computed using some of the analytical and empirical equations available in the literature. The effects of modeling parameters are also studied. The results obtained from small-displacement and large-displacement analyses are compared, and the effect of using a strain-hardening material model is also investigated.

To better understand the behavior of pipe elbows, under out-of-plane bending and internal pressure, it was deemed important to know how the cross-section deforms, and to study the distribution of stresses that cause it to deform in a particular manner. An elbow with pipe bend factor h=0.1615 is considered, and the results of a detailed analysis thereof are examined.

The collapse moment was found to increase and then decrease significantly with increasing internal pressure. The instability moment was found to increase, then decrease, and finally increase slightly, before the high end of the internal pressure range is reached. Before plastic instability, many points of the bend’s structure exhibited through-the-thickness plastification. The loaded end of the elbow was found to be the most severely strained cross-section. It was then found that internal pressure shifts the locations of maximum stresses and strains, around this critical section.

Table of Contents

List of Tables

List of Figures

Nomenclature

D_e	elastic deflection
D_i	inner diameter
D_o	outer diameter
E	Young's modulus
F	external force
F_a	average force
F_i	internal force
F_r	force residual
M	moment
$\mathbf{M}$	artificial mass matrix
M_c	collapse moment
M_i	instability moment
M_l	limit moment
M_p	full plastic moment
M_y	first-yield moment
P	internal pressure
R	radius of curvature of bend's center-line
Z	section modulus
c	correction of the solution variable during an iteration
h	pipe bend factor
m	number of terms in Fourier series
r	mean pipe radius
t	pipe wall thickness
$\mathbf{v}$	vector of nodal velocities
Δ	change in the solution variable during an increment
α	included angle of bend
ε_{ep}	equivalent plastic strain
ε_y	yield strain

ϕ	angle around circumference
γ	radius ratio
λ	flexibility characteristic
ν	Poisson’s ratio
θ	end-rotation
σ_ϕ	hoop stress
σ_u	ultimate strength
σ_y	yield stress
ψ	pressure factor
ζ	damping coefficient

Chapter One

Introduction and Literature Review

1.1 Introduction

Large pipelines and pipe networks are part of almost every industrial setup today. These are most commonly found in petroleum rigs, refineries, factories producing chemicals and pharmaceuticals, and in power plants. In these and other industrial applications, pipes are very often used to carry substances that, by virtue of their pressure, temperature, physical and chemical characteristics, can have serious negative effects on health, property and the environment, if released into the atmosphere. Examples of such substances include steam, oil and chlorine gas.

Failure in a piping system could cause problems, like an unscheduled, and hence costly, plant shutdown for maintenance; or even a catastrophe, like exposing the core of a nuclear reactor. Therefore, the integrity of pipes in industrial contexts is of paramount importance. This integrity relies heavily on the correctness of design codes and practices, which can only be achieved through a thorough understanding of the behavior of piping components and systems under different types of loads.

Stresses in piping systems are developed as a result of sustained loads, like the weight of the pipe itself and the pressure of the fluid running inside it. The effects of this kind of loads is minimized by selecting an adequate type of supports, and using a sufficient number of them. Dynamic loads, of seismic origin or generated by a defective attached device (e.g. pump or compressor), and thermal loads, which cause different pipe segments to expand, also create stresses within the piping system. In general, dynamic and thermal loads are more important, and more complex to deal with. Hence, it is vital that some means or mechanism, for relieving these stresses, be present in the design of a piping system, to avoid overloads which might in turn lead to failure of a pipe segment, or cause damage to an attached device, vessel or support.

It has been known for a long time, at least since the first theoretical stress analysis of pipe bends was published (Von Kármán, 1911), that the flexural rigidity of pipe bends is smaller than that of a straight pipe of the same material and dimensions. This added flexibility is attributed to the tendency of the bend, by virtue of its geometry, to embrace a shell-type behavior that is not displayed significantly by straight pipes, which tend to behave like beams instead of shells. Because of this characteristic behavior, the bend's cross-section abandons its original roundness, turning into an oval shape. In addition, the bend's initially plane cross-section, tends to deform out of its own plane, which also provides some additional flexibility. These two deformation patterns are termed "ovalization" and "warping", respectively.

Due to these characteristics, pipe bends are used extensively in piping systems, not only to change the direction of a pipe run, but also to provide flexibility, especially in response to thermal strains. For typical primary piping loop elbows (pipe bends) in nuclear reactors, cross-sectional deformation is known to give a pipe bend 5-20 times the flexibility of a straight pipe of the same material and size. This flexibility is not gratuitous however; it is typically accompanied by stresses and strains that are 3-12 times those present in a straight pipe of the same material and size, under the same loading conditions, with high strain gradients around the bend's circumference and through its wall thickness (ABAQUS, 1998).

For this reason, pipe bends are considered the critical components in the piping system, and hence it is necessary, to be able to predict their response accurately, and to have a deep understanding of their elastic-plastic behavior under different types of loads. It is also useful, for safe design purposes, to have accurate and conservative estimates of the limit loads, beyond which the structure of the pipe bend undergoes excessive plastic deformation, that tends to increase disproportionately under the influence of small load increments, leading eventually to failure, when the elastic portions of the structure become insufficient to resist the load.

In addition to experimental investigations, several attempts have been made using analytical and numerical approaches, to gain a deeper understanding of the problem, based on which safer and more reliable design codes and practices can be formulated and adopted. Different theories and simplifying assumptions have been adopted by the different investigators in analyzing the problem. The main contributions, approaches, theories and assumptions will be examined in this chapter, through a review of the literature.

The simplest loading configuration is when the pipe bend is loaded in its own plane, either in the opening or closing direction; i.e. the load tends to reduce or increase the curvature of the bend's centerline, respectively. Due to its simplicity, most of the work previously done in this area was centered on this specific case, extending it to include internal pressure effects and/or end-constraints. This study aims at treating the more complex and less popular case of out-of-plane moment loading, combined with internal pressure.

1.2 Theoretical Analysis of Pipe Bends

It was first demonstrated experimentally by Bantlin (1910) that a curved pipe behaves differently under load than predicted by simple beam theory. The first theoretical explanation of this discrepancy was presented by Von Kármán (1911), and much of the theoretical work done subsequently was an extension of his work, or at least based on the same principle of potential energy minimization. Other closed-form solutions were based on the mechanics of materials principles, or thin shell theory. All these solutions acknowledge the fact that pipe bends have higher flexibility and stresses, and a different stress distribution, from the ones predicted by simple beam theory.

The general approach followed in piping system flexibility calculations, and still widely adopted in design codes, relies on the use of "flexibility factors" and "stress-intensification factors", which are simply the ratios of actual flexibility and stress to those predicted by simple beam theory. The different approaches aim at providing more accurate estimates of these correction factors, in a form that can adequately be simplified, to become readily usable in design contexts.

A common drawback of most theoretical solutions however, is that they are based on elastic analysis concepts, and cannot be used for the purpose of nonlinear analysis, which is required to predict the response of a pipe bend correctly, especially in accident conditions where plasticity dominates its behavior. Nonlinear theoretical analysis has been explored by a small number of workers, like Spence (1972), but these efforts didn't realize enough success to warrant their use in design. In addition, theoretical solutions are only useful in the analysis of pipe bends of circular cross-section.

1.2.1 Minimum Potential Energy Approach

Von Kármán (1911) published the first theoretical stress analysis of the problem of in-plane bending of pipe bends, which was later generalized by Vigness (1943), to include out-of-plane bending. In both of these analyses, the deformation of the bend's wall was represented by a trigonometric series, whose coefficients were determined by minimizing the total potential energy.

Major simplifying assumptions were made in these analyses:

- Internal pressure effects are ignored.
- The pipe bend is not connected to any straight pipes or flanges. In other words, end-effects are ignored and a standalone pipe bend is assumed.
- The ratio of the pipe radius to the bend radius (r/R) is negligible relative to unity, i.e. long radius elbows (R/r>>1) were assumed.
- The pipe bend's cross-sections remain plane and perpendicular to the bend's centerline even after deformation. This precludes warping effects from the analysis.
- Under torsional moment loading, the pipe bend was assumed to behave like a straight pipe, keeping a circular cross-section.
- The hoop membrane strain in the circumferential direction was assumed to be nil, which means that the cross-section ovalizes without any changes in the length of its circumference.

Both of the analyses, agreed with Bantlin's results (1910), by indicating that longitudinal tensile and compressive stresses, in the tube's wall, produce component forces acting towards and away from the center of curvature, respectively. These forces result in the flattening of the cross-section into an oval shape, as shown in Fig. 1.2.1, which in turn accounts for the increased flexibility and the different stress distribution, compared to those predicted by simple beam theory and those found in straight pipes.

They also showed that the bend's maximum stresses and its deformation, namely its end-rotation, are higher than those of a straight pipe of the same size and material. These results, expressed as flexibility and stress-intensification factors that are greater than unity, depend only on a dimensionless parameter, the pipe bend factor (h), defined as:

$$h = \frac{R.t}{r^2} \qquad (1.2.1)$$

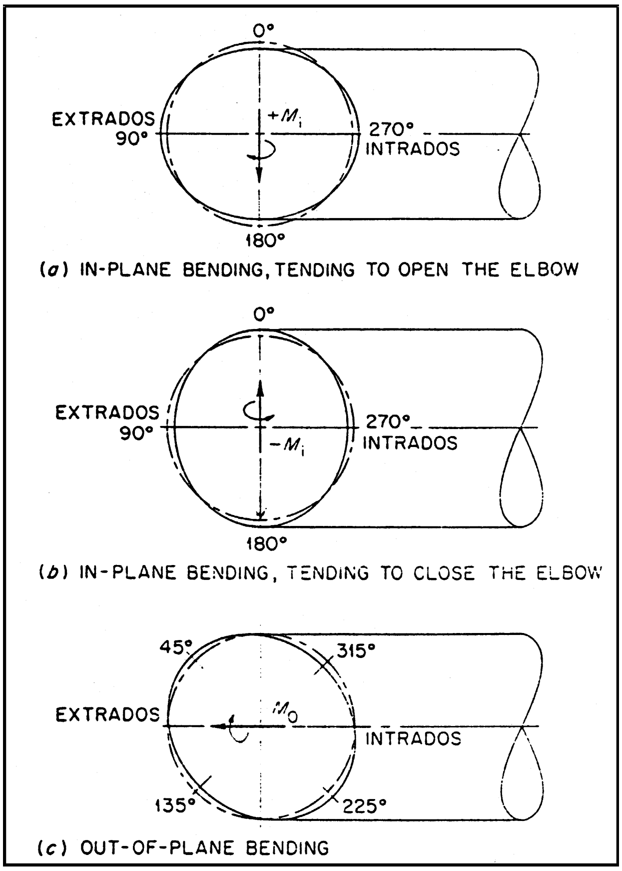

Fig. 1.2.1 Cross-Sectional Deformation of a Pipe Bend Under In-Plane and Out-of-Plane Loading (Dodge and Moore, 1972)

A definition of the pipe bend's cross-sectional geometry, and of terms used to describe "key" or "reference" points on the section is shown in Fig. 1.2.2.

By comparing experimental results to the analytical results obtained from Von Kármán's theory, Gross (1952) detected a logical inconsistency in the way the circumferential membrane force is treated theoretically. He demonstrated that a "correction for transverse compression" was needed to maintain static equilibrium in the structure. He then developed an expression that yields a more accurate estimate of the circumferential membrane force, based on the assumption that Von Kármán's analysis gives a correct estimate of the axial membrane force.

Attempts to include internal pressure effects in Von Kármán's in-plane bending analysis were made by Barthélemy (1947), and later by Kafka and Dunn (1956) who used, and experimentally validated, a theory developed earlier, to deduce the pressure effect, by Clark, Gilroy and Reissner (1952).

These works were based on another dimensionless parameter, the flexibility characteristic (λ), instead of the pipe bend factor (h):

$$\lambda = \frac{R.t}{r^2.\sqrt{(1-\nu^2)}} \tag{1.2.2}$$

It is noted that the term $\sqrt{(1-\nu^2)}$ did not appear in the earlier analyses of Von Kármán, Vigness and Gross, due to their use of uniaxial stress-strain relations.

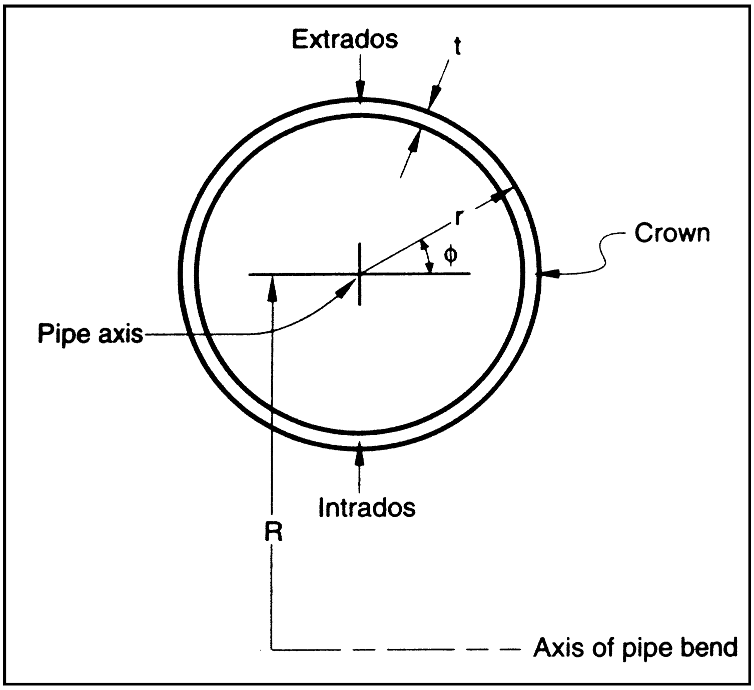

Fig. 1.2.2 Pipe Bend Cross-Section Geometry (ABAQUS, 1998)

Rodabaugh and George (1957) presented a more complete analysis, in which they derived explicit expressions for the flexibility factors, and for the in-plane as well as the out-of-plane stress-intensification factors, based on the analyses of Von Kármán and Vigness, and including the effect of internal pressure. They introduced a second dimensionless parameter (ψ) related to the pressure:

$$\psi = \frac{P.R^2}{E.r.t} \tag{1.2.3}$$

In this work, the flexibility and stress-intensification factors were shown to be dependent only on the two dimensionless parameters (λ) and (ψ). The expressions were derived as an infinite series that was claimed to have a faster convergence for higher values of λ and internal pressure (P). They showed that for a long-radius elbow (R/r=3) with a flexibility characteristic of λ=0.03, it was necessary to include five terms of the series to obtain an accuracy within ±2 percent. Simplified formulas with adequate accuracy were provided for purposes of practical piping stress analysis, and were adopted for purposes of nuclear power piping design (Dodge and Moore, 1972).

Dodge and Moore (1972) developed a corrected expression for the circumferential membrane force in the case of out-of-plane bending, to complement the one for in-plane bending, contributed previously by Gross (1952). They recommended the use of these corrected expressions in conjunction with the above-mentioned work of Rodabaugh and George. This required the introduction of the radius ratio as a third dimensionless parameter ($\gamma = \frac{R}{r}$).

1.2.2 Mechanics of Materials Approach

Turner and Ford (1957) used mechanics of materials principles to reach a closed-form solution for the in-plane bending case. Smith (1967) developed a solution for the out-of-plane loading case, following the same approach closely. He also suggested a procedure to find the maximum stresses due to combined in-plane, out-of-plane and torsional moment loads. Smith and Ford (1967) showed that the deflections and stresses, calculated using this method, compared satisfactorily with their experimentally determined values.

The most significant advantage of these analyses, over the ones derived using the minimization of potential energy theory, is that they avoid two of the major simplifications made in the energy approach. The ratio of the pipe radius to the bend radius (r/R) was not assumed to be negligible relative to unity, which allowed the developed expressions to be used with short-radius as well as long-radius elbows. In addition, the circumferential strain on the mid-wall surface was not assumed to be zero.

The results obtained using this approach were claimed to be in good agreement with the Von Kármán type results, within five to ten percent. This agreement is due to some common fundamental assumptions. Both are based on elastic small-deflection theory, and assume that plane sections remain plane, thereby neglecting cross-sectional warping. It is also noted that both obtain the expressions for the flexibility and stress-intensification factors in the form of infinite trigonometric series.

A major disadvantage of this approach is its complexity. Due mostly to this drawback, no further development was done using mechanics of materials principles, to include the effect of internal pressure. Incorporating this effect into the Von Kármán / Vigness analyses was more simply accomplished, since it only required the addition of an auxiliary term to the elastic energy equation.

1.2.3 Thin Shell Theory Approach

Using this third approach, Tueda (1936) reduced the problem of in-plane bending to two coupled ordinary differential equations, and a power series was used for integration. Reissner (1949) further developed the theory, and later Clark and Reissner (1951) obtained a solution by solving two coupled ordinary differential equations with variable coefficients. They had to make simplifying assumptions that were equivalent in essence to those made by Von Kármán.

Later, Cheng and Thailer (1968) succeeded in integrating the same set of differential equations without making the same simplifying assumptions. Their series solution converges more rapidly than the mechanics of materials solution of Turner and Ford, and gives results of similar accuracy. However, the importance of rapid convergence has shrunk considerably since the initial development of the theory, due to the enormous increase in power and availability of computers since then.

Whatham (1978) analyzed the effect of end-constraints, specifically flanges, on the behavior of pipe bends under in-plane bending using thin shell theory. That work was extended, by Whatham and Thompson (1979), to pipe bends terminated by equal-length tangents (i.e. straight pipe segments) with flanged ends, subjected to in-plane bending moments, and including the effect of internal pressure. They found that tangents longer than one pipe circumference have a minor effect, compared to flanges directly connected to the bend, in reducing the stresses and deformations caused by the moment load. They also found that the presence of internal pressure reduces the effect of end-constraints. Further development is needed to generalize this analysis to include out-of-plane loading.

1.3 Experimental Investigation of the Behavior of Pipe Bends

Many attempts were made to investigate the behavior of pipe bends experimentally. A large portion of this work however, is restricted to the problem of in-plane bending only, or was performed to complement a theoretical or numerical study and to validate its results, or to examine a specific effect. In this section, the most important experimental investigations are covered, special emphasis being placed on the most complete ones, in particular those that involve out-of-plane loading, which is the loading type of interest in this study.

The most comprehensive study, and the one that is referred to most frequently in the literature, is the one conducted by Greenstreet (1978), at the Oak Ridge National Laboratory (ORNL). In this study, load-deflection responses were determined for twenty 6-inch nominal diameter commercial pipe elbows, sixteen of which were made of ASTM A-106 grade B carbon steel and the remaining four were made of ASTM A-312 type 304L stainless steel. A summary of the different tests and their loading conditions, along with the properties of the specimen used in each test are presented in Table 1.3.1.

Pipe extensions of ASTM A-106 grade B carbon steel of the same thickness as the elbow being tested were welded by the tungsten-arc inert-gas method to the ends of the elbows, with the exception of test PE-18 where 347 stainless steel extensions were used. The assemblies were not heat treated after the welding operations, to simulate the metal conditions found in actual piping systems.

One extension was then rigidly mounted on a pedestal attached to a load frame, and a single force was applied in each case, with the point of load application on the free extension, at a distance of four to five pipe diameters from the nearer end of the elbow. This relatively long moment arm helped minimize shear forces in comparison with the moments, which were the loading of interest. The test rig is shown schematically in Fig. 1.3.1.

Deflections and strains were measured by means of dial indicators and strain gages, respectively. The dial indicators readings were the primary source for response determination in the study, and the strain gage data were used for checking purposes. The location of the dial indicators is shown in Fig. 1.3.1. The load magnitude was measured using a strain-gage-based load cell. Figure 1.3.2 shows a sample load-strain curve obtained in the study for test PE-3, which involved loading a carbon steel elbow out of its plane, without applying any internal pressure.

Each specimen was loaded with an external force of sufficient magnitude to produce predominantly plastic response. In-plane and out-of-plane loading was applied and the effect of internal pressure on the response was studied. It was also possible to study the dependence of the response on material properties by comparing the results from stainless steel and from carbon steel elbows. Greenstreet concluded that internal pressure generally increases the moment at collapse, although the load at the onset of nonlinear response is decreased. He also noted that collapse moments of stainless steel elbows became increasingly smaller than those of carbon steel elbows of the same dimensions, and under the same loading conditions, when the flexibility characteristic (λ) was decreased.

Hilsenkopf, Bonet and Sollogoub (1988) conducted two series of tests on 90° long-radius elbows. The first series, which consisted of 10 tests, was conducted on thick-walled TU 42 C (equivalent to ASTM A-106 grade B) ferritic steel elbows, with an outside diameter to wall thickness ratio ($D_o/t=6.7$). A second series of 15 tests was conducted on thin-walled Z2 CN 18-10 (equivalent to ASTM A-312 Type 304L) austenitic stainless steel elbows with $D_o/t = 90$.

During the tests, the elbows were subjected to in-plane bending moments, in either the opening or the closing direction, or to out-of-plane moments. From the results obtained, and especially for the thin-walled elbows, Hilsenkopf et al. reported that the cross-section of the elbow tends to ovalize as soon as a bending moment is applied, in any direction, to one of the elbow’s extremities. This ovalization keeps increasing with the increasing applied moment. The tests were extended sufficiently to observe the ovalization modes under different types of loading and to reveal the failure mode.

Table 1.3.1 Summary of Properties and Loading Conditions of Specimens Used in the Tests Conducted by Greenstreet (1978)

Specimen	Nominal Dimensions			Material	Moment Loading			Pressure
	Outer Diam. (in.)	Inner Diam. (in.)	Wall thick. (in.)		In-plane		Out-of-Plane	
					Opening	Closing		
PE-1	6.625	6.065	0.280	Carbon St.	X			
PE-2	6.625	6.065	0.280	Carbon St.		X		
PE-3	6.625	6.065	0.280	Carbon St.			X	
PE-4	6.625	6.065	0.280	Carbon St.	X			X
PE-5	6.625	6.065	0.280	Carbon St.		X		X
PE-6	6.625	6.065	0.280	Carbon St.			X	X
PE-7	6.625	5.761	0.432	Carbon St.	X			
PE-8	6.625	5.761	0.432	Carbon St.		X		
PE-9	6.625	5.761	0.432	Carbon St.			X	
PE-10	6.625	6.065	0.280	Carbon St.	X			
PE-11	6.625	6.065	0.280	Carbon St.		X		
PE-12	6.625	6.065	0.280	Carbon St.			X	
PE-13	6.625	6.065	0.280	Carbon St.	X			X
PE-14	6.625	6.065	0.280	Carbon St.			X	X
PE-15	6.625	6.065	0.280	Stainless St.		X		
PE-16	6.625	6.065	0.280	Stainless St.		X		
PE-17	6.625	6.065	0.280	Stainless St.		X		
PE-18	6.625	5.761	0.432	Stainless St.		X		
PE-19	6.625	6.065	0.280	Carbon St.		X		
PE-20	6.625	5.761	0.432	Carbon St.		X		

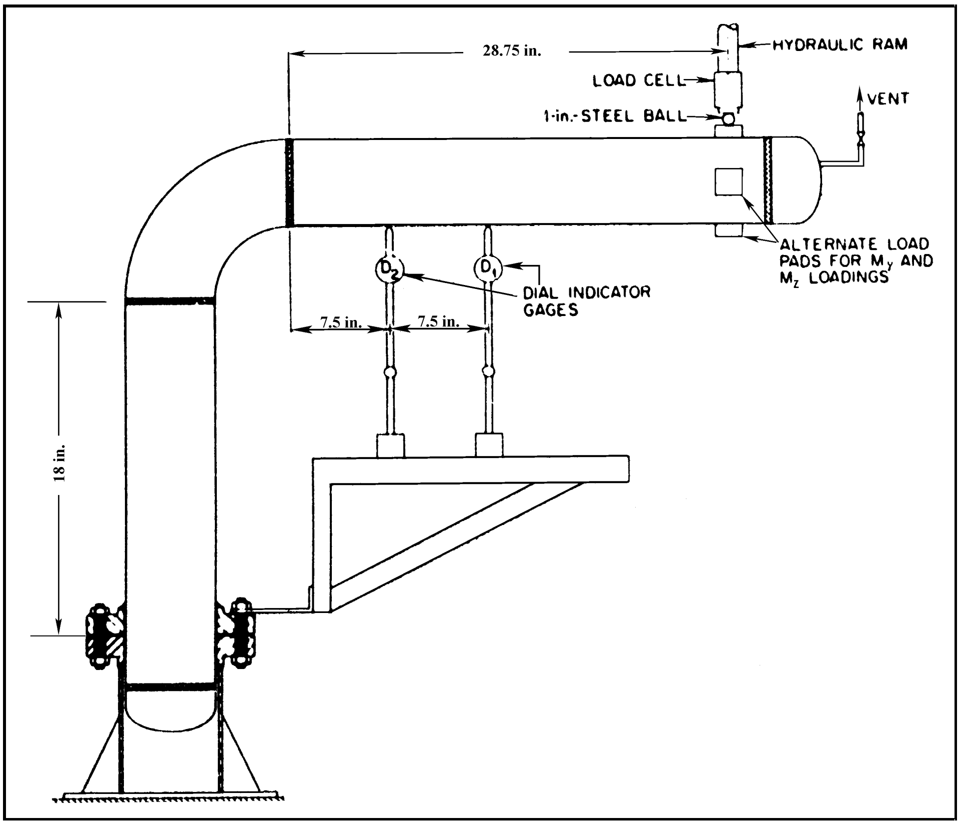

Fig. 1.3.1 Diagram of the Test Setup Used by Greenstreet (1978)

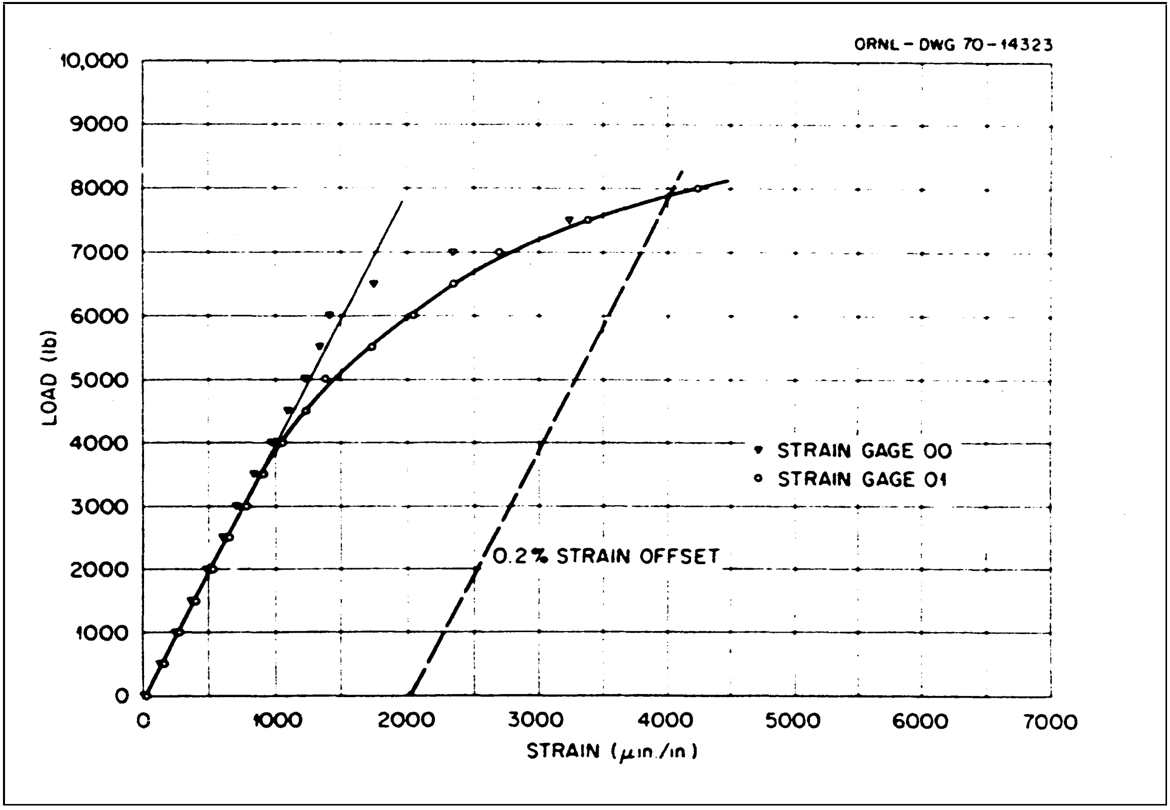

Fig. 1.3.2 Sample of the Load-Strain Response, Obtained by Greenstreet (1978), Test PE-3 (Out-of-Plane Loading, Without Pressure)

They concluded that in the case of in-plane bending in the opening direction, the ovalization of the elbow tends to increase its stiffness, and displace the weak spot in the assembly towards one of the junctions between the elbow and the adjacent straight pipe segments. Failure takes the form of a crease that appears at this weak spot and absorbs all subsequent deformation, preventing the elbow from deforming any further. In-plane bending in the closing direction tends to decrease the stiffness of the elbow, and failure takes the form of excessive ovalization, or flattening of the mid-section. It is reported that this mode of loading is the most critical, since failure takes place at a relatively low value of the applied moment.

The case of out-of-plane loading was also studied, and a sample of the load-deflection curves obtained is shown in Fig. 1.3.3. In this loading mode, the elbow is reported to undergo cross-sectional deformation that becomes irregular as the moment is increased beyond the limit value. At collapse, the elbow twists back on itself and a localized instability area appears in the form of a reentrant crease. It is reported that sudden failure does not occur, and that the moment at which instability occurs (instability moment) has a value that is higher than the one for in-plane closing, but lower than the one for in-plane opening.

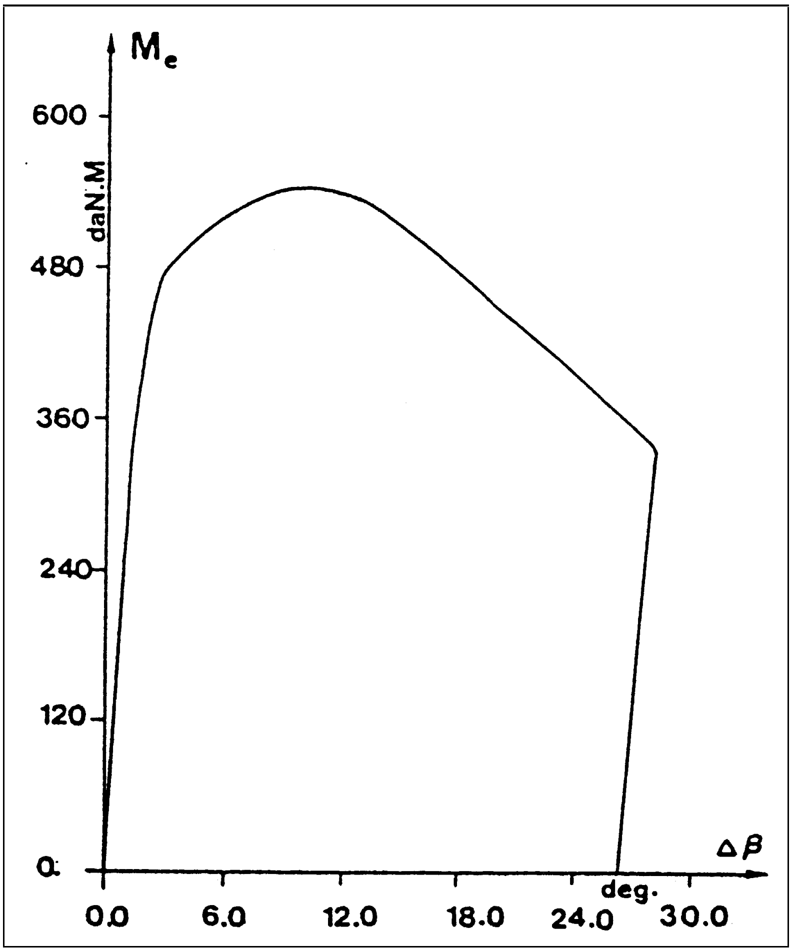

Fig. 1.3.3 **Load-Deflection Curve Obtained by Hilsenkopf et al. (1988), Thin-Walled Austenitic Stainless Steel Elbow Under Out-of-Plane Loading (Test 15)**

The effects of internal pressure and cyclic loading were also investigated. It was found that the pressure stiffens the elbow and opposes ovalization, but causes premature local instability to occur in some cases. This stiffening effect results in a marked increase of the limit moment, with a gain reaching 55% in the case of in-plane closing. Cyclic loading, on the other hand, was found to decrease the limit moment by as much as 11% and leads to a quicker transition from elastic to plastic response.

Another important experimental study was conducted by Smith and Ford (1967), to investigate the flexibility and the stresses in a three-dimensional pipeline under in-plane and out-of-plane loading. This work was an extension of an earlier investigation conducted by the same authors (1962) to study the flexibility of a two-dimensional pipeline.

In the first part of their study, Smith and Ford investigate the flexibility of the full-scale three-dimensional two-anchor pipeline, by measuring the end-reactions resulting from controlled anchor movements. Their pipeline was secured between two anchor frames which were bolted to the floor, and each end of the pipeline was attached to the corresponding anchor frame by means of six turnbuckles, arranged so that displacements can be imposed in any required direction.

The second part of this investigation was concerned with experiments on individual 90° pipe bends, in which measurements were made of the deflections, stresses and cross-sectional distortion resulting from in-plane and out-of-plane bending moments. Three pipe bends were used in these experiments, the first two being thin-walled long-radius bends, and the third a thick-walled welding elbow.

Testing was performed by applying bending moments about the principal axes of the bends. A combination of loads was applied in order to keep the moments constant throughout the length of the pipeline, and eliminate shear force effects. In the case of out-of-plane loading, a combination of torsion and out-of-plane bending was applied to produce a state of pure out-of-plane bending at the mid-section of the elbow, where measurements were made.

Longitudinal and transverse stresses were measured at the mid-section, their distribution around the section was plotted, as shown in Fig. 1.3.4. These stresses were compared to their theoretical values, according to the analysis of Turner and Ford (1957) for in-plane bending and the analysis of Smith (1967) for out-of-plane bending. The components tested in this study did not undergo any plastic deformation, and hence the measured values agree well with the estimates of these elastic analyses. However, some minor differences were found between the measured and the theoretical stress values, since the theories in question do not take end-effects into consideration. Another reason for the discrepancies is the fact that the cross-section of the pipe does not maintain its roundness, and its wall thickness does not remain constant, while a straight pipe is being bent to form an elbow. Measured instead of nominal dimensions were used in this second part of the experimental study to minimize such effects.

Kussmaul, Diem and Blind (1987) conducted an experimental study to evaluate the behavior of thick- and thin-walled pipe bends under dynamic loading conditions. In this study they sought to determine the quasi-static deformation behavior of pipe bends, subjected to in-plane bending, in the nonlinear range, and to describe the local and global failure behavior as a function of load history. They found that bends loaded in the in-plane closing direction attained a clear plastic instability load, contrary to the ones loaded in the opening direction. This was attributed to intense strain hardening that occurs in the fully plastic state. They also found that initiation of yielding occurs on the inner surface of the wall, near the crown of the elbow in thin-walled bends, whereas it occurs on the outer surface at the intrados in thick-walled bends.

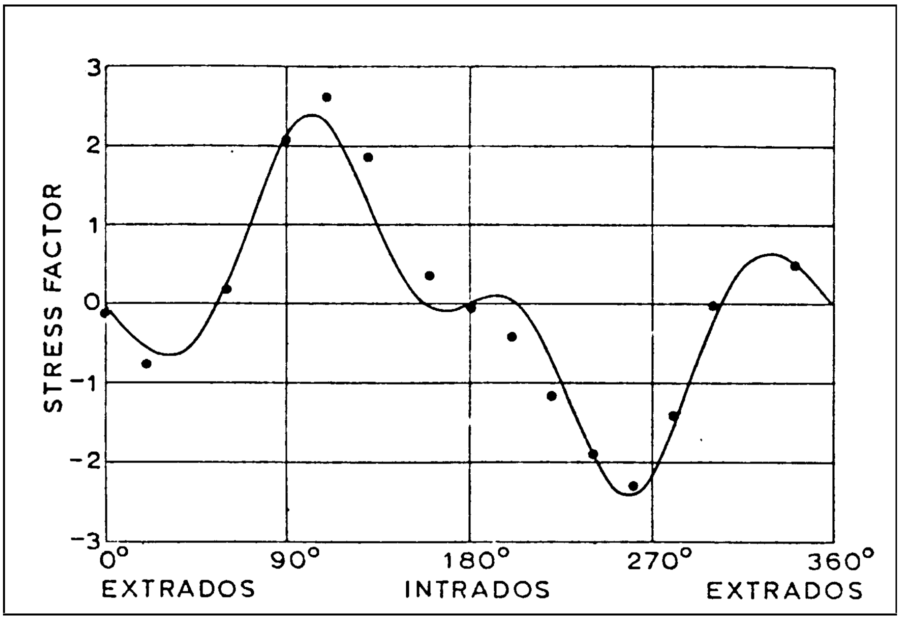

Fig. 1.3.4 Axial Stress Distribution in the Mid-Section of the First Bend Tested by Smith and Ford (1967), Out-of-Plane Loading

1.3.1 Comparisons with Theoretical and Numerical Work

As mentioned before, several researchers attempted to validate their theoretical or numerical findings using experimental methods. An example of such an investigation is the one conducted by Rodabaugh and George (1957) to validate their analytical solution of the problem of in-plane bending of pressurized pipe bends. They tested a 90° long-radius welding elbow with an outer-diameter of 30 inches, and a nominal wall thickness of 0.5 inch. The experiment was first conducted without applying any pressure, and then repeated three times, in which pressures of 400, 800 and 1100 psi were first applied to the elbow, and maintained while the bending moment was increased gradually. They noted that internal pressure does not alter the stress distribution significantly, but reduces the values of stress. They also concluded that their experimental results agree generally with their theory, and attributed the slight differences to end-effects and the non-uniformity of the wall thickness.

Sobel and Newman (1980, 1983, 1986) conducted three experiments on nominally identical 90° long-radius pipe bends, with an outer diameter of 16 inches and a wall thickness of 0.42 inch. In the first test, which was conducted at room temperature, and in the second test conducted at 1100°F (593°C), an in-plane moment was applied in steps until plastic collapse occurred. In the third test, conducted at 1100°F, the moment was increased to a value of 567,400 lb-in. and maintained at that value for about 2800 hours, to examine the creep behavior of the elbow.

These results were compared with those obtained from detailed elastic-plastic and creep analyses performed with the finite element program MARC. A comparison was also made with results obtained from computationally cheaper finite element analyses, using a simplified pipe bend element, whose formulation does not take end-effects into consideration, and a simplified creep modeling method. They concluded that the simplified analysis considerably overestimates the measured results, especially for the case of creep behavior. They also found that the correlation between the predictions of their detailed analysis and the measured results was satisfactory for elastic-plastic analyses, and inconclusive for creep analyses.

As a continuation of this series of tests, conducted at the Multi-Load Test Facility (MLTF) at the Westinghouse Advanced Energy Systems Division, Dhalla (1987) performed two buckling tests on long-radius thin-walled pipe bends, to validate a detailed nonlinear finite element analysis. The first test was performed at room temperature and the second at 1100°F. He also used the program MARC to model the problem and analyze it numerically, and included the stiffening effect of connected straight pipes into his analysis. He concluded that the correlation between numerical and experimental results is reasonable except for higher values of the applied moment. He reported that the analysis over-predicts the deformation, at collapse, by as much as 30 percent.

1.3.2 Effect of End-Constraints

The effect of end-constraints is one aspect of the pipe bend problem which lends itself more readily to experimental, rather than theoretical or numerical study. Most theories ignored this effect at first, for simplicity, and then tried to accommodate it later; while experiments always included this effect, due to the difficulty associated with supporting a pipe bend and subjecting it to external loads in the absence of connected straight pipe segments and/or flanges. Therefore, there has been a number of early experimental investigations treating this specific point.

Beskin (1945) presented some experimental results obtained by Symonds and Vigness which showed the importance of end effects. They tested a 90° pipe bend which has a theoretical flexibility factor of 38.4, and showed that when connected to straight pipe segments of the same size its flexibility factor is reduced to 32, and that in the case of a flange directly connected to the bend, the experimental flexibility factor is only 8. They concluded that flanges substantially diminish the bend's flexibility, and are clearly the most severe type of end-constraints.

Pardue and Vigness (1951) conducted a series of experiments on short-radius bends with different end-constraints, under a variety of loading conditions. Their results were difficult to compare with specific theories however, since they presented averaged factors from different loadings. They also used flanges with a thickness of 12.5 mm. which were later found to be too thin to realistically represent actual flanges.

Gross and Ford (1952) showed experimentally that the ovalization of the bend's cross-section varies along the axial direction, in the presence of end-constraints, and demonstrated the gradual decrease in ovalization from the mid-section towards the constrained ends. They presented some results obtained by Pardue and Vigness which show that more rigid end-constraints cause the point with maximum hoop stress to move from the two crowns towards the intrados of the bend.

1.4 Numerical Analysis of Pipe Bends

Flexibility factors and stress-intensification factors have been calculated accurately and verified with experiment. These are therefore suitable for direct use, in conjunction with three-dimensional beam theory, to predict the response of pipe bends. This approach however, is limited to linear elastic analysis, and although some attempts have been made to extend it to cover plastic response, more work is needed in this area to make it suitable for practical use. Detailed numerical analysis based on the shell-type behavior of pipe bends can therefore be used as a practical alternative, in cases where inelastic behavior - plasticity or viscoplasticity - dominates the response.

The finite element method, a general approach for the solution of problems in continuum mechanics, is a well established numerical analysis tool, and the most widely used, particularly in the area at issue. To model the behavior of pipe bends correctly, the structure can be represented by a group of doubly-curved thin shell elements. This type of analysis however, can prove to be costly in terms of the time and expertise required to model such a problem. It can also be very expensive in terms of the computer time needed to solve the governing equations, even with the huge leaps in computer power achieved recently, and expected in the near future.

The complexity of this problem is augmented by the fact that a fine mesh of elements, and hence a large set of equations, is generally needed to obtain accurate results. Furthermore, nonlinear analyses are solved in an incremental manner, and several iterations are generally needed to solve each increment, which makes a nonlinear analysis of a certain problem hundreds or even thousands of times more expensive than a linear analysis of the same problem.

1.4.1 Special Elbow Elements

For the above-mentioned reasons, special elements had to be developed, to make modeling the problem simpler and more economical, by taking advantage of the particular geometry and behavior of elbows. For example, knowing that strain gradients along the longitudinal direction of the elbow are usually mild, compared to those around the cross-section, the formulation of special elbow elements can be simplified, so as to minimize the computational cost. Moreover, an elbow can be thought of as a beam with a deforming cross-section, exhibiting shell-like behavior. Hence, like axisymmetric shell elements, special elbow elements can be designed to look like beams and yet behave like shells. This “centerline”, or “wireframe” representation makes the elements easier to use for modeling, especially when it is required to connect them to other types of elements like beams or straight pipes.

Hibbit (1974) described the formulation of the first special elbow element. In this element, piecewise cubic interpolation of displacement was used in the circumferential direction. To simplify the formulation, it was assumed that strain gradients along the axial direction are very small, and hence strains were assumed to be constant over each element’s length. This assumption gives rise to undesirable displacement discontinuities across element boundaries, and makes it impossible to include the effect of end-constraints on the elbow's behavior. The initial implementation of the pipe bend element, of the commercial finite element package MARC, was based on this formulation, and did not account for the axial stress caused by internal pressure.

Ohtsubo and Watanabe (1976, 1978) developed a ring-shaped element based on thin shell theory. This element allows the mid-wall surface to have radial, axial and circumferential components of displacement, thus accounting for both ovalization and warping of the cross-section. For interpolation in the circumferential direction, the element uses complete Fourier series truncated after m terms. Ohtsubo and Watanabe (1978) conducted a detailed numerical investigation and found that six Fourier modes (m=6) are sufficient, in a 90° elbow, to give accurate predictions for most practical thin-walled piping system applications. Elbows with a larger bend factor (h) are less flexible, and have a less complex stress distribution, and hence need fewer Fourier modes, with a minimum of m=4.

The number of degrees of freedom per element amounts only to 12m (only 72 degrees of freedom for m=6). A full shell model needs about 240 degrees of freedom per segment to achieve a comparable accuracy, and hence would be considered much more computationally expensive. The element also uses piecewise cubic Hermite polynomials for interpolation in the longitudinal direction which makes displacements and their derivatives continuous across element boundaries, but adds somewhat to the element's computational cost. The main drawback of this formulation is that, because of the chosen interpolation scheme, strains result from rigid body motion of the elbow, which makes the element ill-suited for modeling multi-elbow pipelines.

An extension of this element was developed by Takeda et al. (1979), in which two-dimensional cubic Hermite polynomials were used for interpolation, along with Fourier series. This element produced high-accuracy results, but was shown to be relatively expensive. The elbow elements of ABAQUS, the nonlinear finite element software used in this study, are based on the same ring element of Ohtsubo and Watanabe. In ABAQUS, cross-sectional motion is modeled with respect to a coordinate system that translates and rotates with the bend's axis, in order to deal properly with rigid body motions. In addition, the cost of computation is reduced by using linear or quadratic functions, instead of the original cubic polynomials, for interpolation in the longitudinal direction.

Bathe and Almeida (1980) implemented the classical potential energy approach in another special elbow element, and made the same set of simplifying assumptions that Von Kármán originally suggested. They did not even include the “correction for transverse compression” introduced by Gross (1952). Hence, only pure bending was allowed in the plane of the cross-section and warping was neglected. Gradients of axial and shear strains across the elbow’s wall thickness were also neglected.

The assumption of a long-radius elbow (R/r>>1), originally suggested by Von Kármán was also made in the formulation of this element. Therefore, in the Fourier series used to interpolate displacements around the cross-section, only even numbered terms were included. In addition, a maximum of three Fourier modes are allowed in the formulation, making the element unsuitable for modeling of more flexible elbows. Piecewise cubic Lagrange polynomials are used to interpolate in the longitudinal direction, although they are more expensive than the Hermite polynomials used by Ohtsubo and Watanabe, and later by Takeda et al.

This element has been enhanced later by Bathe and Almeida to include the effect of end-constraints (1982), and again to include the stiffening effects of internal pressure (1982). The same element was extended by Abo-Elkhier (1990), to fully capture the doubly-curved shell behavior of the elbow. The number of Fourier terms used in this formulation depend on the pipe bend’s flexibility characteristic (λ), with a maximum of four terms for the most flexible elbows. Abo-Elkhier also implemented the element and conducted some linear analyses for comparison with other numerical and experimental results from the literature. He concluded that the element was relatively efficient and accurate.

1.4.2 Numerical Analysis Using the Finite Element Method

Ohtsubo and Watanabe (1976) presented an investigation of the flexibility and stress-intensification factors for pipe bends under in-plane and out-of-plane loading, using their finite “ring” element. The effects of varying the wall thickness, end-constraints and initial deflections were also investigated in their analysis. The results of their elastic analysis show good agreement with experimental data. As shown in Fig. 1.4.1, they show that in the case of an unconnected (standalone) pipe bend under out-of-plane loading, the axial and hoop stresses have maximum values near the loaded end of the elbow. The location of these maximum values is shifted towards the mid-section of the elbow when it is connected to straight pipes.

Moreover, they stated that the code equations give an estimate of the stresses in the elbow which are higher by 0-15 percent, in the case of in-plane bending, and by 40-50 percent in the case of out-of-plane bending, than the values obtained from their numerical analysis of a connected pipe bend. Therefore, they recommended that the design equations be based on the combined piping system, rather than on the individual components. They concluded that the non-uniformity of the wall thickness, caused by the manufacturing process, has a strong effect on the flexibility and stresses in the pipe bend.

Mello and Griffin (1974) carried out an elastic-plastic analysis of elbows made of different strain-hardening materials, under in-plane bending, using the special pipe-bend element (library element 17) of the MARC software. They ignored geometric nonlinearity in their analysis. Consequently, the load-deflection curves they obtained showed that the load increases monotonically with the displacement, and did not indicate a well defined buckling or (geometric) instability load. They relied on a number of methods, described in detail in the next chapter of this study, to determine the plastic (material) collapse load.

Sobel and Newman (1977) conducted a similar analysis using the same software and element, and accounted for geometric nonlinearity effects. They stated that when these effects are included, instability occurs at the first relative maximum in the load-deflection curve, and ovalization of the cross-section becomes evident. They maintained that this instability load was lower for the case where the applied moment tended to close the elbow, and they obtained a definitive value for this load. In the other case, where the moment tended to open the elbow, their results were inconclusive, since the value of the instability (limit) load appeared to be higher than the highest value of the applied moment. Hence, they determined that the closing mode is the critical one. They concluded that geometric nonlinearity effects are important, and that they should be taken into consideration, especially since including them does not raise the computational cost of an elastic-plastic analysis excessively.

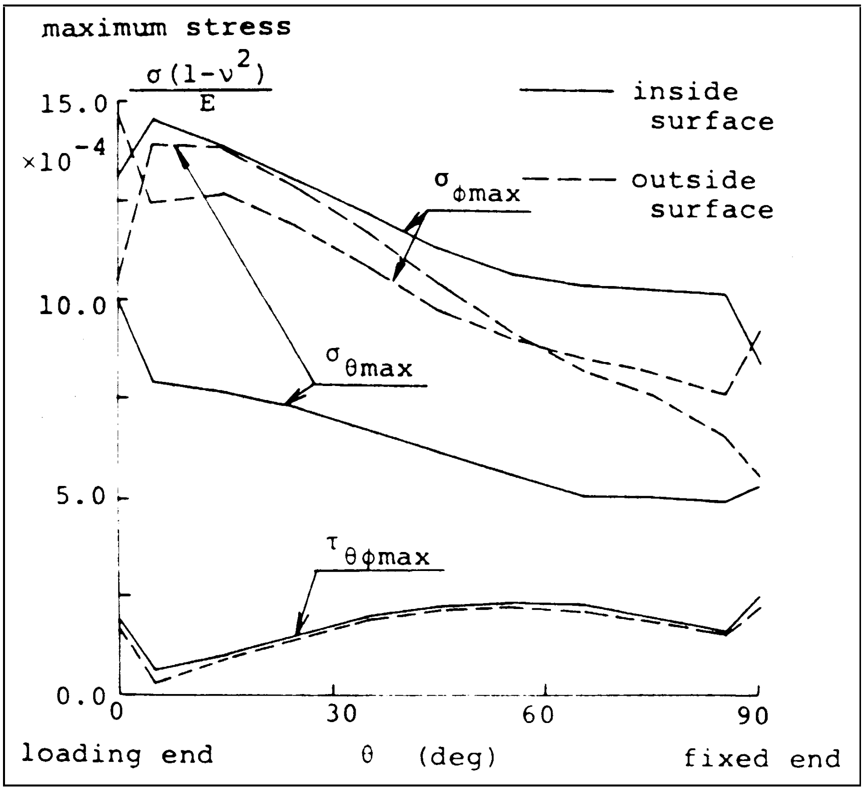

Fig. 1.4.1 **Longitudinal Distribution of Maximum Axial, Hoop and Shear Stresses in a Long-Radius (R/r = 2.88) Standalone 90° Pipe Bend With a Bend Factor h=0.108 (Ohtsubo and Watanabe, 1976)**

Dhalla (1980) performed a nonlinear boundary value analysis of a Liquid Metal Fast Breeder Reactor (LMFBR) elbow under in-plane bending. He used the doubly-curved isoparametric bicubic shell element of the MARC general purpose finite element software. The purpose of this analysis was to provide guidance in the selection of a finite element mesh density, and incrementation parameters, and to explore the effects of residual stresses due to thermal transients on the load carrying capacity of an elbow.

He showed that in the linear elastic range, axial mesh refinement had no significant effect, while mesh refinement from five to nine elements around the half-section, altered the predicted displacements by three percent and the predicted stresses by 10 percent. He stated that the elastic analysis gave a lower bound on the limit load, which increased when the mesh was refined, and concluded that the coarser mesh is sufficient for routine design applications, to predict elastic stress distributions in the elbow.

He argued that the inelastic analysis gave an upper bound on the limit load, which decreased with load step refinement especially in the range where large displacements become predominant. He also stated that mesh refinement beyond seven elements around the half-section did not improve the accuracy significantly. Concerning residual stresses, he concluded that these do not affect the response, unless they significantly alter the cross-sectional shape.

Sobel and Newman (1980, 1986) extended this work, and compared the results obtained numerically using the same shell element, and using the special pipe-bend element (MARC library elements 4 and 17, respectively), with experimental data. Figure 1.4.2 shows a comparison between the load-deflection curves obtained using the different approaches. Dhalla (1987) also compared his results to the same experimental results, and concluded that good agreement existed up to 80 percent of the measured instability load.

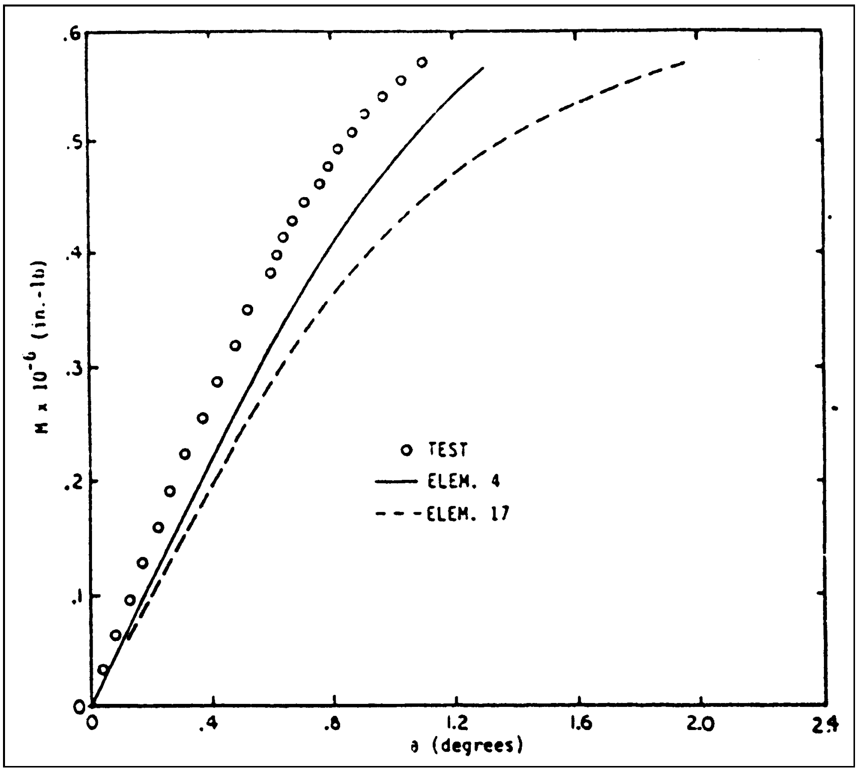

Fig. 1.4.2 Comparison Between Numerical and Experimental Load-Deflection Results (Sobel and Newman, 1986)

Hibbit and Leung (1985) presented a comprehensive report which documents the verification of the ABAQUS special elbow elements, and their application to realistic pipeline design problems. The verification is based on the international piping benchmark problem number (2): the Battelle-Columbus piping elbow creep test (McAfee, 1979), which involves extensive creep and plastic deformation of a single 90° elbow in its own plane, and for which experimental and numerical results were previously reported by Dhalla and Newman (1978). They also analyzed the same problem using the degenerate form of the elements, where warping and axial gradients of ovalization are neglected, and using conventional shell elements, to provide further comparative results.

They found that there are some inconsistencies between the experimental results and the numerical results obtained from all the models, even the full shell model of Dhalla and Newman. They attributed this inconsistency to the difficulty of establishing reliable constitutive models and data for materials whose behavior is as complex as that of stainless steel at 1100°F (600°C), and hence they pointed out the need for care and conservatism in qualifying design by inelastic analysis in such cases.

A different realistic pipeline was analyzed three times using the special ABAQUS elements, to predict its response to a loading sequence that includes rapid thermal and mechanical load transients, and high-temperature creep loads. The first and second models used the full-formulation element, which allows continuous ovalization in the pipeline, and the third model used the degenerate form of the element, which causes ovalization to be discontinuous across element boundaries, and hence neglects the effect of the interaction between elbows and adjacent straight pipes (end-constraints). The first model was fully constrained at its ends, and the second was allowed to ovalize but not to warp.

Results were compared to those of another numerical study conducted on the same pipeline by Dhalla (1982), using the MARC pipe-bend element, which does not allow for continuous ovalization in the pipeline. The results of all models showed good agreement. This was unexpected, given the different results given by the different modeling approaches in the verification study, and given that axial stress gradients did exist. This apparently paradoxical finding was attributed to the fact that the analysis was driven by thermal (expansion) loads instead of external mechanical ones. It was also argued that the very high pressure applied in this analysis, might have reduced the severity of the end-effects.

Shalaby (1996) and Shalaby and Younan (1998a, 1998b, 1999a, 1999b) presented a comprehensive study of the elastic-plastic behavior of pipe bends under in-plane bending, using the degenerate form of the special ABAQUS elbow element. The effect of internal pressure on the value of the limit loads, for several elbow geometries was also studied. A complete stress analysis was performed, including a detailed analysis of the stress and strain distributions around the elbow's cross-section.

They found that the behavior of pipe bends under in-plane bending, in the opening direction, was very similar in the elastic range, to the one under bending in the opposite direction. The behavior was quite different however, in the plastic regime, where the bend displayed much higher stiffness, and underwent much larger deformations in the opening mode. In this mode, the way the cross-section deforms makes the structure stiffer in response to the moment load. This effect is reversed in the closing mode.

They also found that internal pressure generally decreases the first yield load. In the closing mode, instability loads were found to increase with the increase in internal pressure, up to a certain value, and then decrease again. In the opening mode, this trend was reversed. They showed that the effect of internal pressure was directly associated with geometric nonlinearity, and they argued that the pressure tends to keep the cross-section circular in both cases, thereby moderating the geometric stiffening effect in the opening mode, and its equivalent weakening effect in the closing mode. The effect of strain hardening was also studied, and found to increase the value of the limit loads.

1.5 Limit Load Analysis

In piping systems, allowing some measure of controlled plastic deformation without endangering the safety of components is sometimes considered good design practice. Limit analyses are one method of avoiding undesirable structural response in the components of such systems.

It is known from classical limit analysis theorems that, if in a structure a stress distribution can be found, which satisfies internal equilibrium and balances a certain external load without violating the yield condition, this load can be carried safely by the structure, and can be considered a lower bound estimate of the limit load. This is generally known as the lower bound theorem. The upper bound theorem states that an estimate of the limit load, found by equating the rate of energy dissipation, inside the structure, to the rate at which work is done by external forces, is either high or correct.

Gross (1952) presented estimates of limit moments for short-radius pipe bends obtained experimentally. Marcal and Turner (1961) utilized linear elastic analyses as a means of obtaining lower bound estimates of the limit load. They argued that using an exact elastic analysis in conjunction with a relevant yield criterion produces first yield loads, which are by definition lower bounds on collapse (limit) loads.

Marcal (1967) reviewed the theory of symmetrically loaded shells of revolution, and modified a previously developed computer program to conduct an elastic-plastic numerical analysis of pipe elbows under in-plane bending. He presented load-strain plots obtained from this analysis, and showed that the maximum bending moment obtained from such an analysis can be considered an estimate of the collapse moment. He also found his results to be in good agreement with the experimental results of Gross.

Bolt and Greenstreet (1971) presented estimates of first yield moments, proportional limit moments and plastic collapse moments for 15 pipe bends of different dimensions, under in-plane and out-of-plane loads. They compared these values with those obtained using theoretically derived formulas, and studied the effect of internal pressure on the value of the limit moments. Greenstreet (1978) expanded this work to cover results from five additional tests, and interpreted those results on the broader basis afforded by the added information.

Spence and Findlay (1973) further developed Marcal and Turner's approach of using the results of linear elastic analyses in estimating limit loads. They used the analysis method of Clark and Reissner (1951), which is based on thin shell theory, to calculate the elastic direct and bending stresses. They stated that the most highly stressed position in the case of in-plane bending is at the neutral axis of bending (i.e. crown), and gave simplified formulas for the stress-intensification factors at this position. They also gave lower and upper bounds on the limit load, which can be expressed as:

$$M_L \geq \frac{A + B}{\dfrac{2A}{3} + B} M_y \tag{1.5.1.A}$$

$$M_L \leq \frac{2(A + B)}{\left[\dfrac{2}{3}(1 + \nu)A + B\right]} M_y \tag{1.5.1.B}$$

Where A=1.892 $h^{-2/3}$, B=0.96$\left(\frac{r}{R}\right)$$h^{-1/3}$, and M_y is the moment required to initiate first yield. They also manipulate the results of a creep analysis of bends, performed by Spence (1973), to give approximate lower and upper bounds for limit moments. An approximate estimate of the limit moment is given by:

$$M_L = 0.8h^{0.6}\frac{D_o^3 - D_i^3}{6}\sigma_y \quad \text{, for } h \le 1.45 \qquad (1.5.2.A)$$

$$M_L = \frac{D_o^3 - D_i^3}{6}\sigma_y \quad \text{, for } h > 1.45 \qquad (1.5.2.B)$$

They compared their estimates with those of Gross(1952), Marcal (1967) and those of Bolt and Greenstreet (1971), and found the agreement to be reasonable. They also concluded that the low values of limit moments for pipe bends, compared to those of straight pipes, should prompt designers to treat bends carefully, even in simple piping systems.

Rodabaugh (1979) gave crude estimates of the limit moments as:

$$M_L = \frac{3}{2}\frac{h^{3/2}}{1.8}Z\sigma_y \quad \text{, for in-plane bending} \qquad (1.5.3.A)$$

$$M_L = \frac{3}{2}\frac{h^{3/2}}{1.5}Z\sigma_y \quad \text{, for out-of-plane bending} \qquad (1.5.3.B)$$

Where Z is the section modulus of the elbow's cross-section, given by $Z = \frac{\pi}{32}\frac{(D_o^4 - D_i^4)}{D_o}$ for circular cross-sections. These equations are based on the assumptions that the limit moment is 3/2 times the first-yield moment, and that the maximum stress in a pipe bend occurs in the hoop direction, and is given by $\sigma_\phi = \frac{1.8}{h^{2/3}}\frac{M}{Z}$ for in-plane bending, and $\sigma_\phi = \frac{1.5}{h^{2/3}}\frac{M}{Z}$ for out-of-plane bending. Rodabaugh stated that these hoop stresses are almost entirely due to through-the-wall bending, and that the membrane stresses in the hoop direction are relatively negligible.

He also compared estimates of limit moments computed using several formulas with the experimental results of Bolt and Greenstreet, and found the formulas of Spence and Findlay (Eq. 1.5.2) to be reasonably accurate and conservative for both in-plane and out-of-plane moments, although they were originally developed for the case of in-plane bending only. He also showed that the formula used in the ASME Boiler and Pressure Vessel Code gave highly conservative estimates, compared to the experimental data. The Code formula, which accounts for both pressure and moment loading, was given as:

$$\frac{PD_o}{2t}+\frac{3}{4}\frac{1.95}{h^{2/3}}\frac{M_L}{Z}\leq 1.5\sigma_y \tag{1.5.4}$$

Calladine (1974) followed closely the approach taken by Spence and Findlay and developed an expression for the in-plane bending moment that causes gross plastic deformation (M_p) in the structure of thin-walled pipe bends ($h\leq 0.5$). He showed that the ratio of the full plastic moment to the first yield moment (M_p/M_y) can be easily determined from his findings, and that this ratio is slightly dependent on the value of Poisson’s ratio (ν). He noted that for $\nu\approx 0.3$, $M_p/M_y\approx 2.0$ irrespective of the value of the pipe bend factor (h). Finally, he concluded that his results were in close agreement with those of Spence (1972, 1973) and Marcal (1967).

Kitching, Zarrabi and Moore (1971) gave a lower bound on the limit moment for the case of in-plane bending of smooth circular pipe bends of uniform thickness, also based on the same approach. They avoided the assumptions made by Calladine and by Spence and Findlay in their analyses, which impose restrictions on geometric variables, like the radius ratio (R/r) and the bend factor (h). In their analysis however, the assumptions of thin shell theory are made, end-effects are ignored and the included angle of bend (α) is not taken as a variable. They gave their results in the form (M_L/M_y), and showed that they depended on the radius ratio as well as the bend factor. They compared their results to the experimental results of Bolt and Greenstreet, and concluded that the limit moment can be overestimated by more than 10 percent by those analyses that assume a long-radius elbow ($R/r>>1$).

Chan, Boyle and Spence (1984) generalized the same approach, to include the effect of end-constraints. They gave approximate limit loads for α=90° and α=180° pipe bends with end-constraints, under in-plane and out-of-plane loads. The stiffening effect of internal pressure was not included in their analysis however. They showed that the limit load for out-of-plane bending is closer to the straight pipe value, as compared to a similar bend under in-plane bending. Their results were in close agreement with the test data of Bolt and Greenstreet.

1.6 Rationale for the Investigation

Pipe bends, or elbows, were shown to have substantially more flexibility and much higher stresses than straight pipes and are considered the critical components in a piping system. Hence, for the purpose of designing and/or qualifying a pipeline structurally, it is useful to have a reliable estimate of their load carrying capacity, along with a deep understanding of their structural behavior until instability, under different and combined loading conditions.

As seen from the previous sections, there are many investigations in the literature that are concerned with the structural behavior of these piping system components. However, while the larger part of these investigations tackle the problem of in-plane loading of pipe bends, relatively little work has been done on the out-of-plane loading problem.

Moreover, the majority of the investigations in the literature ignore very important effects, such as geometric and material nonlinearity, and the effect of internal pressure. In fact, most theoretical developments involve simplifying assumptions of this kind, and even classical limit analysis concepts are based on small deflection theory.

1.7 Scope of Work

The primary goal of the present work is to study the elastic-plastic behavior of pipe bends, under out-of-plane moment loading. It is also required to study the effects of changing the value of the pipe bend factor ($h=Rt/r^2$), and the value of internal pressure, on that behavior, and to determine the limit moments in each case.

The finite element method is used throughout the analysis. ABAQUS, a commercial finite element code, is used as the modeling and analysis tool. A special elbow element, selected from the software's element library, was found to be suitable for modeling the problem, since its implementation takes ovalization and warping into consideration, and uses quadratic interpolation along the elbow's axial direction, guaranteeing continuity of the solution variables across element boundaries.

A standalone, long-radius (R/r=3) pipe bend is used as the model throughout the study. A parametric study is then performed, in which the pipe bend factor takes ten different values between 0.0632 and 0.4417. To vary the pipe bend factor (h), the value of the wall thickness is varied, between 0.165 in. and 1.031 in. The nominal diameter of the pipe is kept constant at a value of 16 in. and the bend radius (R) is kept at a value of 24 in. to keep the radius ratio constant.

For each of these ten models, several analyses are performed at different values of internal pressure. The range of pressure for each model starts from zero, and is incremented by 100 psi until a value of the pressure is reached, where the elbow undergoes plastic instability due solely to pressure.

The results of these analyses are presented in the form of load-deflection plots, for each load case belonging to each model. From the load-deflection curves, the limit moments of each case are obtained. The limit loads are then compared to those computed using some of the analytical and empirical equations available in the literature. The effects of modeling parameters are also studied. The results obtained from small-displacement and large-displacement analyses are compared, and the effect of using a strain-hardening material model is also investigated.

To better understand the behavior of pipe elbows, under out-of-plane bending and internal pressure, it was deemed important to know how the cross-section deforms, and to study the distribution of stresses that cause it to deform in a particular manner. An elbow with pipe bend factor h=0.1615 is considered, and the results of a detailed analysis thereof are examined.

Chapter Two

Modeling and Analysis

2.1 Finite Element Modeling and Analysis

2.1.1 Geometry

One main goal of this study is to investigate the effect of internal pressure on the behavior of pipe bends, with different values of the bend factor ($h=Rt/r^2$), under out-of-plane moment loading. Therefore, in the parametric study that was conducted, the bend factor was taken as one of the parameters, and was varied by changing the pipe wall thickness (t), keeping the radius of curvature of the bend's axis (R) and the mid-wall radius (r) constant.

As shown in Fig. 2.1.1, a 90° standalone pipe bend, was used throughout this study. This yields more conservative estimates of limit loads, since the stiffening effect of end-constraints (e.g. attached flanges or connected straight pipe segments) is neglected.

The pipe bend had a nominal diameter of 16 inches, and the bend's axis had a radius of curvature R=24 in., to represent a long-radius elbow with radius ratio (R/r=3). The pipe wall thickness (t) varied between 0.165 in. and 1.031 in., which corresponds to a variation in the bend factor (h) between 0.0632 to 0.4417. These values were chosen to represent standard pipe schedules ranging between Sch.5S and Sch.100.

2.1.2 Material Model

The material used throughout this study is type 304 stainless steel, following the measured response, at room temperature, reported by Sobel and Newman (1979). This material has the following properties:

Young's modulus : $E = 28.1\times10^6$ psi (193.74 GPa)
Yield stress : $\sigma_y = 39440$ psi (271.93 MPa)
Poisson's ratio : $\nu = 0.2642$

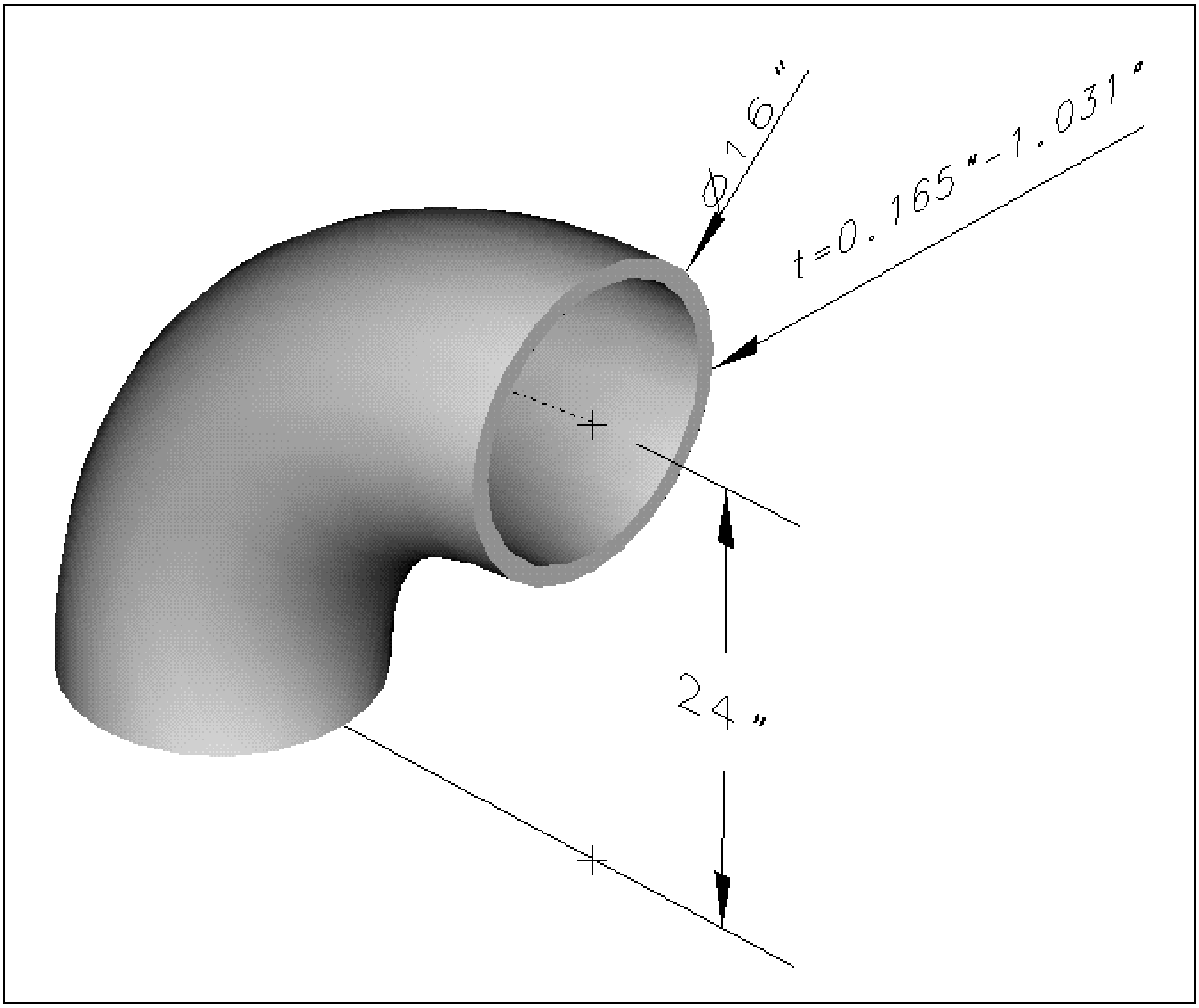

Fig. 2.1.1 Geometry of the Pipe Bend Used in this Study

The material is assumed to be isotropic and elastic-perfectly-plastic throughout this study, as can be seen from the stress-strain curve of Fig. 2.1.2.a. To concentrate on the effect of internal pressure on the behavior of the pipe bend, it was preferred to ignore other effects such as strain hardening, temperature, and end-constraints, and hence this ideal material model was used.

Another reason for making this assumption is that it yields more conservative estimates of the limit loads, which is desirable from a design point of view, especially since Sobel and Newman (1979) point out that the stress-strain curve in Fig. 2.1.2.b has a 0.2%-strain-offset yield stress that is 20% higher than the value for type 304 stainless steel, at room temperature, according to the Nuclear Systems Materials Handbook. For this same reason, the yield stress of the elastic-perfectly-plastic material model was assigned the conservative value of 39440 psi - the reported proportionality limit - instead of taking the reported 0.2%-strain-offset value.

As part of this study, a comparison is made between this material model and the original strain-hardening model (Fig. 2.1.2.b) reported by Sobel and Newman, to investigate the effect of strain hardening on the computed values of the limit moments.

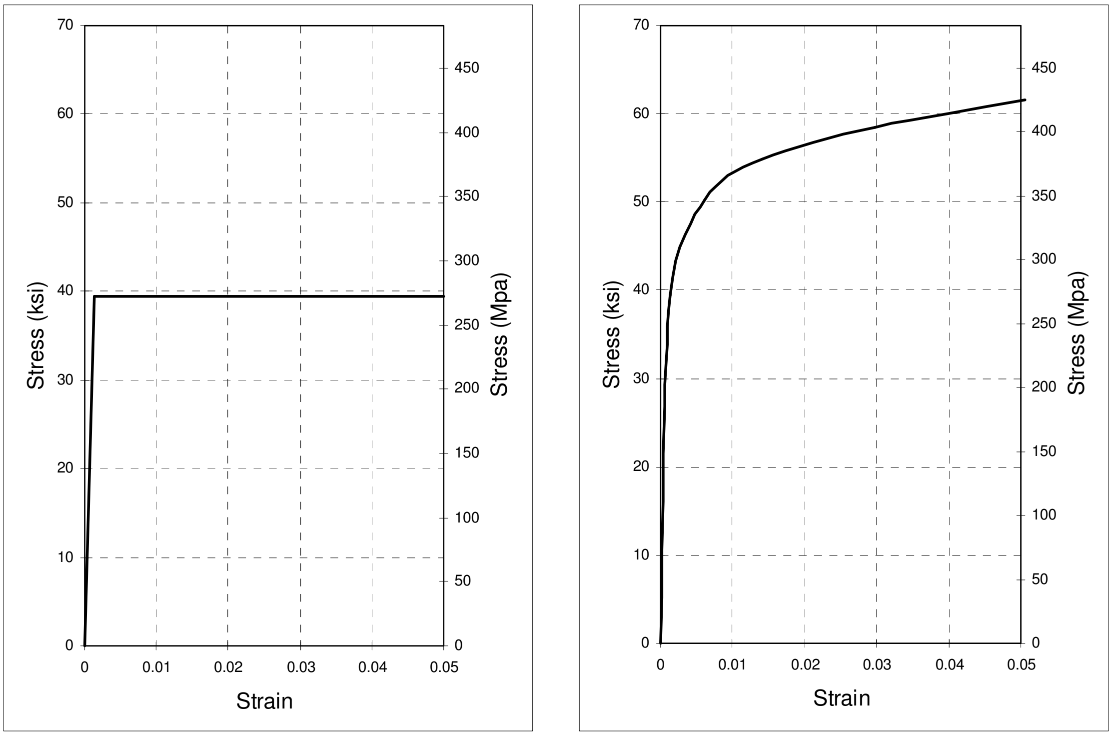

(a) **(b)**

Fig. 2.1.2 Stress-Strain Curves of (a) The Ideal Material Model Used Throughout this Study (b) The Material Model Used to Investigate the Effect of Strain Hardening

2.1.3 Element Selection and Meshing

ABAQUS, the commercial finite element code used, offers a choice between four different special elbow elements, namely ELBOW31, ELBOW31B, ELBOW31C and ELBOW32. In all of these elements, shell theory is used to model the behavior of pipe bends, polynomial interpolation is used along the axial direction, together with Fourier interpolation which is used around the pipe to model the ovalization and warping of the section.

In the usual semi-analytical approach to the analysis of pipe bends, flexibility factors are used to correct the results obtained by simple beam theory. This approach might yield acceptable results in linear analyses, but in nonlinear cases, the pipe must be modeled as a shell to predict the response accurately.

Although the four element types available in ABAQUS use a full shell formulation around the circumference, they have the shape of beam elements, having two nodes at the extremities, except for ELBOW32 which has three nodes along its length. The two-node elements use linear interpolation in the axial direction, and have one integration station (cross-section) per element, along their length. On the other hand, ELBOW32 uses quadratic interpolation in the axial direction and has two integration stations along its length, following a two-point Gauss integration rule.

The integration stations consist of a number of integration points around the cross-section, as shown in Fig. 2.1.3. At each integration point, results (e.g. values of stress and strain) can be obtained at several points across the wall thickness.

The formulation of elements ELBOW31B and ELBOW31C is simplified and hence less expensive. With these elements, warping of the cross-section is not considered, and ovalization is assumed to be constant over each element's length; i.e. axial gradients of ovalization are neglected, thus making ovalization discontinuous between the elements of the model. In the formulation of ELBOW31C, a further approximation is made by neglecting the odd numbered terms in the Fourier interpolation around the section, with the exception of the first term.

Some of these approximations are assumptions made in the flexibility-factor approach used in linear analysis of pipe bends, and they are often satisfactory. However, in this study, the deformation of the elbow's cross-sections, under out-of-plane moment loading, was expected to involve warping and significant gradients of ovalization. This prediction is confirmed by the results presented in the next chapter. Hence, although computationally more expensive, it was necessary to use an element with a more complete formulation, either ELBOW31 or ELBOW32.

Under out-of-plane moment loading, the fixed end of the pipe bend is under torsion, while the loaded end is under bending, and hence the elbow is expected to sustain substantial axial variation and gradients of stress and strain. ELBOW32 was therefore preferred over ELBOW31, due to its use of a quadratic, instead of linear, interpolation in the axial direction; especially since this does not have a strong adverse effect on its computational cost.

The results of a mesh convergence study, for ELBOW elements used to model a 90° pipe bend under in-plane moment loading, are available in the ABAQUS (1998) Example Problems

Manual. These results, suggest that a single quadratic (ELBOW32), or two linear elements (i.e. ELBOW31 or one of the simplified versions thereof) can be used to model the whole pipe bend accurately. Shalaby (1996) reported that a model with 12 ELBOW31B elements predicted limit moments, under in-plane loading, that are up to 12% higher, depending on the value of internal pressure, compared to those predicted by a single-element model. Shalaby also pointed out that no considerable difference existed between the results of both models when no internal pressure was applied.

This leads to the conclusion that a model with six ELBOW32 elements can be considered convergent, and would produce satisfactory results in the present case. Such a model would produce results at 12 integration stations along the length of the model. However, due to the expected complexity of the deformation patterns, and because sharp axial gradients of stress and strain are expected to be present in the case of out-of-plane loading, it was important to produce results at closer intervals along the length of the model.

Therefore, twice the required number of elements were used, and the 90° span of the elbow was equally divided into 12 ELBOW32 elements. This model enables results (i.e. stresses, strains, sectional deformation, etc.) to be examined at 24 different cross-sections along the length of the elbow. The numbering of the associated 25 nodes, as well as the boundary conditions applied onto the model are shown in Fig. 2.1.4.

Since a two-point Gauss rule is used for integration in the axial direction (ABAQUS, 1998), the first and last integration sections are approximately 1.585° away from the elbow's extremities. Also, the integration sections are not exactly equidistant; the distances between consecutive sections follow an alternating pattern instead of being equal. In other words, the two integration sections belonging to the same element are farther apart, compared to two consecutive such sections belonging to two adjacent elements, and the ratio between the two distances is 1.366.

The choice of the number of terms taken in the Fourier series, for interpolation around the cross-section, is based on numerical experiments. According to the ABAQUS Theory Manual (1998), the detailed numerical investigation of this choice, documented by Ohtsubo and Watanabe (1976, 1978), is relevant to the formulation in ABAQUS. Based on this investigation, six modes are recommended for thin-walled elbows. It is also pointed out, in the ABAQUS User's Manual (1998), that less than six Fourier modes would be suitable for use with thick-walled elbows, but would overestimate the stiffness of thin-walled elbows, and hence six modes are required in this case. Hence, Six Fourier modes, the maximum available in ABAQUS/Standard, were used for interpolation around the section.

It was also pointed out that the number of integration points around the section should not be less than three times the number of Fourier modes, to avoid singularities in the stiffness matrix. Consequently, 20 integration points were used per section. The integration points and their numbering system are shown in Fig. 2.1.3. As shown in the figure, results computed at any of those 20 integration points, can be retrieved at seven different depths across the wall thickness.

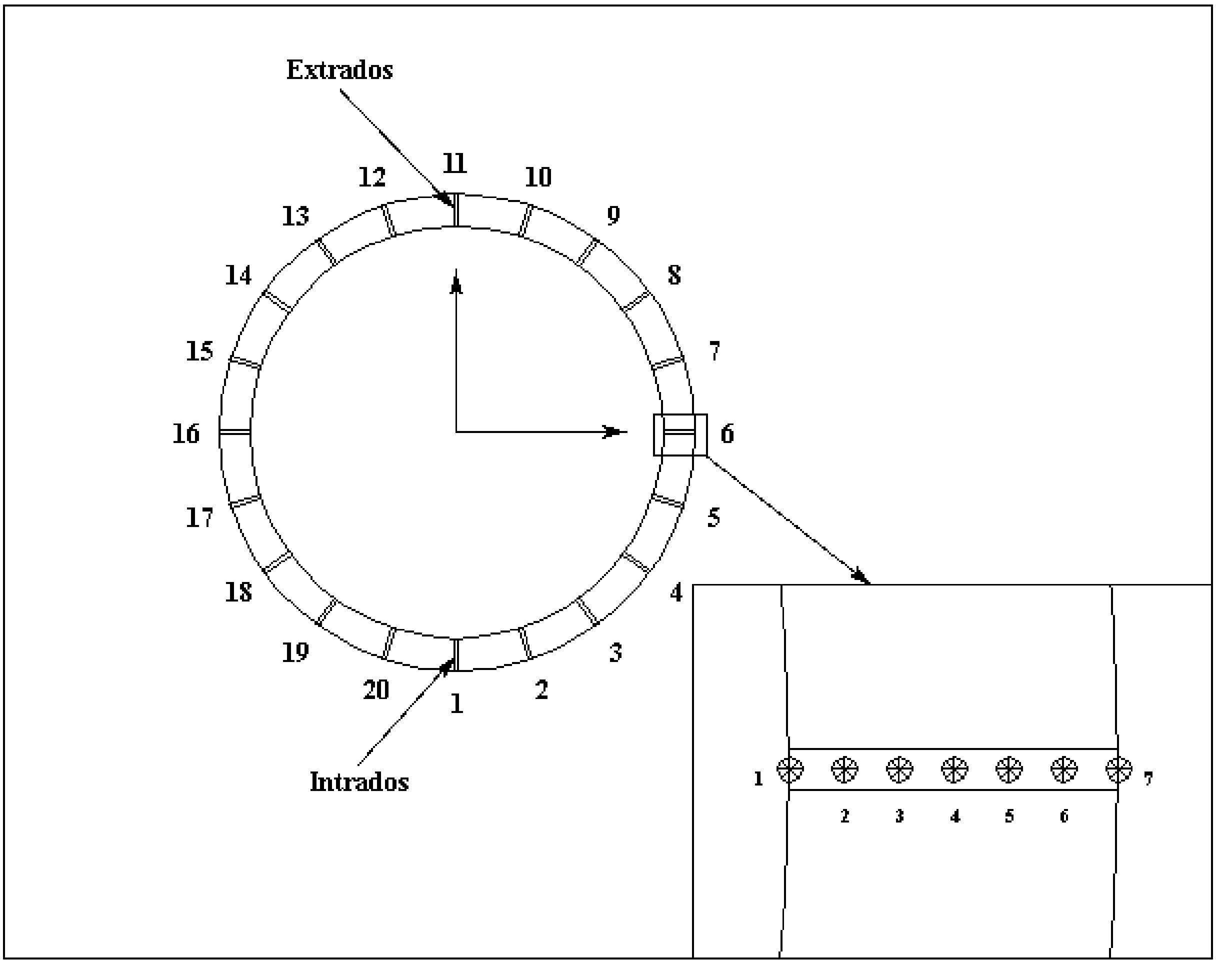

Fig. 2.1.3 Distribution and Numbering of Integration Points Around an Integration Station, and Points, Across the Pipe Wall, at which Results Can Be Obtained

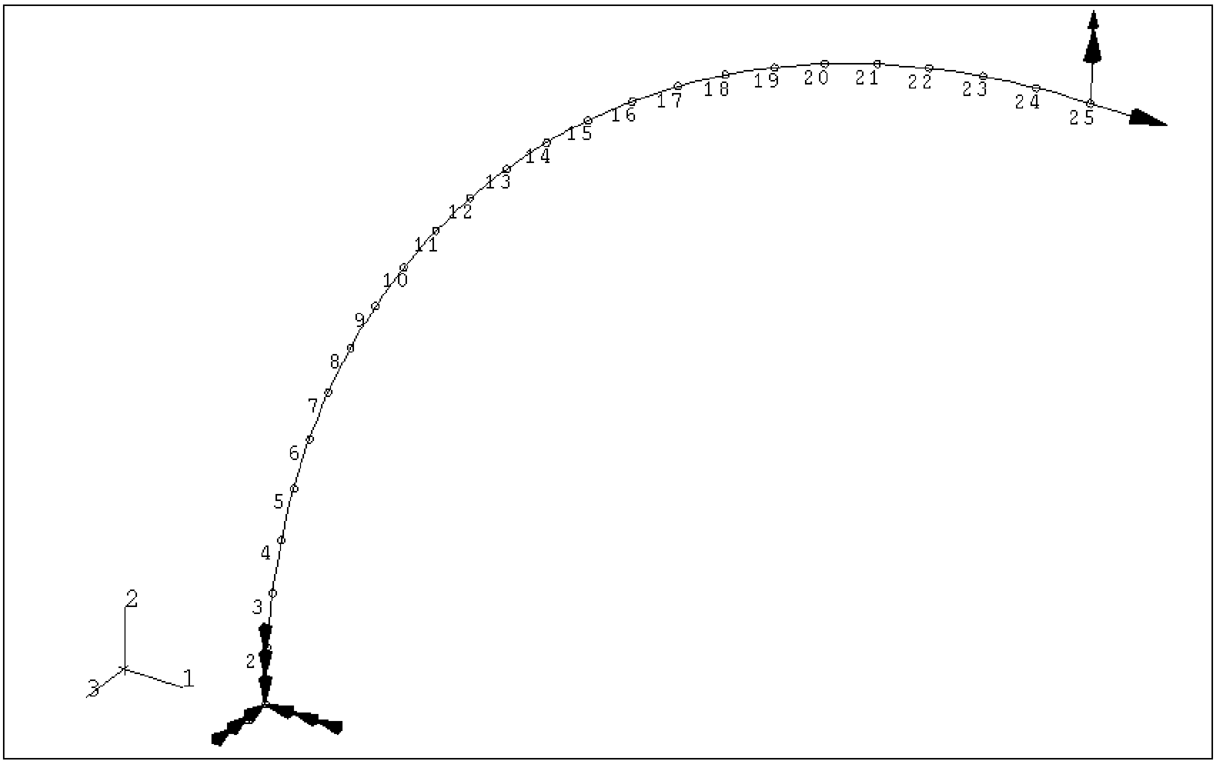

Fig. 2.1.4 Finite Element Mesh and Boundary Conditions Applied to the Model

2.1.4 Boundary Conditions

The special elbow elements in ABAQUS, including ELBOW32, have two degrees of freedom per node that represent cross-section ovalization and warping, in addition to the six kinematic degrees of freedom which represent translations and rotations in three dimensional space. As shown in Fig. 2.1.4, all six kinematic degrees of freedom were restrained at the fixed end, more specifically at the first node, to prevent rigid-body motion; however the cross-section was left free to deform, to simulate the standalone condition as discussed before.

Loading is done in two load steps; during the first step the pressure is incremented, and then it is kept constant, as a “dead load”, during the second step, while the (live) moment load is being incremented. Both load steps take geometric and material nonlinearity into consideration, and at high values of internal pressure, it is possible for the material at some points in the model to go beyond the elastic limit, before the moment load is applied.

In Fig. 2.1.4, the pressure load could not be illustrated, since a center-line representation is used for the elbow, but the axial force due to internal pressure in a closed-end configuration, can be seen at node 25. The closed-end condition was chosen for the analysis, to include the axial component of stress caused by internal pressure. This axial force is incremented proportionally with pressure, and is included as a follower load, i.e. its direction stays tangent to the bend's center-line, at the end node, even after the model deforms.

The moment load, is represented in the same figure, by an upward vector at node 25, the elbow's loaded end. The actual moment follows a right-hand rule around this vector. The second load step, is deflection controlled, or deflection driven. In other words, increments of an out-of-plane rotation are prescribed at the loaded end, instead of moment increments. This method is used in unstable collapse problems, because at the point of instability, the load starts decreasing and cannot be further incremented, while the deflection continues to increase and incrementing it remains possible.

2.2 Solution Procedure

2.2.1 Nonlinear Static Stress Analysis with ABAQUS

2.2.1.1 Time Scale for Incrementation

A simulation in ABAQUS, consists of one or more analysis steps. As discussed before, the present simulation consists of one initial step during which the pressure alone is applied, and a second step during which the pressure is kept constant and the moment load is applied. Both of these steps are nonlinear static stress analyses. In a nonlinear analysis, the solution cannot be computed by solving a system of linear equations, as would be done in a linear analysis. Instead, ABAQUS finds the solution by specifying the load as a function of time, and incrementing time to obtain the nonlinear response.

In some cases, the time scale used in ABAQUS is quite real; for example, the response may be caused by temperatures varying with time, based on a previous transient heat transfer step, or the material properties may involve rate-dependent plasticity, so that a natural time scale exists. The present case however, does not have such a natural scale, and ABAQUS defaults to a time scale in which "time" varies from zero to unity, over each step. The prescribed load, or displacement, is then incremented proportionally with "time". ABAQUS combines incremental and iterative procedures for solving nonlinear problems. Using the Newton method, it takes several iterations to determine an acceptable solution to each time increment.

2.2.1.2 Incrementation Scheme

By default, ABAQUS automatically adjusts the size of the time increments, based on computational efficiency. The only incrementation control parameters that were specified in the input to the code are the following:

- The *initial increment size*=0.01
- The *maximum increment size*=0.01 for the second step (moment loading), and was given the value of 0.1 for the first step (pressure loading). Small increments were required in the second step, to obtain a smooth load-deflection curve.
- The *minimum increment size*=0.0001
- The *maximum number of increments per step*=100 for the first step, 1200 for the second step.

The automatic increment size adjustment procedure works as follows. If the solution has not converged after 16 iterations, or if the solution appears to diverge, ABAQUS abandons the increment and starts over with the increment size set to 0.25 of its current value. If the solution still fails to converge, the increment size is reduced again, and this process is repeated until a solution is found. The analysis is stopped if convergence is not achieved within five attempts, or if the time increment becomes smaller than the user-defined minimum increment size. If two consecutive increments require less than five iterations to achieve convergence, this indicates that the solution is being found easily, and the increment size is increased by 50 percent.

Of course this automatic incrementation scheme can be overridden, but it was found to work efficiently with the problem at hand. The analysis ends when the load is fully applied, i.e. when “time” reaches unity, or when the maximum number of increments for the step is reached.

2.2.1.3 Convergence Criteria for an Increment

After each iteration in an increment, ABAQUS checks whether each node in the model is in equilibrium. The basic statement of equilibrium is that the internal forces, F_i, caused by the stresses in the elements attached to the node, and the external forces, F, applied on that node, must balance each other; i.e. $F-F_i=0$. In a nonlinear problem however, the difference between the external and internal forces will never be exactly zero. This difference is known as the force residual, $F_r=F-F_i$.

The solution is considered as being in equilibrium, if the force residual, F_r, is less than a tolerance value. By default, this tolerance is set to 0.5% of an average force in the structure, F_a, averaged over time. ABAQUS automatically calculates this spatially and time-averaged force throughout the analysis. Of course this tolerance can be overridden (e.g. set to a constant value), but the default scheme was found satisfactory.

ABAQUS also checks the correction, c, to the solution variable performed during the current *iteration*, and compares it to the change, Δ, in that same variable over the current *increment*. In the usual case, the analysis is load driven, and the solution variable is the displacement; i.e. the load is incremented and the displacement is solved for. As discussed above however, the present analysis is displacement driven, and the solution variable in this case is the load. For the solution to be considered convergent, c must be less than a fraction of Δ. The default value of 1% was used for this fraction.

Both of the above criteria have to be met before ABAQUS accepts the solution as converged.

2.2.2 Stabilization Methods

Problems that involve buckling or collapse behavior, like limit load problems or problems that exhibit softening, are known to be ill-conditioned or unstable, because at some point the load-displacement response shows a negative stiffness and the structure must release strain energy to remain in equilibrium. In the simplest cases, displacement control alone can provide a solution, even when the conjugate load (the reaction force) is decreasing as the displacement increases. In more unstable cases however, this is not enough. Several approaches are possible for modeling such behavior.

It is possible to treat the buckling response dynamically, thus modeling the response with inertia effects included as the structure snaps. This is accomplished in ABAQUS, by terminating the static solution procedure, and switching to a dynamic procedure, when the static solution becomes unstable. Another approach is to use an arc-length method, like the modified Riks algorithm described below, to search for points of static equilibrium in the load-deflection plane. Another alternative method, where the structure is stabilized using artificial damping or “dashpots”, is also described below. This method is especially useful in the cases where the instabilities are local (e.g. surface wrinkling), in which case global load-control methods such as the Riks method are not appropriate.

2.2.2.1 Modified Riks (Adaptive Arc-Length) Method

The Riks method solves simultaneously for both load and displacement, using another quantity to measure the progress of the solution. This quantity is the “arc length” along the static equilibrium path in load-displacement space.

Although post-buckling behavior is beyond the scope of this study, it is interesting to note that this approach was able to provide solutions even when both load and displacement decreased instead of increasing. An example of such behavior is illustrated in Fig. 2.2.1. As the moment load decreases, the elbow moves back towards its original configuration. This effect was only observed in thin-walled elbows, in the presence of internal pressure; which suggests that the Bourdon effect of pressure might be the origin of this restoring force.

Despite the ability of this method to find the equilibrium path, regardless of whether the response is stable or unstable, it was found to be inadequate for the problem under investigation. Very tight user control had to be exercised over the incrementation parameters and convergence criteria, and each analysis had to be re-run several times, before usable results could be produced. Figure 2.2.2 illustrates some of the problems encountered with this method.

2.2.2.2 Volume-Proportional Damping Method

With this approach viscous forces of the form $F_v = \zeta.\mathbf{M}.\mathbf{v}$, are added to the global equilibrium equations, $F\text{-}F_i\text{-}F_v=0$, where $\mathbf{M}$ is an artificial mass matrix calculated with unit density, ζ is a damping coefficient, $\mathbf{v}$ is the vector of nodal velocities (“time” being hypothetical, as discussed above); and as defined before, F and F_i are the external and internal forces, respectively.

Instability in a local region appears in the form of a sudden increase in the nodal velocities of that region. Consequently, the viscous forces increase, allowing the released strain energy to be dissipated through the locally applied damping, thereby stabilizing the overall response. The damping coefficient, ζ, is determined in such a way that the dissipated energy, during a step, is a small fraction of the strain energy. This fraction, called the dissipation intensity, was left at its default value of 2×10^{-4}.

While the response is stable, these viscous forces are small enough not to perturb the solution significantly. In fact, as demonstrated by Fig. 2.2.3 the results obtained using this method are in excellent agreement with those obtained by the above-mentioned Riks method. This method was also found to be efficient, and was used throughout this entire study.

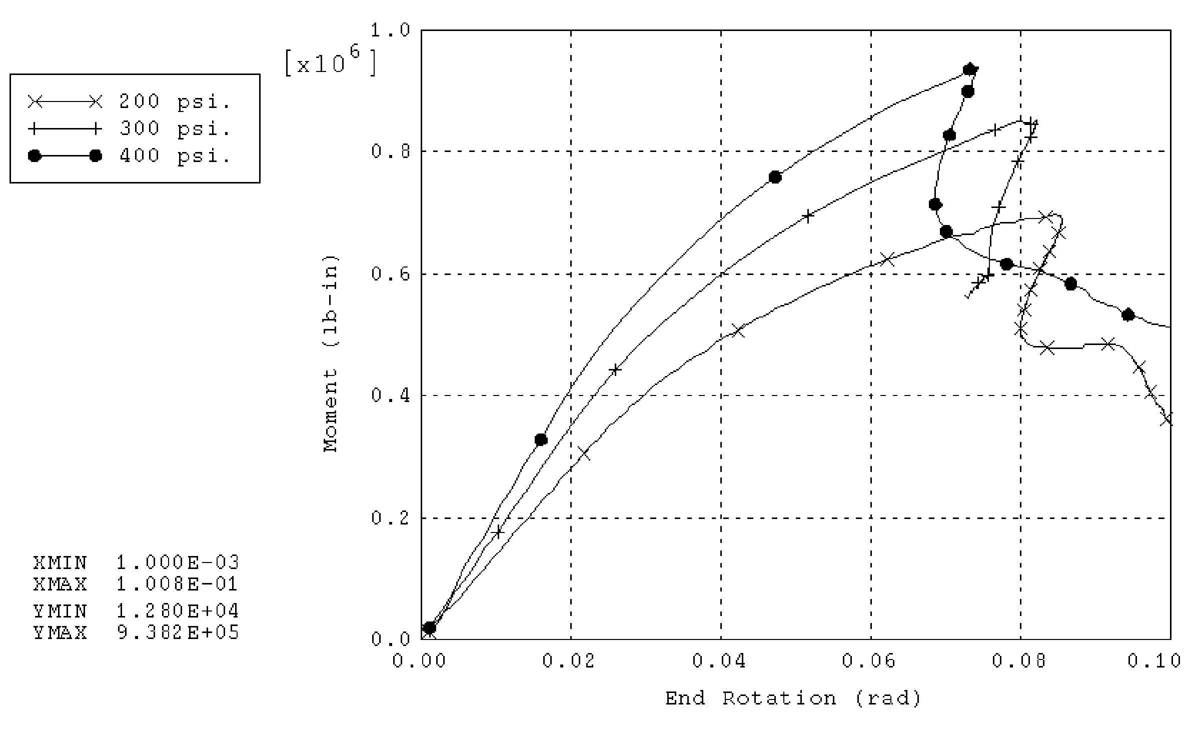

Fig. 2.2.1 **Post-Buckling Behavior of a Thin-Walled Elbow (h=0.0632) Under Different Values of Internal Pressure**

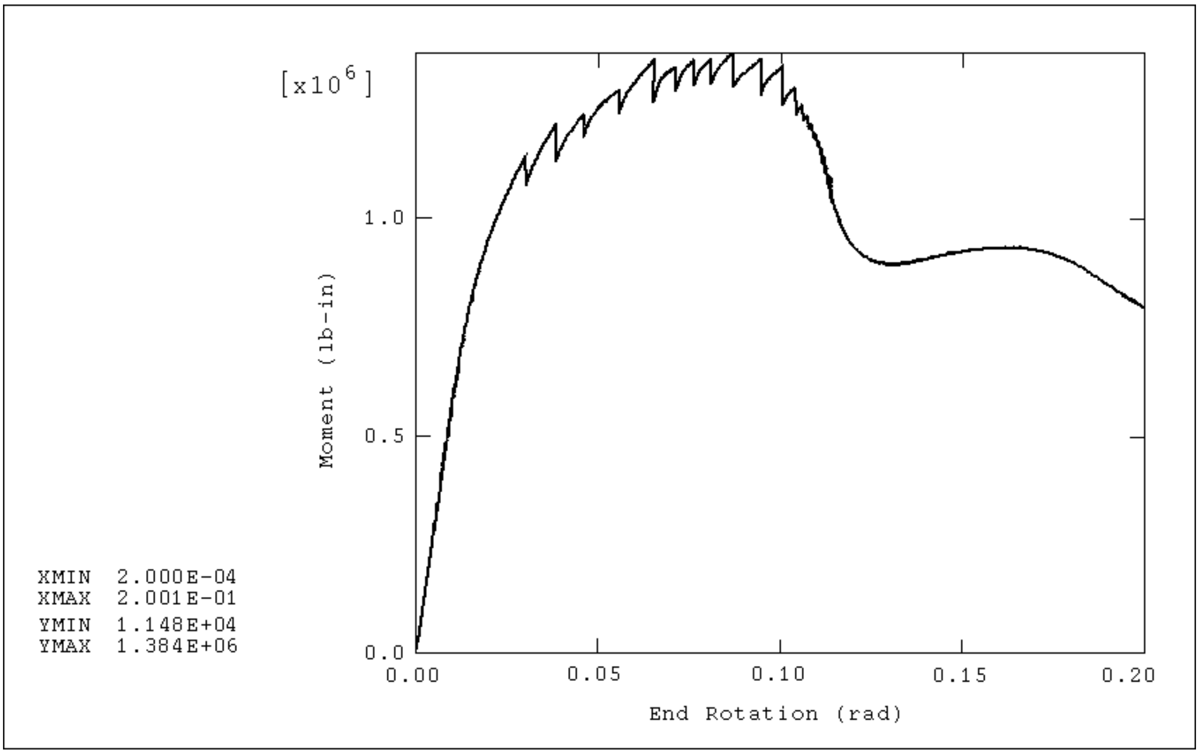

Fig. 2.2.2 Load-Deflection Curve for an Elbow With h=0.1615, Obtained Using the Riks Method With Inadequate Values of Solution Control Parameters - Strain-Hardening Material, No Internal Pressure

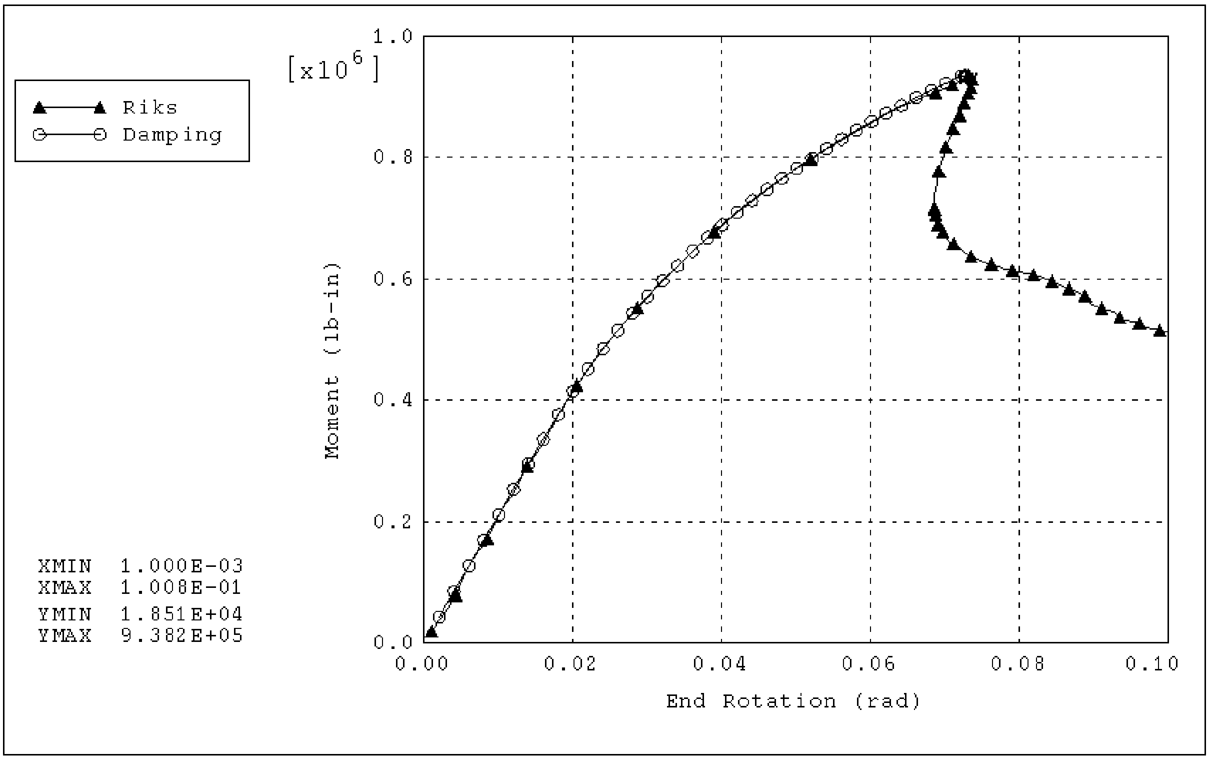

Fig. 2.2.3 Load-Deflection Curves for an Elbow With h=0.0632, Obtained Using the Riks and the Damping Stabilization Methods - Internal Pressure: 400 psi

2.3 Limit Load Analysis

2.3.1 Definitions of Limit Moments

The **first yield moment** M_y i*s* defined here as the moment at which the material of the structure, in this case the pipe bend, first yields at the most highly stressed point. On the load-deflection curve, this moment load does not necessarily correspond with the proportional limit. Moreover, a pipe bend is usually capable of sustaining loads that are considerably higher than M_y, because at this stage in loading history, most of the bend's material is still elastic, and can restrain the bend, as a whole, from undergoing excessively large deformation.

The definition of the **limit moment** M_L, according to classical limit analysis, is an idealized one. It ignores geometric nonlinearity and strain hardening effects, since it is built on small-displacement theory, and assumes that the material response is elastic-perfectly-plastic. According to this definition, there are three stages in load history. The first stage is where the moment applied is less than the first yield moment, no straining occurs in the structure and stresses are less than the yield strength σ_y. Then, as the moment is increased above M_y, but before reaching M_L, part of the material undergoes plastic straining with stresses at σ_y, but the structure is still restrained by the region of the material which is still elastic. Finally, when the limit moment is reached, the elastic region is either nonexistent or insufficient to prevent the structure from deforming excessively. The limit moment, according to this definition, is sometimes referred to as the "yield-point moment", since the *whole structure* is said to "yield" at this point, but the limit moment M_L is different from the first yield moment M_y, defined above.

The **plastic instability moment**, or the "instability moment" M_i, is defined here as the maximum point on a load-deflection curve, characterized by a zero slope; i.e. where additional deflection can be induced without increasing the applied load. The instability moment is considered an important measure, since it is sometimes smaller than the limit moment M_L, defined above, depending on whether large deformations strengthen or weaken the structure, by changing its configuration. Hence, plastic instability, in this text, also referred to as "structural instability", does not strictly indicate material instability, but rather the combined effect of material and geometric instability.

The **plastic collapse moment** M_c, or simply the "collapse moment", is defined loosely as the moment at which significant plastic deformation occurs in the structure of the pipe bend. Several specific definitions, and methods for determining M_c are available in the literature. Out of these definitions and methods, the most applicable to the present case are selected and discussed in detail below. These definitions assume a large-deflection elastic-plastic analysis.

In the present study, the terms "limit moment" and "limit load" do not adhere to the above-mentioned classical limit analysis definition. Instead, they are used to refer, collectively, to the plastic collapse moment M_c and the plastic instability moment M_i. This is because from a design point of view, the collapse and instability moments can be used as indicators of the structure's load carrying capacity, and hence should be regarded as design limits that should not be exceeded.

2.3.2 Methods for Determining the Plastic Collapse Moment

According to the **tangent-intersection method**, the collapse moment can be obtained by drawing tangents to the linear and nonlinear portions of the load-deflection curve, as shown in Fig. 2.3.1. The moment at the intersection of the two tangents is taken as the plastic collapse moment. Of course, this definition has a serious drawback, because it is sensitive to where the tangent is drawn to the nonlinear part of the curve. As a matter of fact, if this tangent is drawn at the highest point in the curve, the result will be the instability moment.

The **twice-elastic-deformation method**, shown in Fig. 2.3.2, defines the collapse moment as the moment at which the deflection is twice the value of the elastic deflection, D_e. This elastic deflection is attained at the point where the value of the moment is equal to the first yield moment, M_y.

Another method for determining the plastic collapse moment, is the **twice-elastic-slope method**. This method is illustrated in Fig. 2.3.3. It defines the collapse moment as the moment at the intercept of a line drawn from the origin of the load-deflection curve, at twice the slope of the linear or "elastic" part of the load-deflection curve. This definition, with reference to Fig. 2.3.3, can be expressed as: $M=M_c$ when $\tan(\phi)=2\tan(\theta)$. A similar method is called the **angle method**, and it is expressed as: $M=M_c$ when $\phi=2\theta$. Of course these two methods are not equivalent, and it is noted that the angle method is sensitive to changes in the scales of the axes of the load-deflection curve.

The **1%-plastic-strain method**, defines the collapse moment as occurring at an equivalent plastic strain of 1%. If the response of the structure is computed numerically, like in the present case, some difficulty might be encountered if the structure reaches instability before an equivalent plastic strain of this magnitude is reached, or if convergence is not achieved up to this point. On the other hand, if the response is obtained experimentally, a large number of strain gages is needed, unless the location of maximum plastic strain is known in advance. The same applies for the **0.2%-offset-strain method**, which defines the collapse moment as the moment causing a permanent strain of 0.2%, in the direction of maximum stress.

Another, less commonly used method, is the **proportional-limit method**. This defines M_c as the moment that causes the load-deflection curve to deviate from linearity. The collapse moment estimated with this method is not the same as the first yield moment M_y; in fact, it is generally greater than M_y, although it is considered lower bound compared to the estimates of the other methods. It can produce consistent results when used with numerical analyses, but is subject to error in determining the point of deviation from linearity of experimental measurements.

The twice-elastic-slope method is the one adopted in sections III and VIII of the ASME Boiler and Pressure Vessel code. Its definition of the collapse moment is clear and precise, which promotes consistency in its results. This method is also convenient in its use, since only the load-deflection curve is needed. It eliminates the need for determining the first yield point, or the location of maximum strains, for each case analyzed. The collapse moment determined by this method is a more conservative estimate of the structure's load carrying capacity, compared to the instability moment. It can be used as an approximation of the instability moment in case convergence is not obtained up to instability.

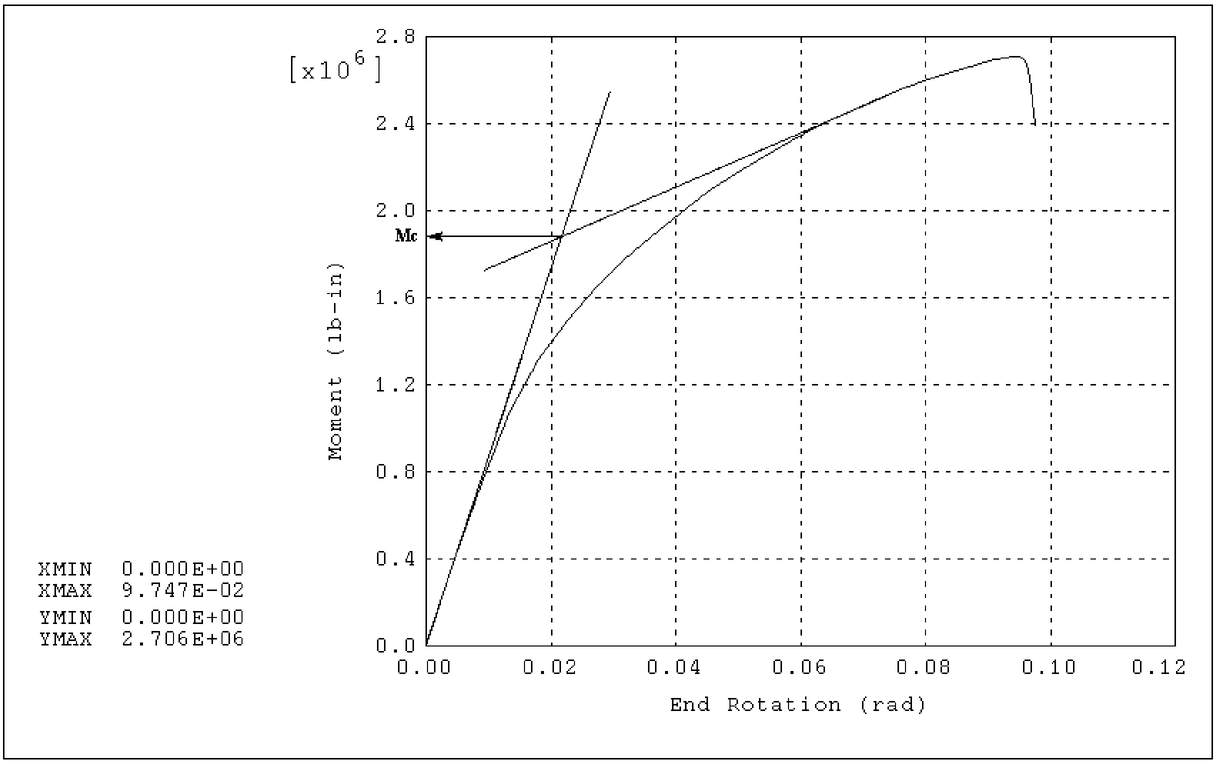

Fig. 2.3.1 **The Tangent-Intersection Method of Determining the Plastic Collapse Moment**

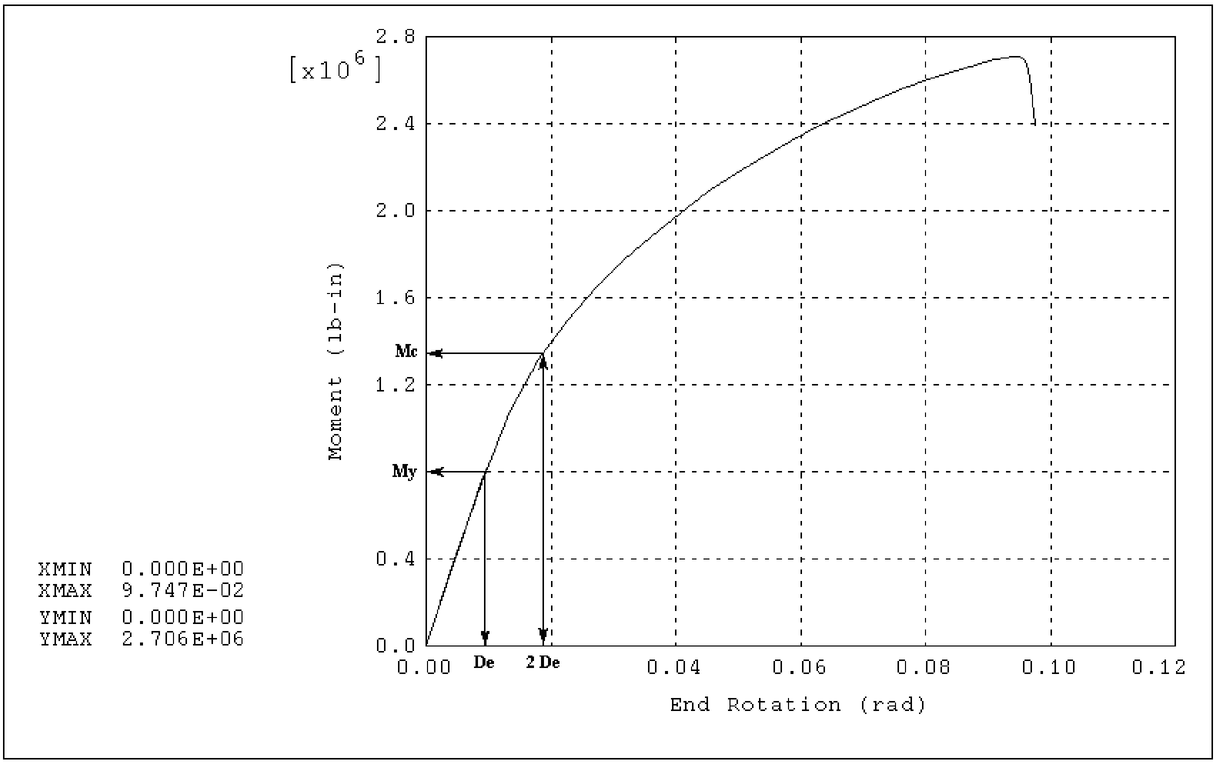

Fig. 2.3.2 **The Twice-Elastic-Deformation Method of Determining the Plastic Collapse Moment**

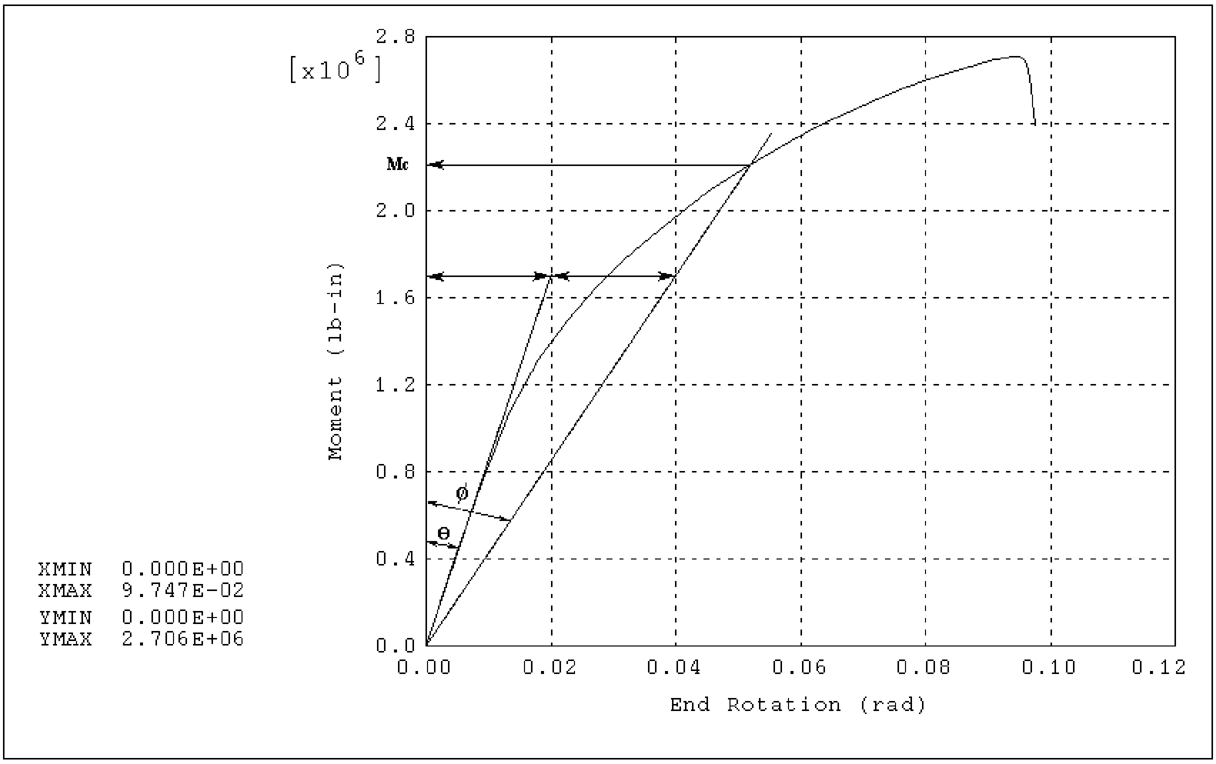

Fig. 2.3.3 The Twice-Elastic-Slope Method of Determining the Plastic Collapse Moment

2.4 Verification Study

In this section, the behavior of a pipe bend under out-of-plane loading, obtained from a finite element analysis, is compared to its behavior, under similar conditions, obtained experimentally. The purpose of this comparison is to verify that the code used, ABAQUS, and its ELBOW32 element do in fact simulate the real behavior of pipe bends accurately, and that they have been used adequately in the modeling and analysis of the problem, throughout this study.

2.4.1 Description of the Experimental Procedure

The experimental results used here are those reported by Greenstreet (1978), for his PE-3 test (refer to Table 1.3.1 for a summary of the 20 tests conducted by Greenstreet). A diagram of the test setup, along with a brief description of the procedure were given in section 1.3, the diagram is repeated in Fig. 2.4.1 for convenience, and a more detailed description of test PE-3 is given here.

No internal pressure loading was applied in test PE-3, and unfortunately, only the limit moment values were reported for test PE-6, which combined out-of-plane and internal pressure loading. Load-deflection and load-strain curves were not given for this latter test, and the values of the limit moments, alone, were considered to be insufficient, for the purpose of comparison and verification.

The specimen used in this test is a long-radius (R/r=3) commercial butt-welding elbow, made from ASTM A-106 grade B seamless carbon steel pipe. The elbow was formed by forcing straight pipe segments over a mandrel, in a furnace with a temperature range of 871°C to 982°C (1600°F to 1800°F).

The nominal dimensions of this specimen are as follows:

Outer diameter : $D_o = 6.625$ in. (168.3 mm.)
Wall thickness : $t = 0.280$ in. (7.1 mm.)
Bend radius : $R = 9$ in. (228.6 mm.)

In Fig. 2.4.1, the straight pipe segments attached to the bend can be seen. These pipe extensions are made of the same material as the elbow and are of the same size and thickness, and they are arc-welded to the elbow. The assembly was not subsequently heat treated, to simulate metal conditions in actual piping systems. Of course, this can be considered a source of discrepancies between the finite element results and the experimental results.

One pipe extension was rigidly mounted on a pedestal attached to a load frame, as seen in Fig. 2.4.1. A single force loading was applied by means of a hydraulic ram, with the point of load application on the free extension at a distance of 28.75 in. from the nearer end of the elbow. Since the moment was the loading of interest, such a long moment arm had to be chosen to make the shear force small in comparison with the moment. The distance from the other end of the elbow to the plane of restraint was 18 inches.

Deflections and strains were measured by means of dial indicators and strain gages, respectively. The dial-indicators readings were the primary source for limit load determination in the experimental study, and the strain gage data were used for checking purposes. The location of the dial indicators is shown in Fig. 2.4.1. The load magnitude was measured using a strain-gage-based load cell.

Single-element, bonded metallic-foil, electrical resistance strain gages were used in this test, and were placed on the outer surface of the tension side of the elbow, near the position of the major axis of expected ovality, as shown in Fig. 2.4.2 (on section B-B of the diagram). These gages were oriented as closely as possible with the directions of principal strains, as indicated by brittle coating tests. However, birefringent coating test results indicated a significant difference between the location of maximum strain and the location of the gages.

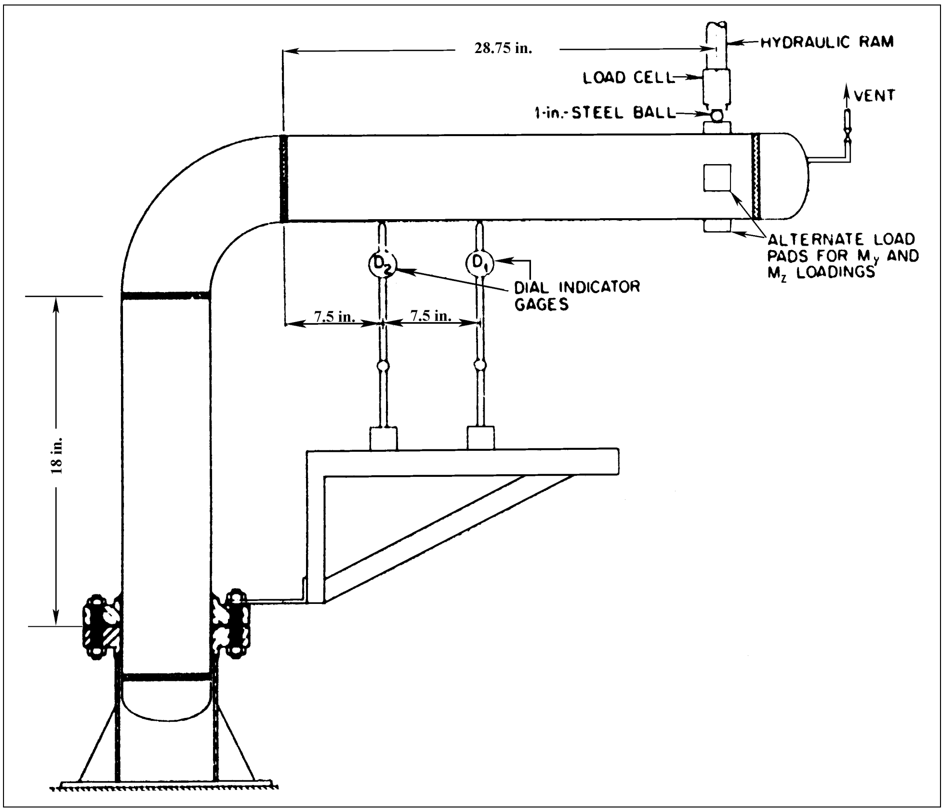

Fig. 2.4.1 Diagram of Test Setup (Greenstreet, 1978)

The material properties of the elbows used in this experiment were obtained from tensile specimens taken from selected elbows after they were tested, which can cause some error in the measurements. However, the coupons for the tensile tests were removed from a region in the elbow which was subjected to low strains during testing, to minimize the error induced by strain hardening. The reported material properties are as follows:

Young's modulus : $E = 30.1\times10^6$ psi (207.54 GPa)
Yield stress : $\sigma_y = 50\times10^3$ psi (344.75 MPa)
Tensile strength : $\sigma_u = 73.6\times10^3$ psi (507.47 MPa)

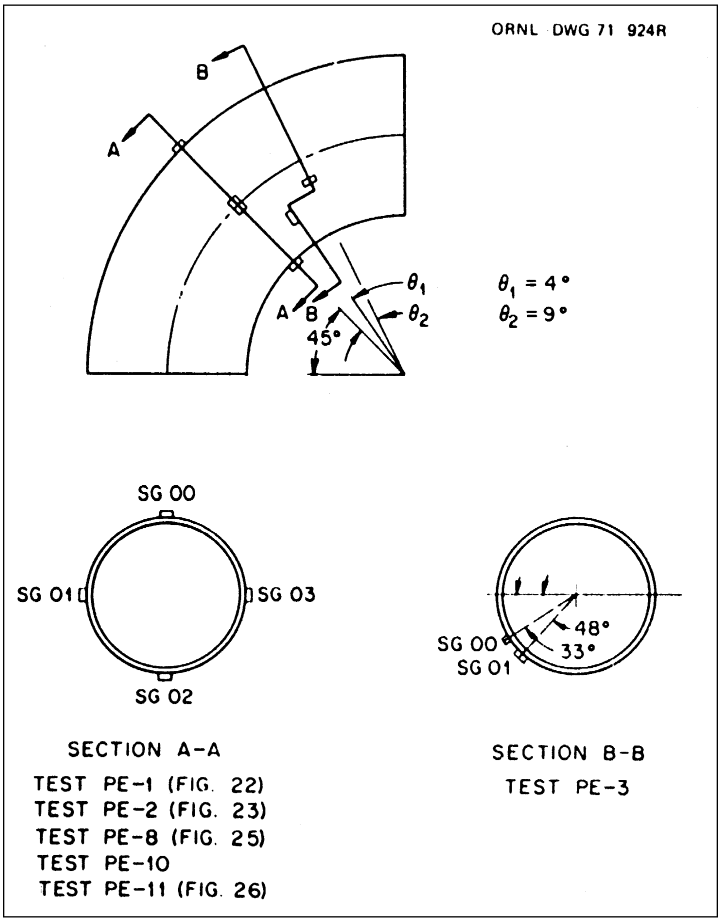

Fig. 2.4.2 Diagram of Strain Gage Locations (Greenstreet, 1978)

2.4.2 Finite Element Modeling and Analysis

The finite element model used is meshed with the same element (ELBOW32) and is analyzed with the same solution technique and parameters, as those used throughout this study. In this case however, the geometry of the problem is different. The extensions had to be modeled, to include the stiffening effects of end-constraints, and to take the flexibility of the straight pipes into consideration when computing the deflection.

For comparison with the strain measurements, the same model was used. In addition, a standalone elbow was modeled and its strain values were also compared to the experimental data. In both standalone and connected models, the elbow was meshed with 12 elements, the same number used to mesh all elbows throughout this study.

As shown in Fig. 2.4.3, which shows a schematic of the connected model, the vertical (fixed) extension is meshed using 15 elements of the same type as the pipe bend. The horizontal (free) extension, had to be divided into one long and two short segments. The long segment, which lies between the point of load application and the first dial indicator, was meshed with 12 elements. The first short segment, which lies between the dial indicators, and the second, which lies between the second dial indicator and the extremity of the elbow, were equal in length and were meshed with six elements each. The characteristic element length in the model ranged between 1.146 and 1.25 inches per element.

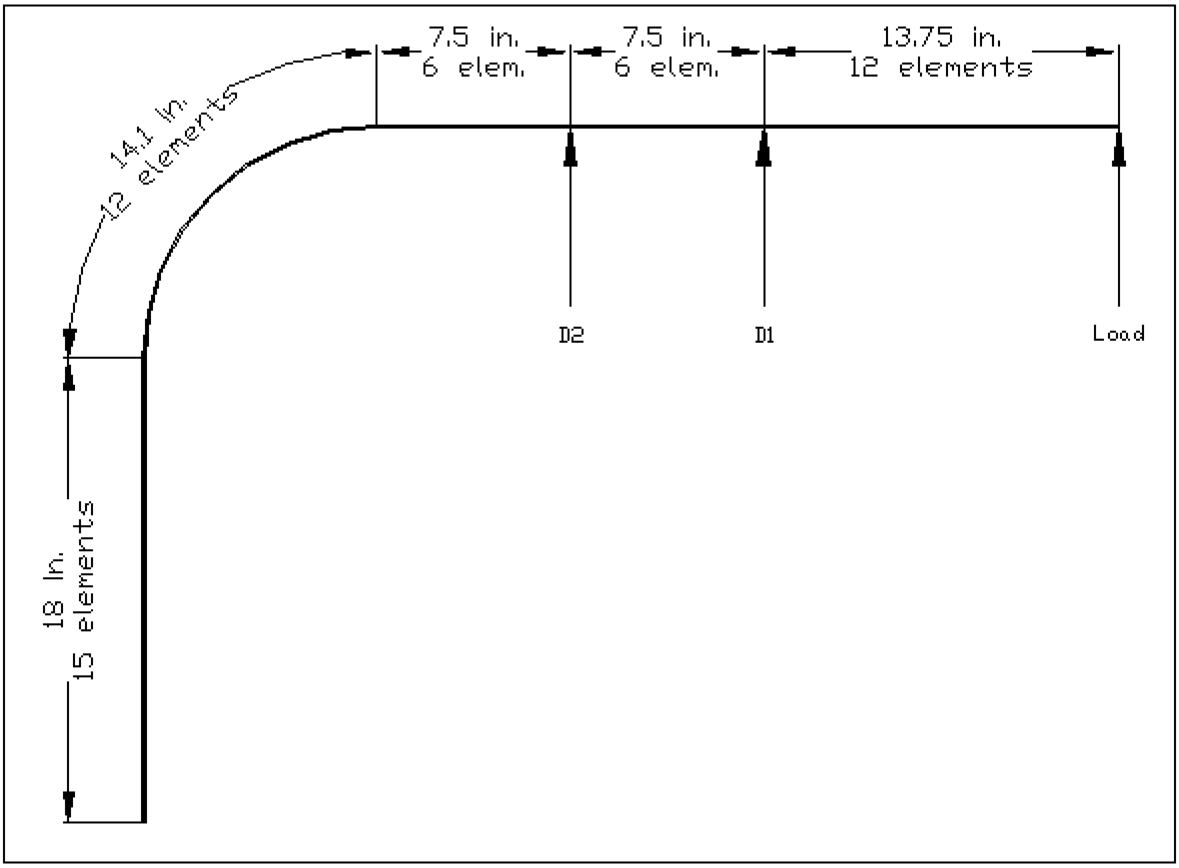

Fig. 2.4.3 Schematic of the Finite Element Model Including Straight Pipe Extensions

Since the 0.2%-strain-offset yield stress was reported, without specifying the proportionality limit, four different material models were used in the analysis, and their results compared. The stress-strain diagrams of these material models are shown in Fig. 2.4.4. It can be seen from this figure that “A” is an elastic-perfectly-plastic material, with the yield stress at 50 ksi. Material “B” is also elastic-perfectly-plastic, but makes the assumption that the proportionality limit, and hence the yield stress are at 35 ksi.

The remaining two material models are both elastic-plastic with strain hardening, following the reported ultimate tensile strength of 73.6 ksi, assuming it occurs at a strain value of 5%. Material "C" takes the proportionality limit and yield stress at 50 ksi, while material "D" assumes the proportionality limit to be at 35 ksi, and follows the reported 0.2%-strain-offset yield stress of 50 ksi.

Discrepancies between experimental and numerical results, due to the assumptions made by the material model, are unavoidable of course; therefore the use of several material models was imperative.

In the connected model, loading was in the form of a lateral force, applied at the end of the free extension. Deflections were computed at the nodes placed at the exact locations of the two dial indicators. Strain was computed, in both connected and standalone models, at four integration points, around the locations of each strain gage, in the direction measured by the gage under consideration. The strain value was then linearly interpolated, first in the hoop and then in the axial direction. Linear interpolation could be considered a source of error, but it was deemed adequate since the integration points were closely located and since strain gradients were mild in these regions, at the relevant load levels.

2.4.3 Comparison of Results

Throughout the present work, a standalone pipe bend was used as the model, and an elastic-perfectly-plastic material model was used, to concentrate on the effects of geometric nonlinearity and internal pressure and to simplify the analysis and interpretation of results, by excluding the effects of strain hardening and end-constraints. A real pipe bend however, is made of a strain-hardening material and must be attached to a flange and/or a straight pipe segment, for the purposes of support and external load application. Therefore the comparison with experimental results must be made more carefully than in usual verification processes.

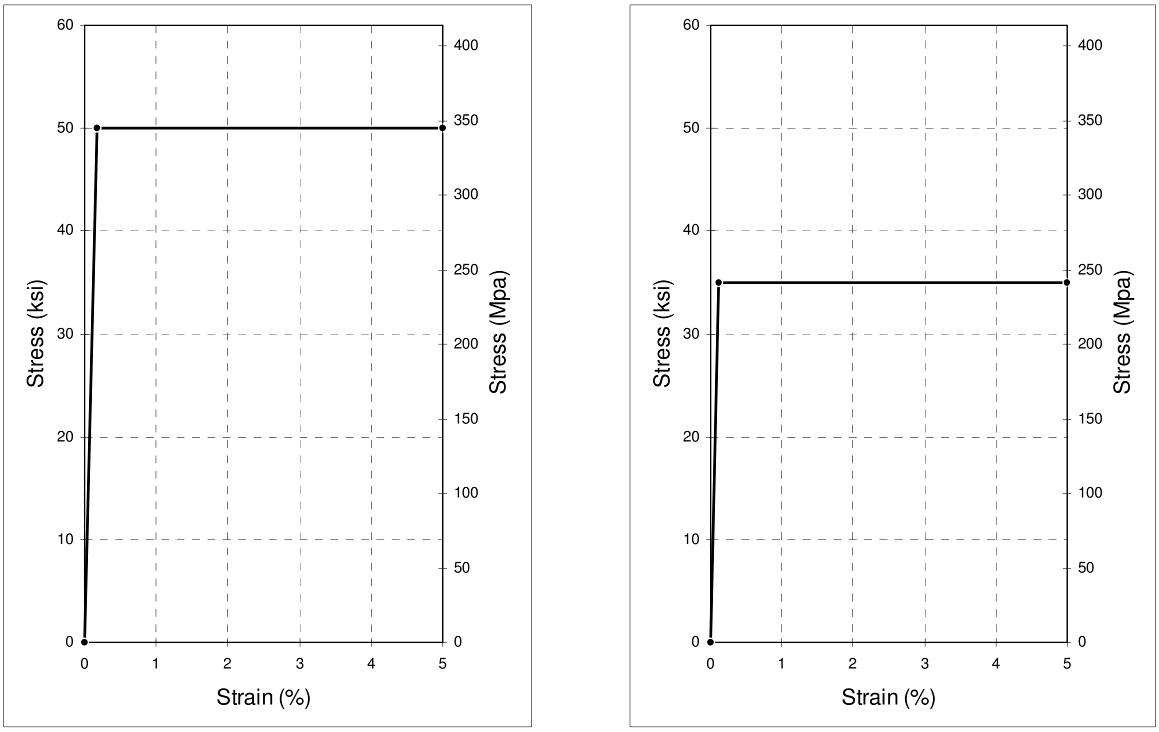

Material Model “A” **Material Model “B”**

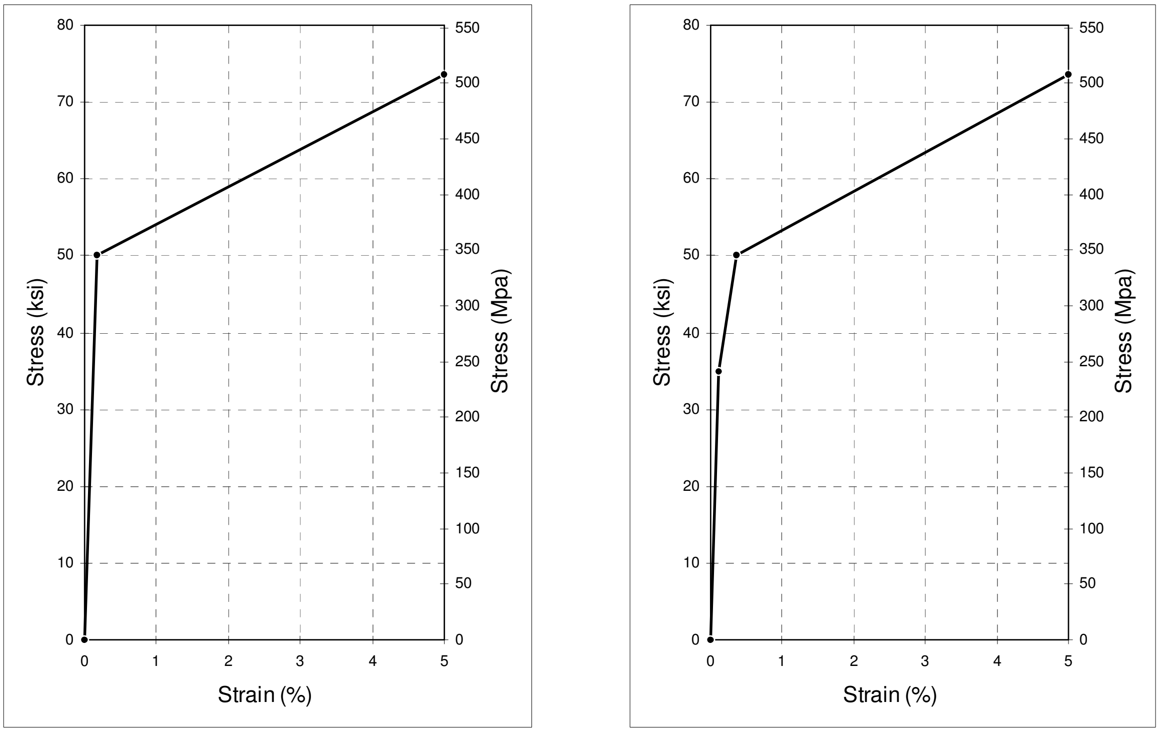

Material Model “C” **Material Model “D”**

Fig. 2.4.4 Material Models Used in the Finite Element Analysis

Figure 2.4.5 shows the computed load-deflection curves, with the deflection computed at the location of the first dial indicator (D1) compared to the response measured by this dial indicator. Figure 2.4.6 shows similar curves for the second dial indicator (D2). From these two figures, it can be seen that material model “B” is the most conservative, and would predict lower limit loads. It is also clear that both materials “A” and “C” are too stiff, and hence would over-predict the limit loads. On the other hand, Material “D” gives the response that is closest to the experimentally determined one, since it is the closest in properties to a real elastic-plastic strain-hardening material.

Figure 2.4.7 compares the load-strain curves obtained numerically, using the connected elbow model, to the one obtained experimentally from strain gage SG00, which measured axial strain. Figure 2.4.8 shows a similar set of curves obtained using the standalone elbow model. From these two figures, it can be seen that material “B” is the most conservative in terms of the predicted response, while “D” remains the closest to the measured response. It can also be seen that all numerical models show more stiffness than the actual test elbow as loading is started, and then there is a change in the measured response, indicating a sudden increase in “stiffness”, at an axial strain value of 1.3×10^{-3}.

Figures 2.4.9 and 2.4.10 show similar load-strain curves obtained using the connected and the standalone elbow models, respectively. These two figures compare the numerically obtained hoop strain values to those measured with strain gage SG01. In Fig. 2.4.9, the connected model with material “D” is in very close agreement with the experimental data. The same material model yields more conservative results with the standalone elbow, as shown in Fig. 2.4.10. As a matter of fact, the stiffening effect of end-constraints is obvious from these two figures, and it is clear that the standalone elbow model would produce more conservative estimates of the limit loads.

Collapse (limit) loads have been obtained from the load-deflection curves presented above using the departure from linearity (proportionality limit) method discussed before. From the load-strain curves, the collapse load was determined using the 0.2%-strain-offset method, also discussed previously.

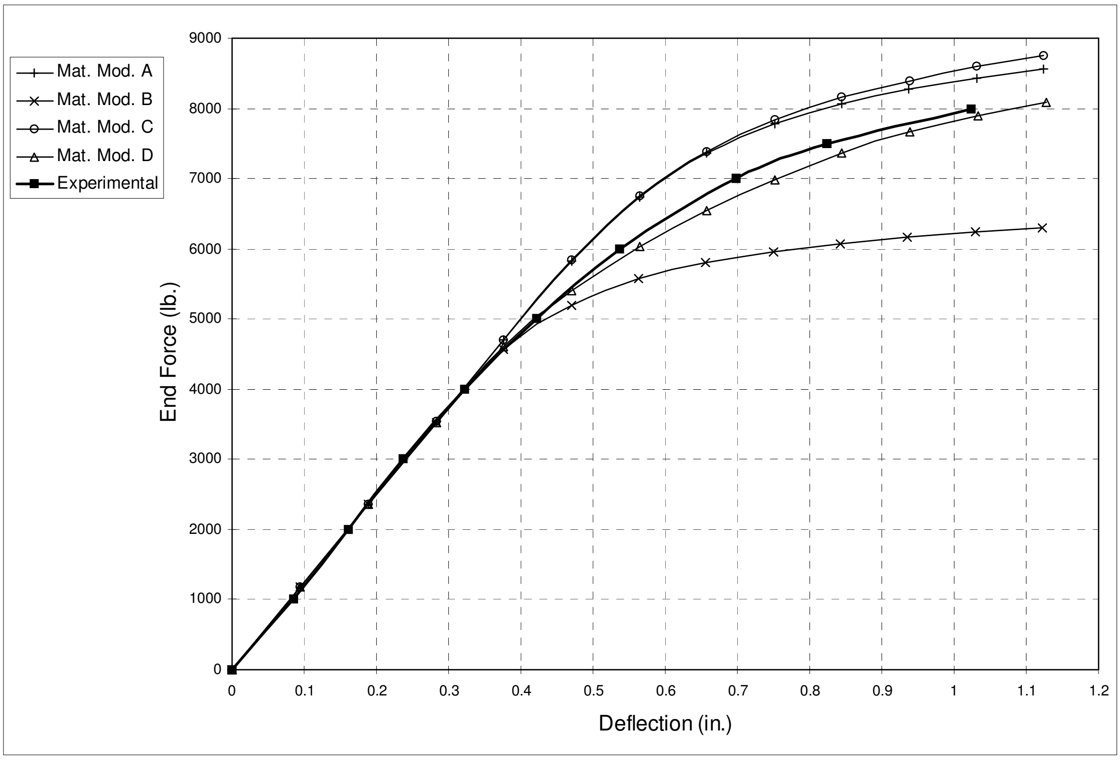

Fig. 2.4.5 Computed Load-Deflection Curves, Compared to the Response Measured by GreenStreet (1978) Using Dial Indicator D1 in his Test PE-3

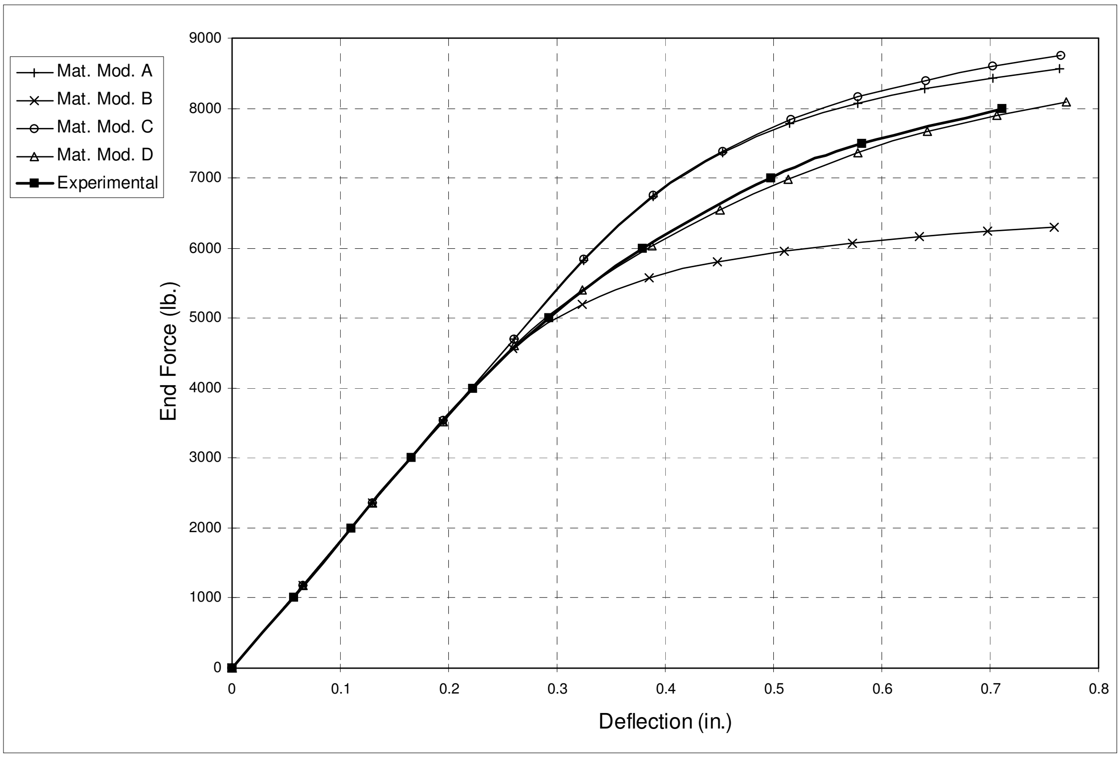

Fig. 2.4.6 Computed Load-Deflection Curves, Compared to the Response Measured by GreenStreet (1978) Using Dial Indicator D2 in his Test PE-3

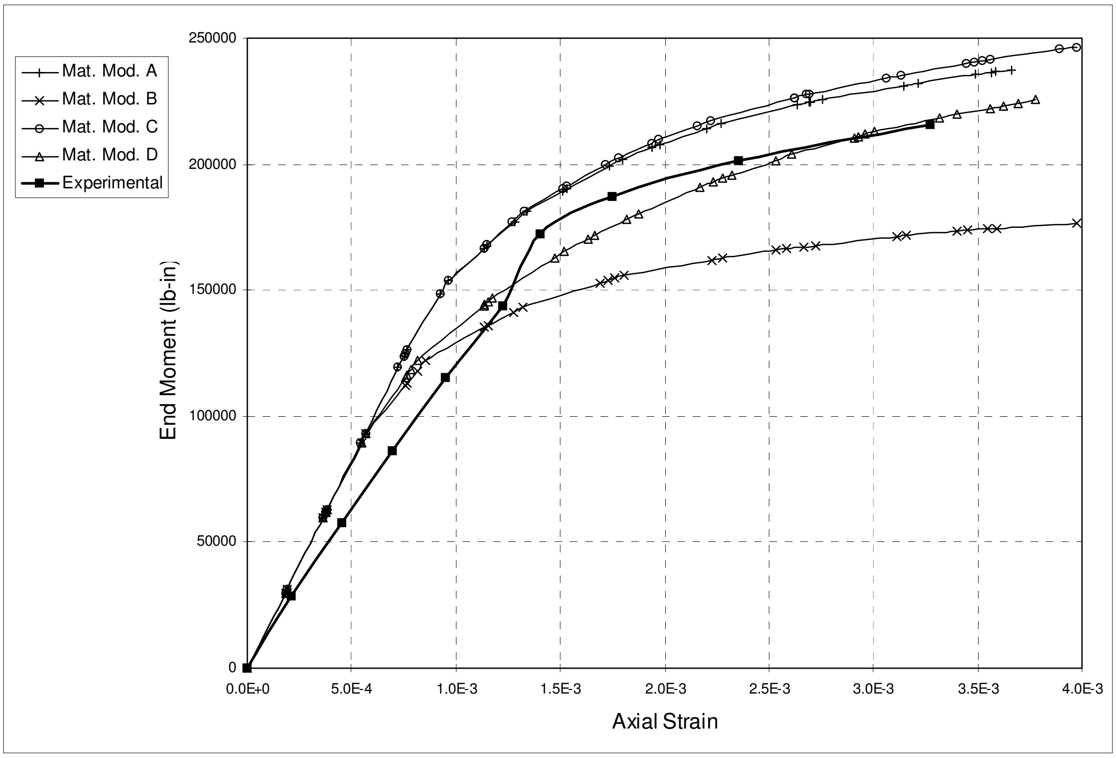

Fig. 2.4.7 Computed Load-Strain Curves (Connected Elbow), Compared to the Response Measured by GreenStreet (1978) Using Strain Gage SG00 (Axial Strain) in his Test PE-3

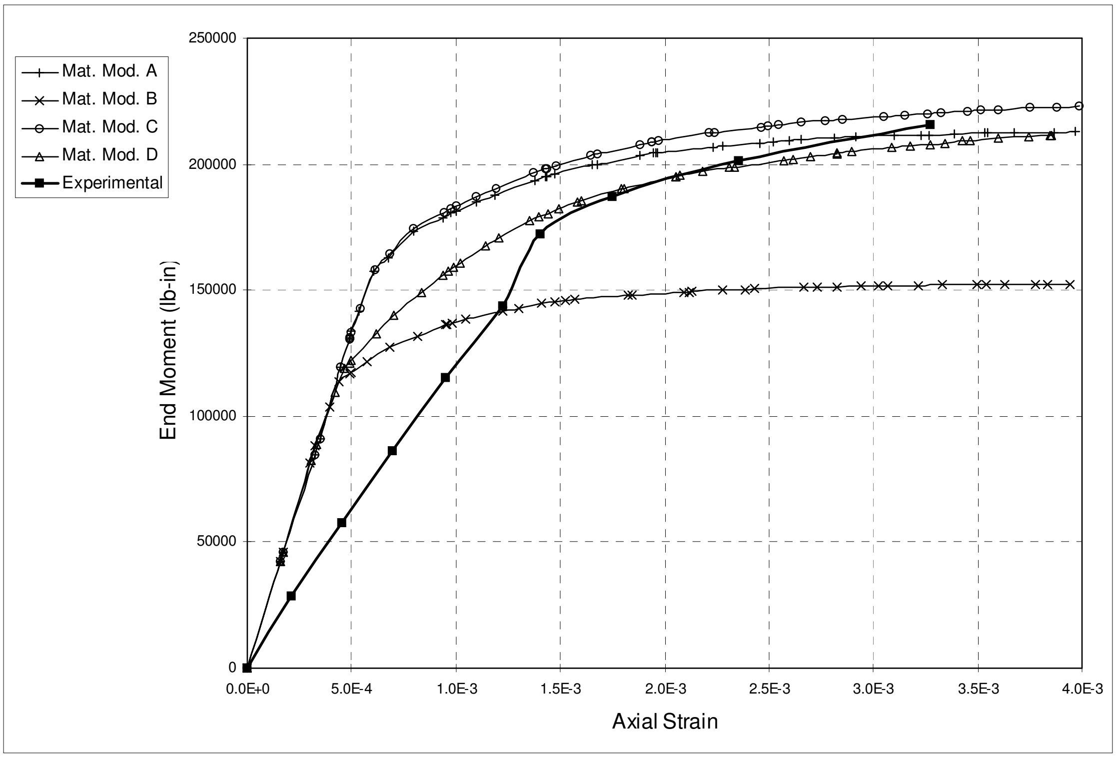

Fig. 2.4.8 Computed Load-Strain Curves (Standalone Elbow), Compared to the Response Measured by GreenStreet (1978) Using Strain Gage SG00 (Axial Strain) in his Test PE-3

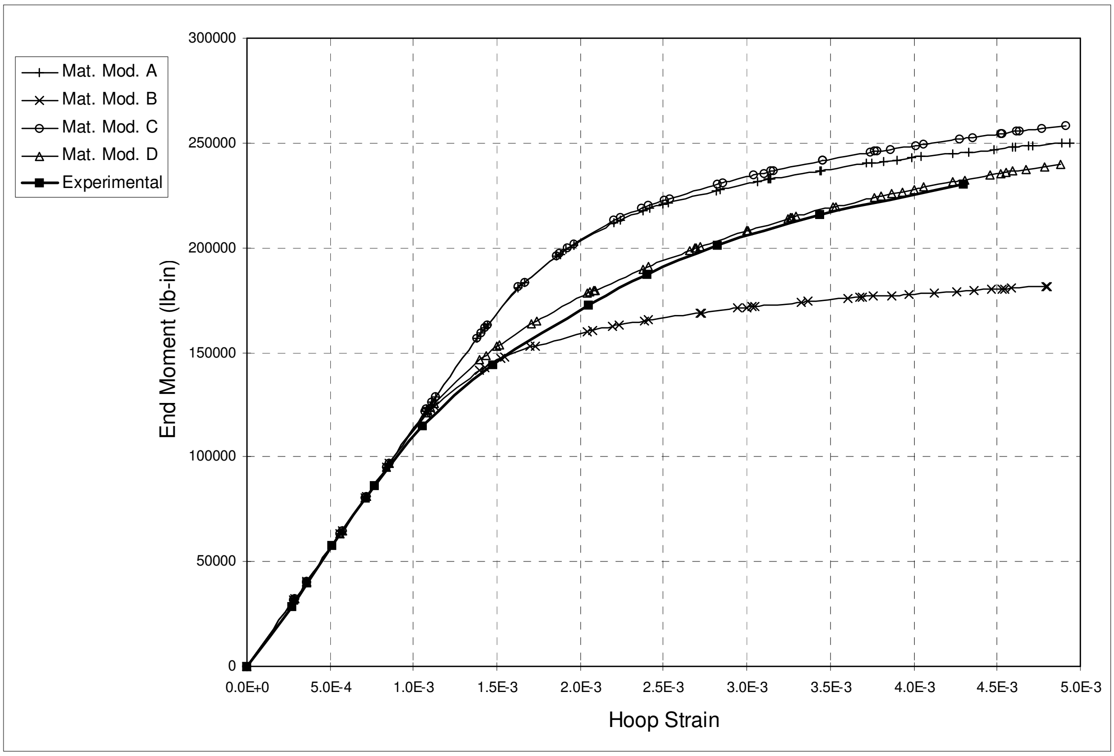

Fig. 2.4.9 **Computed Load-Strain Curves (Connected Elbow), Compared to the Response Measured by GreenStreet (1978) Using Strain Gage SG01 (Hoop Strain) in his Test PE-3**

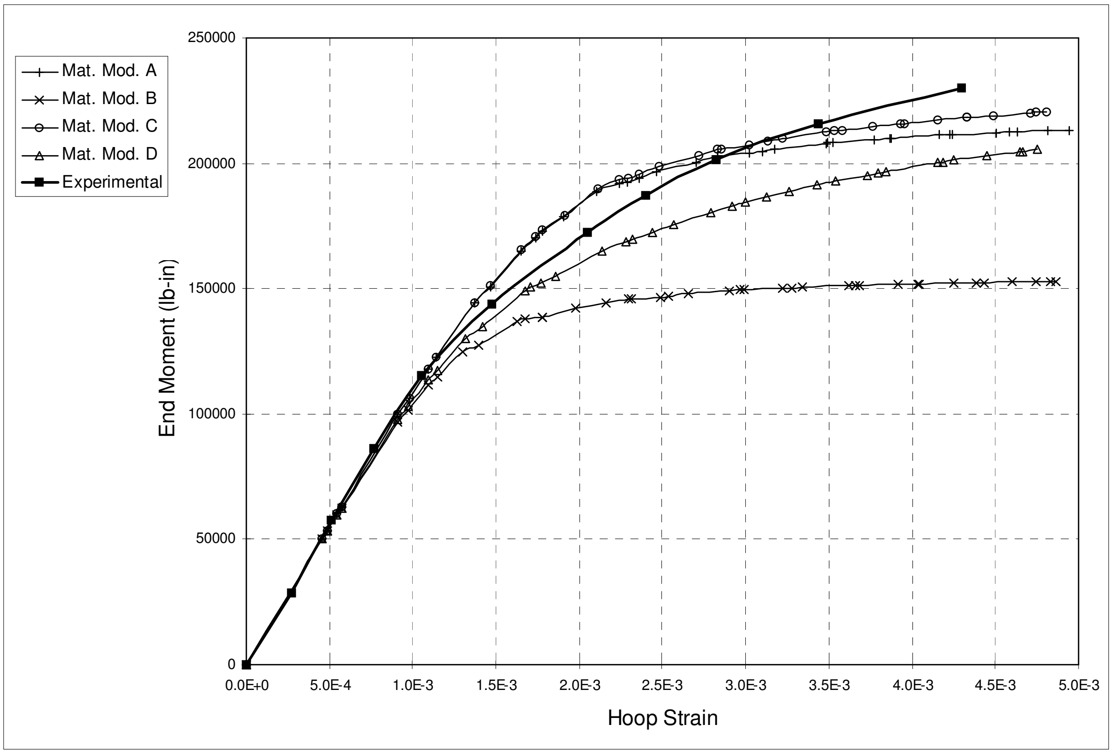

Fig. 2.4.10 **Computed Load-Strain Curves (Standalone Elbow), Compared to the Response Measured by GreenStreet (1978) Using Strain Gage SG01 (Hoop Strain) in his Test PE-3**

The values of these collapse moments are presented in table 2.4.1, along with the error, which is the difference between the numerical and the experimental values. The magnitude of this error is also expressed as a percentage of the experimental value. From the values in this table, it can be seen that the standalone models always give a lower estimate of the collapse moment than the experimental value. It is also evident that material model “B” is the one that gives the lowest estimates of the limit loads, in both the connected and the standalone elbow models. It is also noted once again that material “D” gives very low error values, compared to the other materials.

It can be concluded at this point that the assumptions and parameters used throughout this study are bound to produce conservative results, specifically because a standalone elbow model is used, along with a material model that is similar to material “B” used above. It was seen that most of the difference that existed between experimental and numerical data was mainly due to assumptions made while modeling the geometry and material properties related to the problem. The four material models used produced different results. This difference was expected, and justified. Hence, the code and the element used can be considered capable of predicting the behavior accurately, and the modeling approach used throughout the study can be considered adequate and conservative.

Table 2.4.1 **Comparison Between Numerical and Experimental Limit Loads. Connected and Standalone Elbows Were Modeled. Four Different Material Models Are Compared.**

Limit Load by Method	Mat. Mod. A Conn. (lb.)	Mat. Mod. A Stand. (lb-in.)	Mat. Mod. B Conn. (lb.)	Mat. Mod. B Stand. (lb-in.)	Mat. Mod. C Conn. (lb.)	Mat. Mod. C Stand. (lb-in.)	Mat. Mod. D Conn. (lb.)	Mat. Mod. D Stand. (lb-in.)	Experimental (lb.)	Experimental (lb-in.)
Proportionality Lim. (D1)	5800	--	4500	--	5800	--	4500	--	3750	--
Error	2050	--	750	--	2050	--	750	--	--	--
Percent Error	54.67%	--	20.00%	--	54.67%	--	20.00%	--	--	--
Proportionality Lim. (D2)	5800	--	4250	--	5800	--	4250	--	3750	--
Error	2050	--	500	--	2050	--	500	--	--	--
Percent Error	54.67%	--	13.33%	--	54.67%	--	13.33%	--	--	--
0.2%-strain-offset (SG00)	8200	210000	5900	150000	8400	220000	7700	210000	7700	221375
Error	500	-11375	-1800	-71375	700	-1375	0	-11375	--	--
Percent Error	6.49%	5.14%	23.38%	32.24%	9.09%	0.62%	0.00%	5.14%	--	--
0.2%-strain-offset (SG01)	8500	210000	6100	150000	8700	215000	7900	195000	7800	224250
Error	700	-14250	-1700	-74250	900	-9250	100	-29250	--	--
Percent Error	8.97%	6.35%	21.79%	33.11%	11.54%	4.12%	1.28%	13.04%	--	--

2.5 Types of Results

The first goal of this research is to study the elastic-plastic behavior of pipe bends, under out-of-plane moment loading. It was also required to study the effects of changing the value of the pipe bend factor ($h=Rt/r^2$), and the value of internal pressure, on that behavior, and to determine the limit moments in each case.

A standalone, long-radius ($R/r=3$) pipe bend was used as the model throughout the study. A parametric study was then performed, in which the pipe bend factor took ten different values between 0.0632 and 0.4417. To vary the pipe bend factor (h), the value of the wall thickness was varied, between 0.165 in. and 1.031 in. The nominal diameter of the pipe was kept constant at a value of 16 in. and the bend radius (R) was kept at a value of 24 in. to keep the radius ratio constant.

For each of these 10 models, several analyses were performed at different values of internal pressure. The pressure for each model started from zero, and was incremented by 100 psi until it reached the limit value, where the elbow underwent plastic instability due solely to pressure. A listing of the ten models used, along with their geometric and loading parameters is presented in Table 2.5.1 below. The upper ends of the pressure ranges given for the models in Table 2.5.1, were reported by Shalaby (1996). These are smaller, by a maximum of 100 psi, than the limit pressures of the 10 models.

The results of these analyses are presented in the form of load-deflection plots, for each load case belonging to each model. A sample of this output is shown in Fig. 2.5.1. As shown in the figure, the applied moment is plotted against the rotation, in the same direction as the moment, of the loaded (free) end of the elbow.

From the load-deflection curves, the limit moments of each case were obtained. The plastic instability moment was taken as the highest point on the curve, i.e. the maximum moment that could be attained. The plastic collapse moment was found, for each case, using the twice-elastic-slope method discussed previously. This information was then used to plot these limit moments against internal pressure, as shown in Fig. 2.5.2, to study the effect of the pressure and the bend factor on the collapse behavior of the elbows.

The limit loads were then compared to those computed using some of the analytical and empirical equations available in the literature. The effects of modeling parameters were also studied. The results obtained from small-displacement and large-displacement analyses were compared, and the effect of including strain hardening effects was also investigated.

Table 2.5.1 List of the Models Used in the Parametric Study, to Investigate the Effect of Varying the Bend Factor and the Internal Pressure, on the Behavior of Pipe Bends Under Out-of-Plane Bending

Model Number	Nominal Diameter D (in.)	Radius Ratio R/r	Pipe Wall Thickness t (in.)	Pipe Bend Factor h	Number of Load Cases	Internal Pressure Range (psi)
1	16	3	0.165	0.0632	8	0~800
2	16	3	0.188	0.0722	11	0~1000
3	16	3	0.250	0.0967	13	0~1200
4	16	3	0.312	0.1217	16	0~1500
5	16	3	0.375	0.1475	20	0~1900
6	16	3	0.410	0.1615	23	0~2200
7	16	3	0.500	0.1998	27	0~2600
8	16	3	0.656	0.2675	35	0~3400
9	16	3	0.844	0.3527	45	0~4400
10	16	3	1.031	0.4417	55	0~5400

To better understand the behavior of pipe elbows, under out-of-plane bending and internal pressure, it was deemed important to know how the cross-section deforms, and to study the distribution of stresses that cause it to deform in a particular manner. The importance of the cross-section lies in that its deformation, by ovalization and/or warping, is what gives the elbow its greater flexibility, compared to straight pipes. In addition, the problem owes a great part of its complexity to the coupling between the cross-sectional deformation and the overall deflection of the elbow, because this coupling gives rise to high geometric nonlinearity, even at relatively small overall deflection.

It was first necessary to decide on a specific section to be studied. An elbow with pipe bend factor h=0.1615 was considered, and the results of a detailed analysis thereof were examined. First, the variation, over the elbow's length, of Mises stress and equivalent plastic strain were studied, to determine the most severely loaded, or critical, cross-section of the elbow. Thus, the loaded section was chosen.

Next, the progression of yielding, at each of the integration points around this critical cross-section, was examined by plotting the equivalent plastic strain against the end-rotation, as shown in Fig. 2.5.3. Studying the yield progression was then extended, by treating the pipe bend as a whole, and looking for the loads that cause first yielding to occur, and examining the number of plastic hinges that are present at different loading stages.

The distribution of some components of stress and strain, as well as Mises stress and equivalent plastic strain, around the critical cross-section, were then plotted and examined, both at the onset of yielding and at instability. A sample of such a plot is shown in Fig. 2.5.4. Finally, deformed shapes of the elbow were presented, to show the overall deflection, and more importantly the cross-sectional deformation, at instability, and under different values of internal pressure.

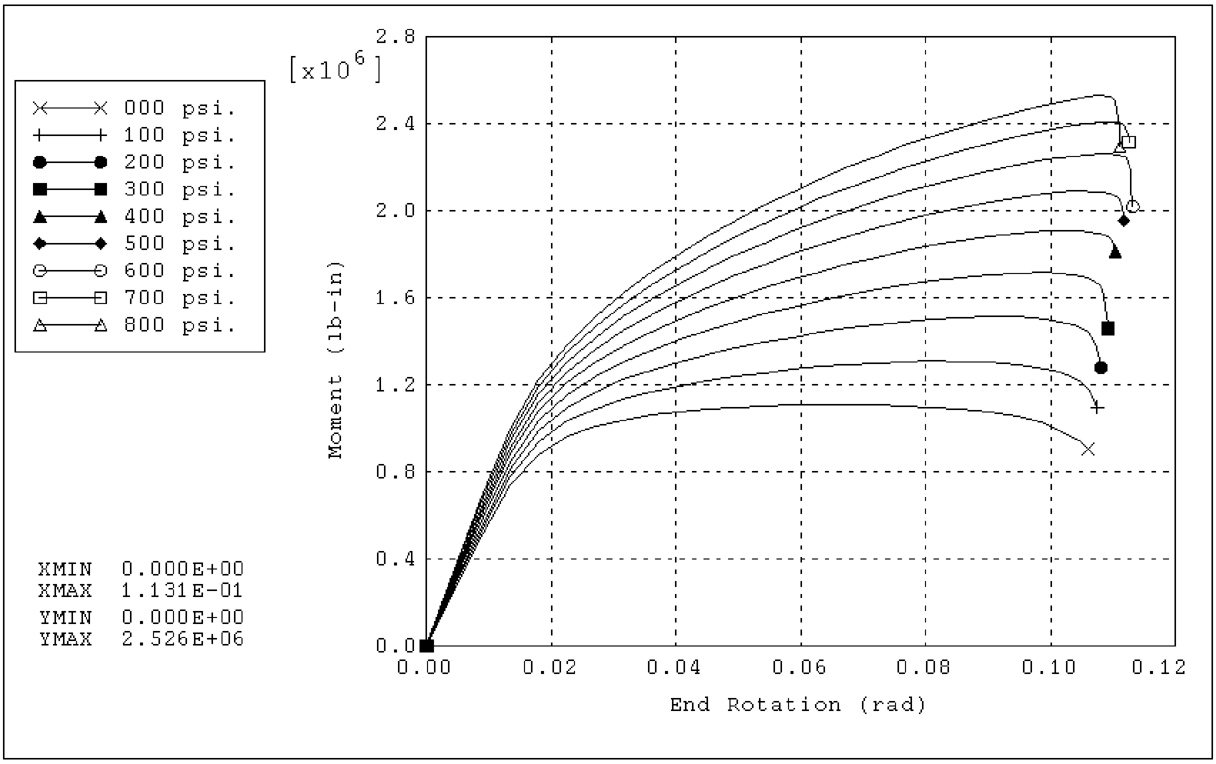

Fig. 2.5.1 Sample Load-Deflection Curves of an Elbow With h=0.1615 - Internal Pressure Range: 0~800 psi

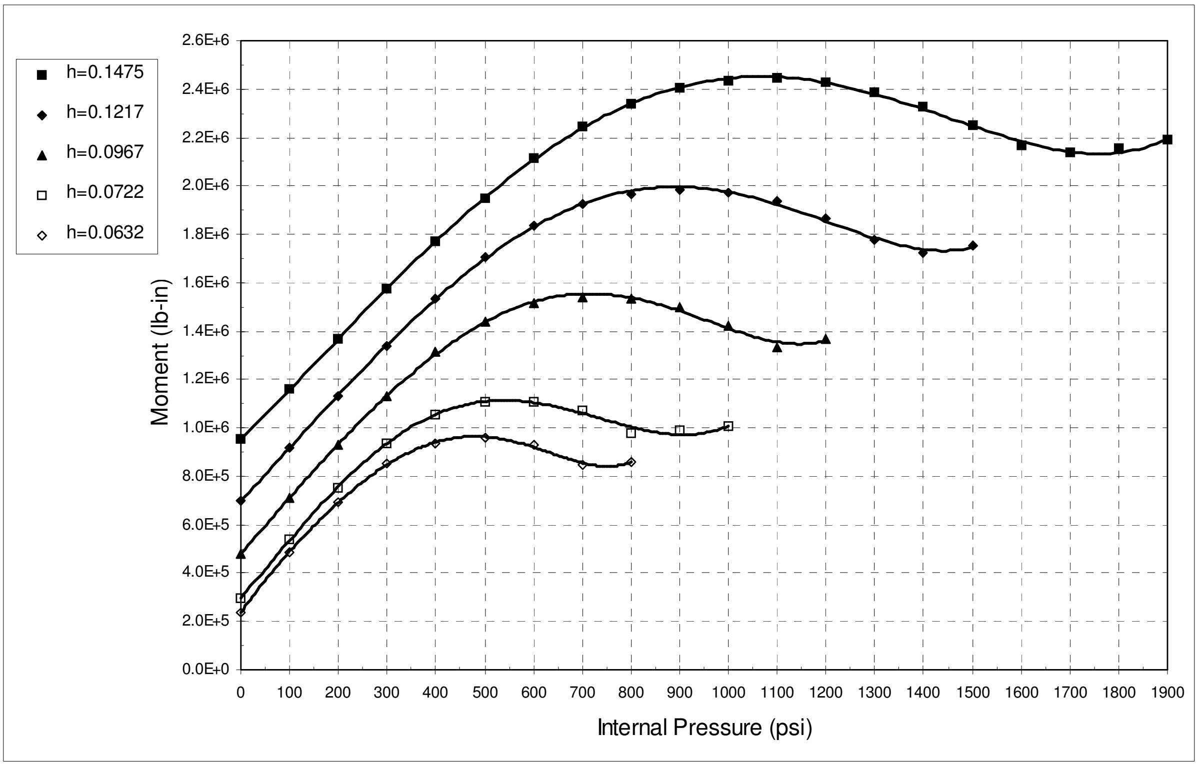

Fig. 2.5.2 Sample Limit Curves Showing the Variation of Instability Moment With Internal Pressure and Pipe Bend Factor

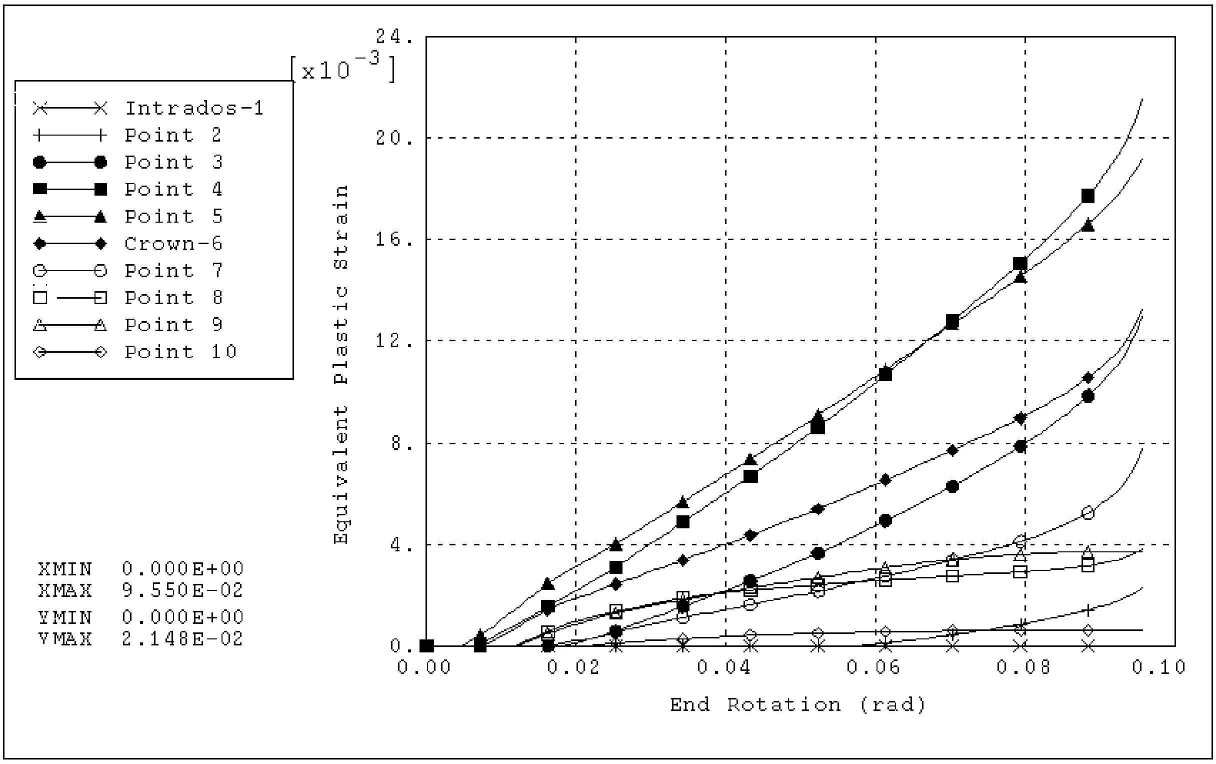

Fig. 2.5.3 Sample Plot of the Variation of Equivalent Plastic Strain With End-Rotation, Used to Study Yield Progression

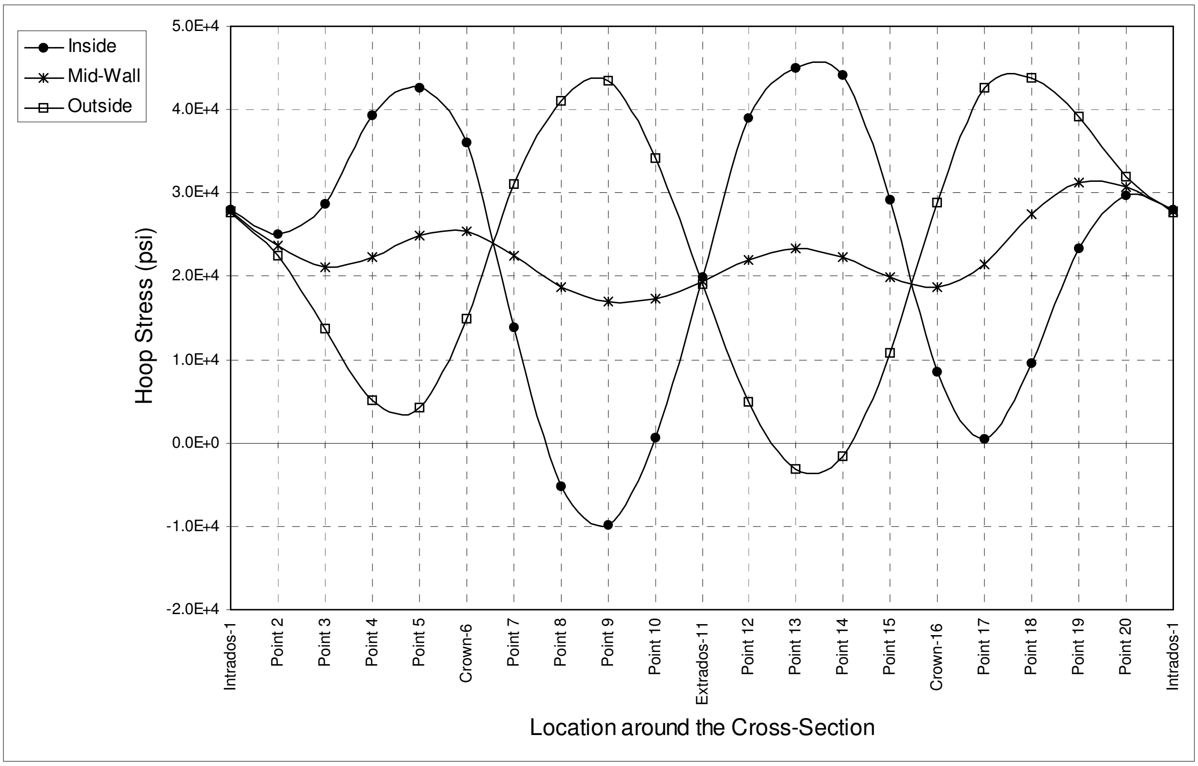

Fig. 2.5.4 Distribution of Hoop Stress around the Cross-Section at Start of Yielding - Internal Pressure: 1200 psi

In the next chapter, the results obtained in this study are presented and discussed in detail.

Chapter Three

Results and Discussion

This chapter consists of five main sections. The load-deflection behavior of pipe elbows subjected to an out-of-plane moment load is discussed in the first section. Then, several load-deflection curves are presented, in the second section, for each of the different geometries studied, to illustrate the effect of internal pressure on the deflection behavior of these elbows under the moment load. In the third section, limit curves are presented, for each different geometry, to show the effect of internal pressure on the values of the limit moments, both instability and collapse. The effects of geometric nonlinearity and strain hardening, on the analysis results, are considered in the fourth section. Finally, a detailed analysis is conducted, in the last section, to show the cross-sectional deformation patterns and the distributions of stresses and strains, in the critical cross-section, at different values of internal pressure.

3.1 Load-Deflection Behavior of Pipe Bends

To visualize the deflection behavior of pipe bends under out-of-plane moment loading, the displaced shape, at the point where the elbow reaches instability, is shown in Fig. 3.1.1 along with the original shape of an elbow with pipe bend factor h=0.1615. In this figure, a center-line representation is used to show the global deformation of the elbow. Cross sectional deformation is not shown here, but will be dealt with, in detail, later in this chapter. It should also be noted that the deformation is exaggerated in this figure, by a magnification factor equal to five.

The deflection behavior can also be studied, from a more quantitative perspective, by plotting the value of the bending moment, applied at one of the ends of the 90° bend, against the out-of-plane rotation of this same end. Figure 3.1.2 shows the load-deflection curve of the elbow shown in Fig. 3.1.1.

From Fig. 3.1.2, it can be seen that the behavior remains linear at the beginning of the loading history, until the elbow's overall stiffness starts decreasing gradually, and finally reaches instability - represented by the peak point of the curve.

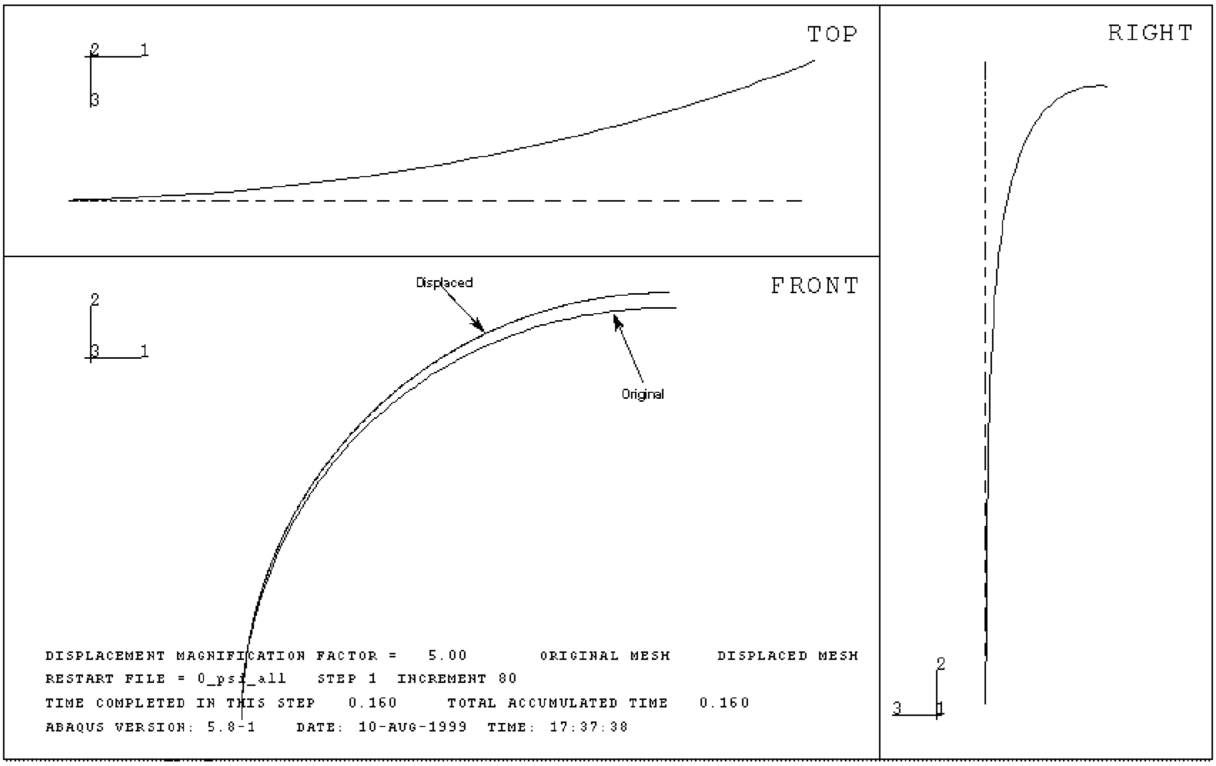

```
DISPLACEMENT MAGNIFICATION FACTOR =   5.00       ORIGINAL MESH     DISPLACED MESH
RESTART FILE = 0_psi_all   STEP 1  INCREMENT 80
TIME COMPLETED IN THIS STEP   0.160     TOTAL ACCUMULATED TIME   0.160
ABAQUS VERSION: 5.8-1    DATE: 10-AUG-1999  TIME: 17:37:38
```

Fig. 3.1.1 **Displacement (Exaggerated) of an Elbow With h=0.1615, at Instability (M=1.108×10^6 lb-in) - No Internal Pressure**

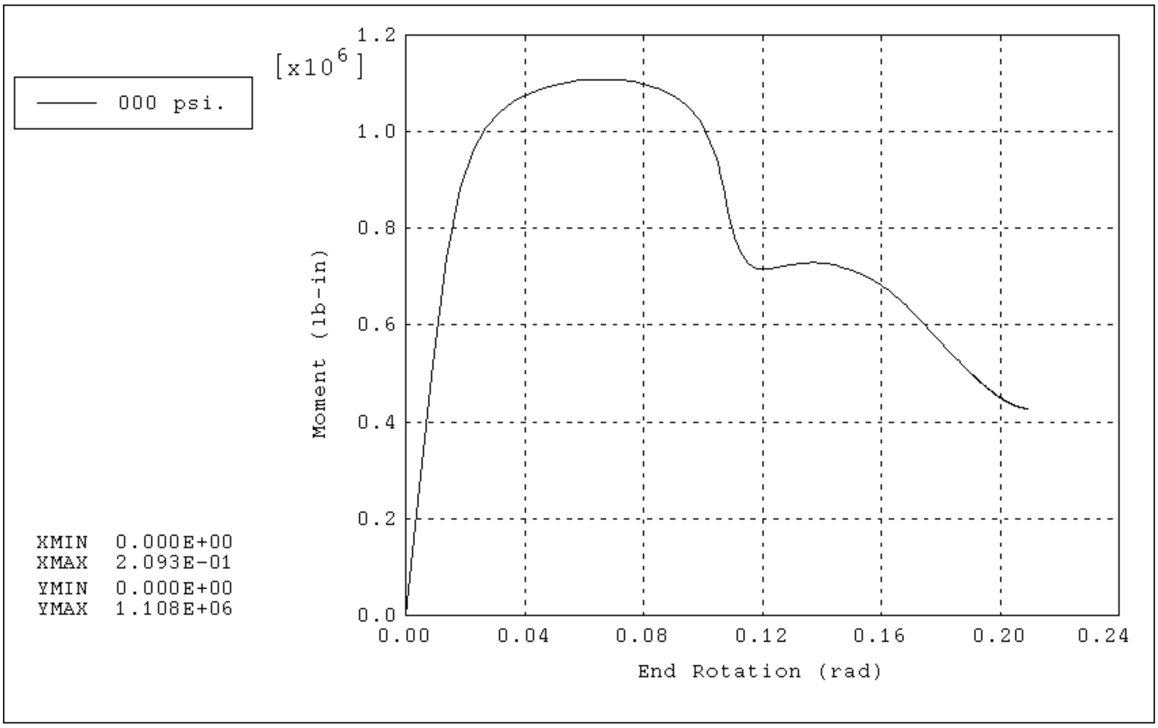

Fig. 3.1.2 **Variation of Moment With End-Rotation for an Elbow With h=0.1615 - No Internal Pressure**

It is noted that the numerical technique used was able to find the solution path, past the instability point, due to the use of stabilization, and the fact that the deflection variable was incremented during the analysis, instead of the load variable. However, this study is mainly focused on the behavior of pipe elbows until instability is reached; therefore, in all the cases presented later in this chapter, the analysis was discontinued shortly after this limit condition was met.

3.2 Effect of Internal Pressure on the Load-Deflection Behavior

To investigate the effect of internal pressure, the same model (h=0.1615) is subjected to a pressure of 1200 psi, which is held constant as the bending load is being applied. The resulting load-deflection behavior, as shown in Fig. 3.2.1, is similar to that of Fig. 3.1.2; however, instability is reached at a much greater value of the moment: 2.706×10^6 lb-in. compared to 1.108×10^6 lb-in. for the case with no pressure. The collapse moment displays a similarly large increase: 2.253×10^6 lb-in. compared to 1.073×10^6 lb-in. The deflection undergone by the elbow, at the point of instability, is also larger in the case with 1200 psi internal pressure: 9.4×10^{-2} radians (~5.39°), compared to 6.8×10^{-2} radians (~3.89°).

The load-deflection curve of the same model, with an internal pressure of 1800 psi is shown in Fig. 3.2.2. When compared to the case with 1200 psi (Fig. 3.2.1), this curve shows a decrease in the instability moment to 2.376×10^6 lb-in., and in the collapse moment to 1.931×10^6 lb-in. However, the deflection of the elbow at instability increased slightly to a value of 9.9×10^{-2} radians (~5.67°).

Figure 3.2.3 shows the case with 2200 psi internal pressure. This is the maximum pressure that this model (h=0.1615) can withstand without undergoing plastic instability under the effect of internal pressure alone (Shalaby, 1996). From this figure it can be seen that the instability moment increased again to a value of 2.682×10^6 lb-in., although the collapse moment decreased sharply to a value of 1×10^6 lb-in. In this case also, the end-rotation at instability increased tremendously to reach its maximum value for this model: 0.449 radians (~25.7°).

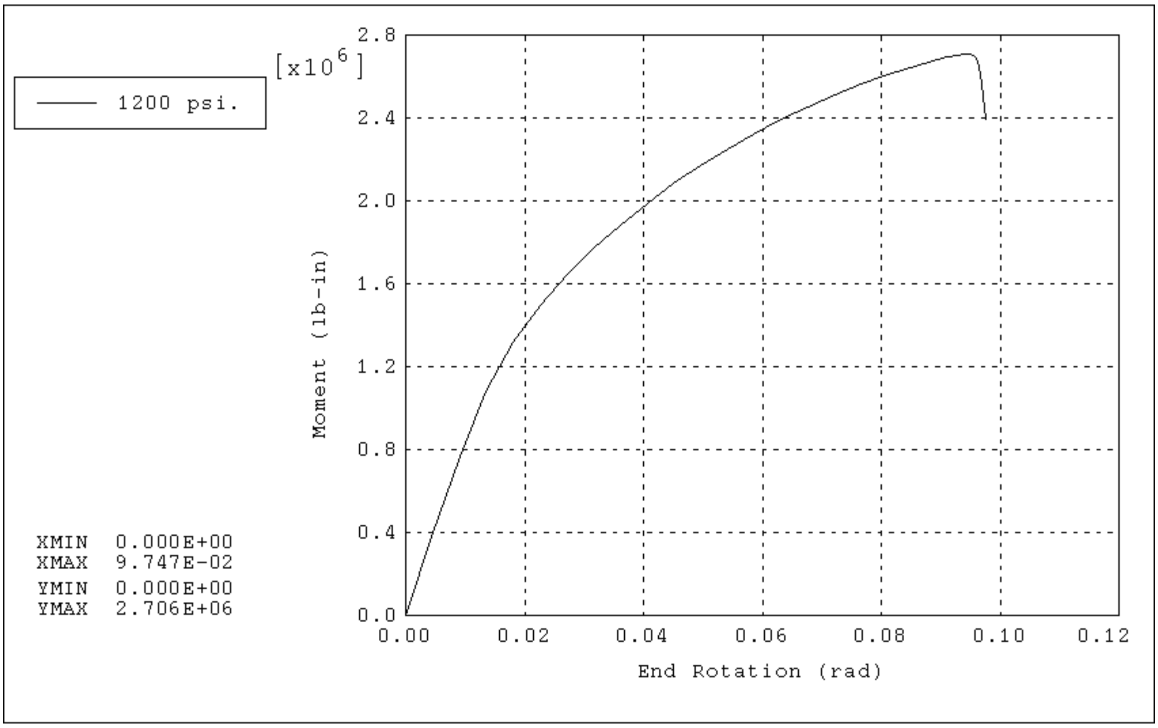

Fig. 3.2.1 **Variation of Moment With End-Rotation for an Elbow With h=0.1615 - Internal Pressure: 1200 psi**

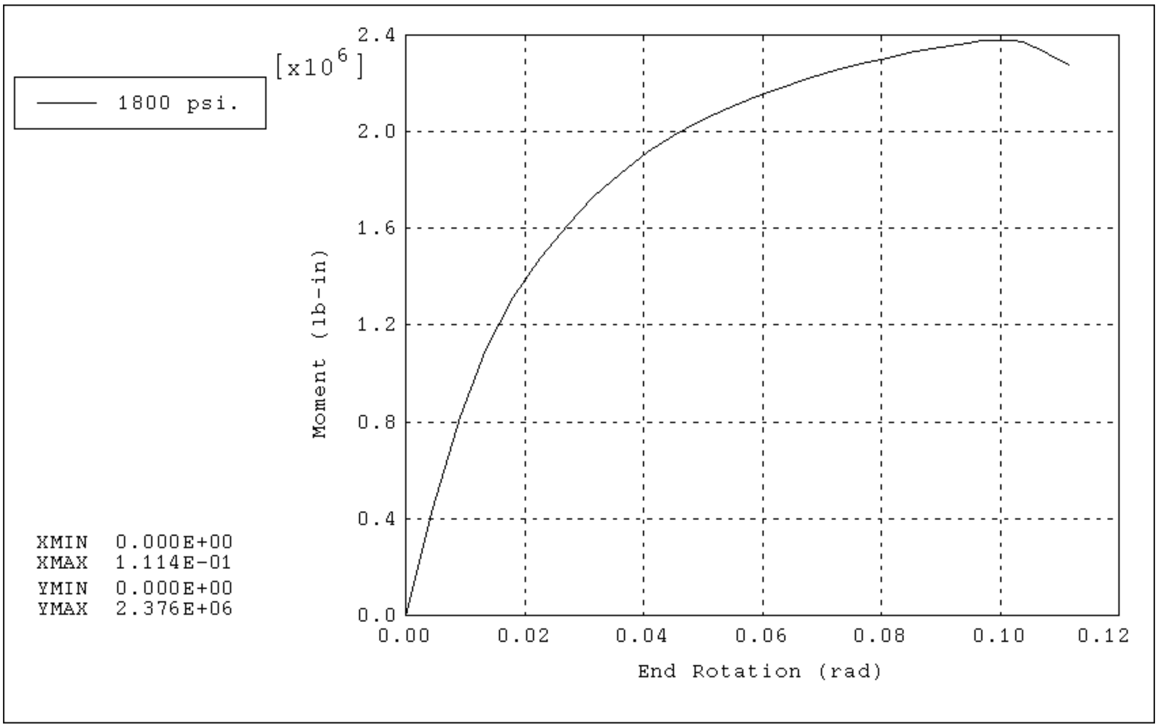

Fig. 3.2.2 **Variation of Moment With End-Rotation for an Elbow With h=0.1615 - Internal Pressure: 1800 psi**

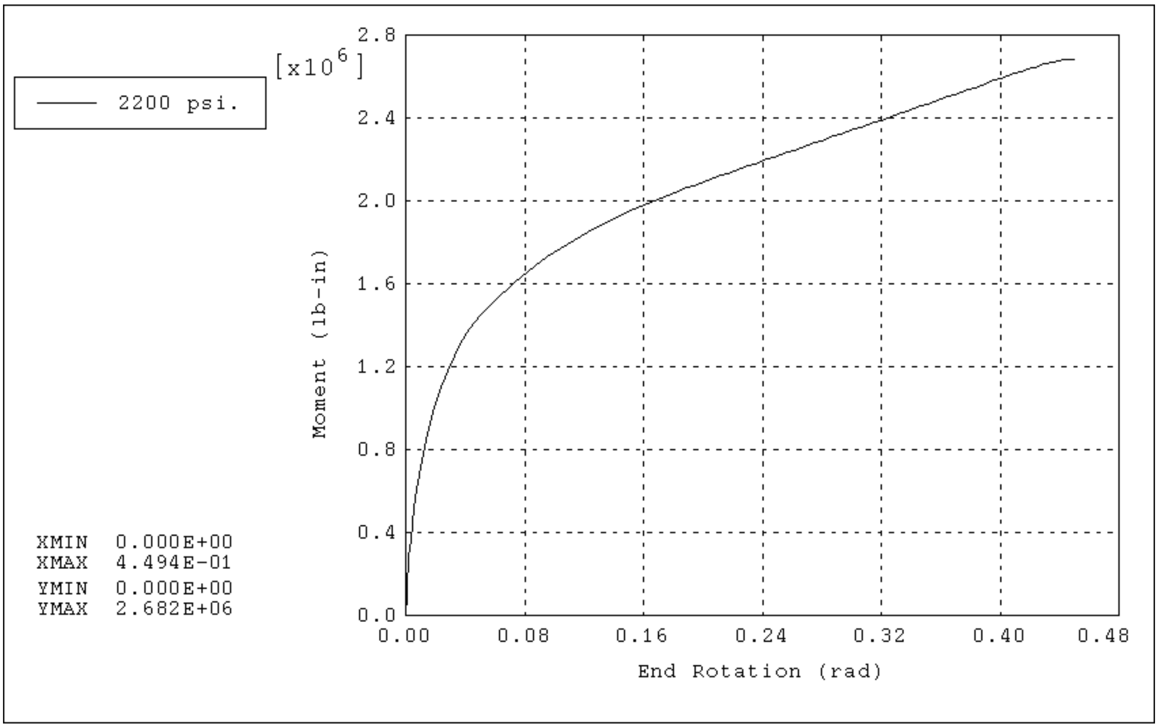

Fig. 3.2.3 Variation of Moment With End-Rotation for an Elbow With h=0.1615 - Internal Pressure: 2200 psi

The patterns followed by the limit moments and the end-rotation at instability, in varying with internal pressure, are very similar in all of the models analyzed. The instability moment starts by increasing rapidly when the value of internal pressure is first incremented, then decreases moderately and finally shows a slight increase at the end of the pressure range. On the other hand, the value of the end-rotation at instability first increases slightly, then decreases quickly, and finally increases again, very significantly.

By inspecting the family of curves that belongs to a different model (h=0.0632), shown in Fig. 3.2.4, these patterns can be seen clearly. Each of the curves, in this figure, corresponds to a different value of internal pressure, covering the range from zero to 800 psi at intervals of 100 psi. The variation of the collapse moment with internal pressure is not immediately evident from these curves, but will be studied in detail later in this chapter.

The families of load-deflection curves for all the other models are also presented, and display the same patterns. Figure 3.2.5 shows the curves of the model with h=0.0722, Figs. 3.2.6 and 3.2.7 those of h=0.0967, Figs. 3.2.8 and 3.2.9 those of h=0.1217, Figs. 3.2.10 and 3.2.11 those of h=0.1475, Figs. 3.2.12 to 3.2.14 those of h=0.1615, Figs. 3.2.15 to 3.2.17 those of h=0.1998, Figs. 3.2.18 to 3.2.21 those of h=0.2675, Figs. 3.2.22 to 3.2.26 those of h=0.3527, and Figs. 3.2.27 to 3.2.32 those of h=0.4417.

It is noted that pipe elbows that have bigger bend factors (h), are affected by internal pressure to a lesser extent, due to their greater wall thickness.

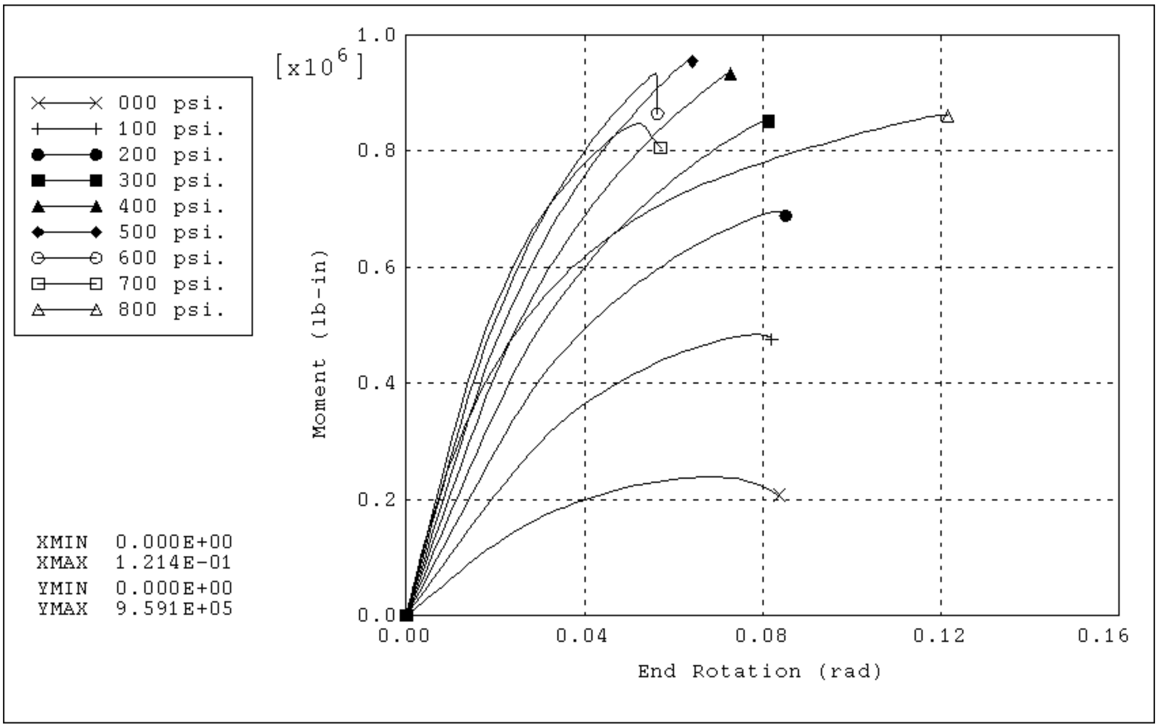

Fig. 3.2.4 Variation of Moment With End-Rotation for an Elbow With h=0.0632 - Internal Pressure Range: 0 ~ 800 psi

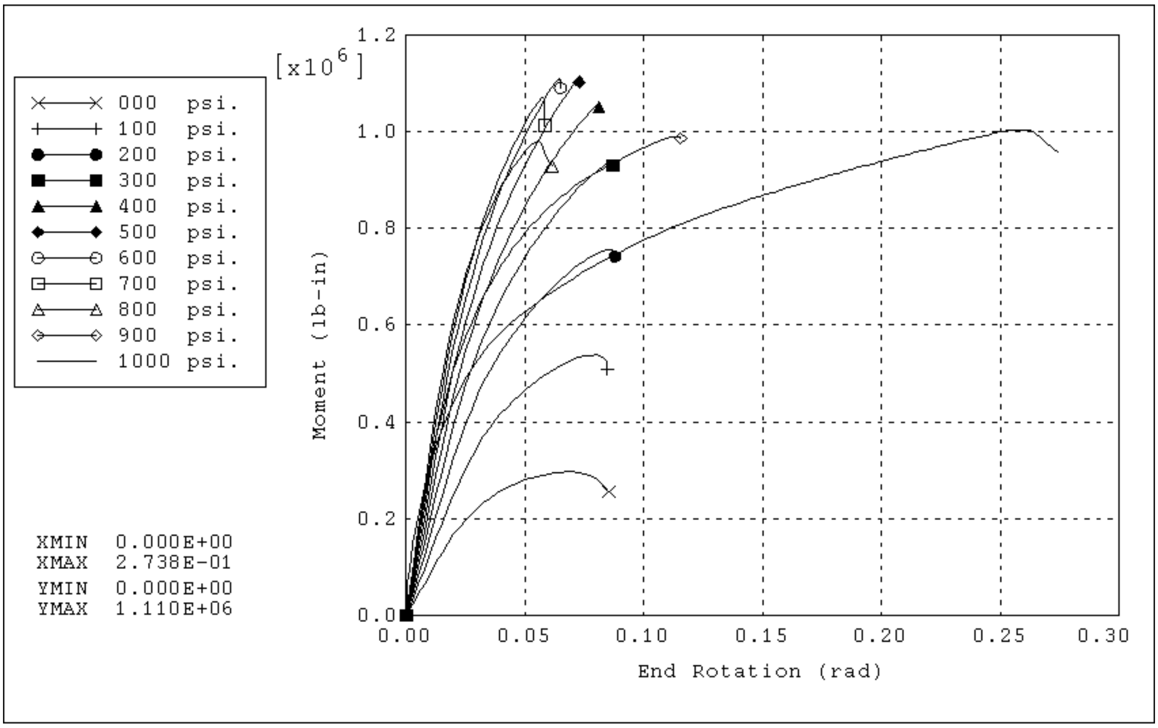

Fig. 3.2.5 Variation of Moment With End-Rotation for an Elbow With h=0.0722 - Internal Pressure Range: 0 ~ 1000 psi

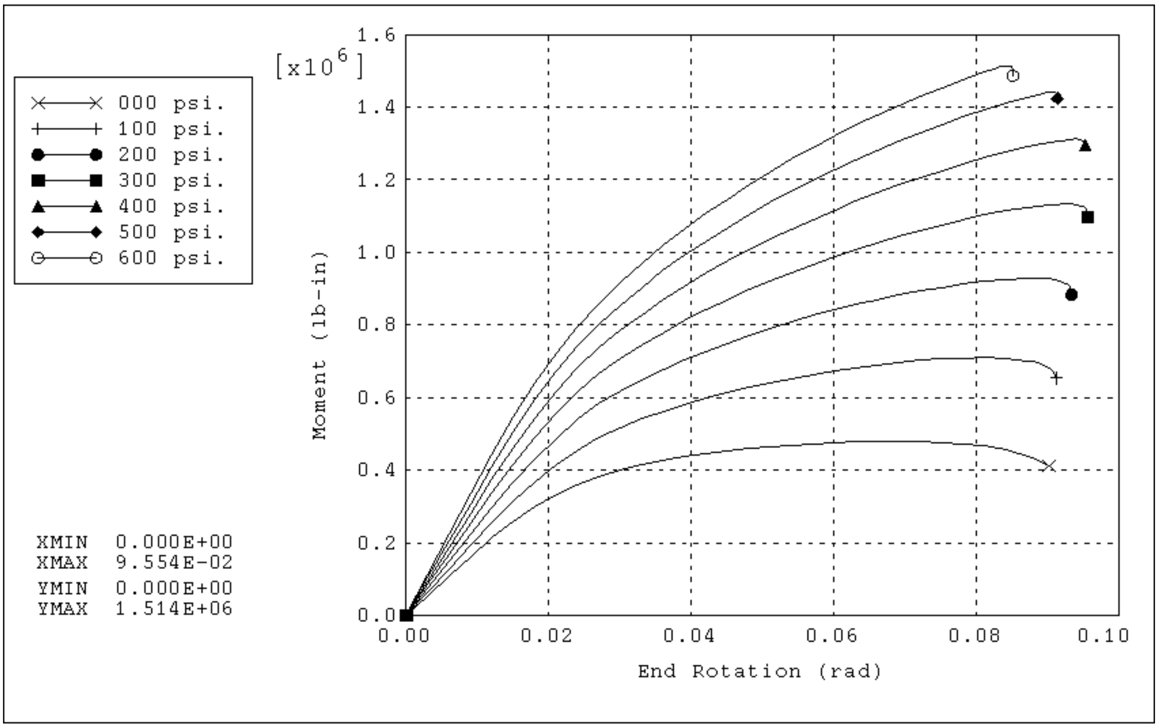

Fig. 3.2.6 Variation of Moment With End-Rotation for an Elbow With h=0.0967 - Internal Pressure Range: 0 ~ 600 psi

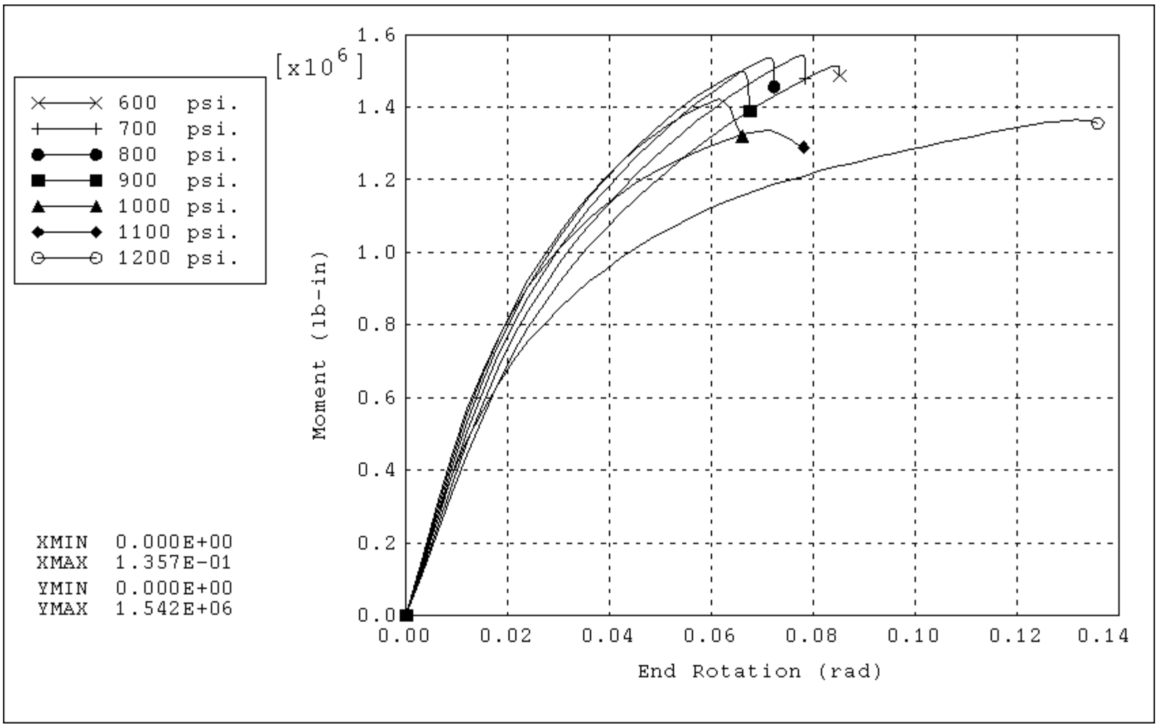

Fig. 3.2.7 Variation of Moment With End-Rotation for an Elbow With h=0.0967 - Internal Pressure Range: 600 ~ 1200 psi

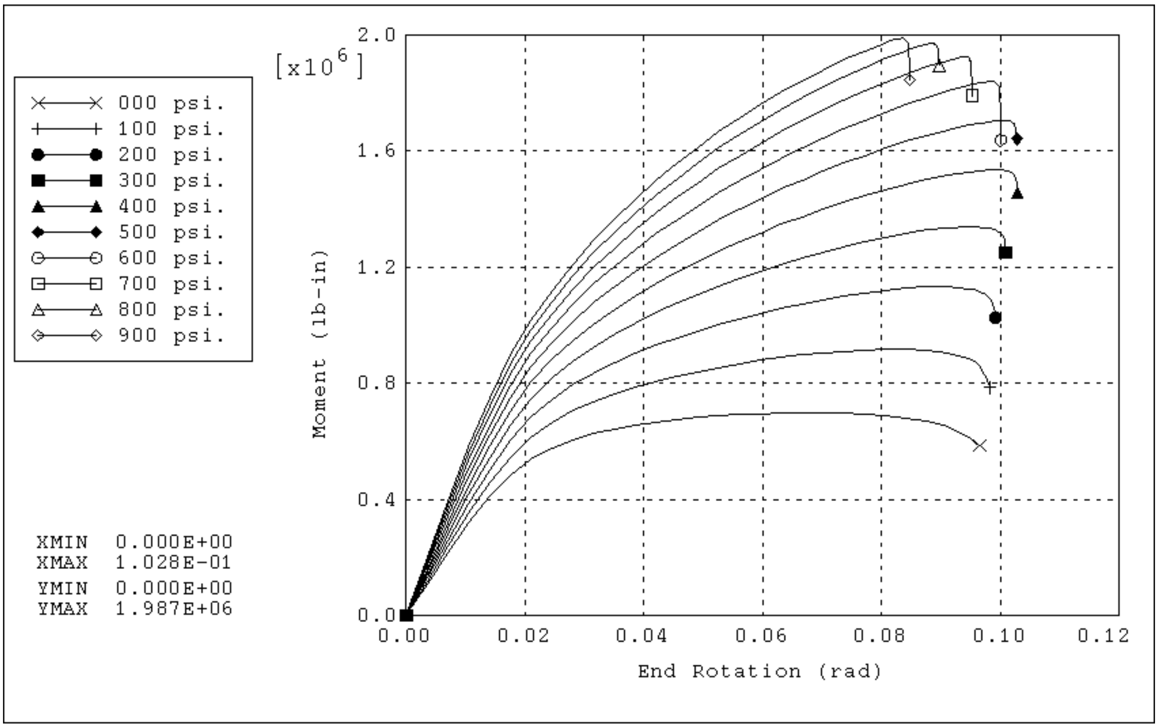

Fig. 3.2.8 Variation of Moment With End-Rotation for an Elbow With h=0.1217 - Internal Pressure Range: 0 ~ 900 psi

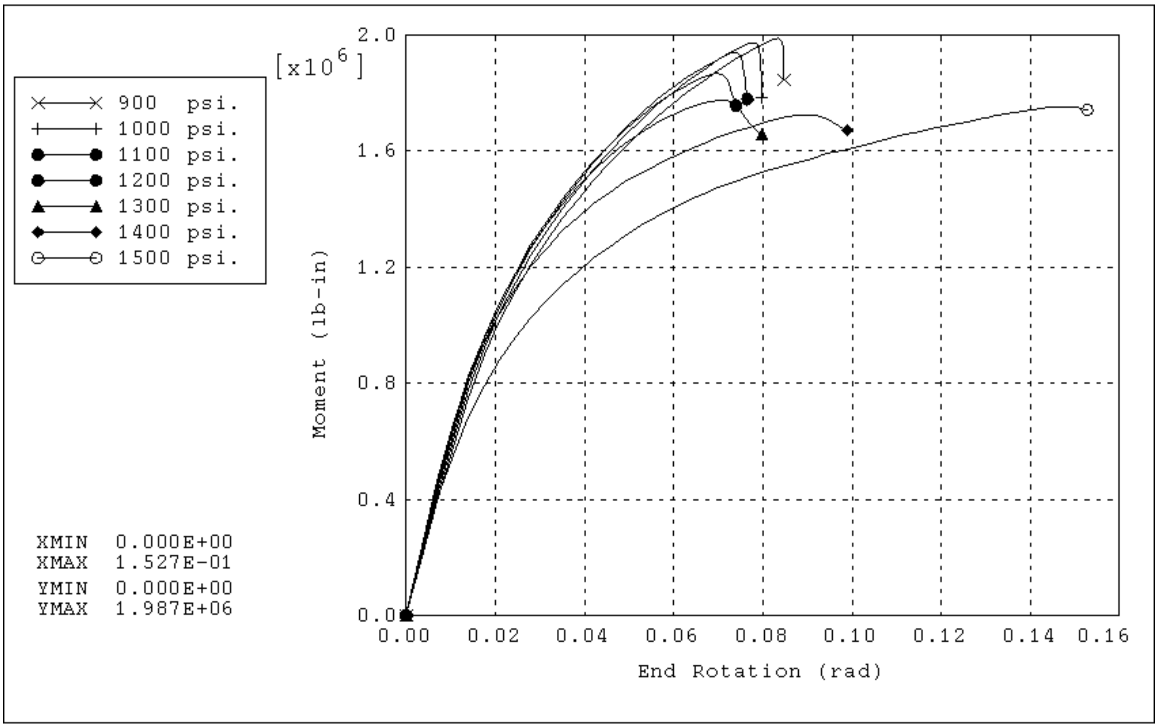

Fig. 3.2.9 Variation of Moment With End-Rotation for an Elbow With h=0.1217 - Internal Pressure Range: 900 ~ 1500 psi

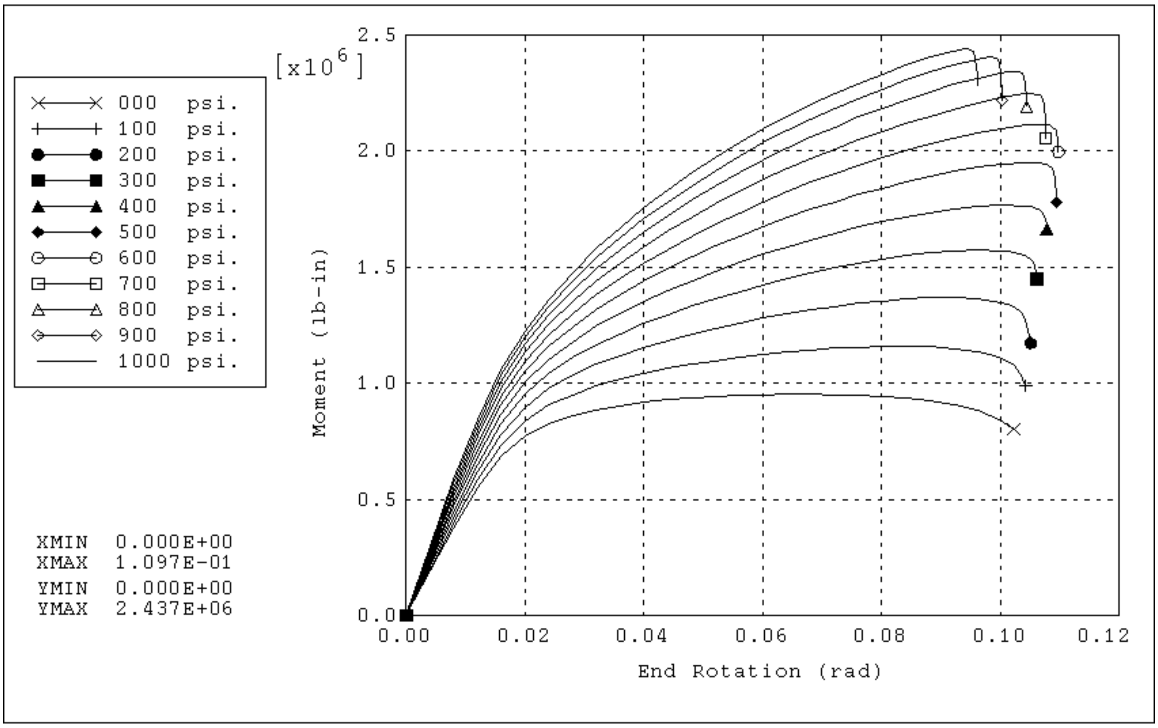

Fig. 3.2.10 Variation of Moment With End-Rotation for an Elbow With h=0.1475 - Internal Pressure Range: 0 ~ 1000 psi

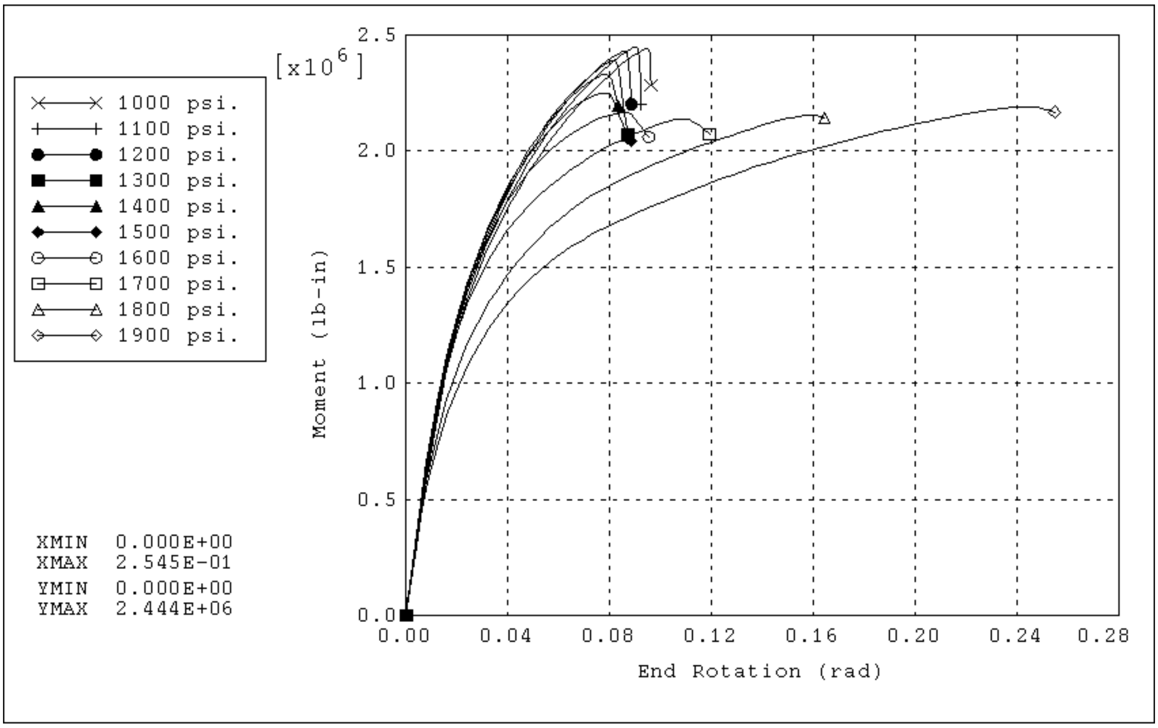

Fig. 3.2.11 Variation of Moment With End-Rotation for an Elbow With h=0.1475 - Internal Pressure Range: 1000 ~ 1900 psi

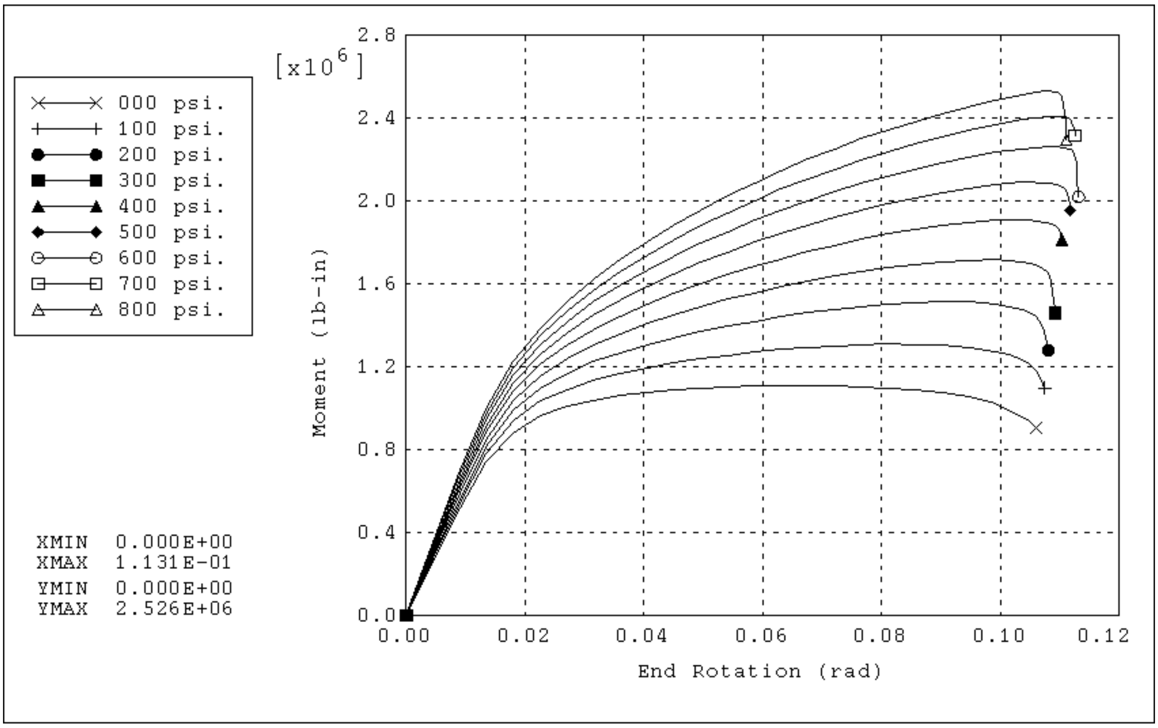

Fig. 3.2.12 Variation of Moment With End-Rotation for an Elbow With h=0.1615 - Internal Pressure Range: 0 ~ 800 psi

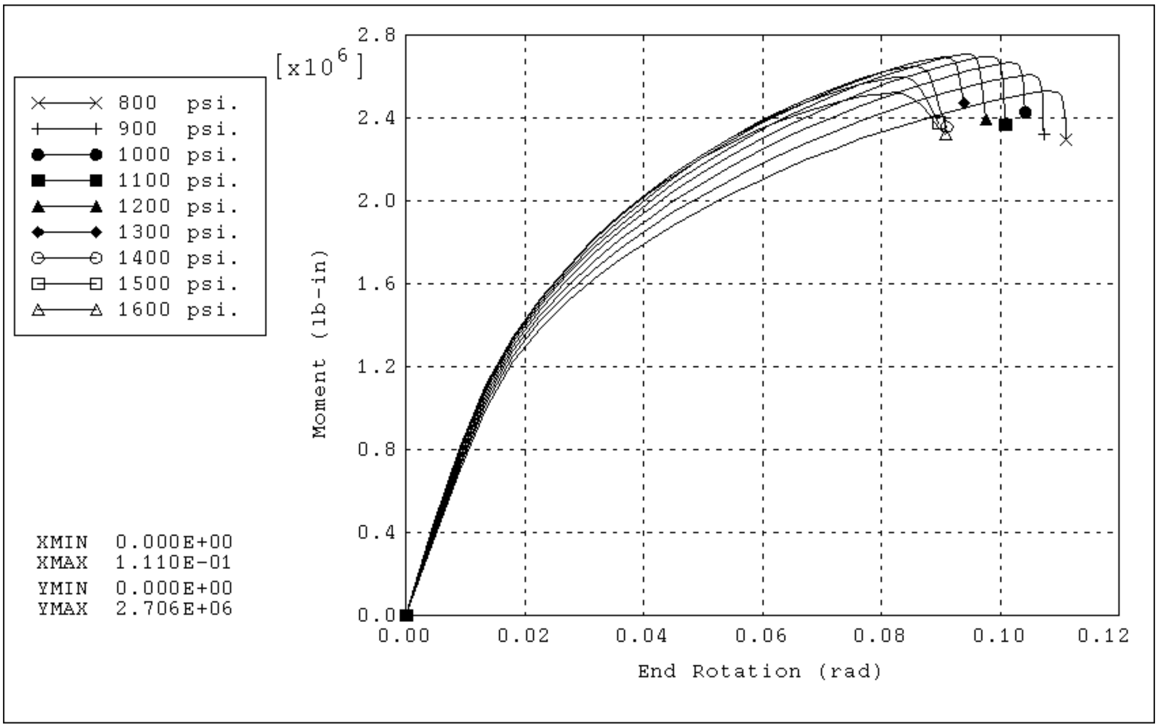

Fig. 3.2.13 Variation of Moment With End-Rotation for an Elbow With h=0.1615 - Internal Pressure Range: 800 ~ 1600 psi

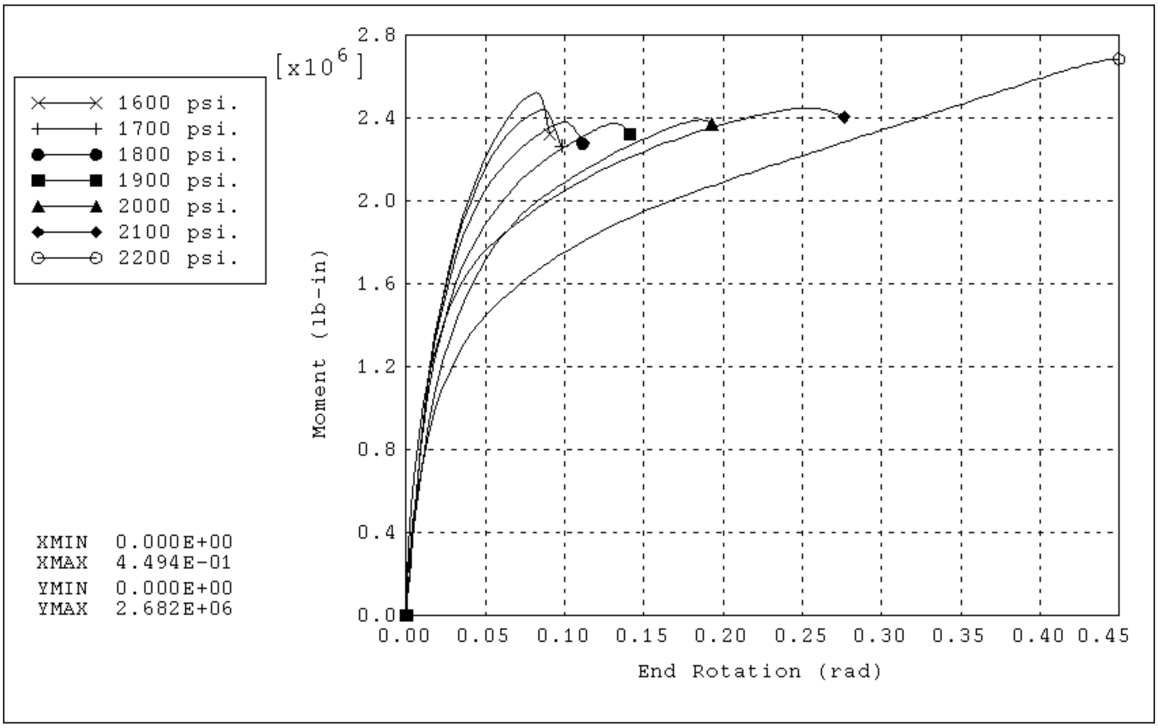

Fig. 3.2.14 Variation of Moment With End-Rotation for an Elbow With h=0.1615 - Internal Pressure Range: 1600 ~ 2200 psi

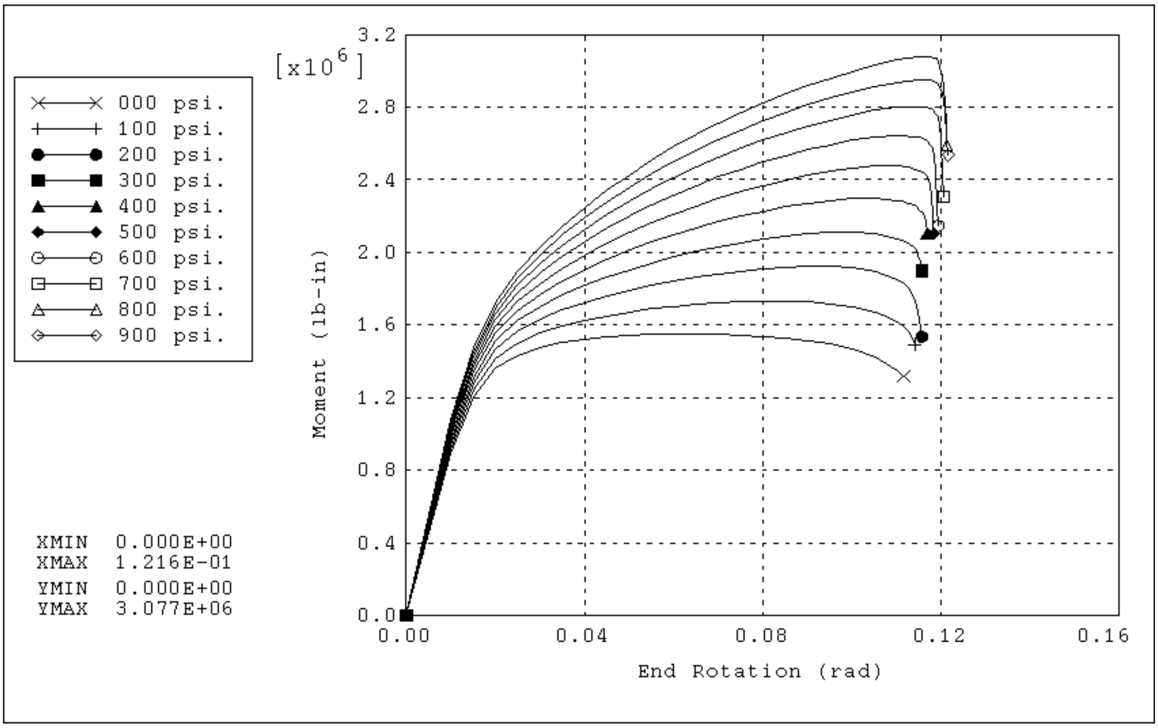

Fig. 3.2.15 Variation of Moment With End-Rotation for an Elbow With h=0.1998 - Internal Pressure Range: 0 ~ 900 psi

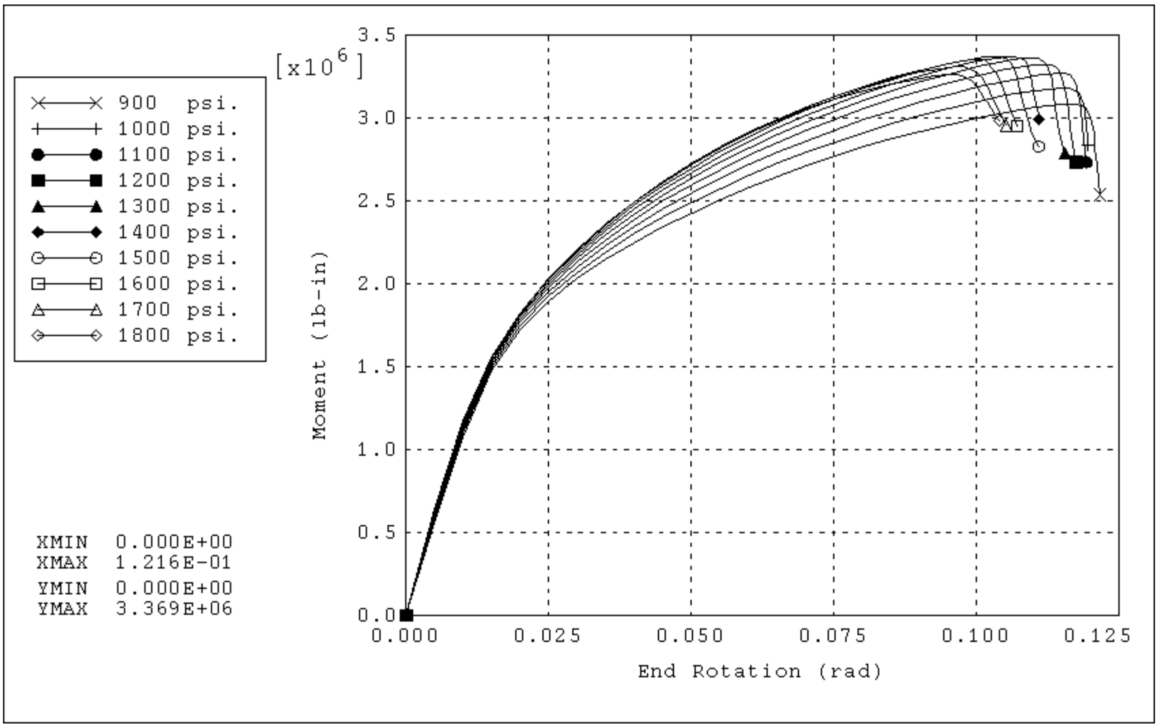

Fig. 3.2.16 Variation of Moment With End-Rotation for an Elbow With h=0.1998 - Internal Pressure Range: 900 ~ 1800 psi

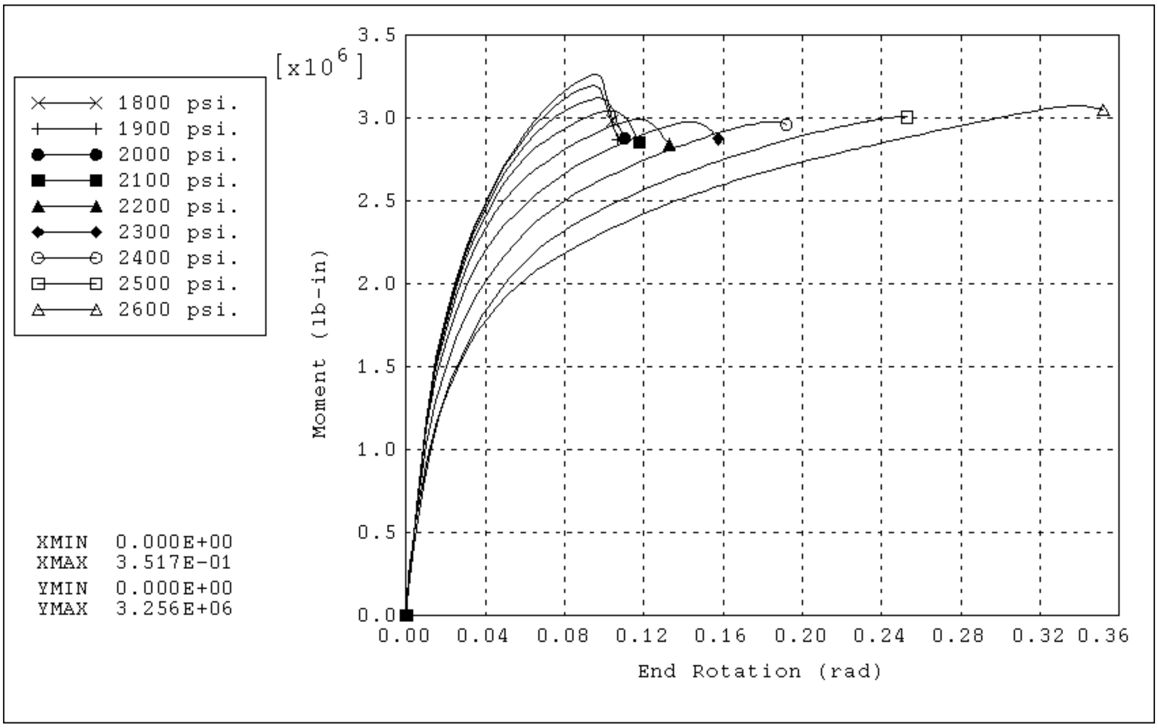

Fig. 3.2.17 Variation of Moment With End-Rotation for an Elbow With h=0.1998 - Internal Pressure Range: 1800 ~ 2600 psi

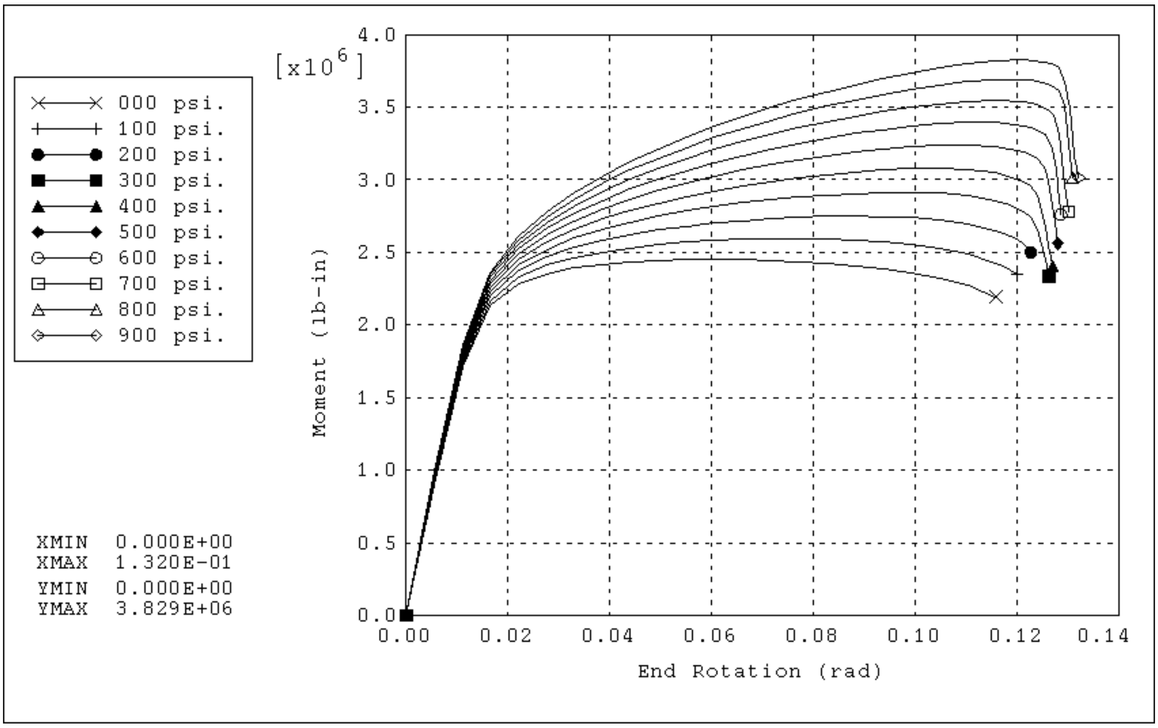

Fig. 3.2.18 Variation of Moment With End-Rotation for an Elbow With h=0.2675 - Internal Pressure Range: 0 ~ 900 psi

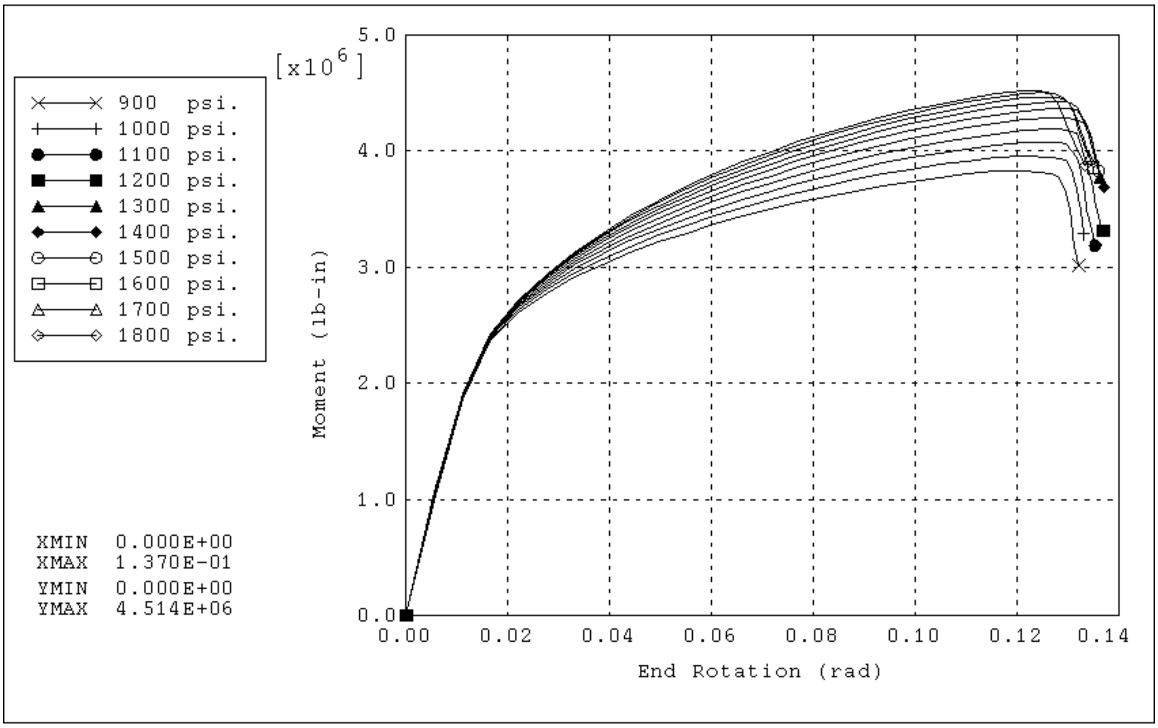

Fig. 3.2.19 Variation of Moment With End-Rotation for an Elbow With h=0.2675 - Internal Pressure Range: 900 ~ 1800 psi

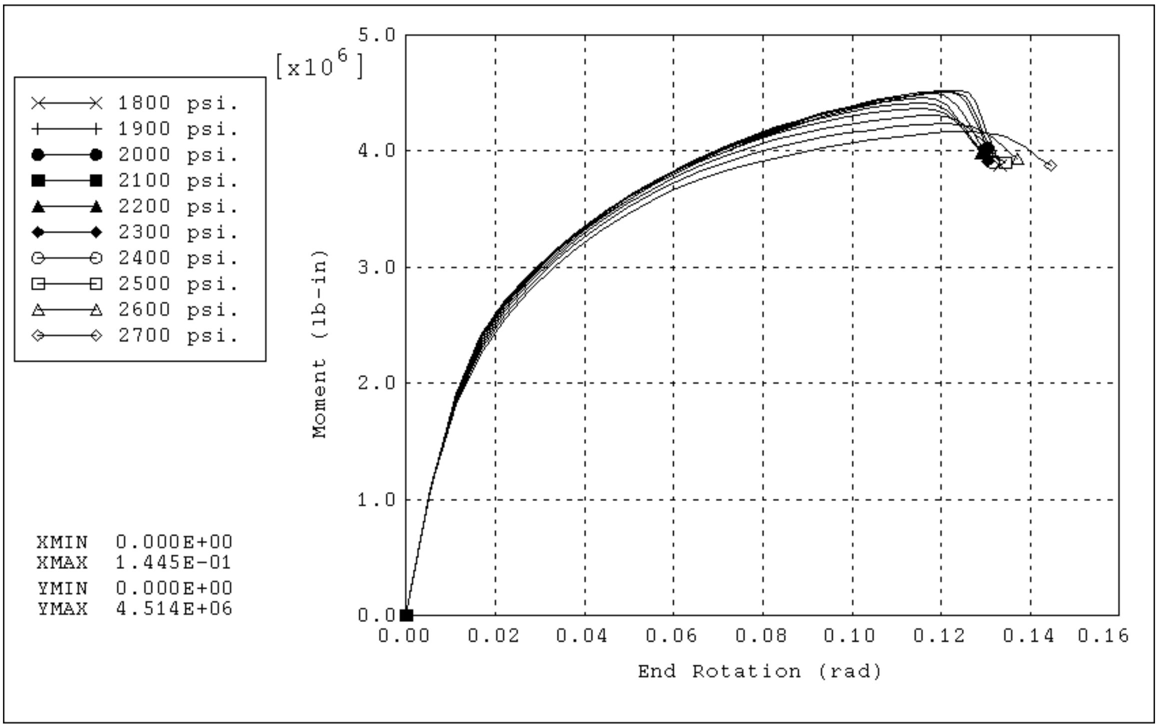

Fig. 3.2.20 Variation of Moment With End-Rotation for an Elbow With h=0.2675 - Internal Pressure Range: 1800 ~ 2700 psi

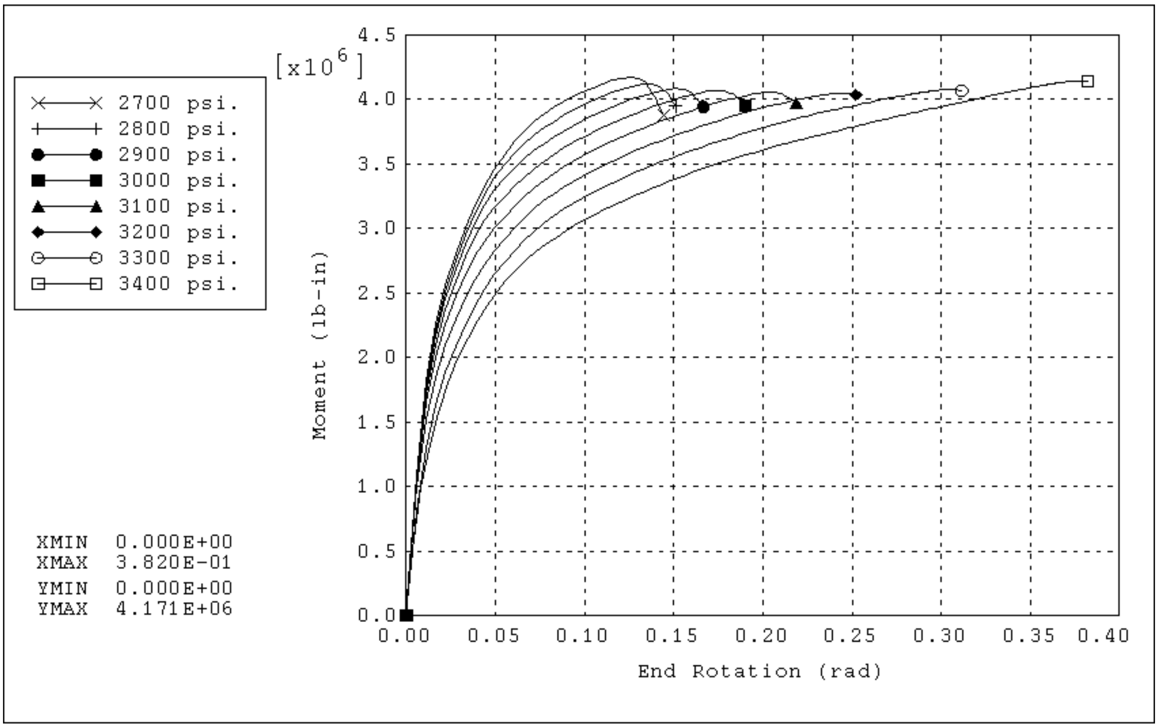

Fig. 3.2.21 Variation of Moment With End-Rotation for an Elbow With h=0.2675 - Internal Pressure Range: 2700 ~ 3400 psi

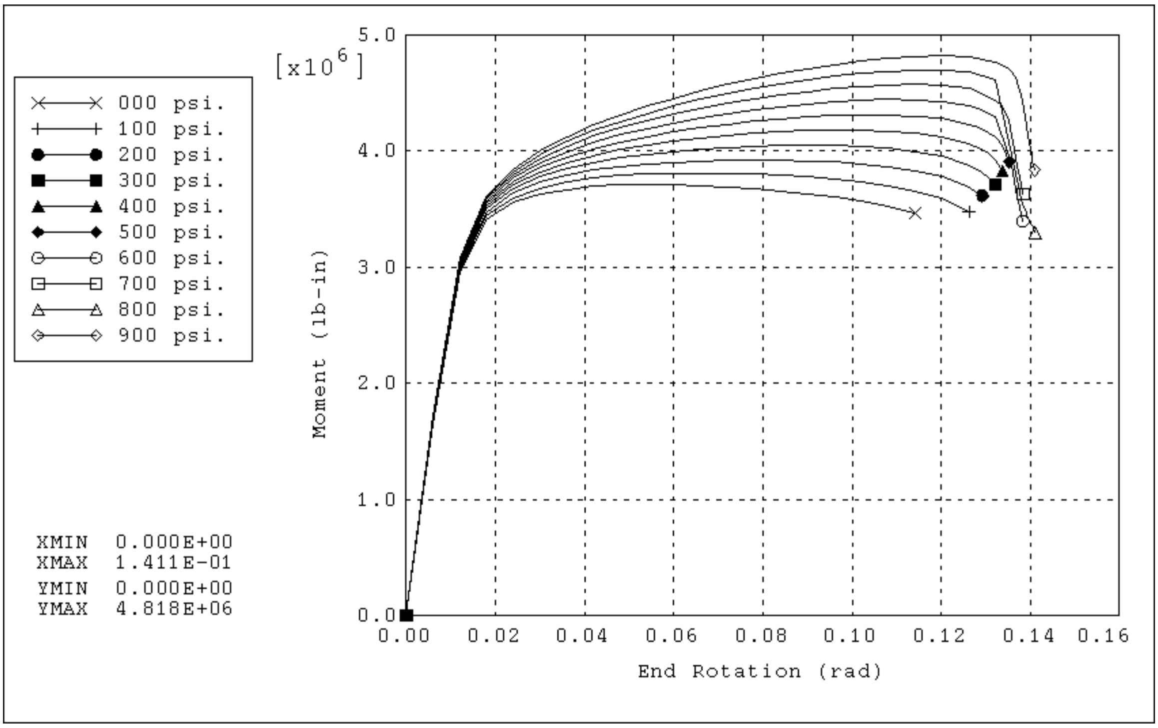

Fig. 3.2.22 Variation of Moment With End-Rotation for an Elbow With h=0.3527 - Internal Pressure Range: 0 ~ 900 psi

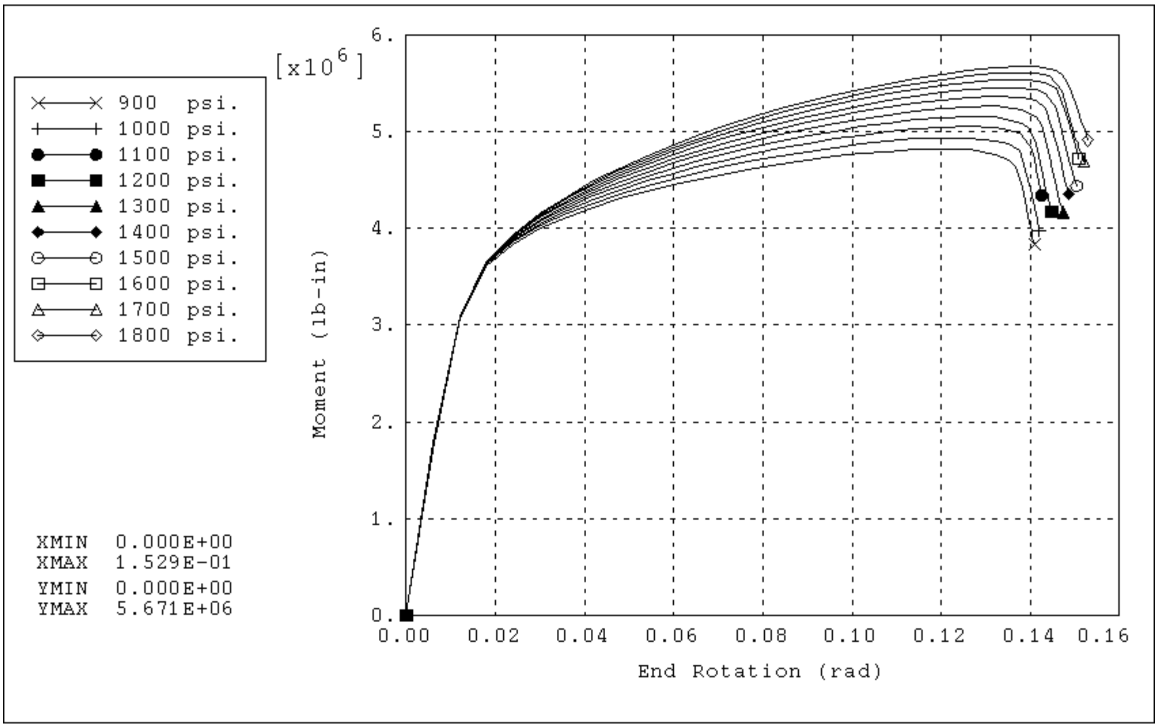

Fig. 3.2.23 Variation of Moment With End-Rotation for an Elbow With h=0.3527 - Internal Pressure Range: 900 ~ 1800 psi

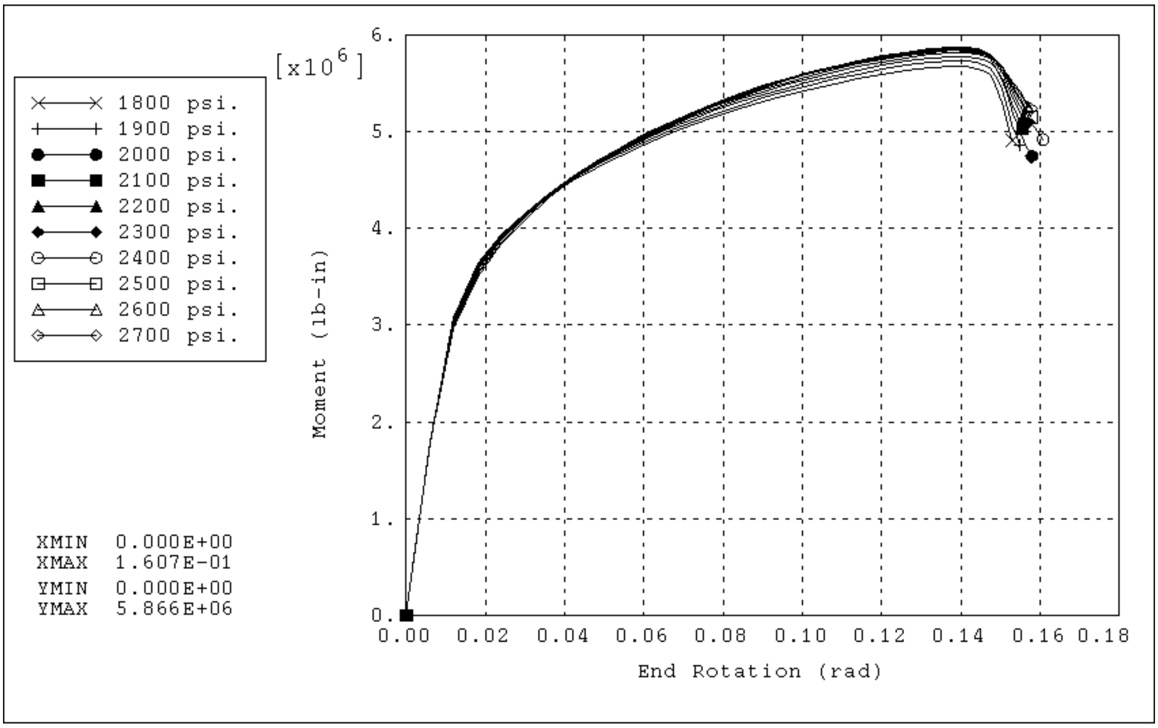

Fig. 3.2.24 Variation of Moment With End-Rotation for an Elbow With h=0.3527 - Internal Pressure Range: 1800 ~ 2700 psi

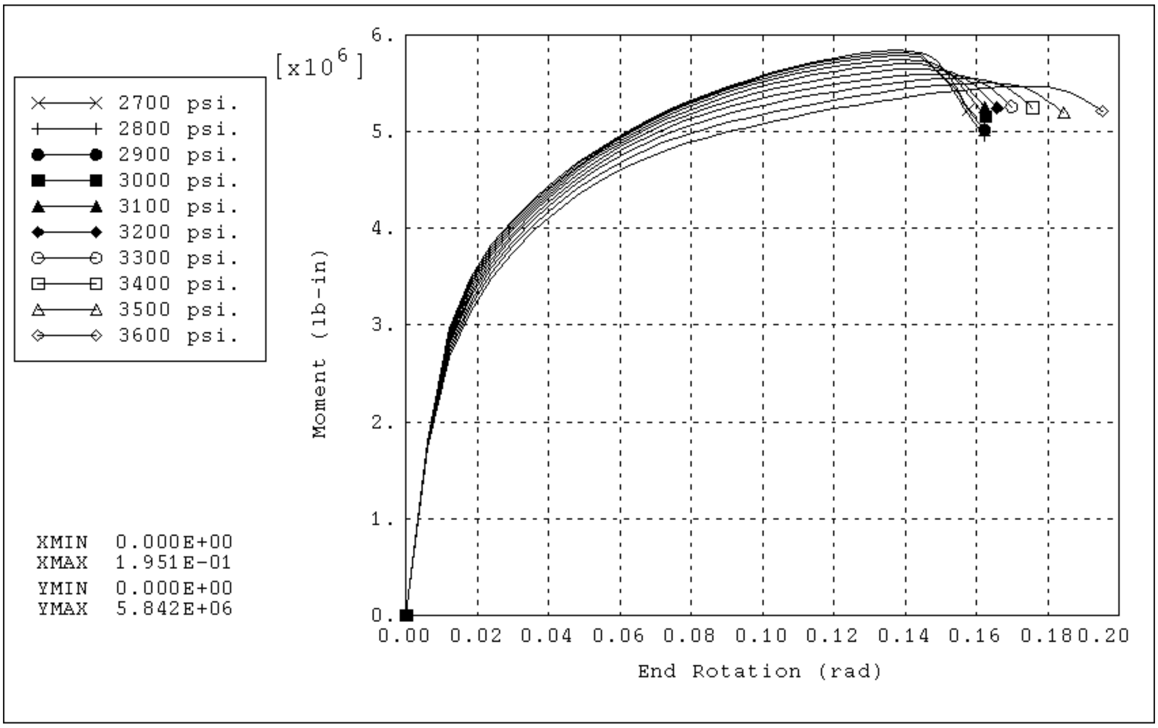

Fig. 3.2.25 Variation of Moment With End-Rotation for an Elbow With h=0.3527 - Internal Pressure Range: 2700 ~ 3600 psi

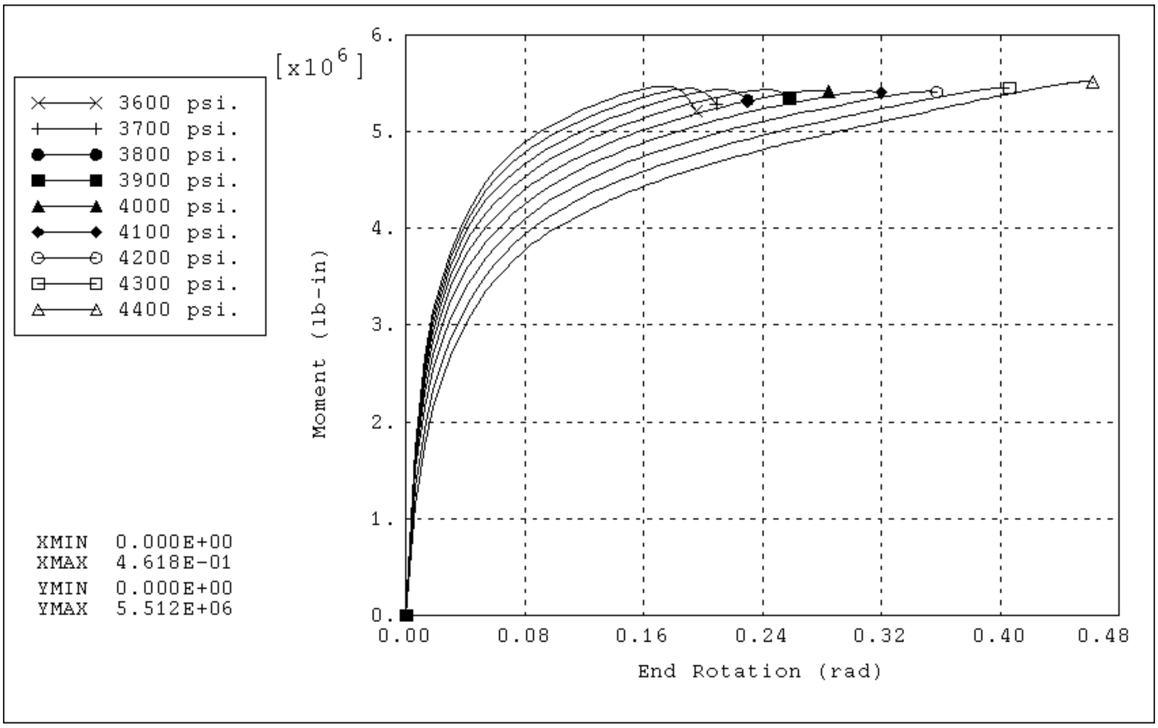

Fig. 3.2.26 Variation of Moment With End-Rotation for an Elbow With h=0.3527 - Internal Pressure Range: 3600 ~ 4400 psi

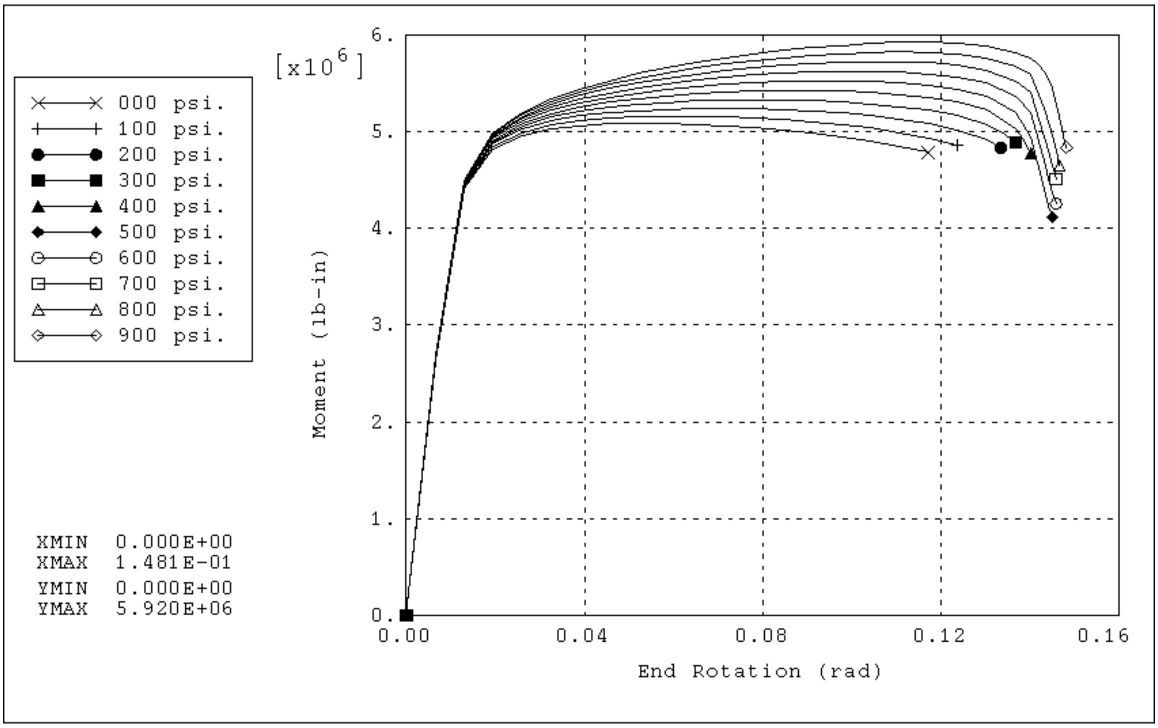

Fig. 3.2.27 Variation of Moment With End-Rotation for an Elbow With h=0.4417 - Internal Pressure Range: 0 ~ 900 psi

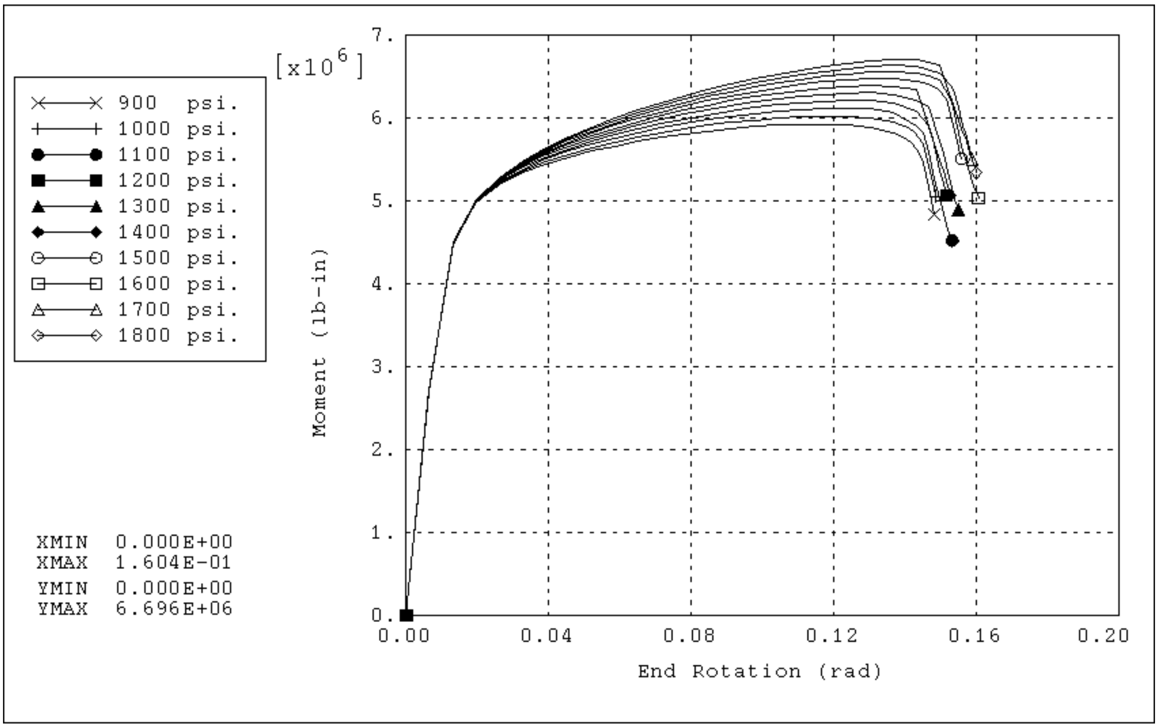

Fig. 3.2.28 Variation of Moment With End-Rotation for an Elbow With h=0.4417 - Internal Pressure Range: 900 ~ 1800 psi

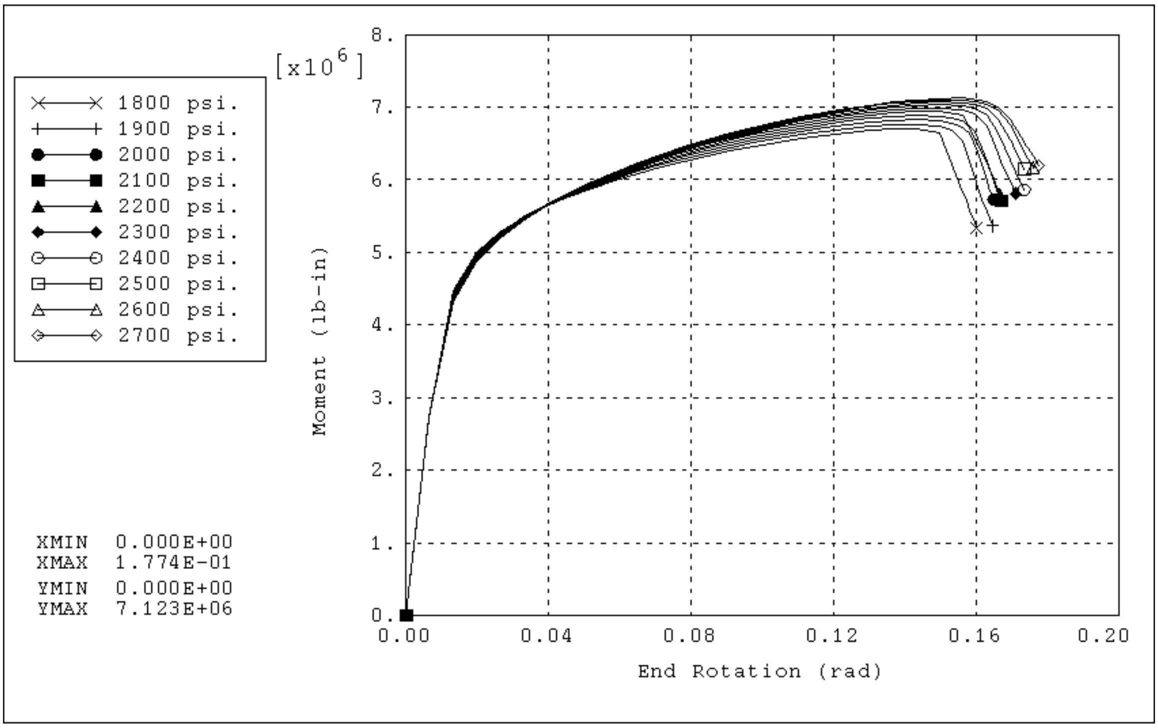

Fig. 3.2.29 Variation of Moment With End-Rotation for an Elbow With h=0.4417 - Internal Pressure Range: 1800 ~ 2700 psi

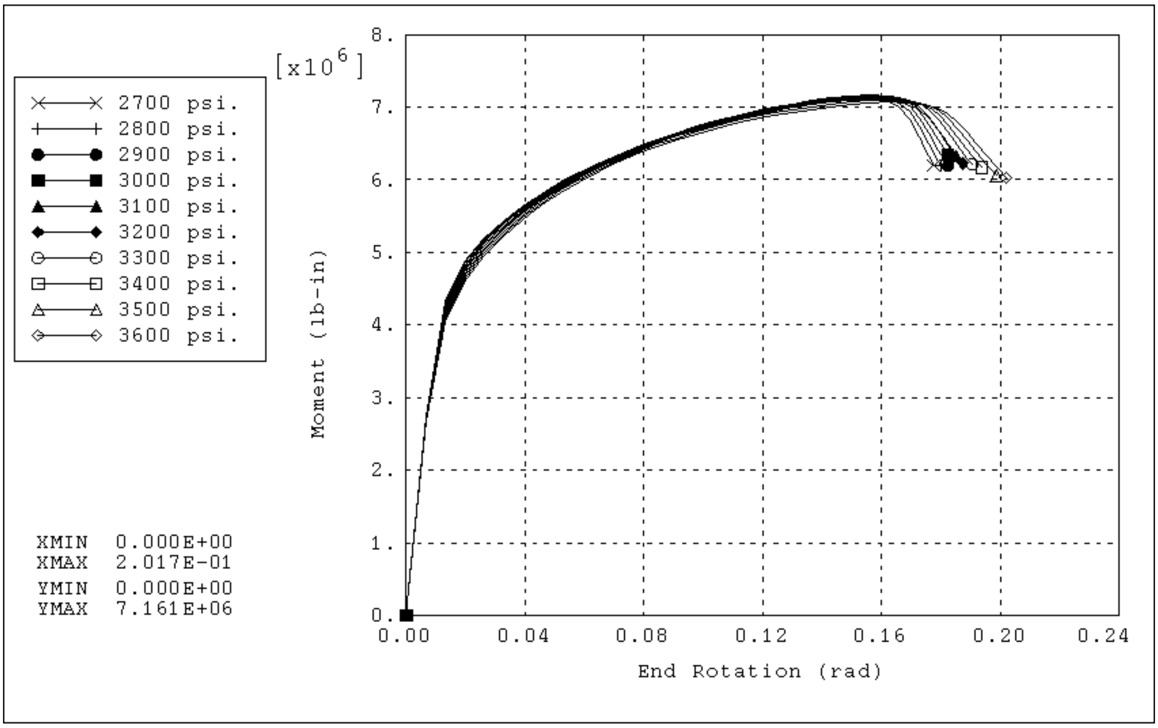

Fig. 3.2.30 Variation of Moment With End-Rotation for an Elbow With h=0.4417 - Internal Pressure Range: 2700 ~ 3600 psi

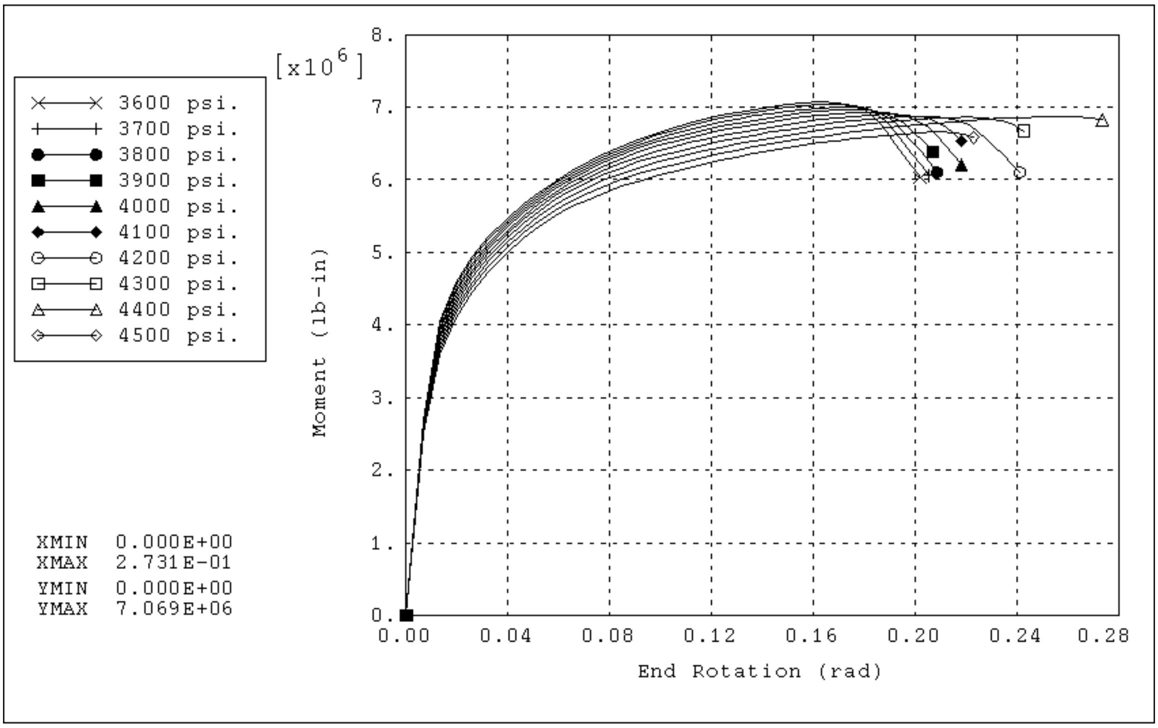

Fig. 3.2.31 Variation of Moment With End-Rotation for an Elbow With h=0.4417 - Internal Pressure Range: 3600 ~ 4500 psi

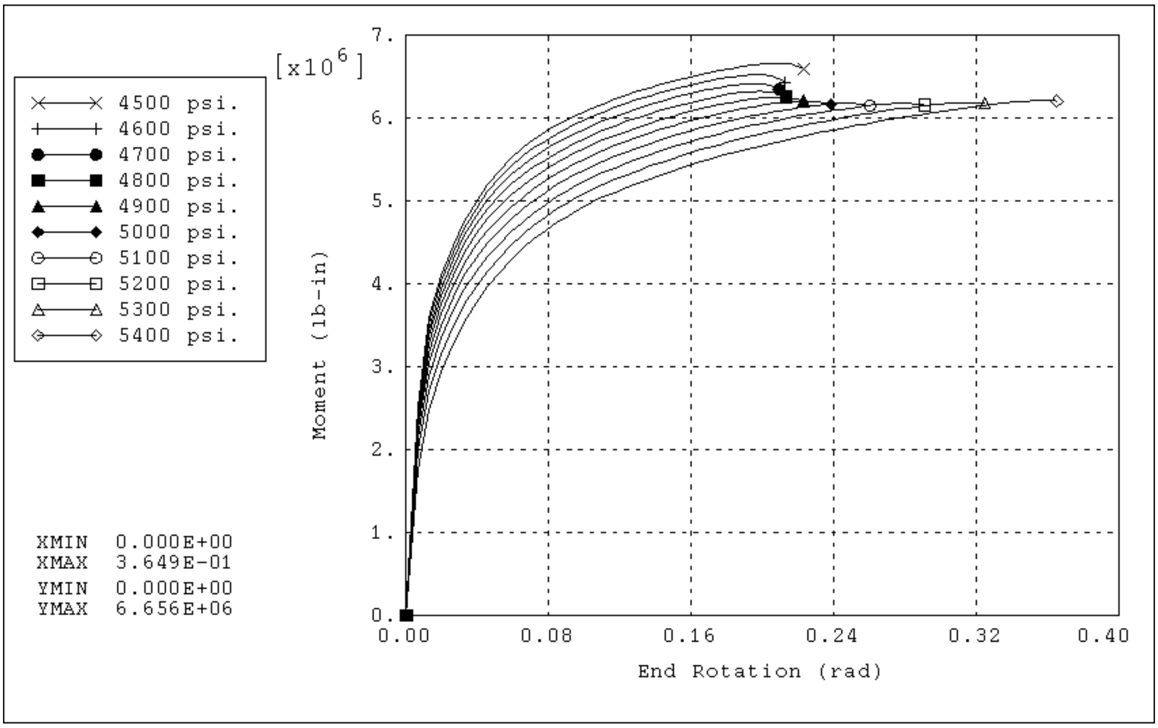

Fig. 3.2.32 Variation of Moment With End-Rotation for an Elbow With h=0.4417 - Internal Pressure Range: 4500 ~ 5400 psi

3.3 Variation of Limit Moment with Internal Pressure and Bend Factor

In the previous section, load-deflection curves were presented, for each of the different models studied. For each model, several curves were plotted, each showing the behavior of the pipe elbow under out-of-plane moment loading, at a specific fixed value of internal pressure.

These curves illustrate the effect of internal pressure on the load-deflection behavior of each model, as well as the effect of the value of the pipe bend factor, which is the only difference between one model and another. However, the load-deflection curves are not suitable for design purposes, where the main interest is to determine the maximum moment load that a certain elbow can sustain, with a specified internal pressure.

Therefore, a set of limit curves was generated from the load-deflection curves, to clearly show the variation of the limit moments - instability and collapse moments - of each model, with the value of internal pressure. Similarly, a set of curves was generated to show the variation of the limit moments with the value of the pipe bend factor.

3.3.1 Limit Curves

Figure 3.3.1 shows the variation of the instability and the collapse moments with internal pressure for the model with the smallest bend factor in this study (h=0.0632). It can be seen that the instability moment increases with the increase of the internal pressure, until a certain value of the pressure, approximately 470 psi, where the effect of pressure is reversed. A local minimum point exists close to the end of the pressure range, after which the instability moment starts rising again slowly.

The variation of the collapse moment is shown for the same elbow geometry, on the same graph. It is noticed that it also follows a pattern that increases at first, but starts decreasing at a certain value of the pressure, that is approximately 450 psi in this case.

Figures 3.3.2 through 3.3.10 show similar graphs for the rest of the models, in which similar patterns are clear. Some minor differences exist between the graphs of each model however; for example, in Fig. 3.3.6 (h=0.1615), the instability moment increases towards the end of the pressure range more notably than other cases.

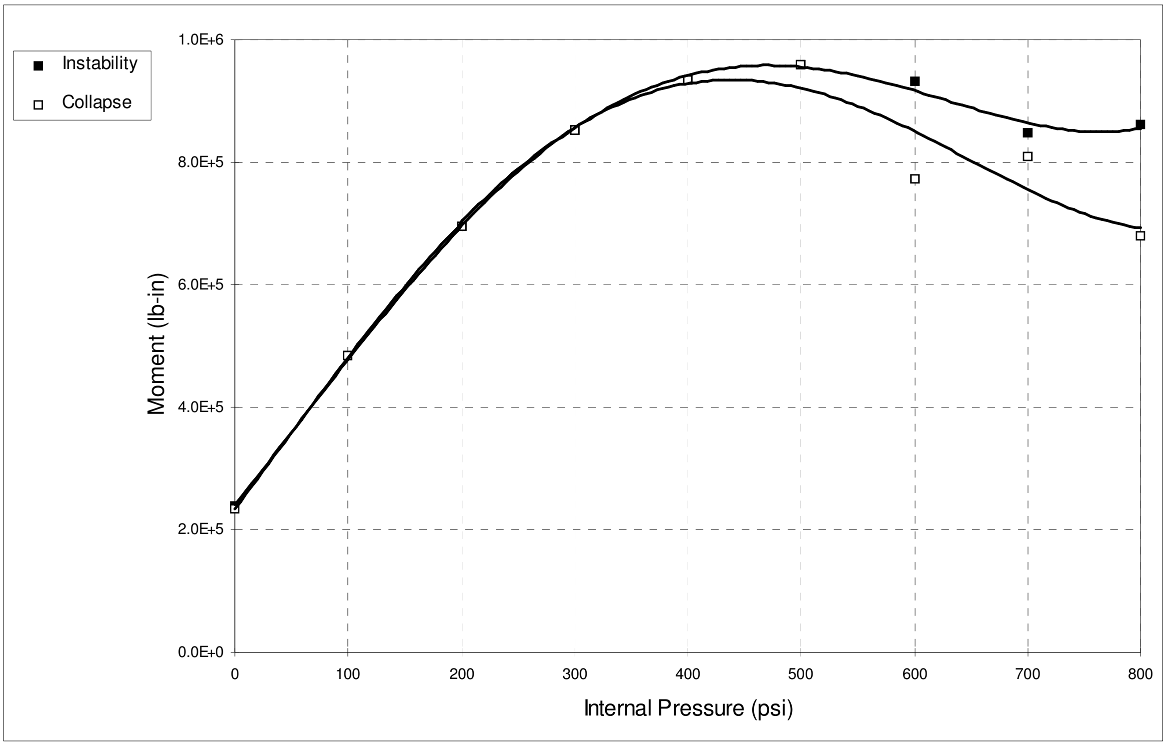

Fig. 3.3.1 Variation of Limit Moments With Internal Pressure for an Elbow With h=0.0632

It is also noted that in all the cases, the value of the collapse moment is very close to the instability moment in the absence of internal pressure. On the other hand, as the internal pressure increases, especially at the very end of the applicable range of pressure for each model, the collapse moment has a lower value than the instability moment.

For the first two models (h=0.0632 and h=0.0722, represented in Figs. 3.3.1 and 3.3.2), at some values of the pressure, the collapse limit line of the twice-elastic-slope method discussed in chapter two, intersects the load-deflection curve after the instability point. The value of the instability moment is taken also as the collapse moment for these cases. This can be considered a drawback of the twice-elastic-slope method. Moreover, because it is a graphical method, it is noticed that the data points of the collapse curve of a certain model are more scattered above and below their curve, compared to the data points of the instability curve of the same model.

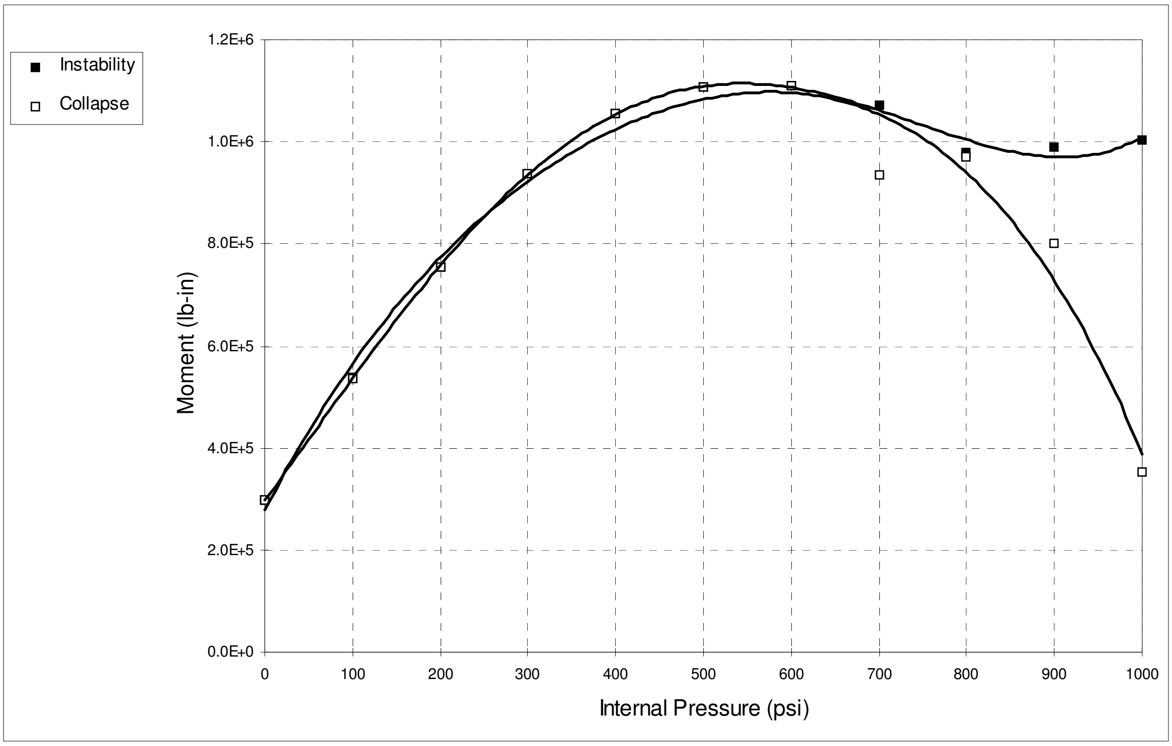

Fig. 3.3.2 Variation of Limit Moments With Internal Pressure for an Elbow With h=0.0722

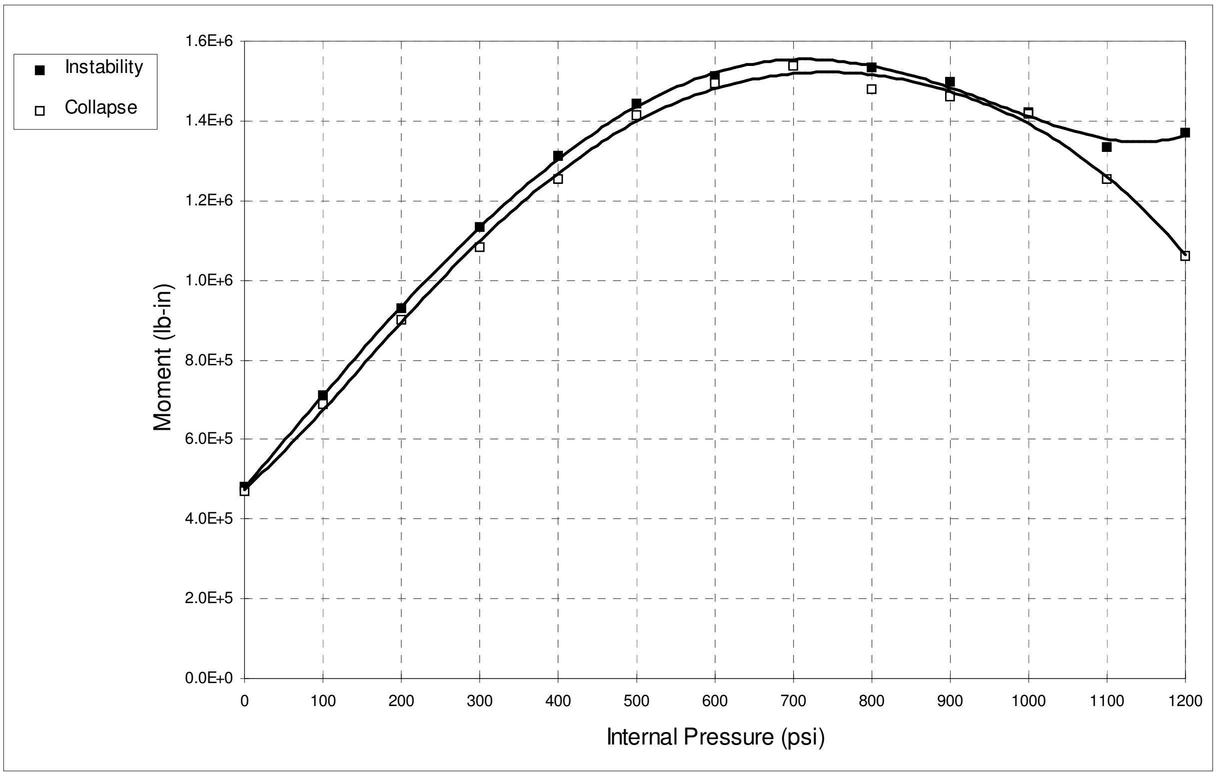

Fig. 3.3.3 Variation of Limit Moments With Internal Pressure for an Elbow With h=0.0967

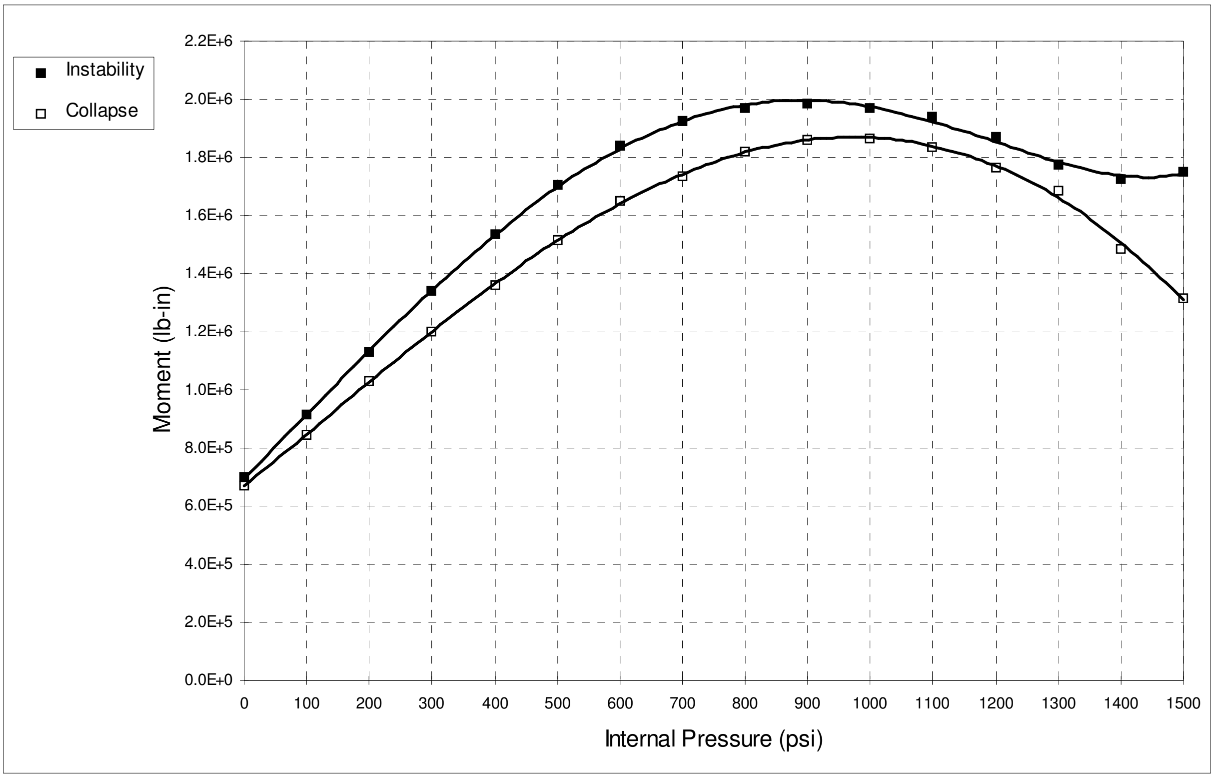

Fig. 3.3.4 Variation of Limit Moments With Internal Pressure for an Elbow With h=0.1217

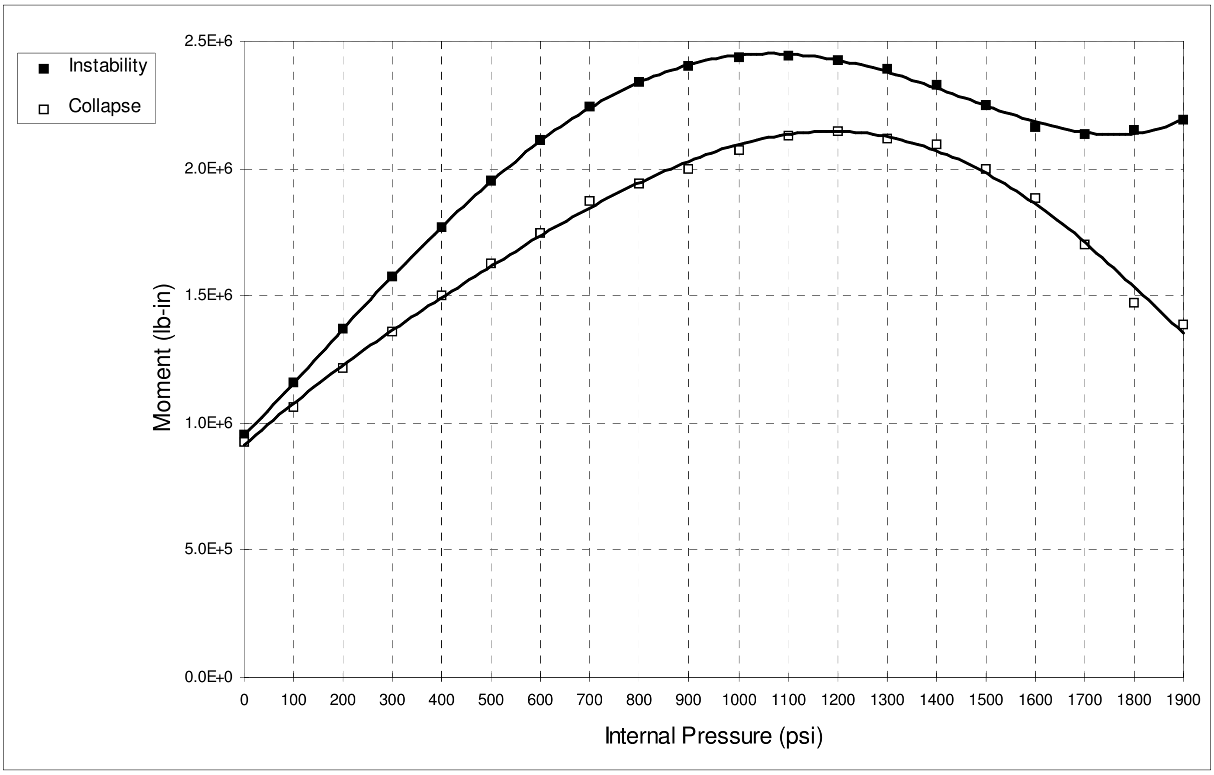

Fig. 3.3.5 Variation of Limit Moments With Internal Pressure for an Elbow With h=0.1475

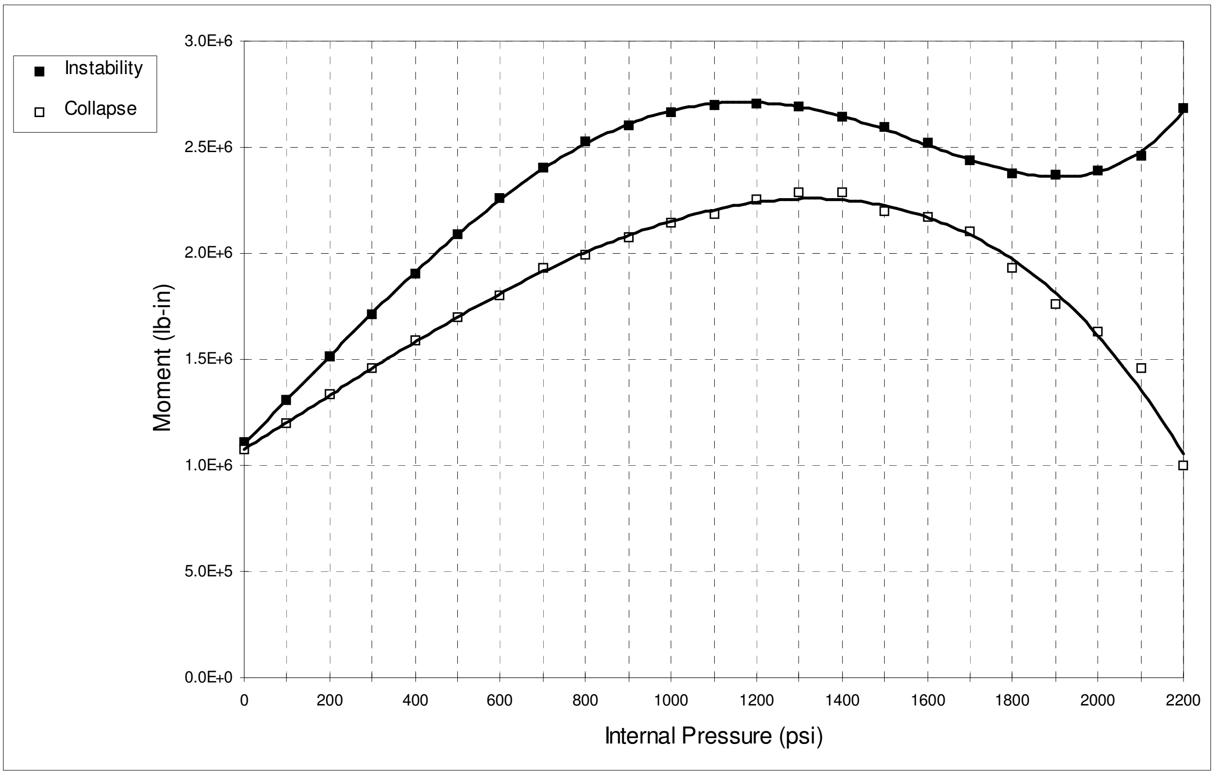

Fig. 3.3.6 Variation of Limit Moments With Internal Pressure for an Elbow With h=0.1615

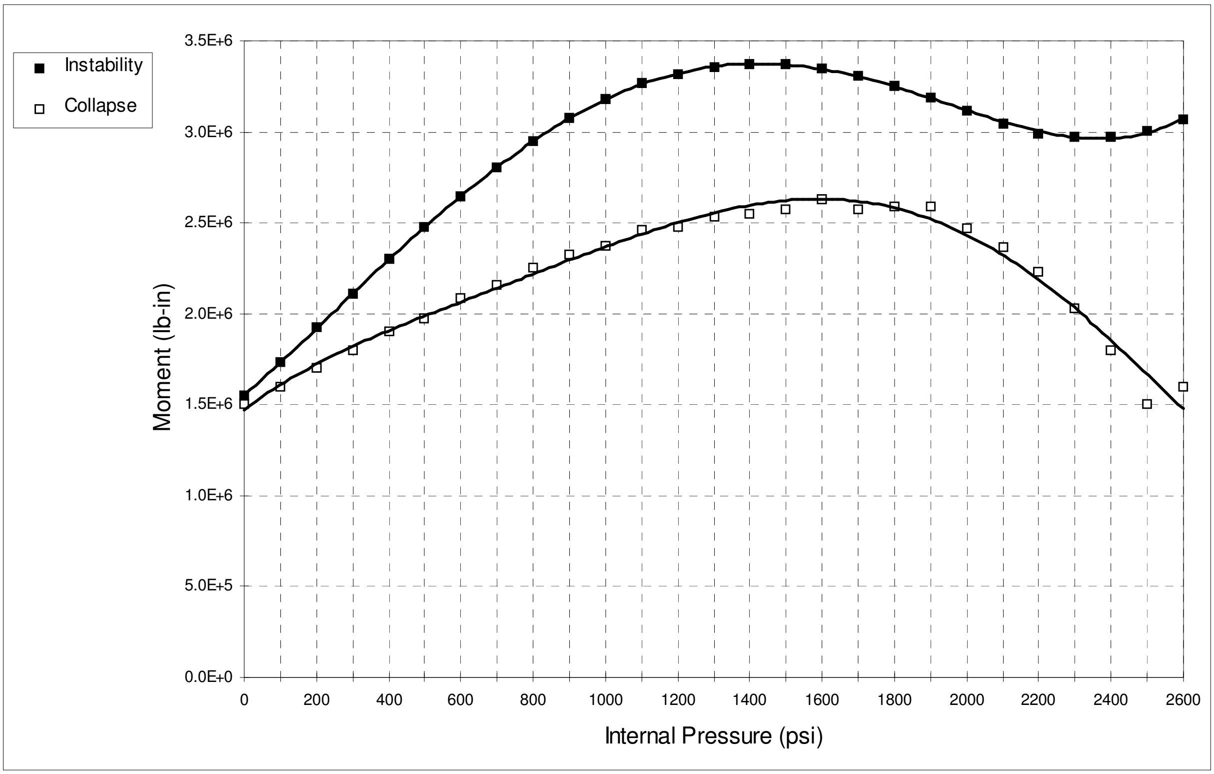

Fig. 3.3.7 Variation of Limit Moments With Internal Pressure for an Elbow With h=0.1998

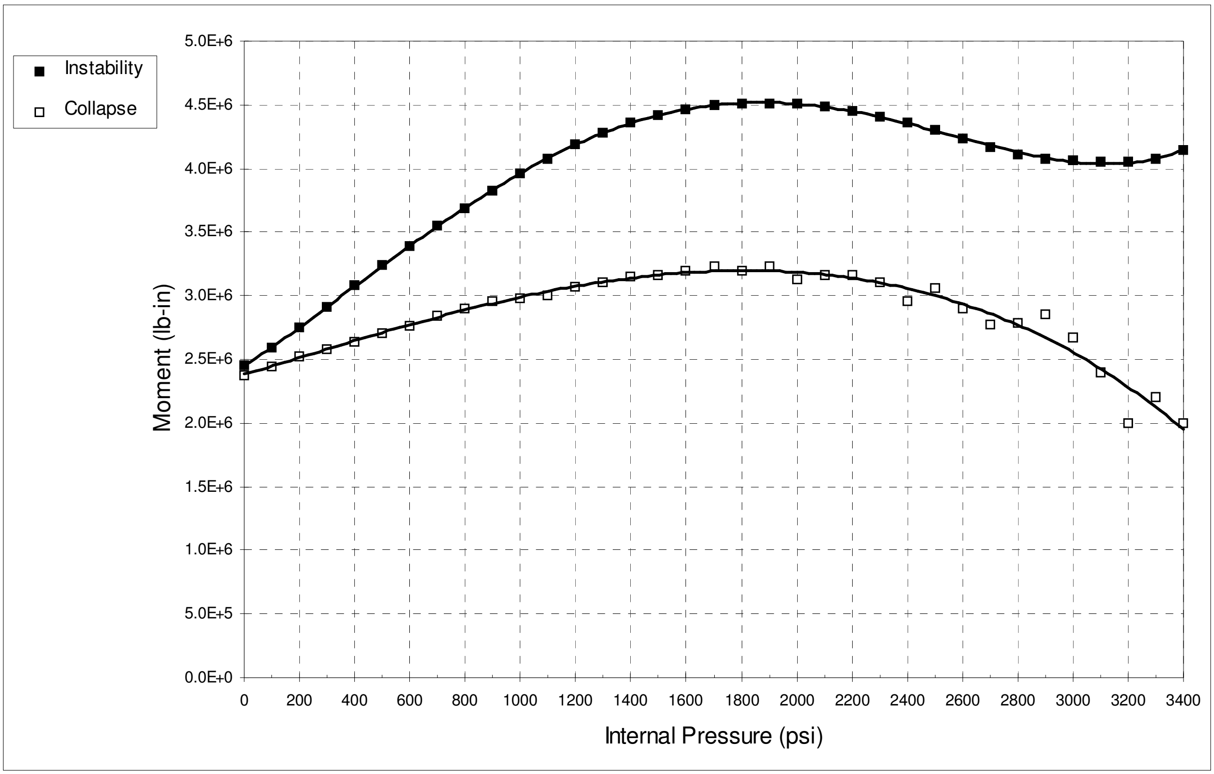

Fig. 3.3.8 Variation of Limit Moments With Internal Pressure for an Elbow With h=0.2675

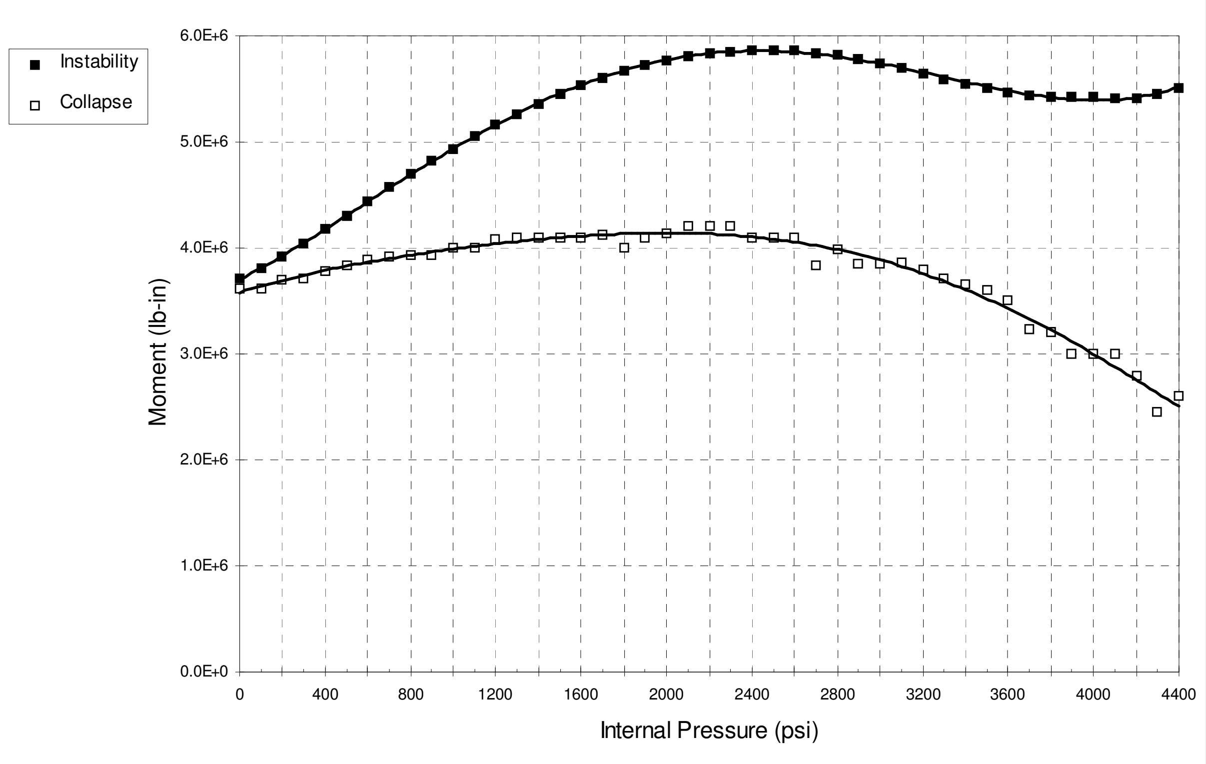

Fig. 3.3.9 Variation of Limit Moments With Internal Pressure for an Elbow With h=0.3527

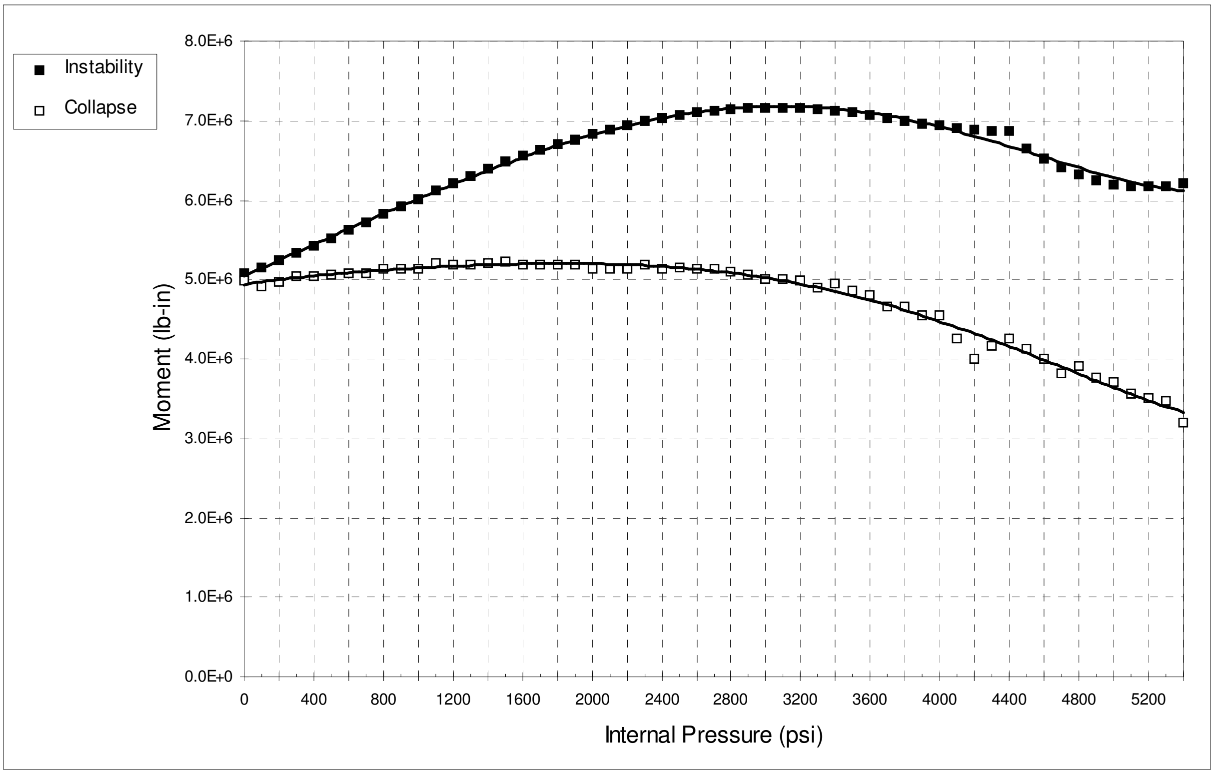

Fig. 3.3.10 Variation of Limit Moments With Internal Pressure for an Elbow With h=0.4417

These limit curves are grouped in Figs. 3.3.11 through 3.3.14. The variation of the instability moment with internal pressure for five different models (h=0.1615 to h=0.4417) is shown in Fig. 3.3.11, and for the remaining five models (h=0.0632 to h=0.1475) in Fig. 3.3.12.

It is clear, from these two figures, that the instability moment is larger for elbows with a higher value of the pipe bend factor (h); which is logical because the larger the wall thickness, the higher the overall stiffness of the elbow.

Furthermore, the limit curve of each model reaches a maximum at a value of the pressure that is slightly higher than half the maximum pressure that the model can sustain, and of course, models with higher bend factors (h), can withstand higher internal pressures. Hence, it is also understandable, that models with a higher bend factor, reach their highest value of the instability moment, at a higher value of the pressure.

In other words, the maximum points for the limit curves of Figs. 3.3.11 and 3.3.12 keep shifting not only up, but also to the right, for models with higher values of the bend factor (h).

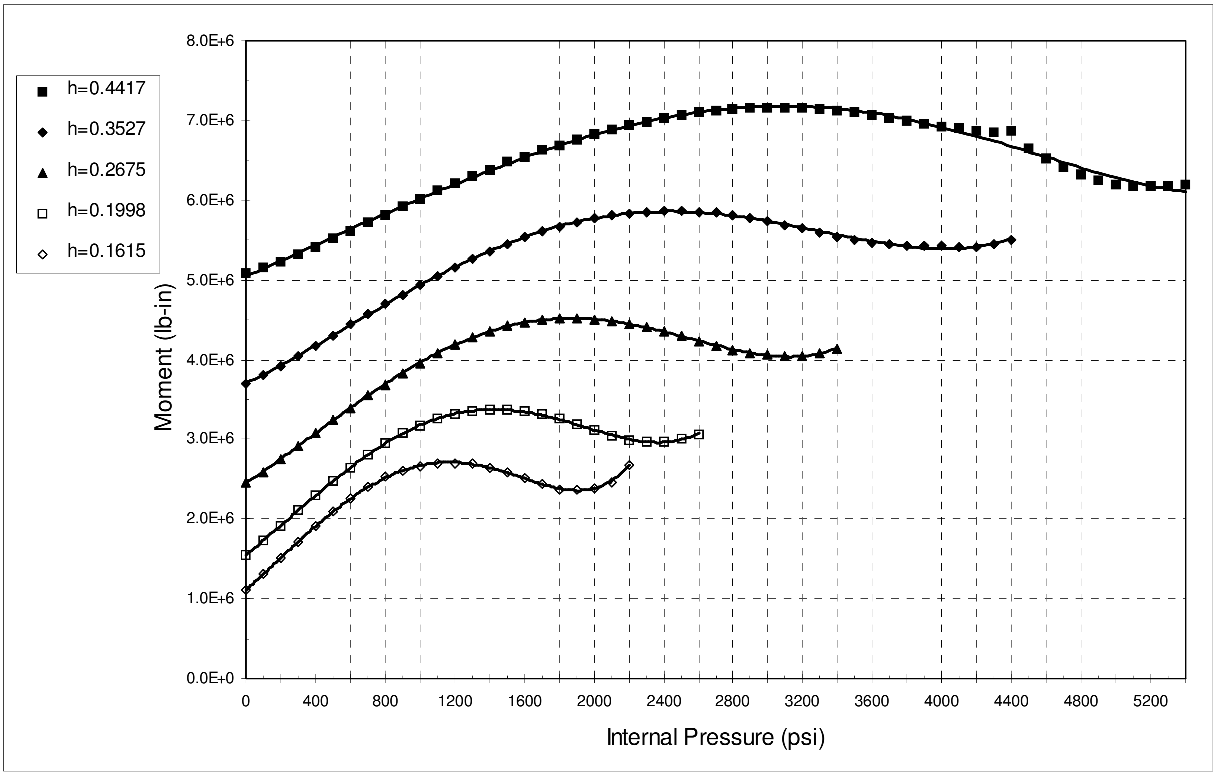

Fig. 3.3.11 Variation of Instability Moment with Internal Pressure

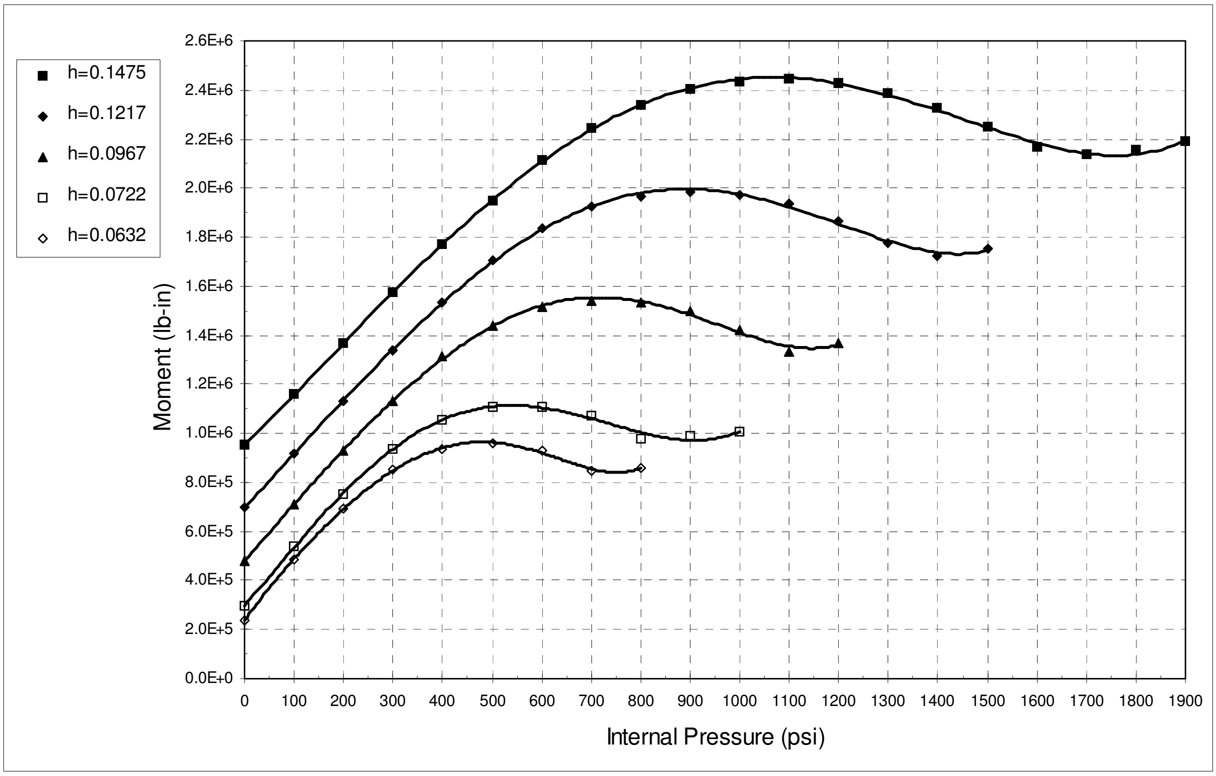

Fig. 3.3.12 Variation of Instability Moment with Internal Pressure

Figure 3.3.13 shows the variation of the collapse moment with internal pressure for five different models (h=0.1615 to h=0.4417), and Fig. 3.3.14 shows this variation for the remaining five models (h=0.0632 to h=0.1475).

From these two figures, it can be seen that the collapse moment starts by increasing with the increase in internal pressure, and after reaching a maximum shortly past the pressure mid-range, starts dropping, without rising again like the instability moment. Collapse moments are also generally higher for models with a higher bend factor, like the case with the instability moment.

Another similarity is that the maximum points of the curves also tend to shift towards the upper-right corner of the graph; but this is clearer for the lower values of (h), shown in Fig. 3.3.14, than it is for the higher values, especially the highest two curves in Fig. 3.3.13.

It is important to note, that the effect of internal pressure is more pronounced with elbows that have a smaller wall thickness - and hence a smaller bend factor - again because of their lower stiffness.

The limit curve of the model with h=0.0632 for instance, in Fig. 3.3.12, shows a 302.3 percent increase in the instability moment, from the case with no internal pressure, to the maximum value of the moment, reached at 500 psi. The limit curve of the model with h=0.4417, shown in Fig. 3.3.11, shows a corresponding increase of only 40.9 percent in the value of the moment.

Similarly, Fig. 3.3.14 shows an increase of 227.2 percent in the collapse moment, for the model with h=0.0967, from the case with no internal pressure, to the maximum value of the moment, attained at 700 psi. The corresponding increase for h=0.4417 is only 4.9 percent; however the same curve shows a decrease of 35.8 percent, from the case without internal pressure, to the minimum value of the moment reached at the end of the pressure range (5400 psi).

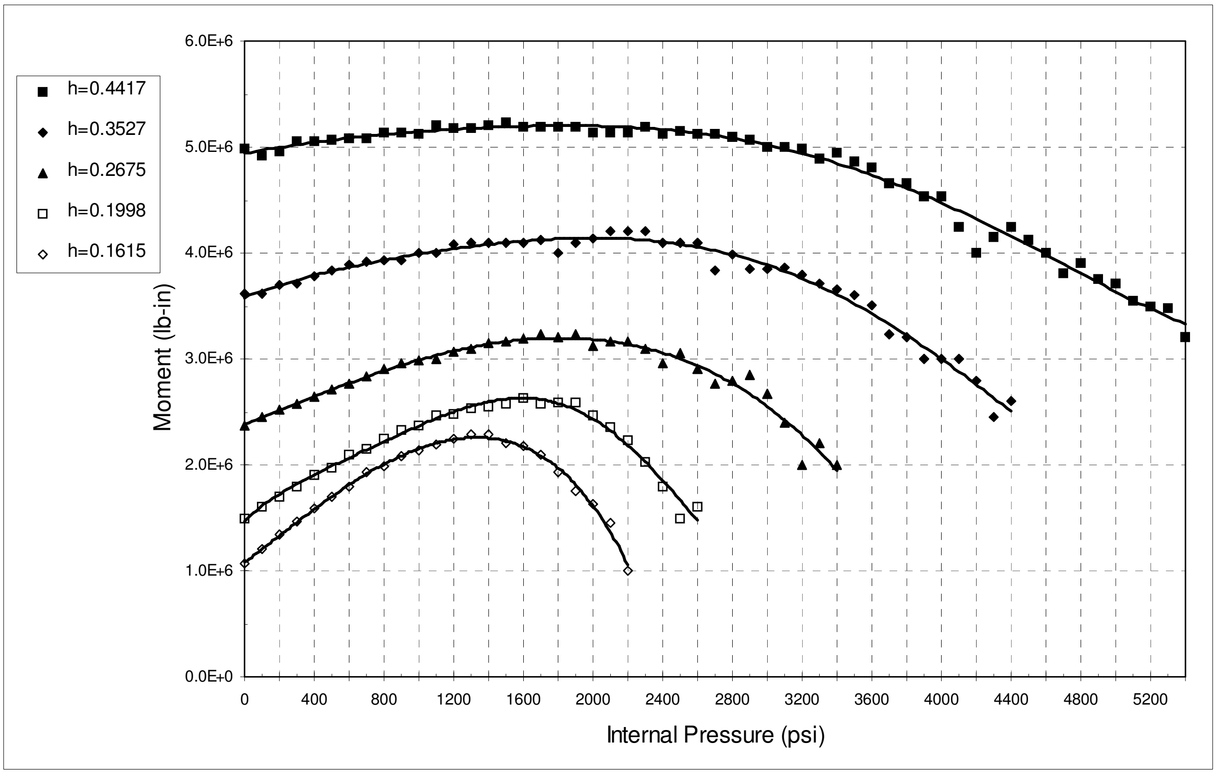

Fig. 3.3.13 Variation of Collapse Moment With Internal Pressure

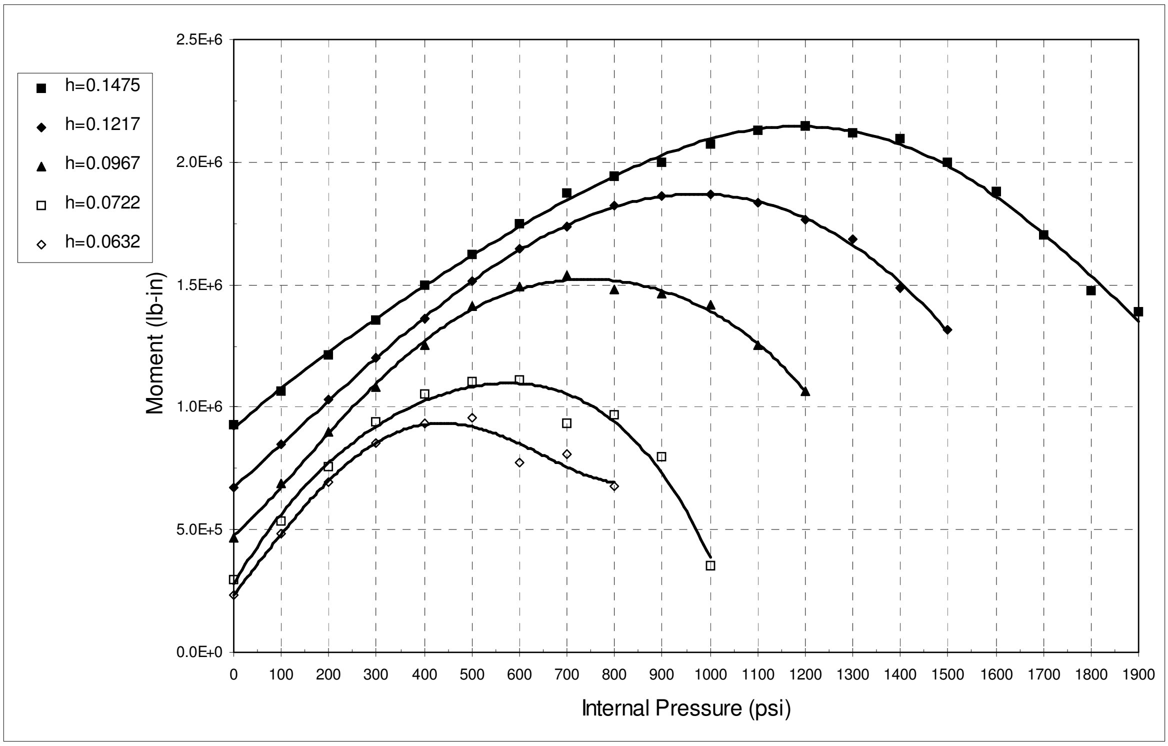

Fig. 3.3.14 Variation of Collapse Moment With Internal Pressure

Finally, it is noted that the data points of the collapse moment curves are more scattered above and below the curve, at higher values of the pressure and of the bend factor (h). This is due to the fact that the graphical twice-elastic-slope method, used to determine the collapse moment, depends strongly on the linear part of the load-deflection curve, which in these cases, deviates from linearity comparatively early. In these cases also, the moments and deflections in question are much larger, and hence small approximation errors are scaled up significantly.

3.3.2 Comparison with In-Plane Bending Results

Figures 3.3.15 and 3.3.16 show the variation of the instability moment with internal pressure in the case where the elbow is loaded in its own plane in the closing direction. When these two figures are compared to the same variation in the case of out-of-plane moment loading, shown in Figs. 3.3.11 and 3.3.12, it is clear that the differences between the values of the instability moment in both cases are very minor, although for most values of h, the instability moment is slightly larger in the case of out-of-plane loading. It is also noted that in both cases, the instability moment increases with pressure at first and then starts to decrease, beyond a certain value of pressure.

The variation of the instability moment with internal pressure in the case of in-plane bending, in the opening direction, is shown in Figs. 3.3.17 and 3.3.18. It is clear from these two figures that the instability moment, in the in-plane opening case, first decreases when the pressure is increased, and then increases again. In other words, the effect of pressure is reversed in this case. The values of the instability moment, in this case, are also much larger than in the other two cases, especially at high values of internal pressure.

Figures 3.3.19 and 3.3.20 show the variation of the collapse moment with internal pressure in the case where the elbow is loaded in its own plane in the closing direction. Again, some similarity is clear between the trend followed by these curves, and the one followed by the curves that belong to the case of out-of-plane moment loading, shown in Figs. 3.3.13 and 3.3.14.

The variation of the collapse moment with internal pressure, in the case of in-plane bending in the opening direction, shown in Figs. 3.3.21 and 3.3.22, also shows a similar trend, unexpectedly. The values of the collapse moment, in this latter case, are however larger than those of the other two cases at low values of internal pressure. At high pressure, all three cases give close values of the collapse moment.

It must be noted however, that the collapse moment was determined by Shalaby (1996) using the angle method, which is similar in essence to the twice-elastic-slope method used in this work. Some minor differences do exist however, between the two methods. Therefore, the instability moment should be considered the main basis of comparison between the results of in-plane and out-of-plane loading cases.

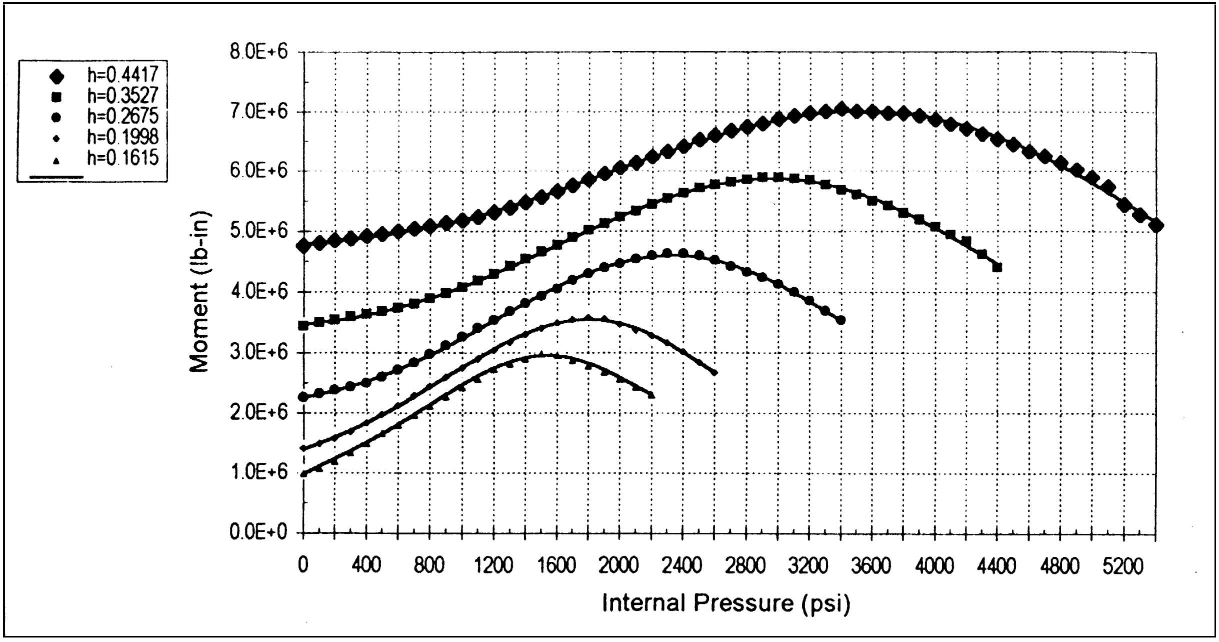

Fig. 3.3.15 Variation of Instability Moment With Internal Pressure, In-Plane Bending in the Closing Direction (Shalaby, 1996)

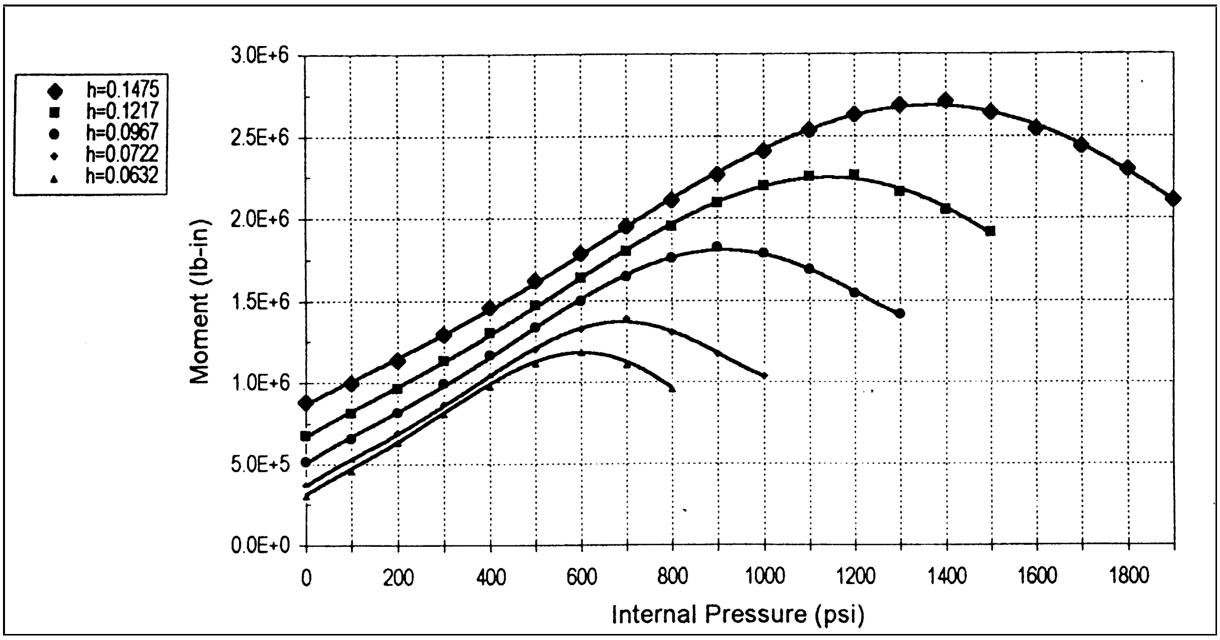

Fig. 3.3.16 Variation of Instability Moment With Internal Pressure, In-Plane Bending in the Closing Direction (Shalaby, 1996)

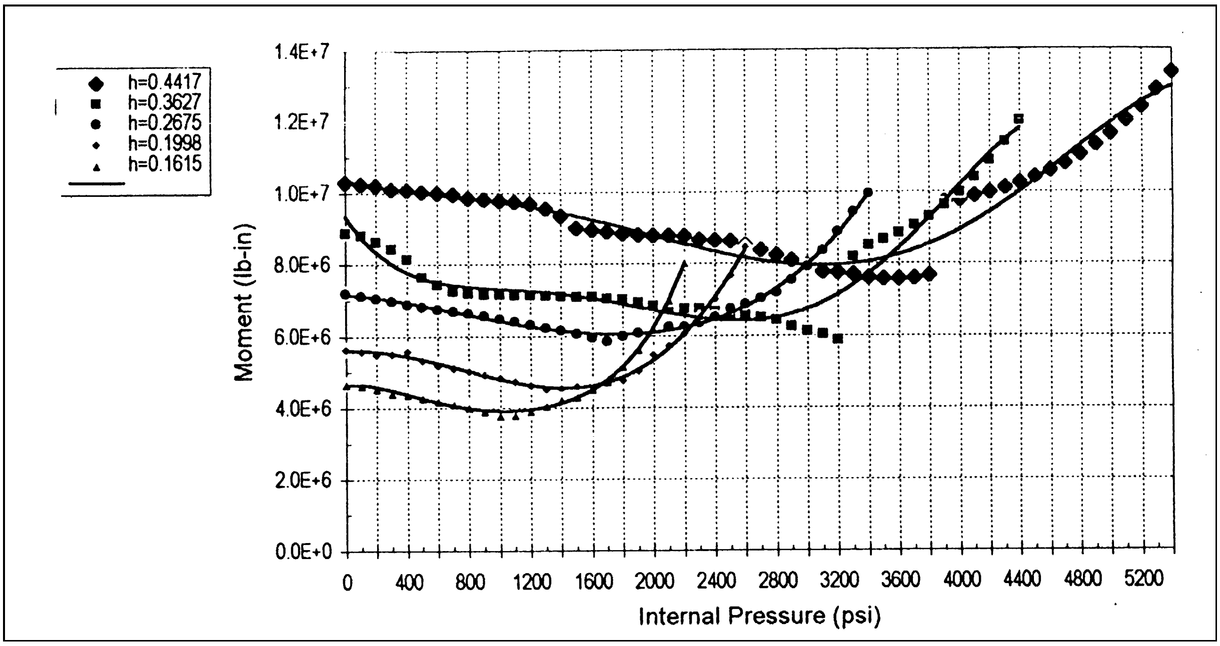

Fig. 3.3.17 Variation of Instability Moment With Internal Pressure, In-Plane Bending in the Opening Direction (Shalaby, 1996)

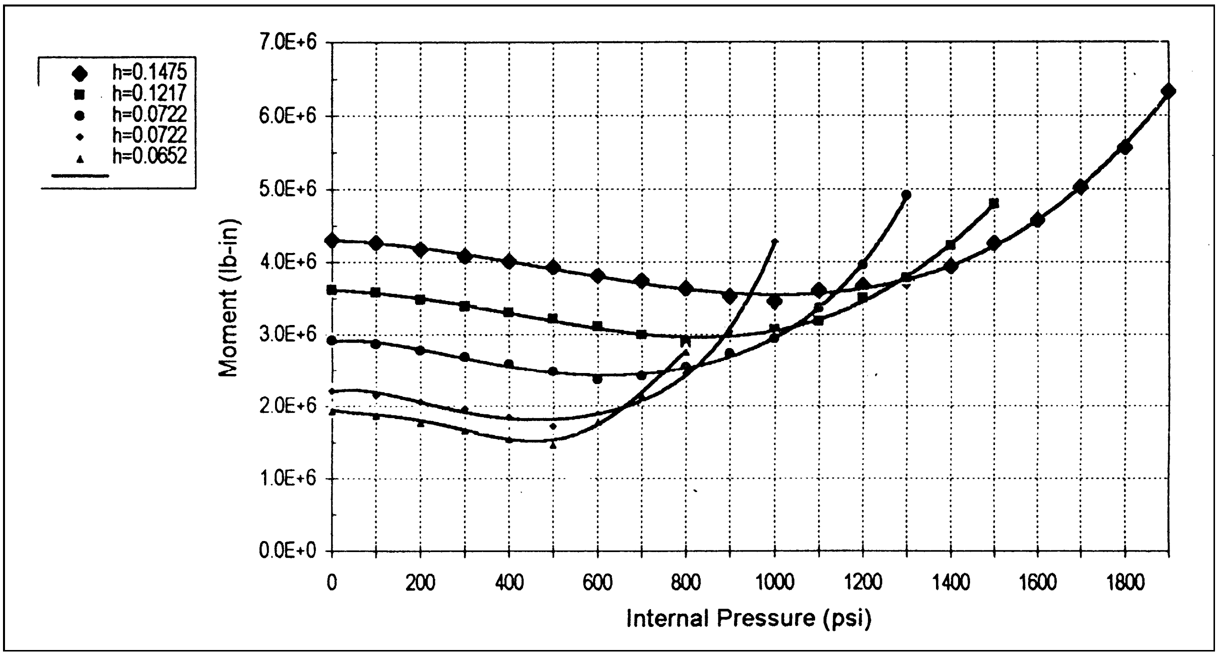

Fig. 3.3.18 Variation of Instability Moment With Internal Pressure, In-Plane Bending in the Opening Direction (Shalaby, 1996)

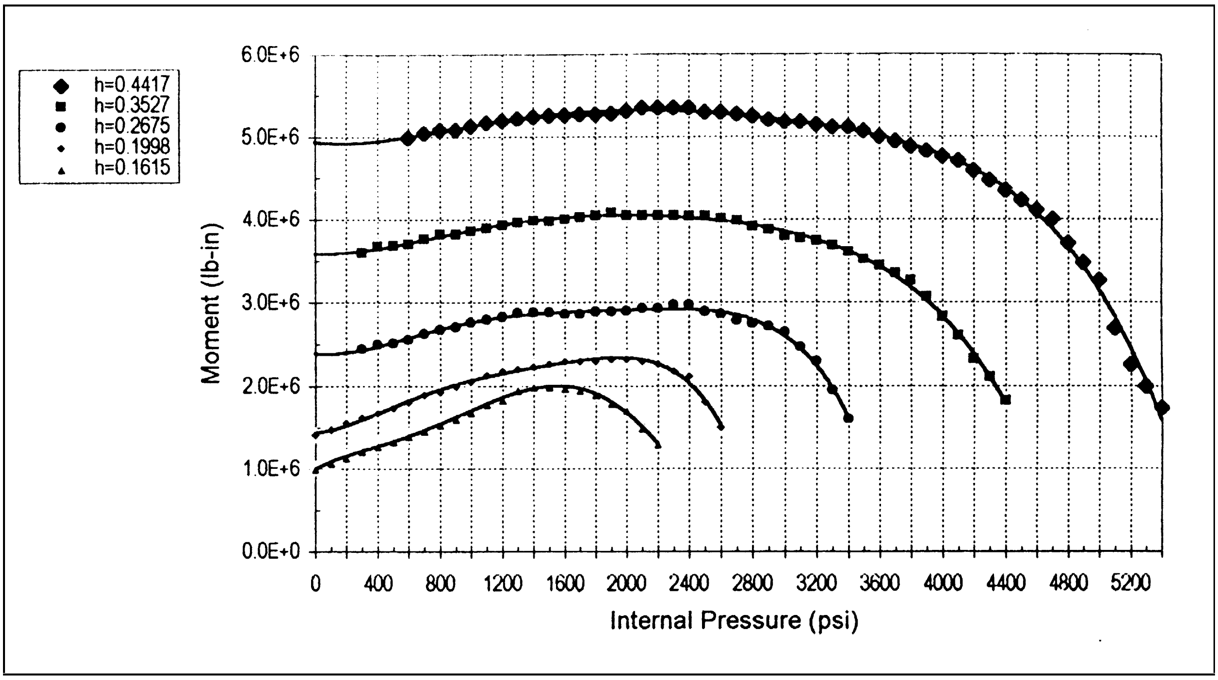

Fig. 3.3.19 Variation of Collapse Moment With Internal Pressure, In-Plane Bending in the Closing Direction (Shalaby, 1996)

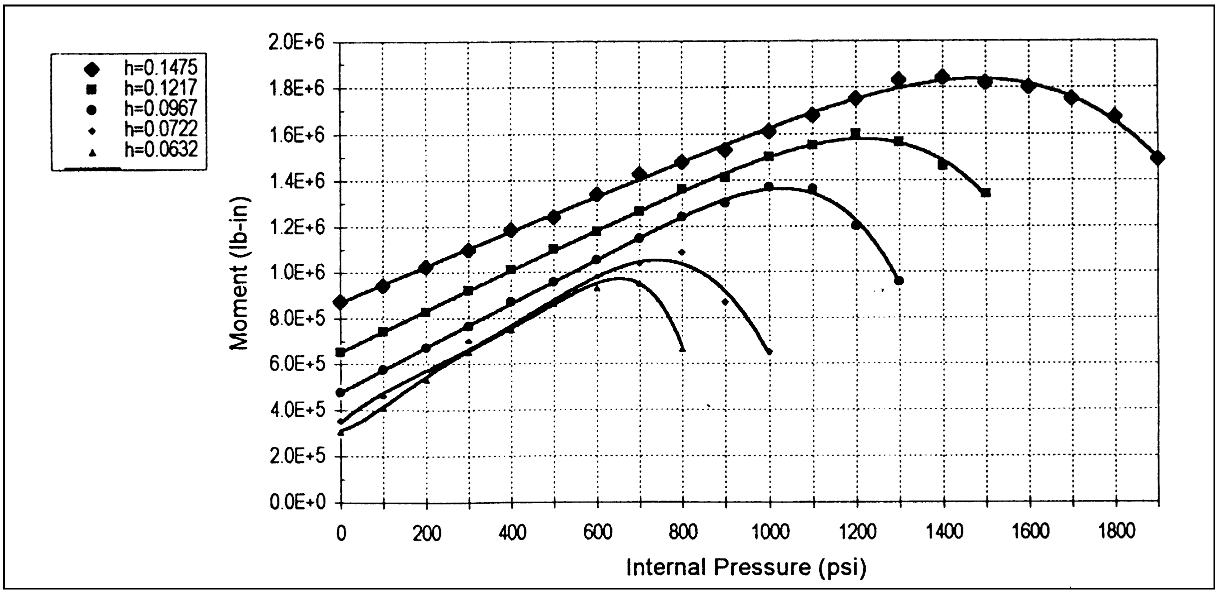

Fig. 3.3.20 Variation of Collapse Moment With Internal Pressure, In-Plane Bending in the Closing Direction (Shalaby, 1996)

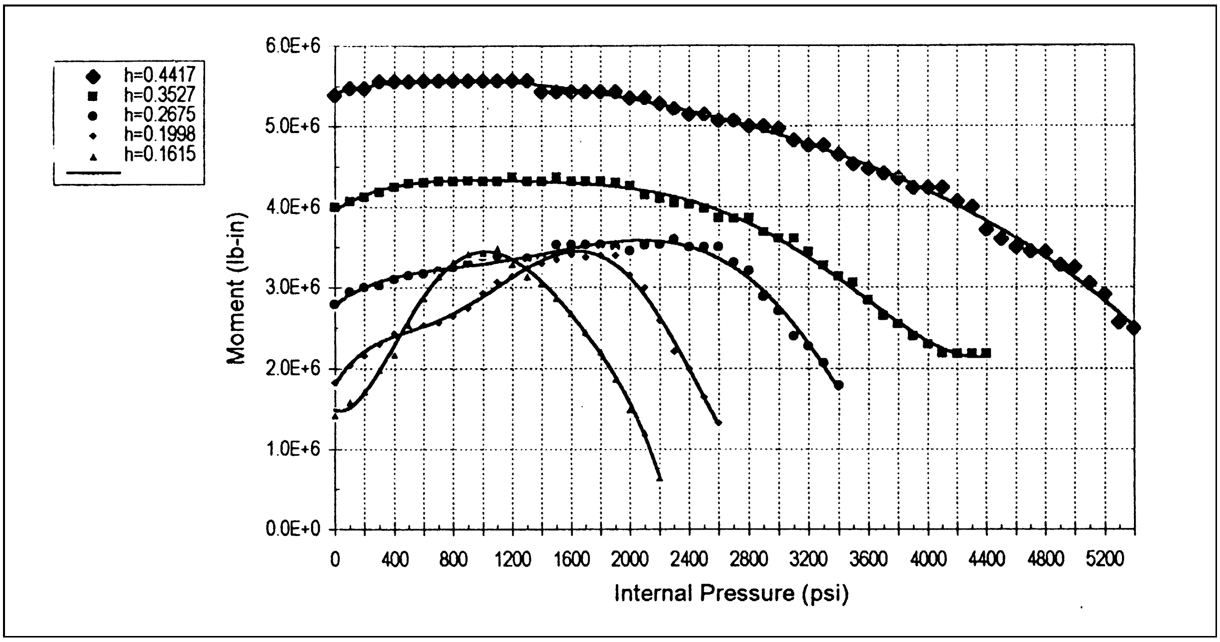

Fig. 3.3.21 Variation of Collapse Moment With Internal Pressure, In-Plane Bending in the Opening Direction (Shalaby, 1996)

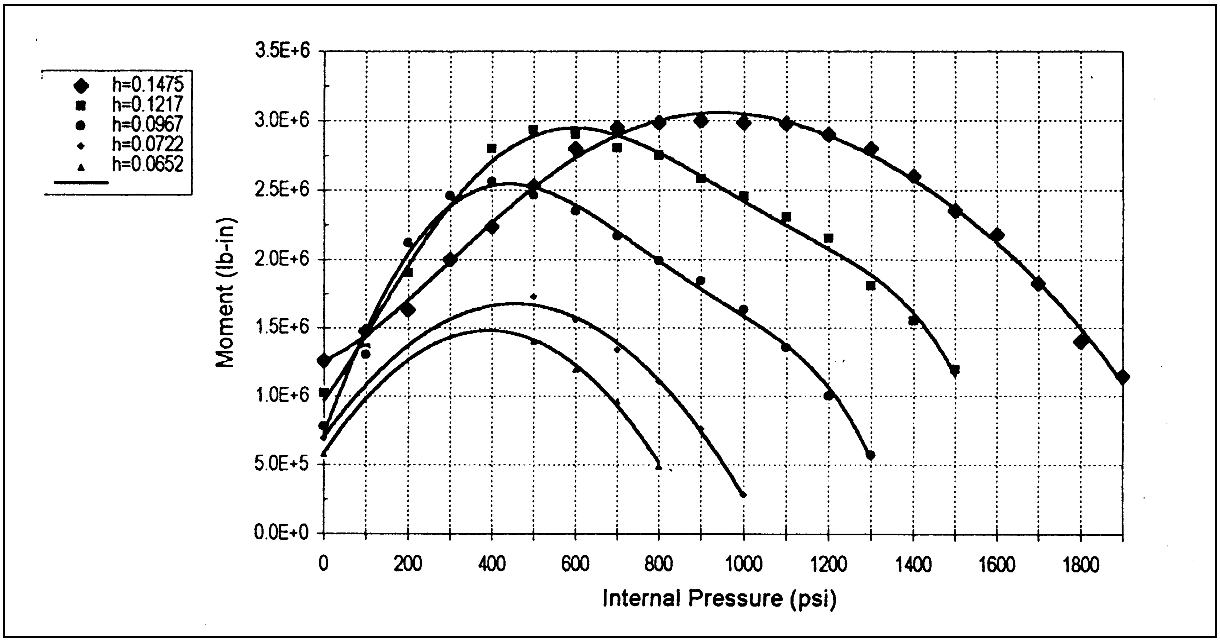

Fig. 3.3.22 Variation of Collapse Moment With Internal Pressure, In-Plane Bending in the Opening Direction (Shalaby, 1996)

3.3.3 Variation of Limit Moments with Pipe Bend Factor (h)

Figure 3.3.23 shows the variation of the limit moments, both collapse and instability, with the pipe bend factor, in the case without internal pressure. This variation is shown in Fig. 3.3.24, for the case where an internal pressure of 500 psi is applied.

From Fig. 3.3.23, it is noted that the value of the collapse moment is almost identical to that of the instability moment, and Fig. 3.3.24 shows that the collapse moment remains close to the instability moment, especially at lower values of the bend factor, even at 500 psi. Note that 500 psi (approximately 34.5 atmospheres) can be considered a large value of pressure in most practical applications. Thus, these two figures can be said to encompass a large portion of the design range of internal pressure.

It is also clear from both figures, that the limit moments increase with the increasing bend factor; and the collapse moment being smaller than the instability moment, is hence a more conservative design limit, for all values of the bend factor, and for both values of internal pressure.

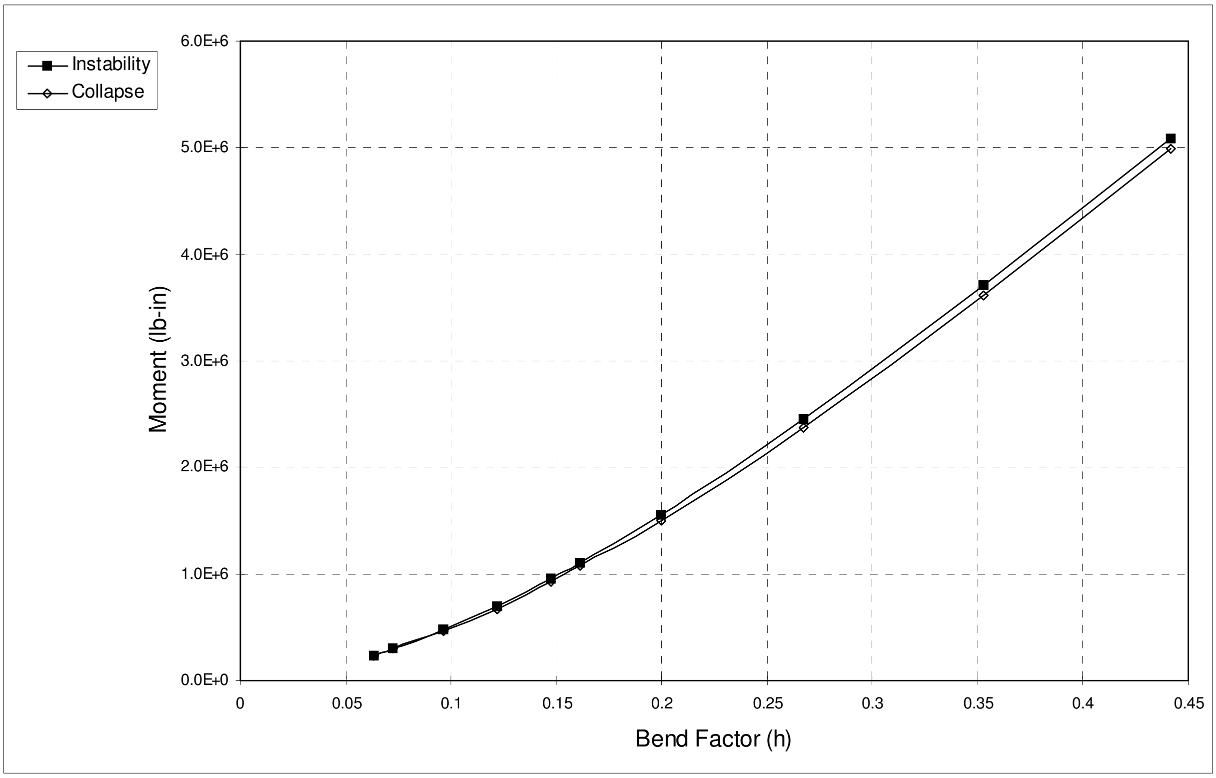

Fig. 3.3.23 Variation of Instability and Collapse Moments With Bend Factor - No Internal Pressure

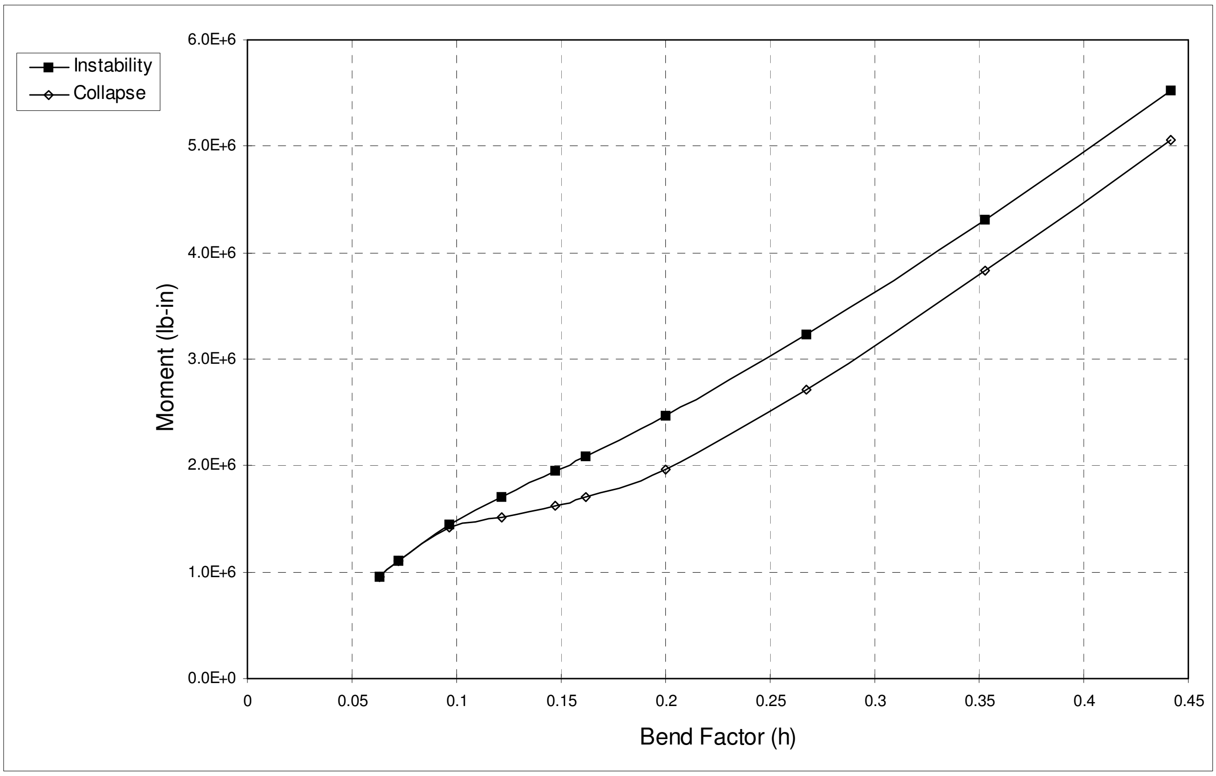

Fig. 3.3.24 Variation of Instability and Collapse Moments With Bend Factor - Internal Pressure: 500 psi

3.4 Effect of Large Deformation and Strain Hardening

The behavior of a pipe elbow under moment loading is greatly affected by the type and amount of deformation that its cross-section undergoes. The ovalization and warping of the cross-section, induce a change in the overall stiffness of the elbow, thus introducing a geometric nonlinearity in the analysis. This effect can accelerate or delay the failure of the elbow, and hence has to be accounted for, especially when the relative displacement between the elbow's extremities is large, which is usually the case, due to the inherent flexibility of pipe elbows.

Due to these large relative displacements also, large parts of the structure usually undergo extensive plastic deformation, before instability is reached. Therefore, strain hardening effects increase the value of the limit load considerably, and if neglected, the analysis will yield more conservative results.

All the analyses discussed so far throughout this study, take geometric nonlinearity into consideration, but assume an elastic-perfectly-plastic material. In this section, the results of these analyses are first compared to those of a small-displacement analysis, using the same material model. A comparison is then made with the results of a large-displacement analysis that adopts a strain-hardening material model. In addition, the combined effects are investigated through a small-displacement analysis assuming a strain-hardening material.

At the end of this section, the instability moments computed in these different analyses are compared to some analytical limit load estimates.

3.4.1 Small-Displacement Analysis

The load-deflection behavior of an elbow with h=0.1615, assuming small displacements, is depicted by the moment-end rotation curve in Fig. 3.4.1, and is compared to the behavior predicted by a geometrically nonlinear analysis. In both cases, no internal pressure was applied and an elastic-perfectly-plastic material model was used.

It is clear from this figure that both curves show the same response at first, until a value of end-rotation is reached beyond which the small-displacement assumption is no longer valid. Instead of the local maximum reached in the large-displacement analysis, and which represents the geometric instability (buckling) moment, the curve becomes almost horizontal as it approaches a certain value of the moment asymptotically.

This horizontal part of the curve indicates that a virtually infinite value of end-rotation can be reached, without significantly incrementing the value of the moment applied. Obviously, this only signifies instability of the elbow. The analysis was therefore stopped at an end-rotation of 0.45 radians, and only the more significant first part of the curve is shown in Fig. 3.4.1.

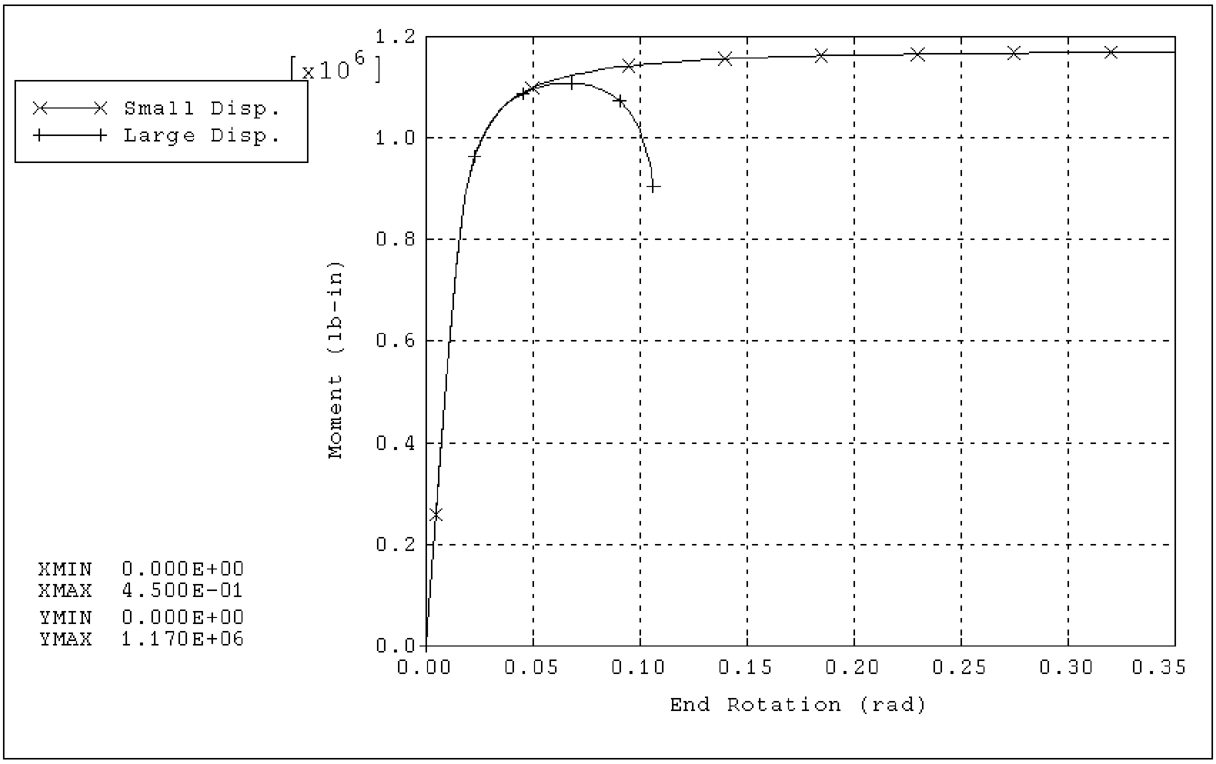

Fig. 3.4.1 Variation of Moment With End-Rotation for an Elbow With h=0.1615, Small- and Large-Displacement Analyses, Elastic-Perfectly-Plastic Material Model - No Internal Pressure

It is noted that the computed instability moment is only slightly higher than the buckling load predicted by the large-displacement analysis. However, this difference is definitely larger in models with higher bend factors, since they reach larger values of end-rotation before instability, and hence the small-displacement assumption becomes less valid. In these cases, limit moment estimates become less conservative, as the value of the bend factor increases.

The stiffening effect of internal pressure is also overlooked by the small-displacement analysis, since cross-sectional deformation is not accounted for. Furthermore, Fig. 3.4.2 shows that the limit moments keep decreasing, ever more rapidly, as the value of internal pressure increases, along with the additional stresses it engenders.

It should be noted that the maximum internal pressure applied here is 2000 psi, compared to 2200 psi in the large-displacement analysis. The reason for that is that, in the small-displacement analysis, the elbow collapsed, under the sole influence of the internal pressure, before reaching 2200 psi.

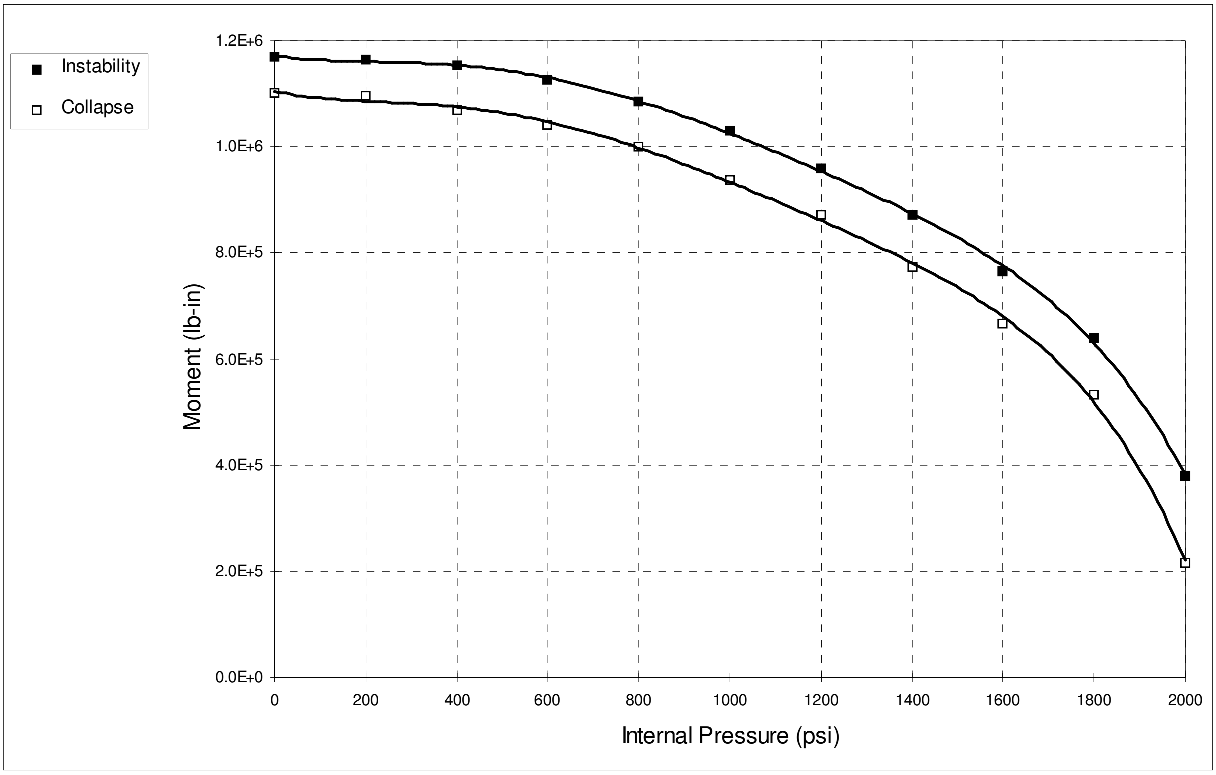

Fig. 3.4.2 Variation of Limit Moments With Internal Pressure for an Elbow With h=0.1615, Small-Displacement Analysis, Elastic-Perfectly-Plastic Material Model

3.4.2 Strain-Hardening Material Model

Figure 3.4.3 shows how strain hardening characteristics of the material model can affect the load-deflection behavior of a pipe elbow, in a large-displacement analysis. As expected, both models show the same behavior at the beginning of loading history, and start to differ more significantly as a larger part of each model undergoes plastic deformation. The stress-strain curves of both material models used are shown in Fig. 2.1.2.

It is clear that due to this material stiffening effect, the instability moment, in this case, is notably higher than the case with an elastic-perfectly-plastic material. It is also noted that the value of end-rotation at instability is clearly higher in this case. It must be noted however, that the elastic-perfectly-plastic material model was assigned a conservative yield stress value. Therefore, the discrepancy between its results and those of the strain-hardening material model might be partially due to the difference in yield stress values, and hence is not attributed to the phenomenon of material strain hardening alone.

The load-deflection curves of the same elbow, under different values of internal pressure, are shown in Figs. 3.4.4 and 3.4.5. Since this is a large-displacement analysis, the group of curves shown in Fig. 3.4.4 exhibit a clear increase, between consecutive curves, in the value of the end-rotation at instability, as well as in the limit moment. This indicates the presence of a stiffening effect due to internal pressure, in the first half of the applicable pressure range.

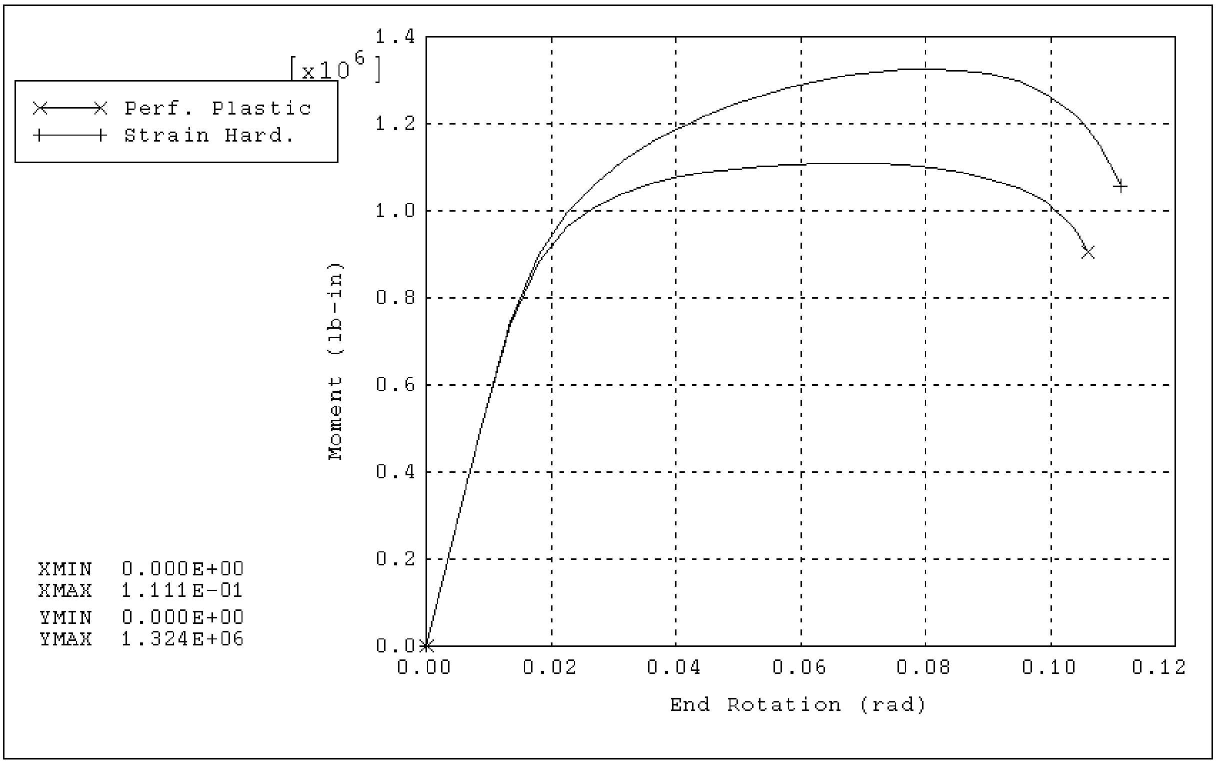

Fig. 3.4.3 Variation of Moment With End-Rotation for an Elbow With h=0.1615, Large-Displacement Analysis, Elastic-Perfectly-Plastic and Strain-Hardening Material Models - No Internal Pressure

Figure 3.4.5 shows the second half of the pressure range. Here, unlike in the case of the elastic-perfectly-plastic material shown earlier in this chapter for the same model (h=0.1615), the effect of internal pressure on the end-rotation at instability is not reversed twice before reaching the end of the pressure range.

In this case, the variation of the limit moments with internal pressure is different, as shown in Fig. 3.4.6. In the presence of strain hardening, the negative effect of internal pressure, in the second half of the pressure range, on the limit moments, is less pronounced than in the case of the ideal material. Therefore, the instability and collapse moments shown in Fig. 3.4.6 keep increasing at first, until they reach their respective maximum values, where they stay almost constant for a few pressure increments, as they approach the end of the pressure range.

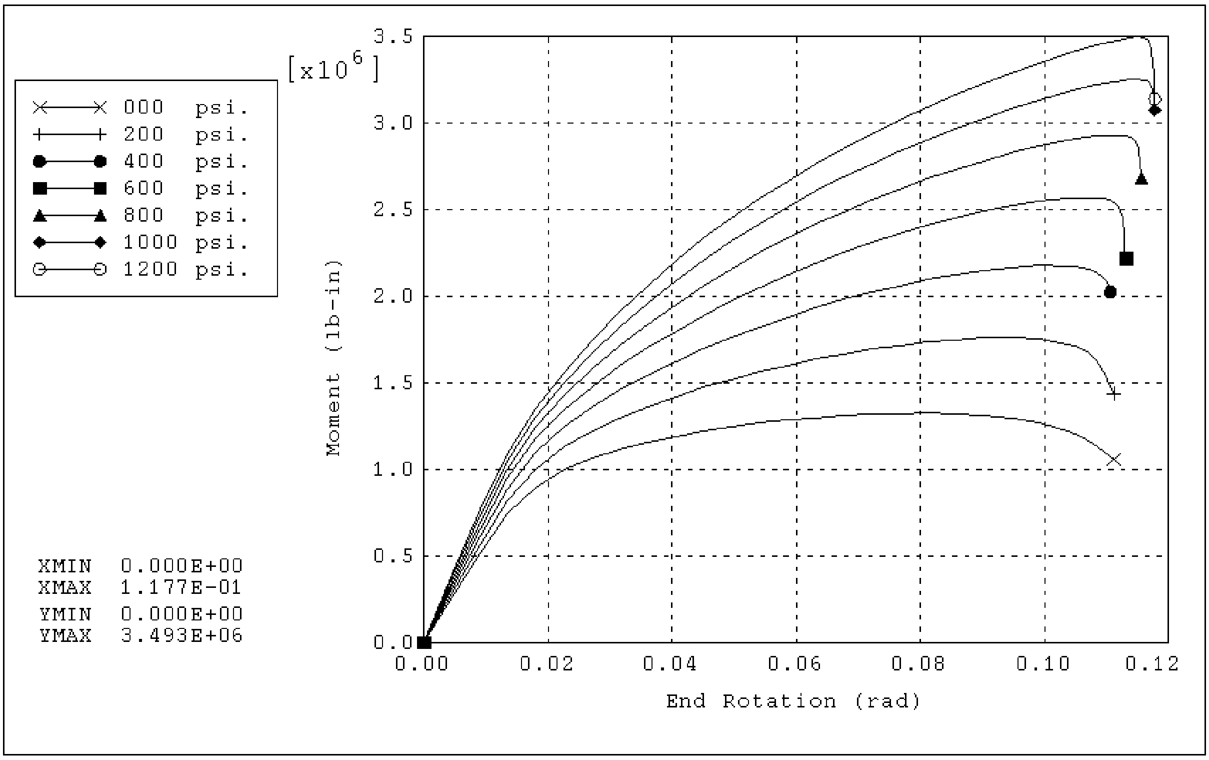

Fig. 3.4.4 Variation of Moment with End-Rotation for an Elbow With h=0.1615, Large-Displacement Analysis, Strain-Hardening Material Model - Internal Pressure Range: 0 ~ 1200 psi

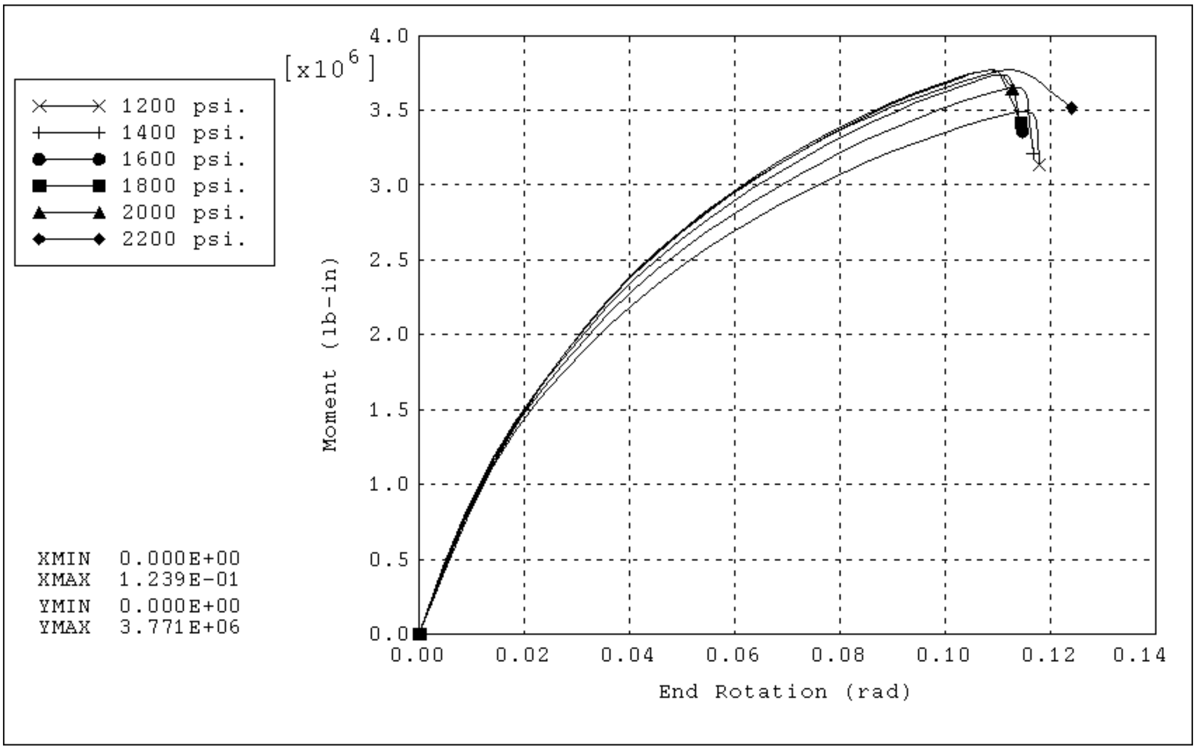

Fig. 3.4.5 Variation of Moment with End Rotation for an Elbow With h=0.1615, Large-Displacement Analysis, Strain-Hardening Material Model - Internal Pressure Range: 1200 ~ 2200 psi

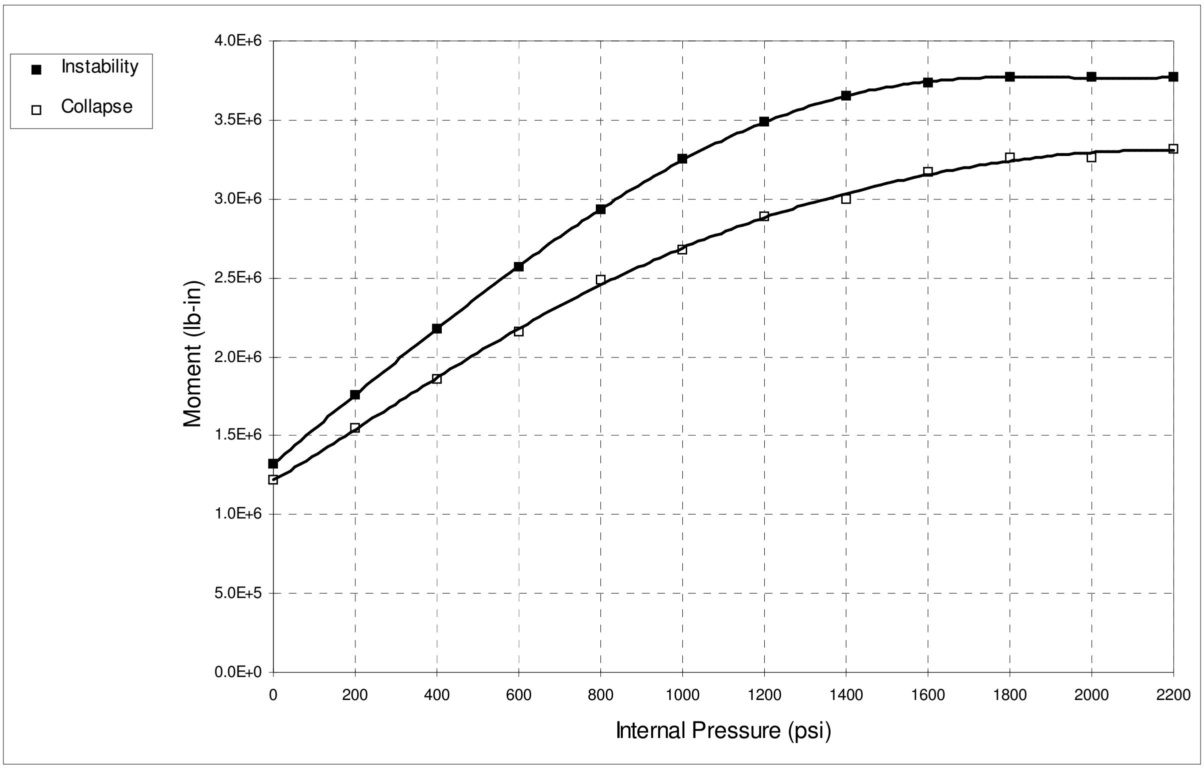

Fig. 3.4.6 Variation of Limit Moments With Internal Pressure for an Elbow With h=0.1615, Large-Displacement Analysis, Strain-Hardening Material Model

3.4.3 Small-Displacement Analysis with Strain Hardening

Figure 3.4.7 shows the load-deflection curves belonging to the model with h=0.1615, generated from the results of two small-displacement analyses, which differ in the material model used only.

Again, it is noted that the curve that corresponds to the strain-hardening material model starts exhibiting a fundamental difference in behavior at a certain point, where inelastic behavior starts to dominate the response. Beyond this point, the curve maintains a constant increasing slope, instead of a constant value of the moment, as in the case of the ideal material model.

The curve virtually extends to infinity, maintaining the same slope, although the analysis was terminated at an end-rotation value of 4 radians, which is completely unrealistic of course, and where the small-displacement assumption is strongly violated. For the purpose of comparison, only the first part of the curve is shown on Fig. 3.4.7.

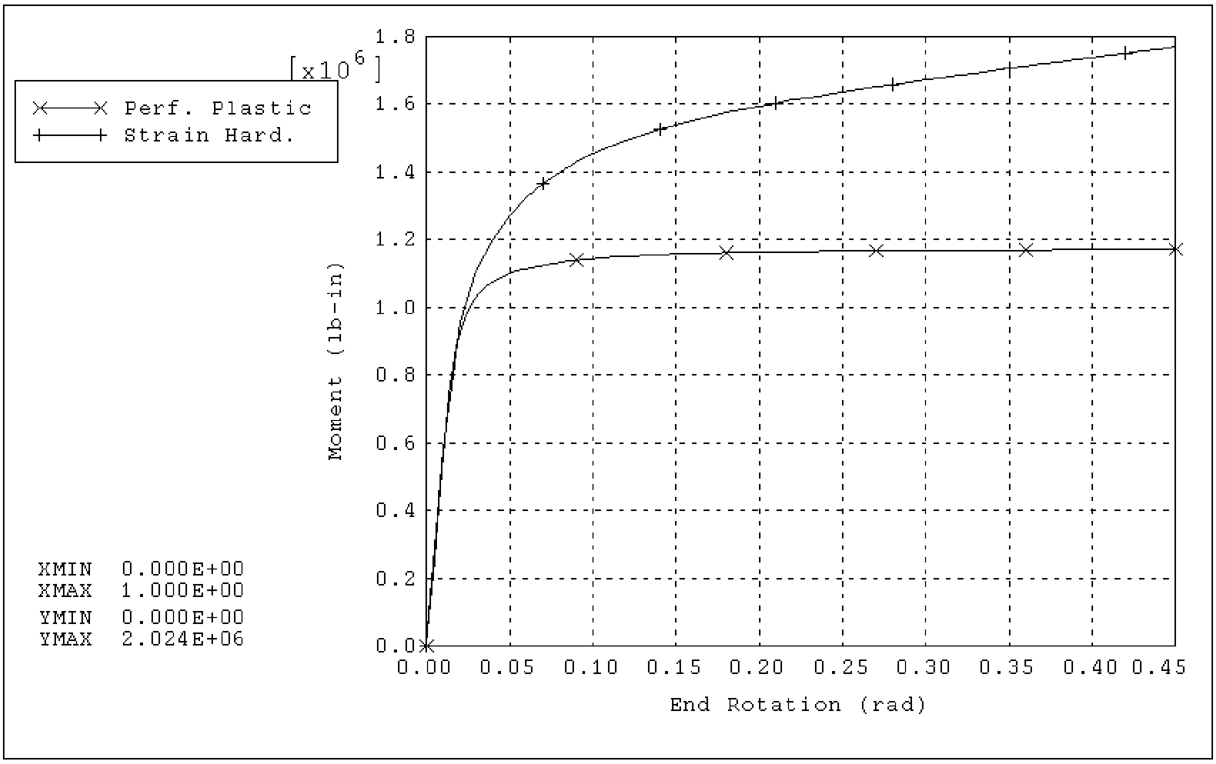

Fig. 3.4.7 Variation of Moment With End-Rotation for an Elbow With h=0.1615, Small-Displacement Analysis, Elastic-Perfectly-Plastic and Strain-Hardening Material Models - No Internal Pressure

Another similar comparison is made, in Fig. 3.4.8, between the load-deflection behavior predicted by this analysis, and the one predicted by a large-displacement analysis that adopts the same strain-hardening material model.

It can be seen from this figure that, due to the constant positive slope of the curve corresponding to the small-displacement analysis, a definite value of the instability moment cannot be obtained. Because geometric nonlinearity is ignored, and in the presence of strain hardening, the model keeps its stiffness as the load is increased, and hence displays more resistance to moment loading than in the large-displacement analysis. This also explains the constant positive slope of the curve.

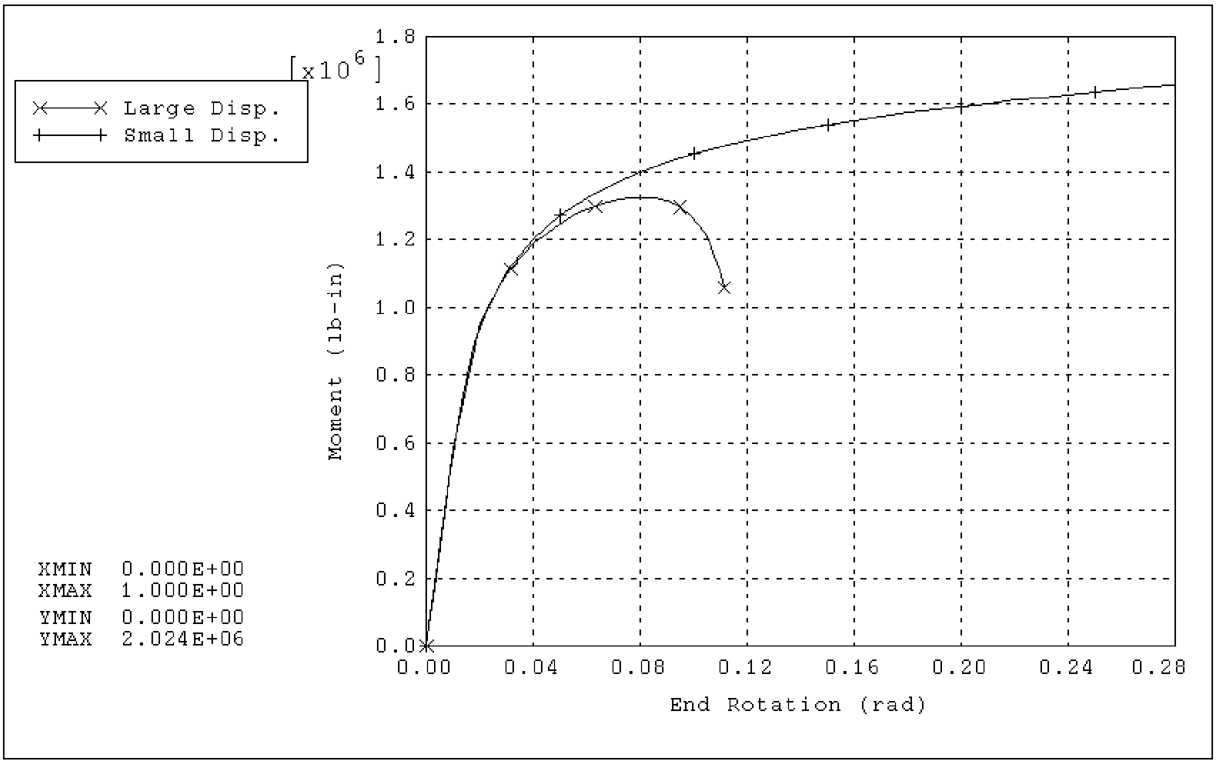

Fig. 3.4.8 Variation of Moment With End-Rotation for an Elbow With h=0.1615, Small- and Large-Displacement Analyses, Strain-Hardening Material Model - No Internal Pressure

As mentioned above, the small-displacement analysis with strain hardening effects does not yield a determined value of the instability moment, since it does not reach a maximum point, and extends to infinity with a positive slope. Therefore, the variation of the collapse moment only, with pressure, was plotted in Fig. 3.4.9.

From this figure, it is clear that no pressure stiffening effects were predicted. Pressure only had a weakening effect, due to the additional stresses it creates. Therefore the curve starts to decline slowly at first, but the rate of decay increases towards the end of the pressure range. However, this rate is much slower than the case where the material is considered ideal.

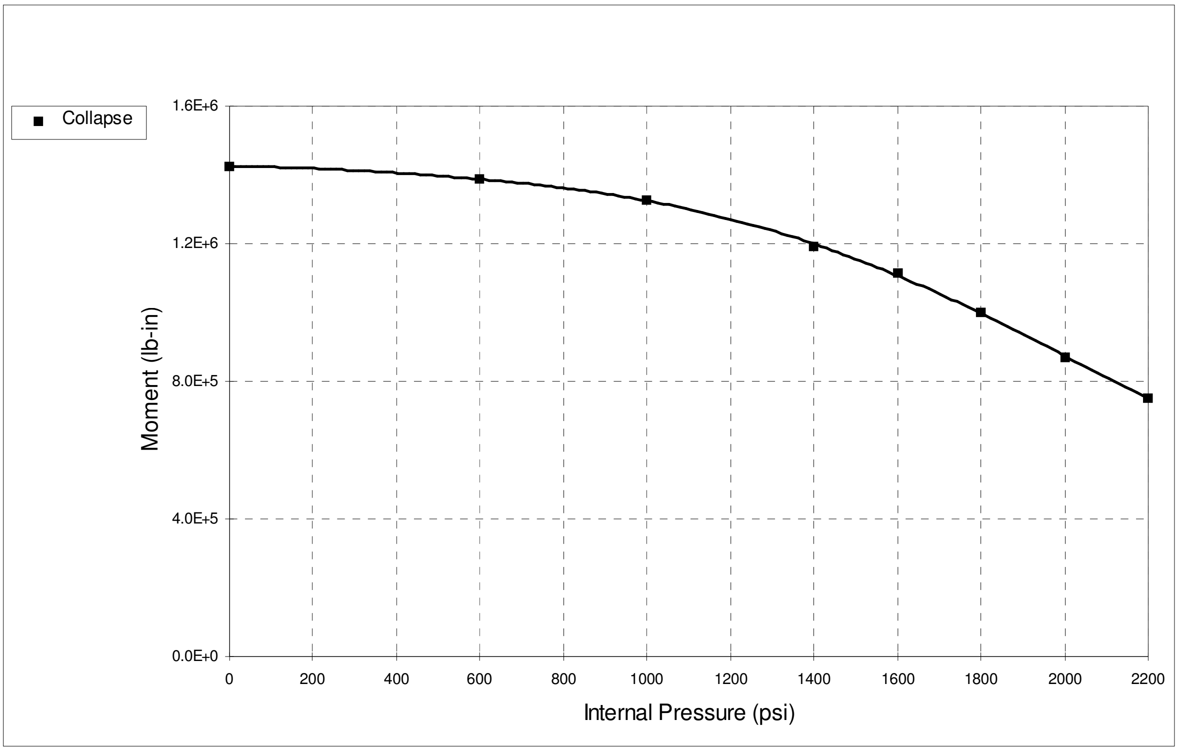

Fig. 3.4.9 Variation of Limit (Collapse) Moment with Internal Pressure for an Elbow with h=0.1615, Small-Displacement Analysis, Strain-Hardening Material Model

3.4.3 Comparison with Analytical Limit Loads

As mentioned in the previous chapter, several approximate formulas for the limit moment are available in the literature. In this section, a comparison is provided between these analytical estimates, the results obtained from the large-displacement finite element analyses, with both ideal and strain-hardening material models, and the small-displacement finite element analysis with ideal material. The small-displacement finite element solution with strain-hardening material is not included in the comparison, since it does not provide a definite estimate of the instability moment, as discussed before.

Figure 3.4.10 shows the variation of the limit moment, as obtained from the different analyses and formulas, with the bend factor (h). It is clear that all the curves, corresponding to the different approaches, essentially show similar trends of variation, increasing more or less rapidly with the increase in the value of the bend factor.

From this figure, it can be seen that the most conservative estimate of the limit moment, is the one obtained using equation 9 of the ASME Boiler and Pressure Vessel Code, Section III, Division I, Nuclear Power Plant Components. The approximate equation given by Rodabaugh (1979), gives a somewhat higher estimate for all values of the bend factor (h).

It is noted that the large-displacement finite element analysis, which assumes an elastic-perfectly-plastic material, yields results that agree almost completely with the equation given by Spence and Findlay (1973). It is interesting to note that Spence and Findlay assumed small displacements, and an elastic-perfectly-plastic material model in their analysis; and although their equation was intended initially for computing in-plane limit moments, it was shown by comparison to experimental results, to be reasonably accurate for both in-plane and out-of-plane moments (Rodabaugh, 1979).

Clearly, when ignoring geometric nonlinearity, the finite element method yields slightly less conservative results. Using the strain-hardening material model has an even greater effect, and hence the large-displacement finite element analysis with strain-hardening material yields the least conservative estimates.

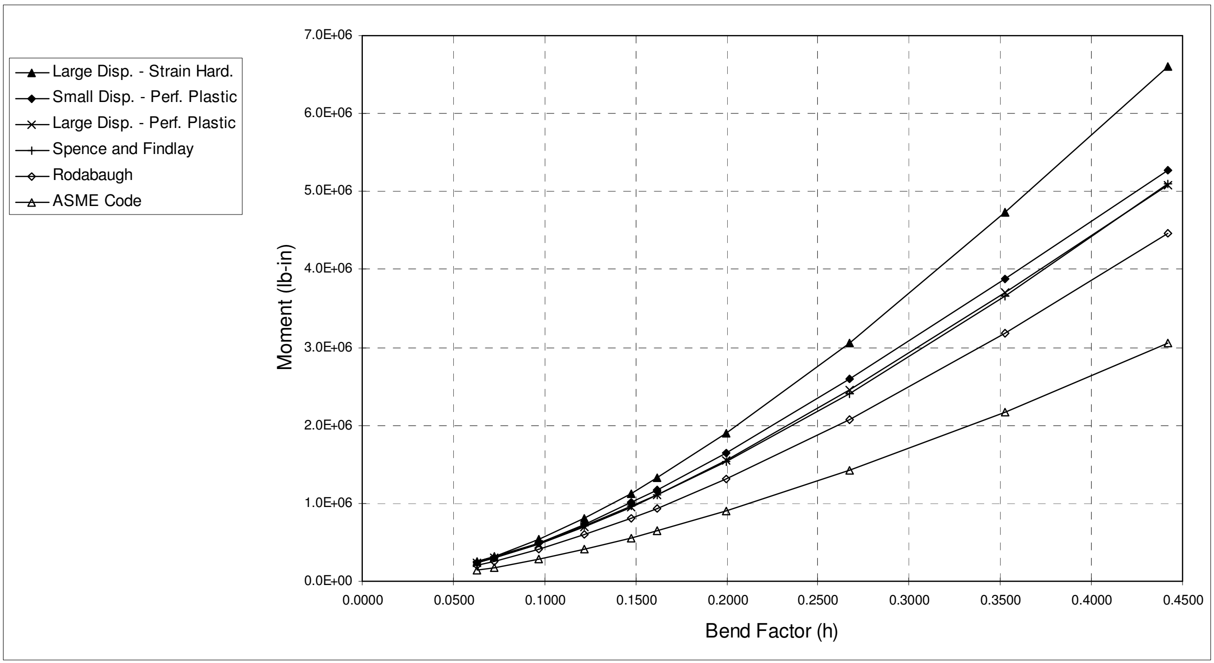

Fig. 3.4.10 Variation of Instability Moment with Bend Factor (h), Large- and Small-Displacement Analyses, Elastic-Perfectly-Plastic and Strain-Hardening Material Models, Compared to Analytical and the ASME Code Estimates - No Internal Pressure

3.5 Cross-Section Analysis

The load-deflection behavior of an elbow is different from that of a straight pipe, mainly because of the greater cross-sectional deformation - ovalization and warping - of the elbow. Therefore, to better understand the behavior of pipe elbows, under out-of-plane bending and internal pressure, it is important to know how the cross-section deforms, and study the distribution of stresses that cause it to deform in a particular manner.

Furthermore, to get a better understanding of how a certain elbow becomes unstable, under particular loading conditions, it is important to study how yielding progresses as the load is increased.

In this section, an elbow with pipe bend factor h=0.1615 is considered, and the results of a detailed analysis thereof are examined. First, the variation, over the elbow's length, of Mises stress and equivalent plastic strain is investigated, to determine the most severely loaded, or critical, cross-section of the elbow.

Next, the progression of yielding, at each of the integration points around this critical cross-section, is examined. The location of the integration points is discussed in the previous chapter, and shown again here, in Fig. 3.5.1 for convenience. Studying of the yield progression is then extended, by treating the pipe bend as a whole, and looking for the loads that causes first yield to occur, and subsequently, plastic hinges to form.

The distribution of some components of stress and strain, as well as Mises stress and equivalent plastic strain, around the critical cross-section, is then examined. And finally, the deformed shape of the elbow is presented, to show the overall deflection, and more importantly the cross-sectional deformation, at instability, and under different values of internal pressure.

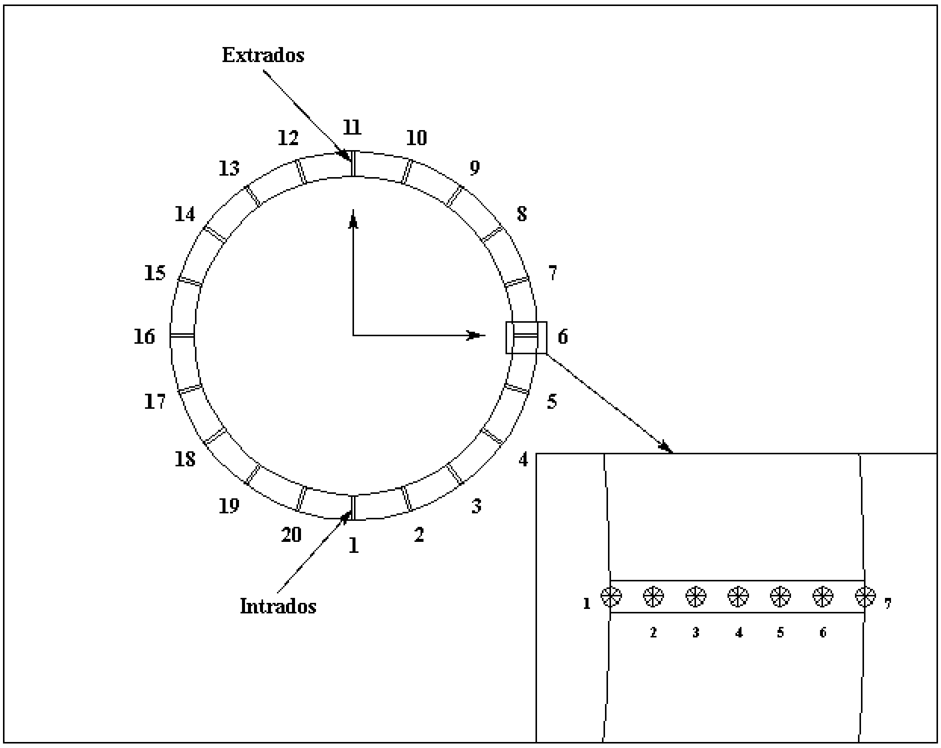

Fig. 3.5.1 The Location of Integration Points around the Section

3.5.1 Axial Distribution of Mises Stress and Equivalent Plastic Strain

The model used, as discussed in the previous chapter, consists of 12 elements. ELBOW32, the element used throughout this study, has two integration stations along its length, and each station has 20 integration points around the circumference, as shown in Fig. 3.5.1.

In other words, the results are available at 24 cross-sections along the length of the model; the first section being the closest to the fixed end of the elbow, and section 24 being closest to the loaded end. It should be noted, however, that due to the numerical integration technique used, these integration stations do not coincide with the extremities of the 90° elbow; they are approximately 1.585° away from the elbow's extremities.

By studying the axial distribution of Mises stress at start of yielding, and equivalent plastic strain at instability, the critical cross-section, the one that is most severely loaded, can be determined, and hence studied in detail. Since an elastic-perfectly-plastic material model is used, the Von Mises stress does not increase beyond the yield strength of the material (σ_y=39440 psi), and hence can be used as a good indicator of points that have started yielding.

At instability, however, the value of Von Mises stress is less meaningful, since many points start yielding long before the model reaches instability. Therefore, at instability, the equivalent plastic strain is used as a measure of the amount of plastification that a point has undergone, and can hence aid in the determination of the critical cross-section.

Two cases are studied here, one where no internal pressure is applied on the elbow, and another with an intermediate value of pressure, namely 1200 psi. It should be noted that a third case, with a high value of pressure, 2200 psi, would not help in determining the critical cross-section; since, in that case, extensive plastic deformation takes place under the effect of the pressure alone, before any moment loading is applied.

3.5.1.1 Case without Internal Pressure

3.5.1.1.a Start of Yielding

Figure 3.5.2 shows the distribution of Mises stress at the inside of the pipe wall, along the length of the elbow, at the load level where the model starts to yield. The value of the moment applied at this level is $M=4.1796\times10^5$ lb-in. and the corresponding end-rotation is $\theta=7.2001\times10^{-3}$ radians (0.41°). Each of the 20 curves on this graph represents a location around the cross-section.

It can be seen from this figure, that the first spots to reach the yield strength, in the entire elbow, are points 8, 9, 13 and 14 of section 24. As can be seen from Fig. 3.5.1, points 8 and 9 are located between the elbow's right crown (point 6) and the extrados (point 11). Points 14 and 13 are their symmetric counterparts, respectively, being between the extrados and the left crown (point 16).

Figure 3.5.3 shows the Mises stress distribution at the outside of the pipe wall; and it can be seen that the same four points, also in section 24, have the highest values of stress; but in this case, the stress at points 8 and 14 is clearly higher than at the other two points.

The results shown in Figs. 3.5.2 and 3.5.3 suggest that in the case where no internal pressure is applied, section 24, which is closest to the loaded end of the elbow, can be considered the critical section; not only because the first points to yield are located on it, but also because most curves reach their maximum at this cross-section.

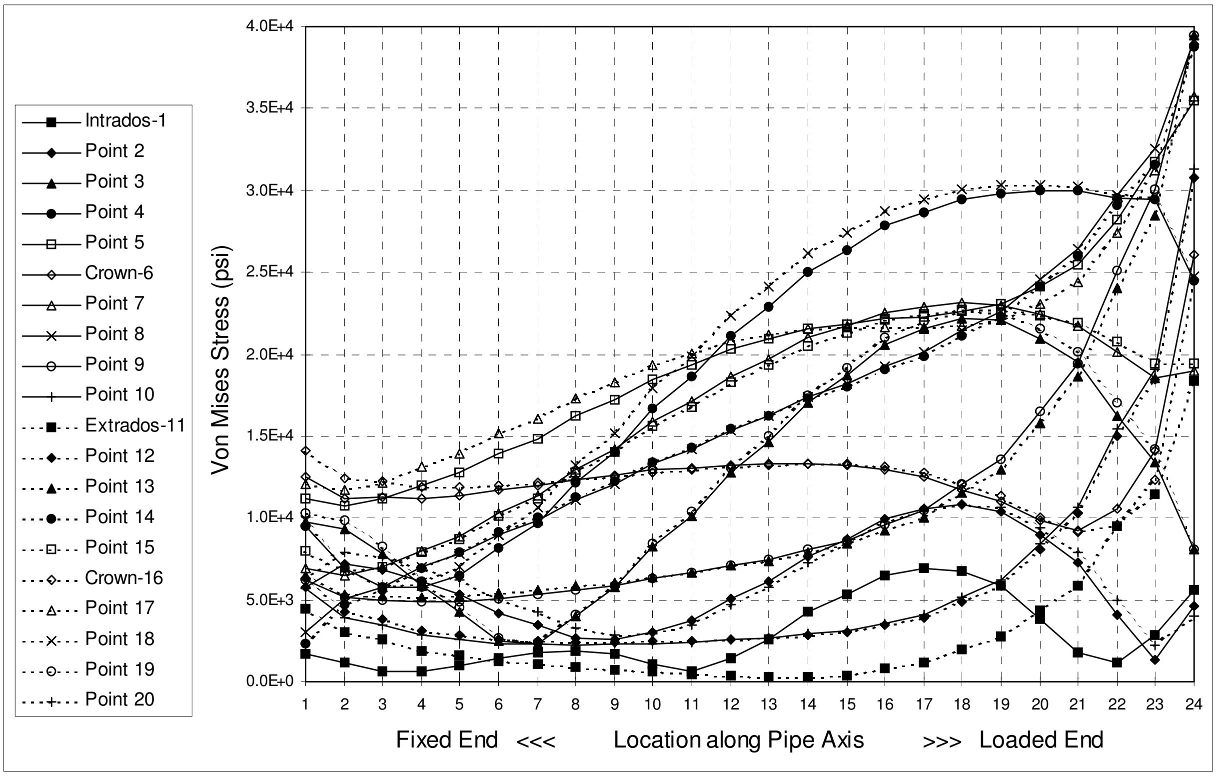

Fig. 3.5.2 Variation of Mises Stress Along the Axial Direction at Start of Yielding, Inside Wall - No Internal Pressure

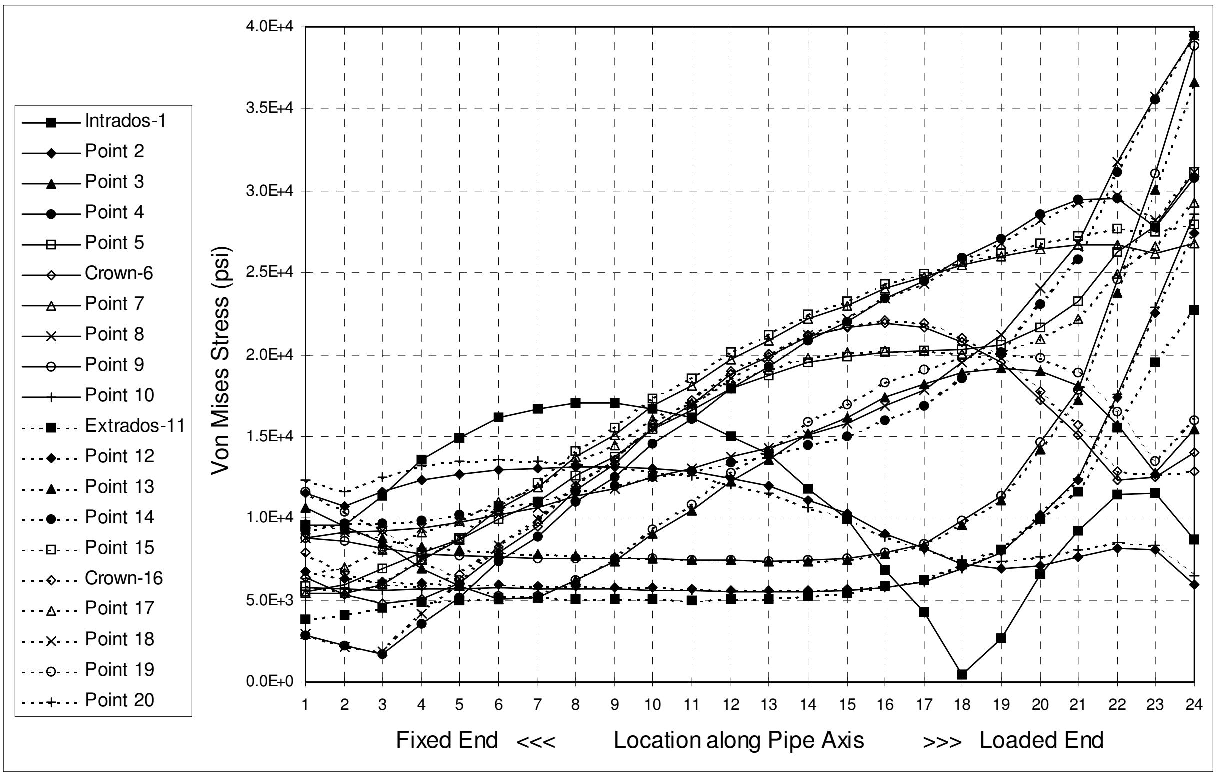

Fig. 3.5.3 Variation of Mises Stress Along the Axial Direction at Start of Yielding, Outside Wall - No Internal Pressure

3.5.1.1.b Instability

Figure 3.5.4 shows the distribution of equivalent plastic strain at the inside of the pipe wall, along the length of the elbow, at the load level where the model reaches instability. The value of the moment applied at this level is $M=1.1089\times10^6$ lb-in. and the corresponding end-rotation is $\theta=6.6651\times10^{-2}$ radians (3.82°).

In this figure, points 9 and 13 of section 24 have clearly higher values of plastic strain than all the other points of the model. On the outer side of the pipe wall, as shown in Fig. 3.5.5, point 9 of section 24 has the highest value of equivalent plastic strain, followed by point 5 of the same section.

Like the Mises stress distribution, the equivalent plastic strain distribution shown in Figs. 3.5.4 and 3.5.5 suggests that section 24 be considered as the critical section, in the case where no internal pressure is applied. Most of the points of section 24 undergo more plastic straining than their corresponding points on the other cross-sections; moreover, the maximum values of equivalent plastic strain belong to points of this section.

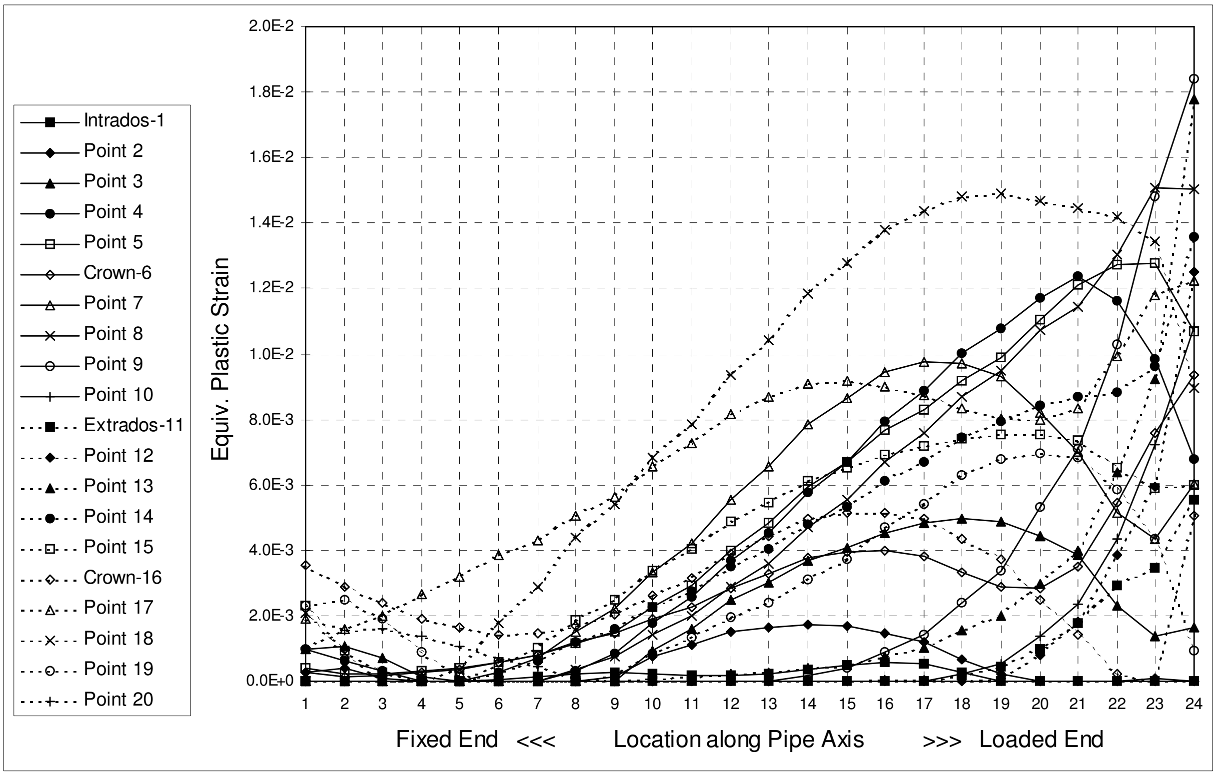

Fig. 3.5.4 **Variation of Equivalent Plastic Strain Along the Axial Direction at Instability, Inside Wall - No Internal Pressure**

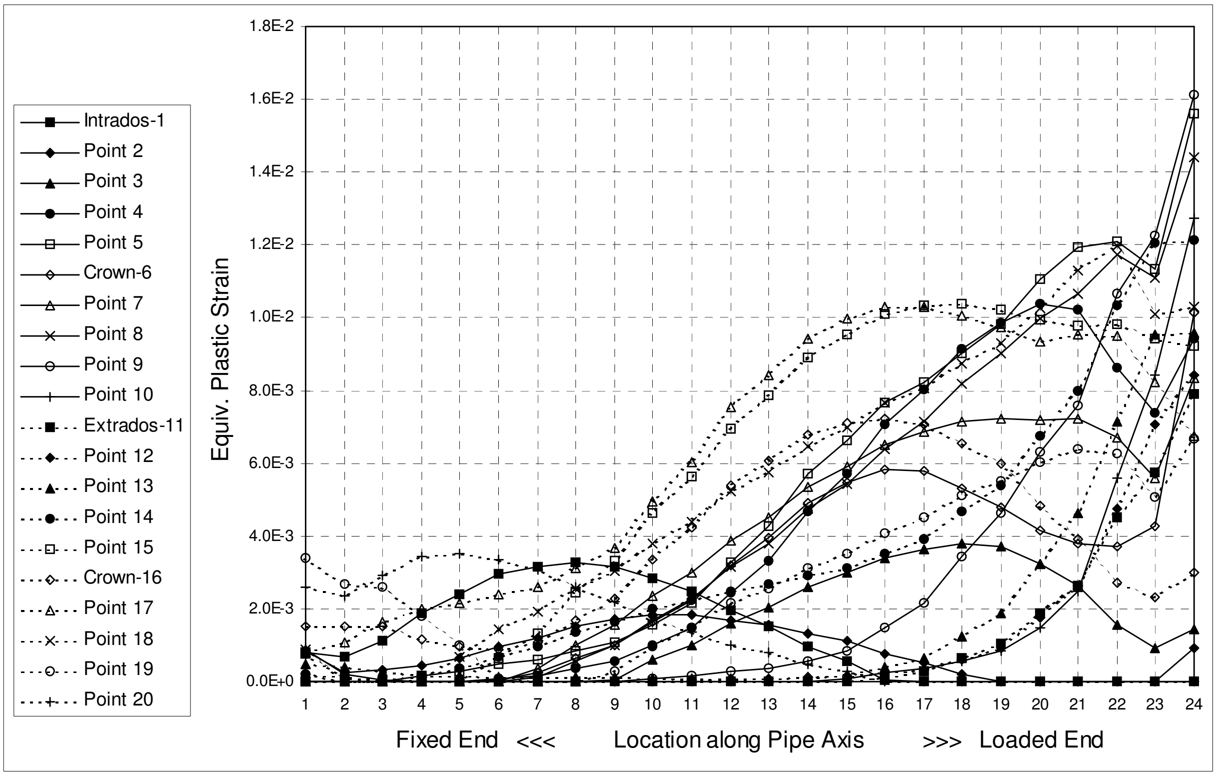

Fig. 3.5.5 **Variation of Equivalent Plastic Strain Along the Axial Direction at Instability, Outside Wall - No Internal Pressure**

3.5.1.2 Case with Internal Pressure of 1200 psi

3.5.1.2.a Start of Yielding

The application of internal pressure changes the way a pipe elbow behaves under external moment loading, not only in terms of its load-deflection behavior, but also in terms of the distribution of stresses and strains. The axial distribution of Mises stress at the inside wall, at the point where yielding starts to take place in the model, is shown in Fig. 3.5.6. This corresponds to an out-of-plane moment $M=4.7535\times10^5$ lb-in. and an end-rotation of $\theta=5.4008\times10^{-3}$ radians (0.31°).

From Fig. 3.5.6, it can be seen that the stress value at point 4 is equal to the yield value of the material, at all sections between 15 and 23, inclusive; but drops at section 24. However, it is clear from the same figure that section 24 has several points that have yielded; namely points 5, 13 and 14.

The axial distribution of Mises stress at the outside wall, and at the same load level, is presented in Fig. 3.5.7. Here, point 18 of sections 19 through 22, is starting to yield. But it can be seen from this figure that points 8, 9 and 18 of section 24 are all yielding.

The results in Figs. 3.5.6 and 3.5.7 suggest that section 24 can be considered critical in the case where an internal pressure of 1200 psi is applied, since it is the only section in the model that has more than one point meeting the yield criterion, both on the outside and the inside of the pipe wall. Furthermore, several points which do not undergo plastic straining at this early stage of loading history, have high values of Mises stress at section 24, and several curves reach their maximum points at this section.

3.5.1.2.b Instability

Figure 3.5.8 shows the distribution of equivalent plastic strain along the length of the elbow, on the inside of the pipe wall, at the load level where the model reaches instability. The value of the moment applied at this level is $M= 2.7175\times10^6$ lb-in. and the corresponding end-rotation is $\theta= 9.5496\times10^{-2}$ radians (5.47°). Figure 3.5.9 shows a similar distribution for points lying on the outer side of the pipe wall, at the same load level.

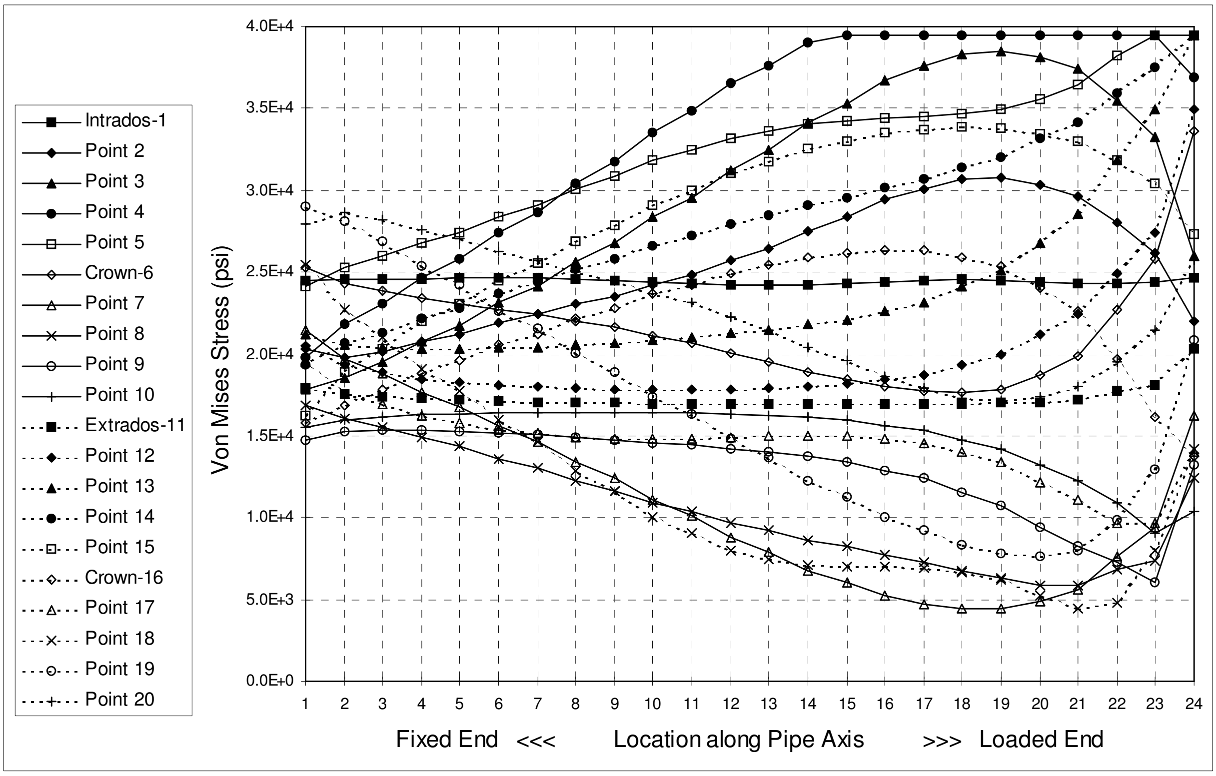

Fig. 3.5.6 Variation of Mises Stress Along the Axial Direction at Start of Yielding, Inside Wall - Internal Pressure: 1200 psi

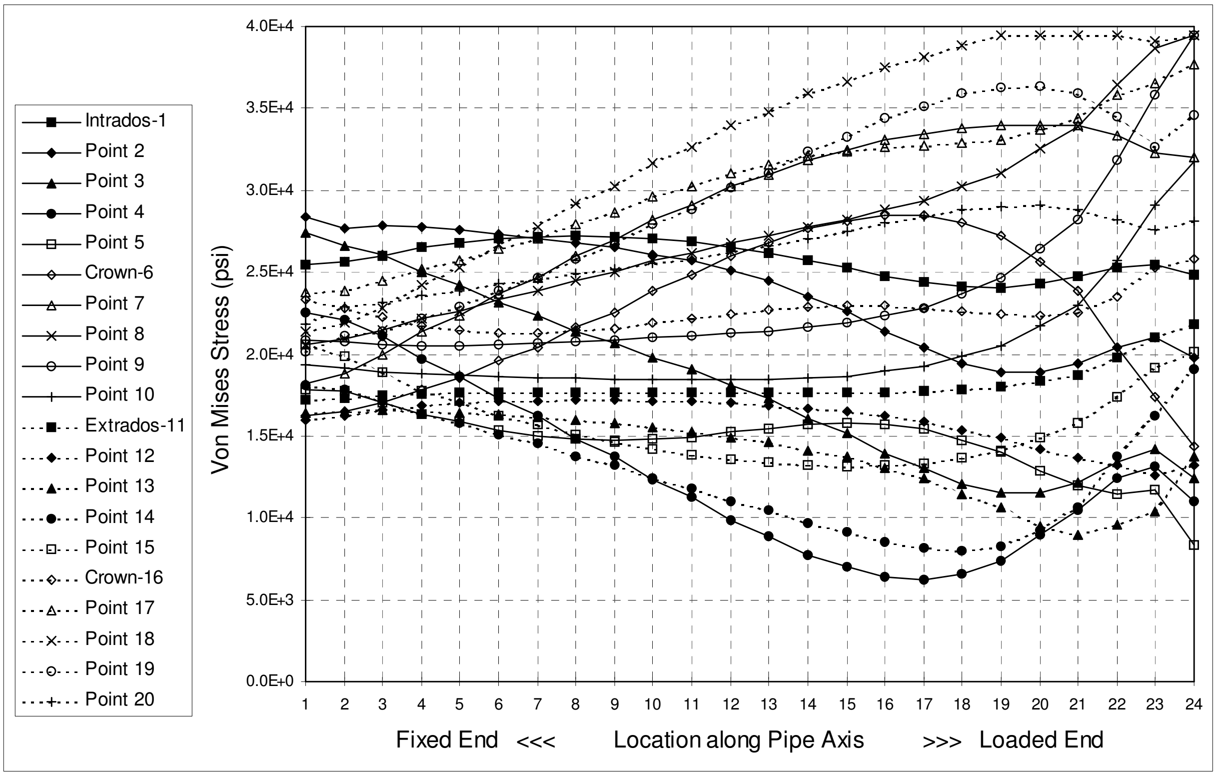

Fig. 3.5.7 Variation of Mises Stress Along the Axial Direction at Start of Yielding, Outside Wall - Internal Pressure: 1200 psi

Contrary to the case with no internal pressure, both of these figures show that the maximum values of equivalent plastic strain do not occur at section 24. In Fig. 3.5.8, the maximum value is at point 5 of section 23, and it is clear that the strain drops to a much lower value at point 5 of section 24. This same sudden drop also occurs at points 4 and 6.

Figure 3.5.9 shows a maximum value of strain occurring at the right crown (point 6) of section 21, and a comparably high value of strain at point 5 of section 21 and 22. A sharp drop similar to the one discussed above exists in this case too, for points 5 and 6, as we approach the free (loaded) end of the elbow.

The drop is undoubtedly due to the effect of internal pressure, since it did not exist in its absence. This can be explained by the fact that internal pressure opposes the ovalization of the section, which is the predominant mode of deformation close to the loaded extremity of the elbow. The effect of pressure is more pronounced close to the extremity, because the end section, being the least constrained, is the one that is most prone to ovalize.

Moreover, as discussed in the previous chapter, a follower force is applied at the loaded end to model the effect of internal pressure in a closed end condition. This tensile force also contributes to the explanation of the above-mentioned drop, since the points in question, namely points 4, 5 and the right crown (point 6), are under axial compression due to the out-of-plane bending moment.

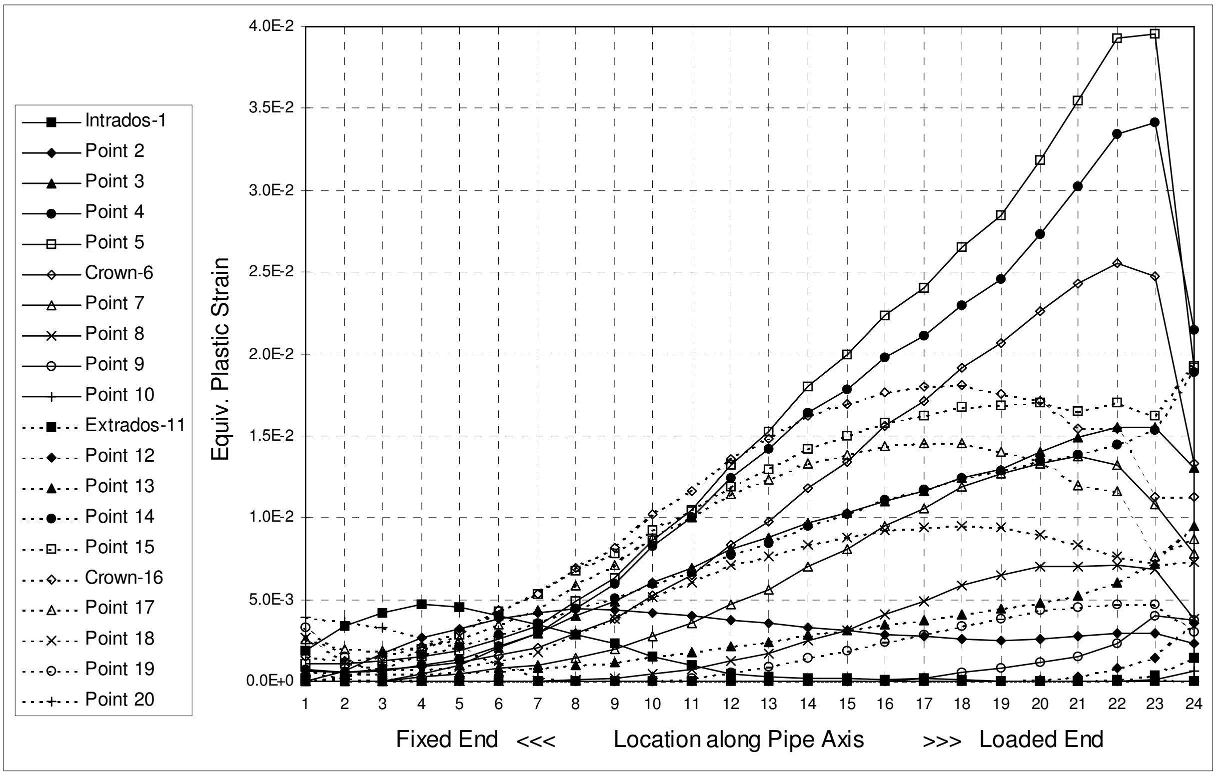

Fig. 3.5.8 Variation of Equivalent Plastic Strain Along the Axial Direction at Instability, Inside Wall - Internal Pressure: 1200 psi

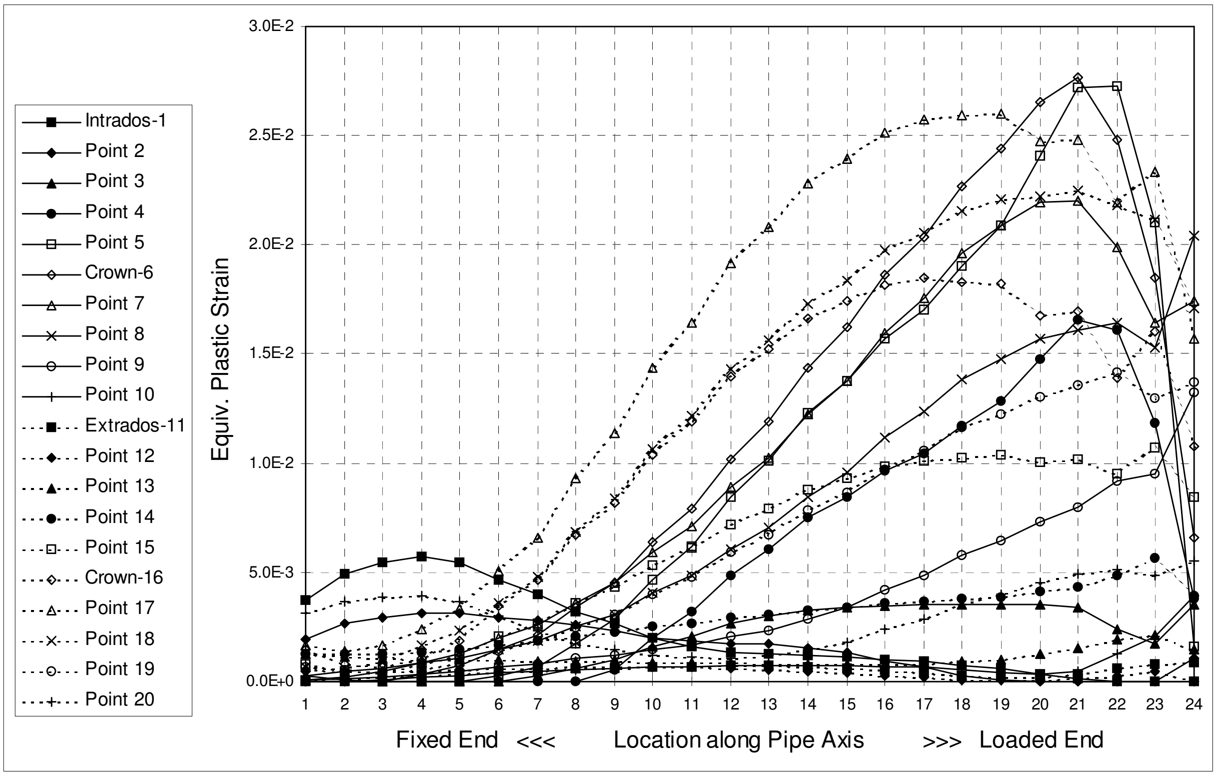

Fig. 3.5.9 Variation of Equivalent Plastic Strain Along the Axial Direction at Instability, Outside Wall - Internal Pressure: 1200 psi

3.5.2 Variation of Equivalent Plastic Strain with Loading History

It is important to study how yielding starts and progresses around the critical section, throughout loading history and until instability. Thus, yield progression is studied, by plotting the equivalent plastic strain versus end-rotation, for each of the 20 points of the critical cross-section. These curves are plotted once for the inside wall, and are repeated for the mid-wall and again for the outside wall.

Three cases are studied, one with no internal pressure applied, another at an intermediate value of internal pressure, namely 1200 psi, and a third at the highest pressure that the model can sustain, namely 2200 psi.

3.5.2.1 Case without Internal Pressure

Figure 3.5.10 shows the variation of equivalent plastic strain with end-rotation at the first 10 points of section 24, starting with the intrados. Figure 3.5.11 shows the same variation at the remaining 10 points, starting at the extrados. Both of these figures contain curves that represent values of strain at the inner side of the pipe wall.

It can be seen from these two figures that the first yield, on the inside wall, occurs at point 9, followed closely by points 8, 13 and 14. It can also be seen that the maximum value of equivalent plastic strain $\varepsilon_{ep}=1.8411\times10^{-2}$, at instability, is at point 9. Point 13 has the second highest value of $\varepsilon_{ep}=1.7771\times10^{-2}$. These values are about 13 times the yield strain value ($\varepsilon_{y}=0.1404\times10^{-2}$).

On the other hand, on the inner side of the pipe wall, yielding does not take place at all, in the area around the intrados, namely at points 1, 2, and 20. This elastic area extends almost to points 3 and 19 which are the last ones to yield, and where very small values of strain are reached before instability.

Figures 3.5.12 and 3.5.13 show the variation of the equivalent plastic strain with end-rotation, at mid-wall. It can be seen from these two figures that, at mid-wall, first yielding occurs very late, compared to the inside wall. The maximum strain value $\varepsilon_{ep}=2.5494\times10^{-3}$ is reached at point 13, at instability; this value is an order of magnitude smaller than the maximum value on the inside wall.

An equivalent set of curves, for the outer side of the pipe wall, is presented in Figs. 3.5.14 and 3.5.15. From these two figures, it can be seen that, on the outer side of the wall, first yielding takes place at point 8, followed closely by points 9 and 14. The maximum value of strain, at instability, $\varepsilon_{ep}=1.6110\times10^{-2}$, occurs at point 9, and is slightly smaller than the maximum value on the inside wall, which was also at point 9.

From Figs. 3.5.10 through 3.5.15, and from the discussion above, it can be concluded that the area around the intrados, namely points 1, 2, 19 and 20, undergo very small plastic deformation, and start to yield comparatively late, if at all yielding occurs at these points. On the other hand, there are two regions that show signs of being severely loaded; i.e. early yielding and high values of equivalent plastic strain at instability. These two regions are symmetrically positioned about the extrados, the first region being at points 8 and 9, and the second at points 13 and 14.

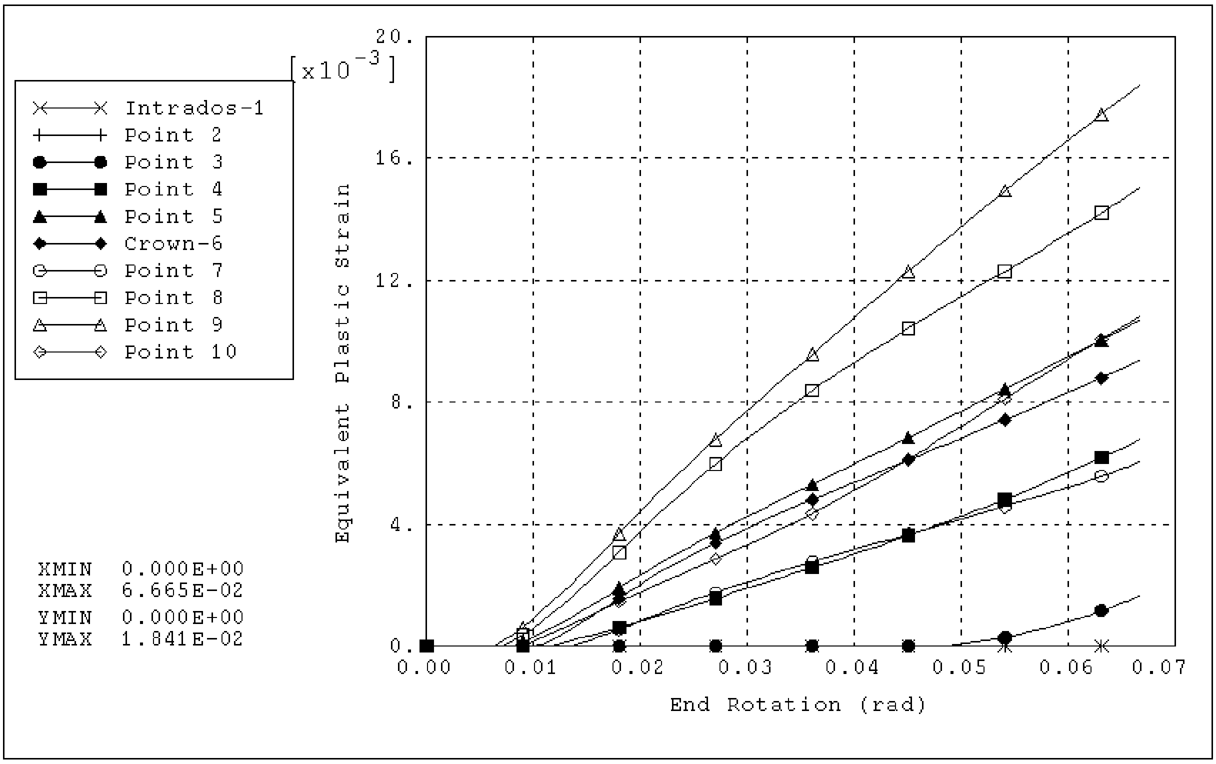

Fig. 3.5.10 Variation of the Equivalent Plastic Strain with End-rotation Around the First Half of the Cross-Section, Inside Wall - No Internal Pressure

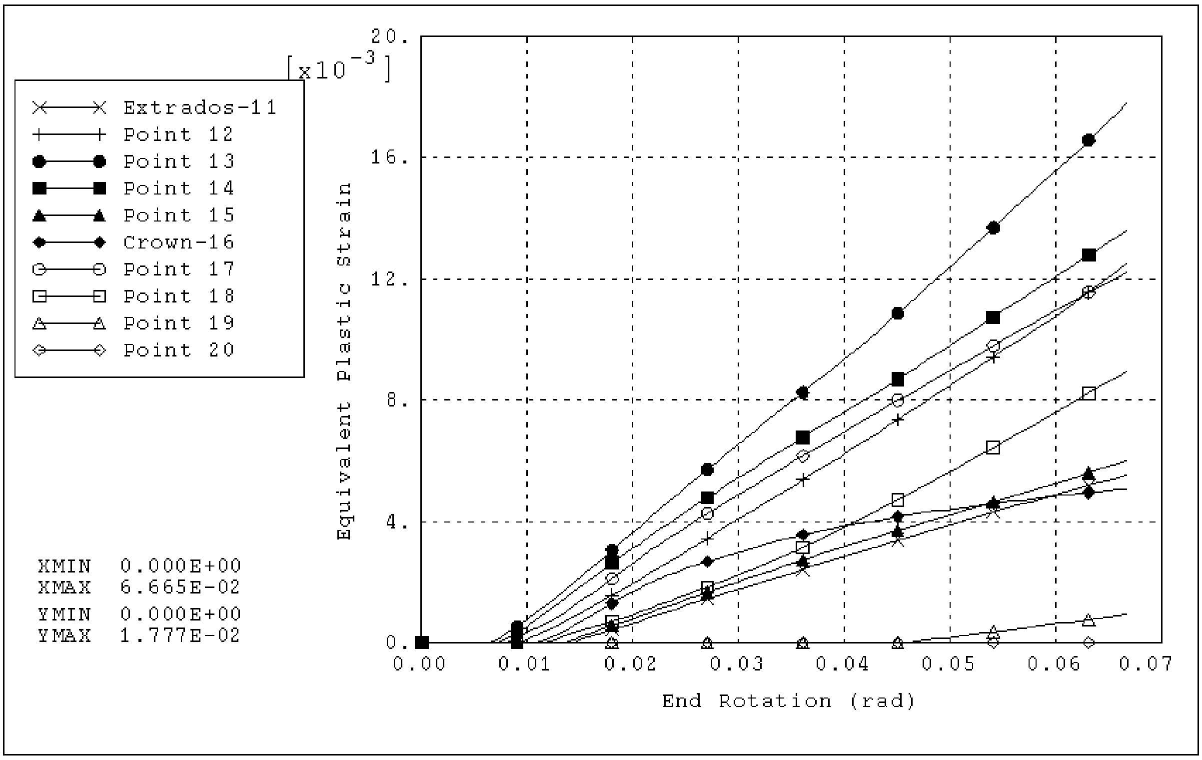

Fig. 3.5.11 Variation of the Equivalent Plastic Strain with End-rotation Around the Second Half of the Cross-Section, Inside Wall - No Internal Pressure

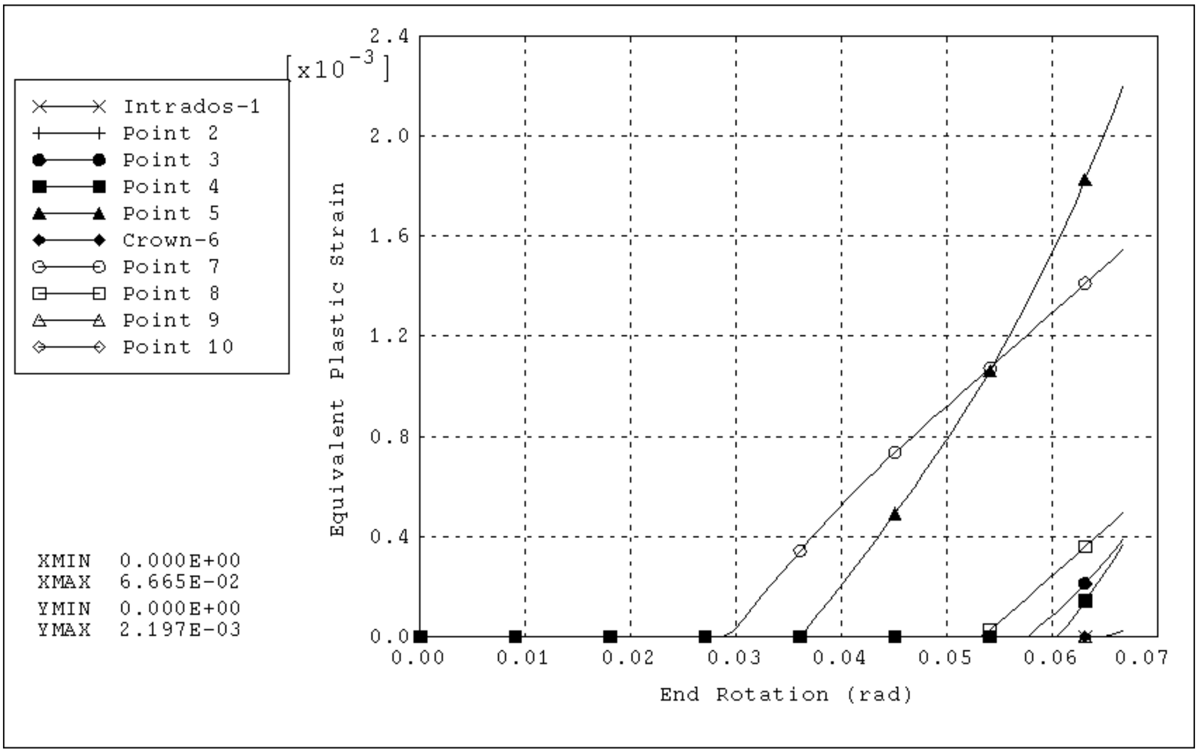

Fig. 3.5.12 Variation of the Equivalent Plastic Strain with End-rotation Around the First Half of the Cross-Section, Mid-Wall - No Internal Pressure

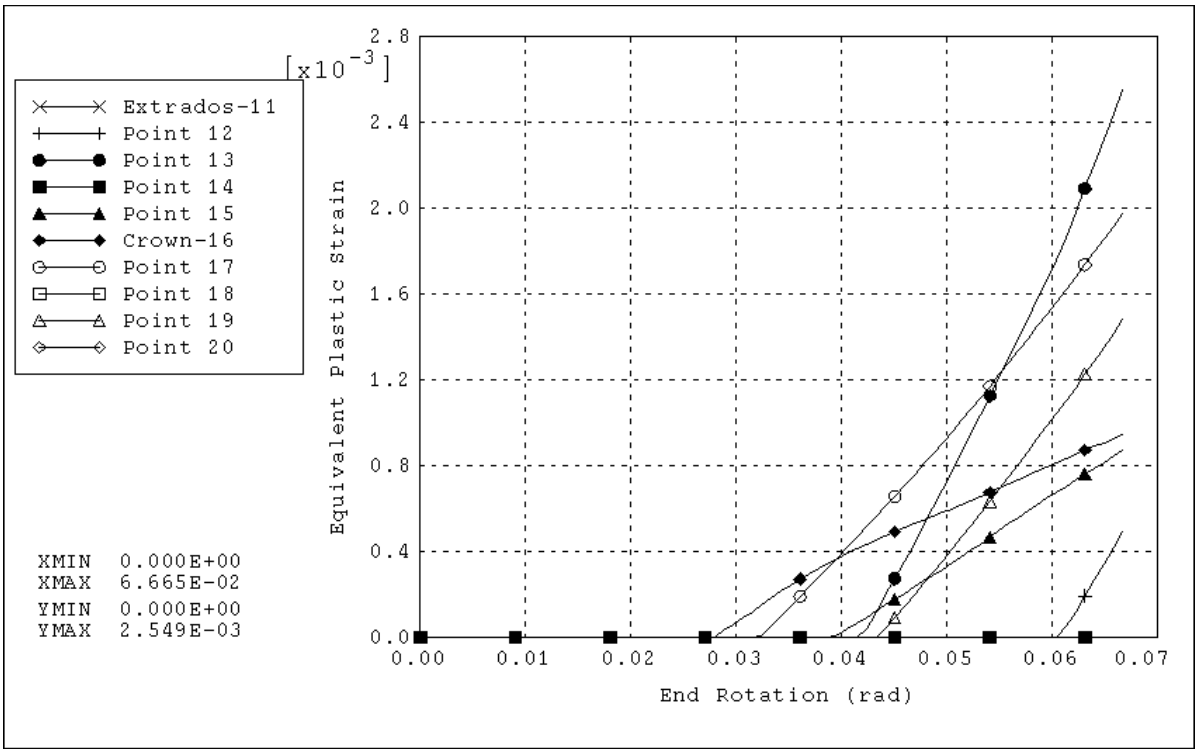

Fig. 3.5.13 Variation of the Equivalent Plastic Strain with End-rotation Around the Second Half of the Cross-Section, Mid-Wall - No Internal Pressure

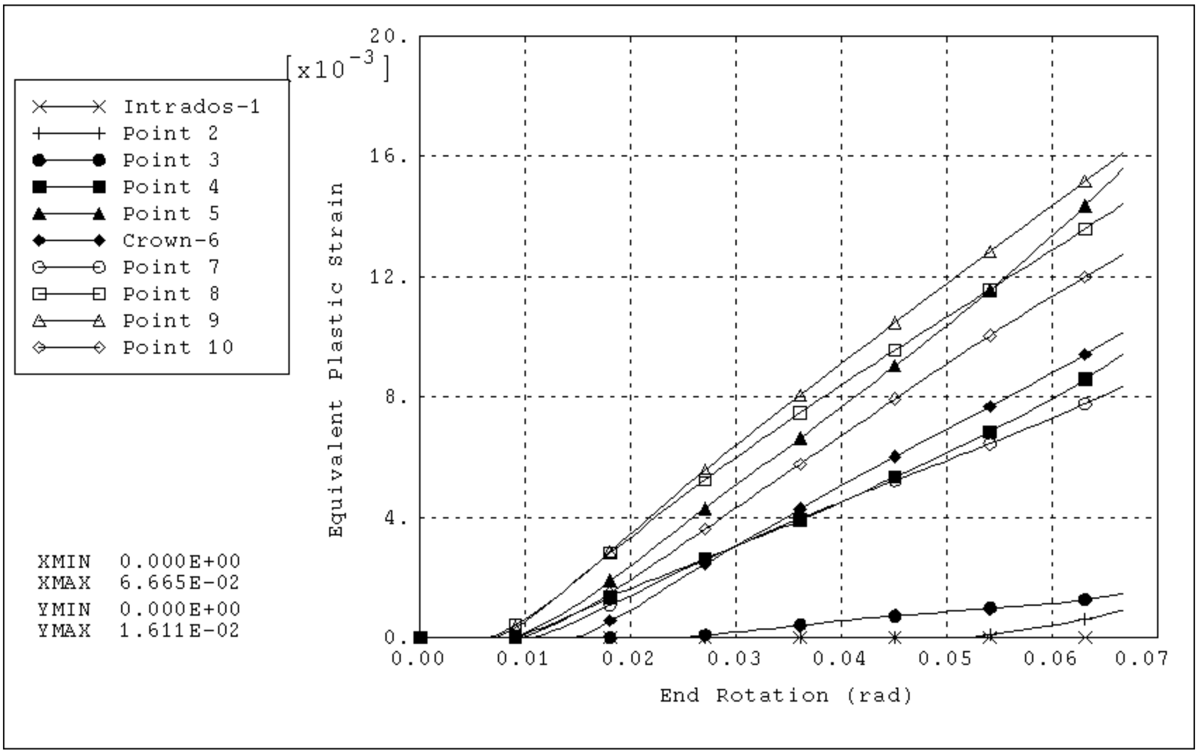

Fig. 3.5.14 Variation of the Equivalent Plastic Strain with End-rotation Around the First Half of the Cross-Section, Outside Wall - No Internal Pressure

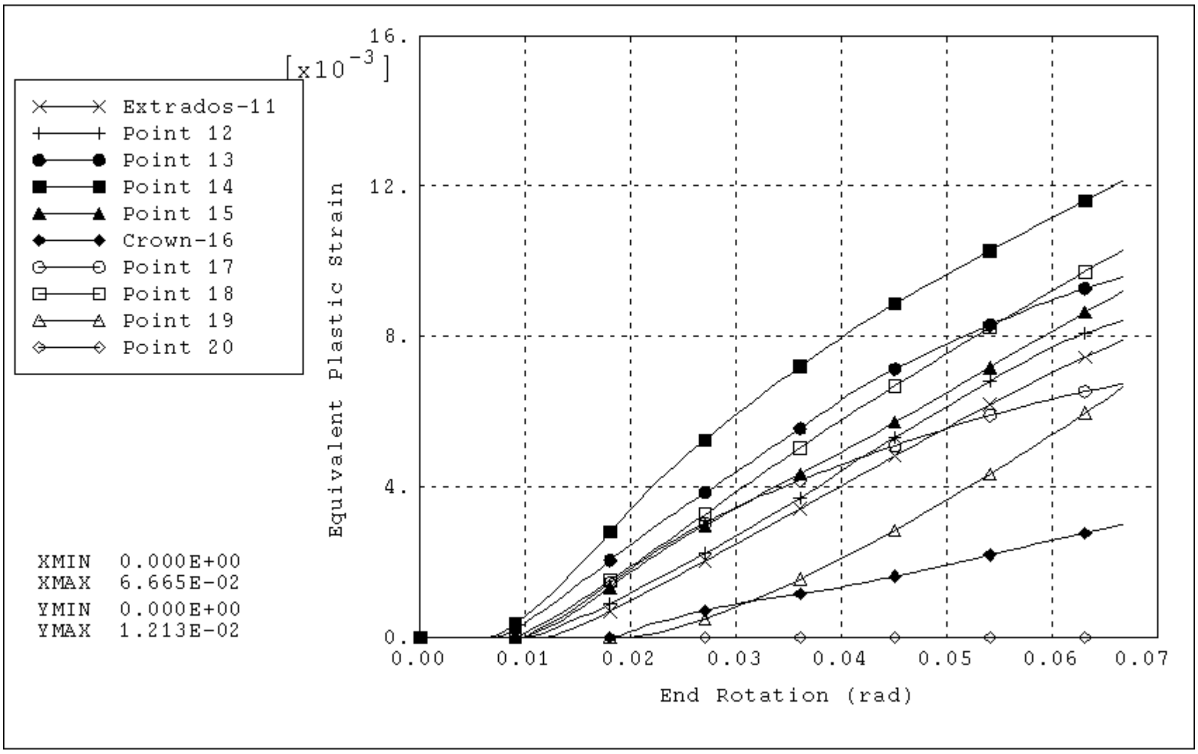

Fig. 3.5.15 Variation of the Equivalent Plastic Strain with End-rotation Around the Second Half of the Cross-Section, Outside Wall - No Internal Pressure

3.5.2.2 Case with Internal Pressure of 1200 psi

Figures 3.5.16 and 3.5.17 show the variation of equivalent plastic strain with end-rotation, at the inner side of the pipe wall, for the case where an internal pressure of 1200 psi is maintained, while the out-of-plane moment is being applied. Figure 3.5.16 contains 10 curves, each representing one point of the critical cross-section, starting with the intrados; and Fig. 3.5.17 contains the curves representing the remaining 10 points of the section, starting with the extrados.

It can be seen from these two figures that, on the inside wall, point 13 is the one that starts yielding first, followed closely by points 5 and 14. It can also be seen that the maximum value of equivalent plastic strain $\varepsilon_{ep}=2.1480\times10^{-2}$, at instability, is at point 4, while point 15 has the second highest value of strain, $\varepsilon_{ep}=1.9208\times10^{-2}$.

It is worth noting that, the high-strain region that existed at points 8 and 9, in the case without internal pressure, has shifted to points 4 and 5. The other high-strain region that existed at points 13 and 14, shifted slightly and extended to include point 15 as well. On the other hand, the area around the intrados, namely points 1, 2 and 20, remains a low-strain region, even under the effect of internal pressure. However, unlike the case without internal pressure, this elastic area is skewed, in the sense that it extends to include point 19, but not point 3. Another skewed low-strain region is also present close to the extrados, and includes points 8 through 12.

The variation of equivalent plastic strain with end-rotation for the points of the critical section, at mid-wall, is shown in Figs. 3.5.18 and 3.5.19. It can be seen from both of these figures, that first yield occurs at a late stage and that the strain values are much smaller, compared to those of the corresponding points of the inside wall. Point 6 - the right crown - is the first to yield, and the maximum strain value at instability, $\varepsilon_{ep}=1.0482\times10^{-2}$, belongs to the left crown - point 16, instead of point 13, as was the case when no internal pressure was applied.

Figures 3.5.20 and 3.5.21 show the same variation, for the outside wall. From these two figures, it can be seen that, on the outer side of the wall, first yielding takes place at point 8, followed closely by points 9, 18 and 17. The maximum value of strain, at instability, $\varepsilon_{ep}=2.0403\times10^{-2}$, occurs at point 8. One region of high strain exists, like the case without internal pressure, around point 8, but is slightly shifted towards point 7; another such region lies between the left crown - point 16 - and extends until point 19. A low-strain region, that starts from point 20, goes through the intrados and until point 5, is still present. Another such region exists at the extrados and includes points 12 and 13.

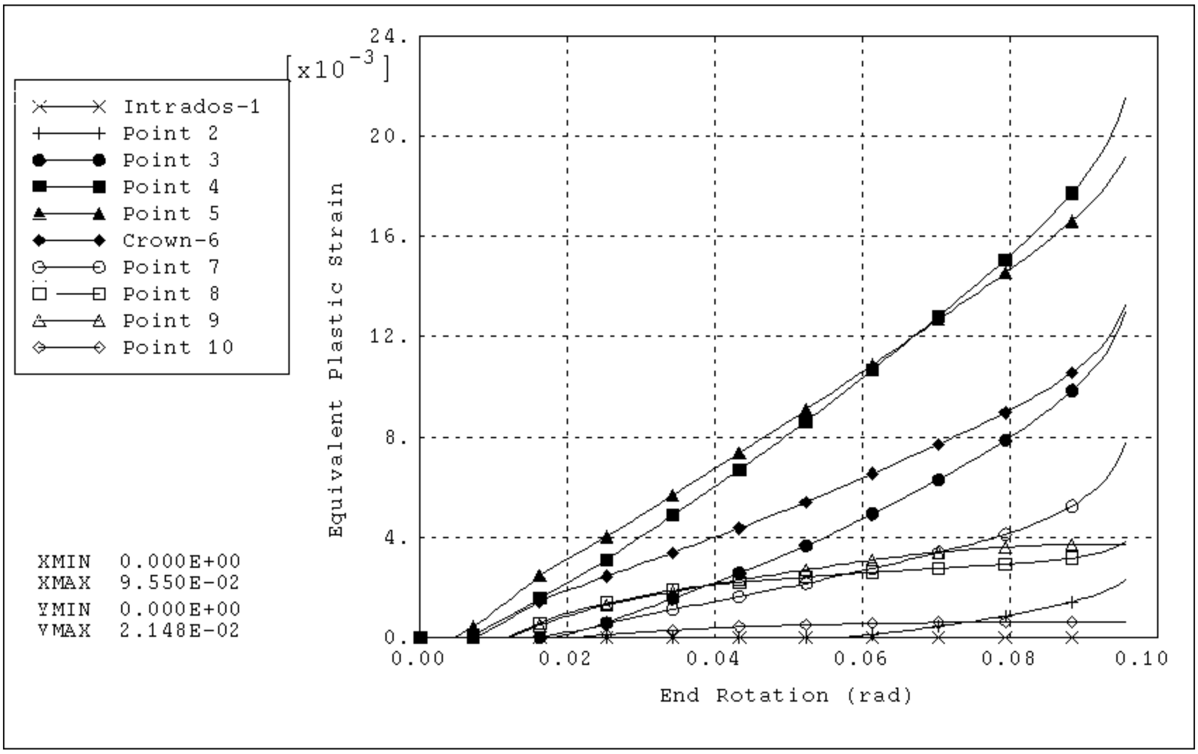

Fig. 3.5.16 Variation of the Equivalent Plastic Strain With End-rotation Around the First Half of the Cross-Section, Inside Wall - Internal Pressure: 1200 psi

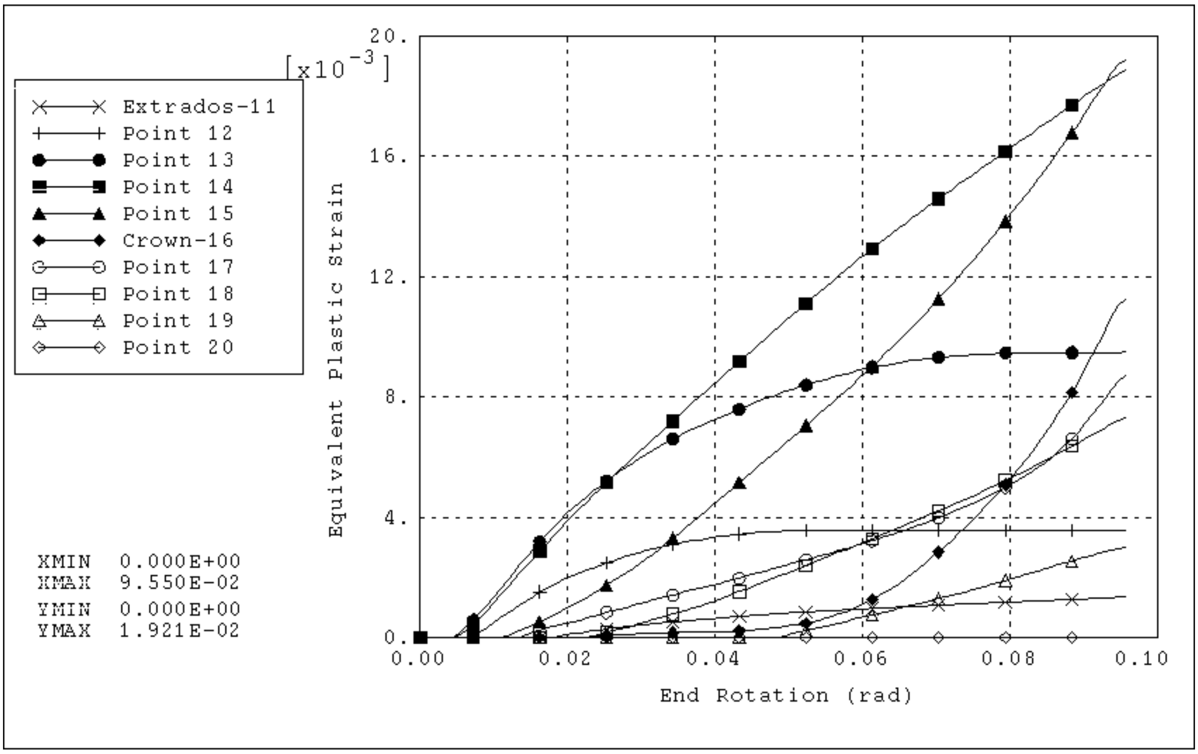

Fig. 3.5.17 Variation of the Equivalent Plastic Strain with End-rotation Around the Second Half of the Cross-Section, Inside Wall - Internal Pressure: 1200 psi

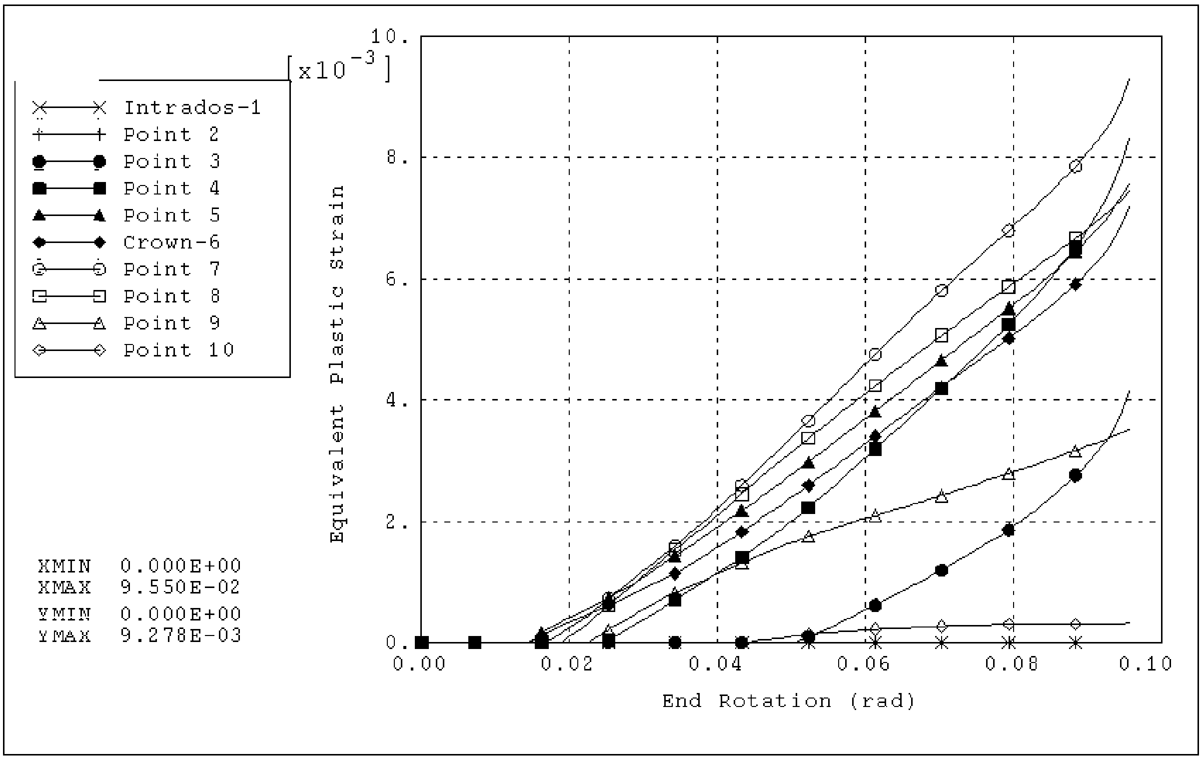

Fig. 3.5.18 Variation of the Equivalent Plastic Strain With End-rotation Around the First Half of the Cross-Section, Mid-Wall - Internal Pressure: 1200 psi

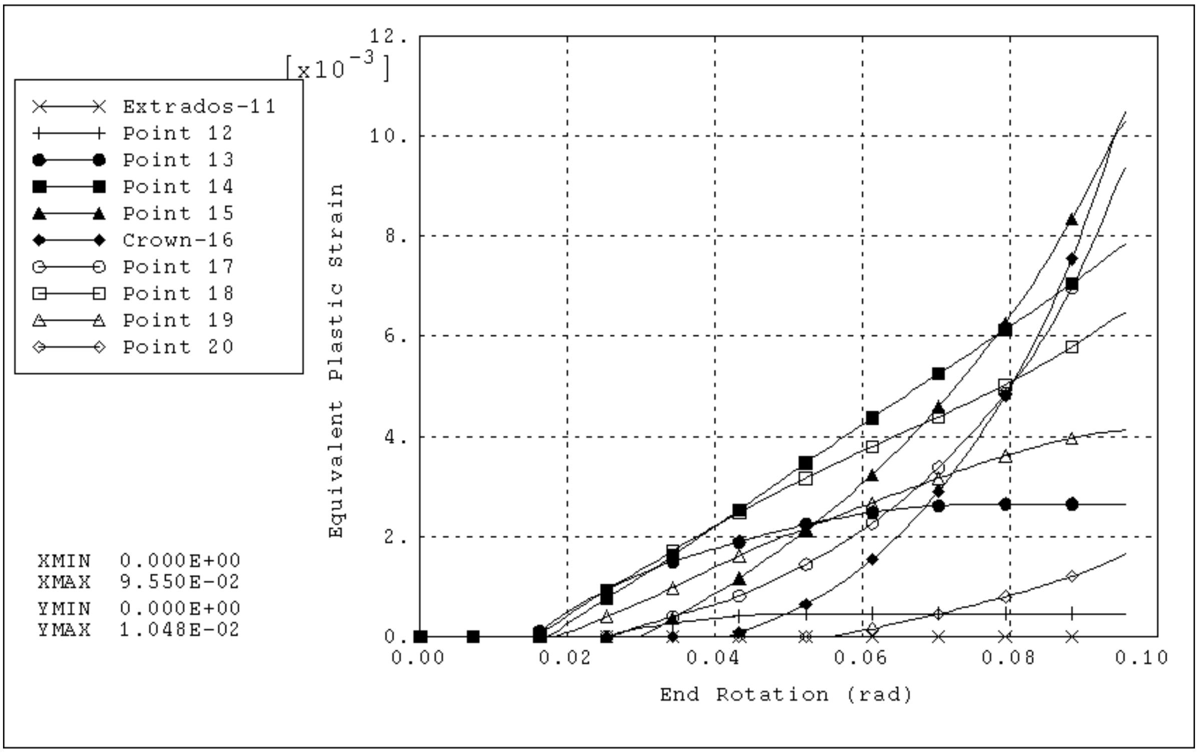

Fig. 3.5.19 Variation of the Equivalent Plastic Strain With End-rotation Around the Second Half of the Cross-Section, Mid-Wall - Internal Pressure: 1200 psi

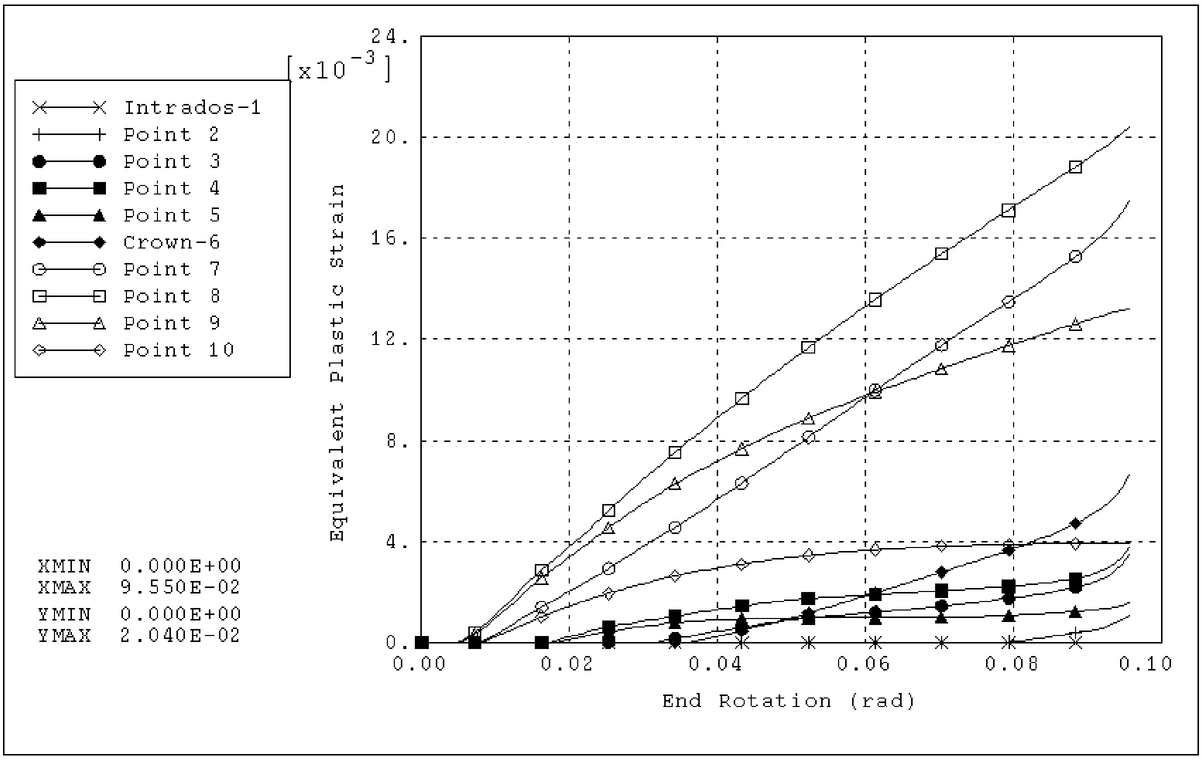

Fig. 3.5.20 Variation of the Equivalent Plastic Strain With End-rotation Around the First Half of the Cross-Section, Outside Wall - Internal Pressure: 1200 psi

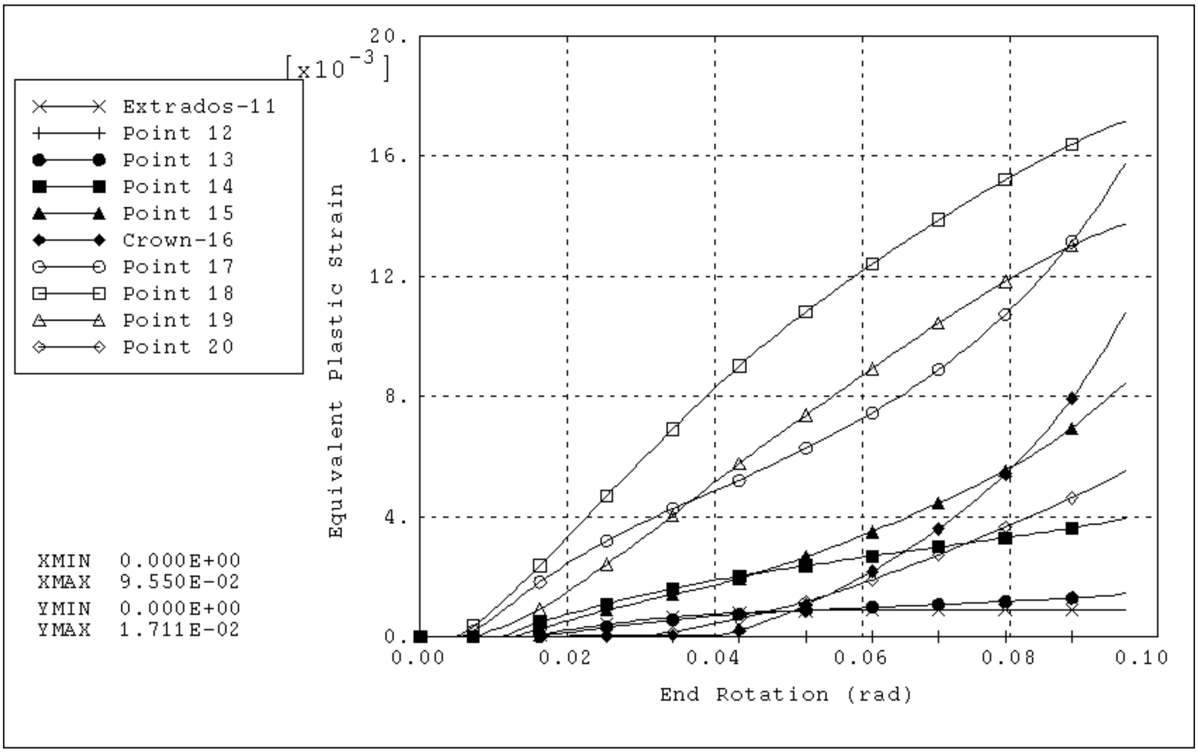

Fig. 3.5.21 Variation of the Equivalent Plastic Strain With End-rotation Around the Second Half of the Cross-Section, Outside Wall - Internal Pressure: 1200 psi

3.5.2.3 Case with Internal Pressure of 2200 psi

This case is quite different from the previous two cases, since yielding is initiated, at many points, under the effect of pressure alone, before any moment loading is applied. Some points even have very high values of equivalent plastic strain, e.g. the intrados has ε_{ep}=0.1747, at start of loading.

The variation of equivalent plastic strain with end-rotation for this case is shown in Figs. 3.5.22 and 3.5.23 for the inside wall, Figs. 3.5.24 and 3.5.25 for the mid-wall, and Figs. 3.5.26 and 3.5.27 for the outside wall. From these six figures, it is clear that there is almost no strain gradient across the wall. In other words, the strain value at a given point in the section, at any given value of end-rotation, is almost the same at the inside wall, the mid-wall and the outside wall.

The highest strain at instability exists at the left crown - point 16 - and has a value of ε_{ep}=0.5330 at the inner side of the wall, ε_{ep}=0.5398 at mid-wall, and ε_{ep}=0.5467 at the outer side of the wall. A high-strain region exists at points 15 through 17, including the crown; and another such region exists at points 2 through 5. On the other hand, a low-strain region exists around the extrados, starting from point 9 and reaching point 12. Unlike the previous two cases, there is no low-strain region near the intrados.

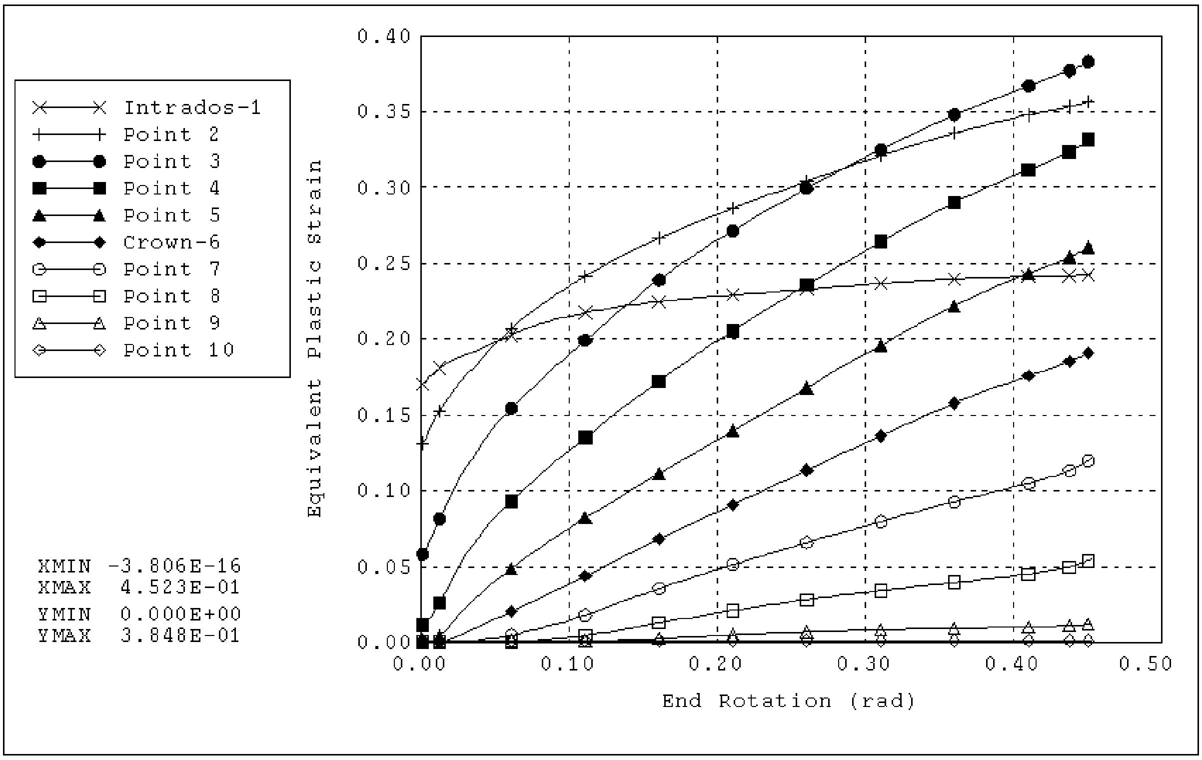

Fig. 3.5.22 Variation of the Equivalent Plastic Strain With End-rotation Around the First Half of the Cross-Section, Inside Wall - Internal Pressure: 2200 psi

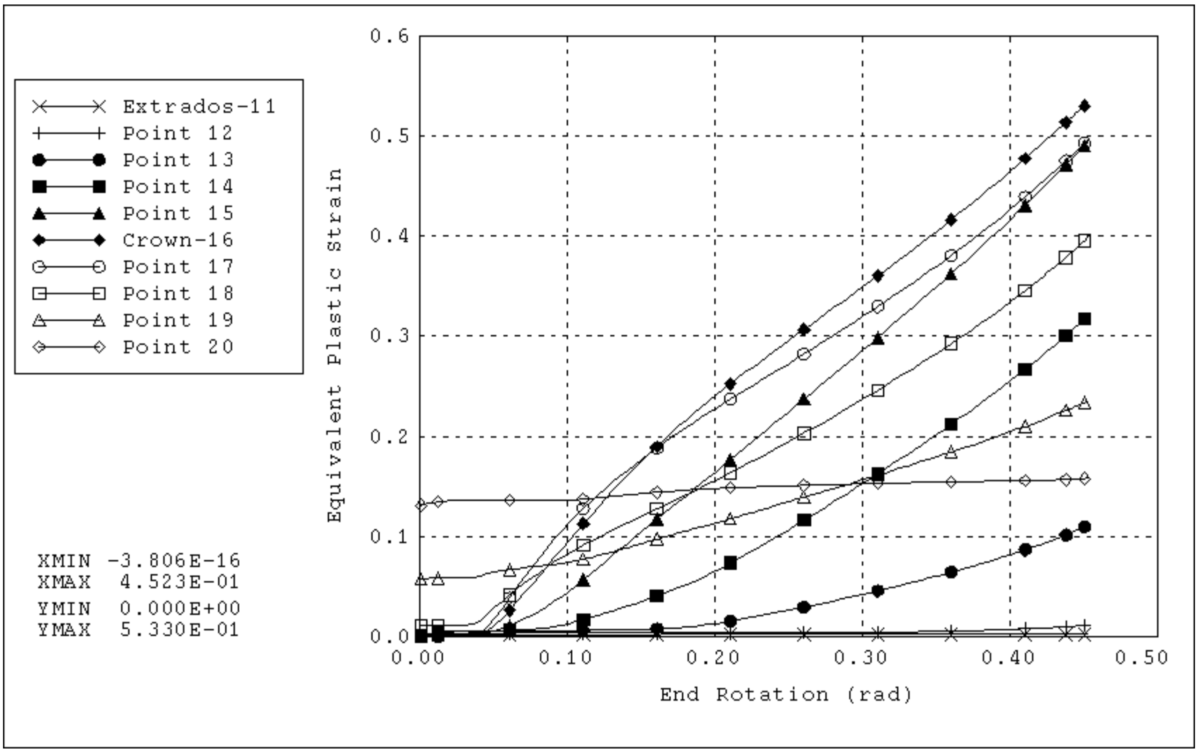

Fig. 3.5.23 Variation of the Equivalent Plastic Strain With End-rotation Around the Second Half of the Cross-Section, Inside Wall - Internal Pressure: 2200 psi

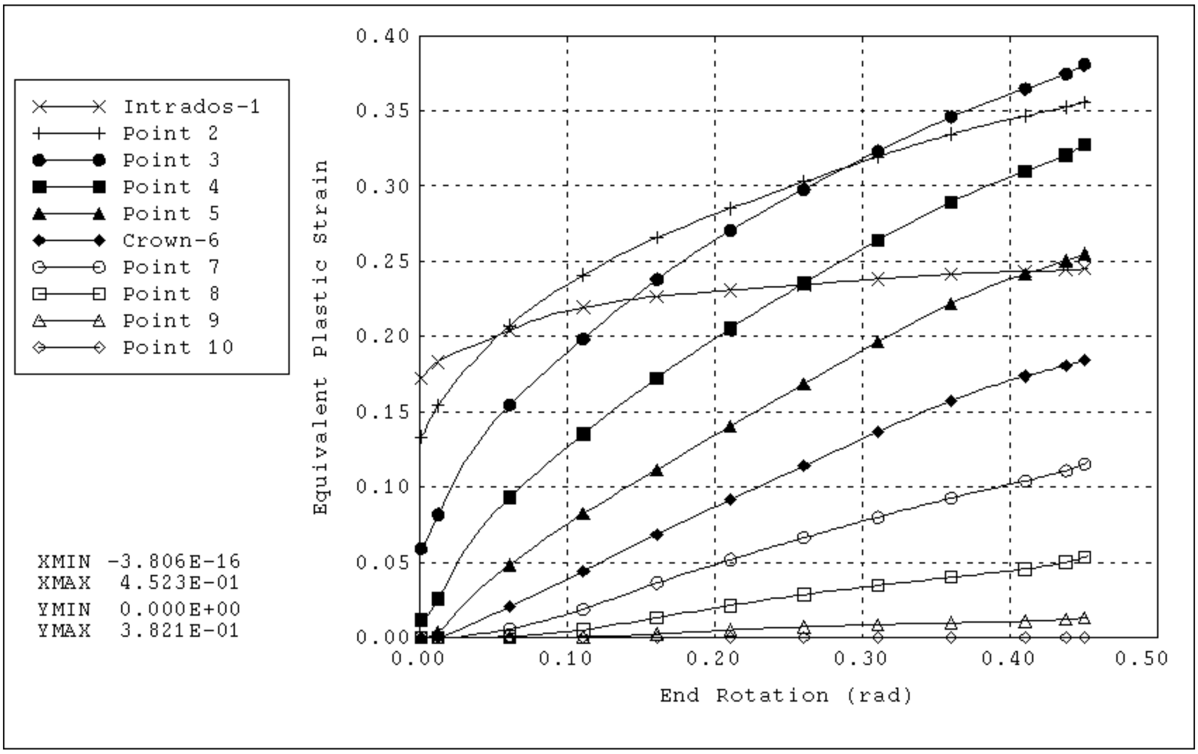

Fig. 3.5.24 Variation of the Equivalent Plastic Strain With End-rotation Around the First Half of the Cross-Section, Mid-Wall - Internal Pressure: 2200 psi

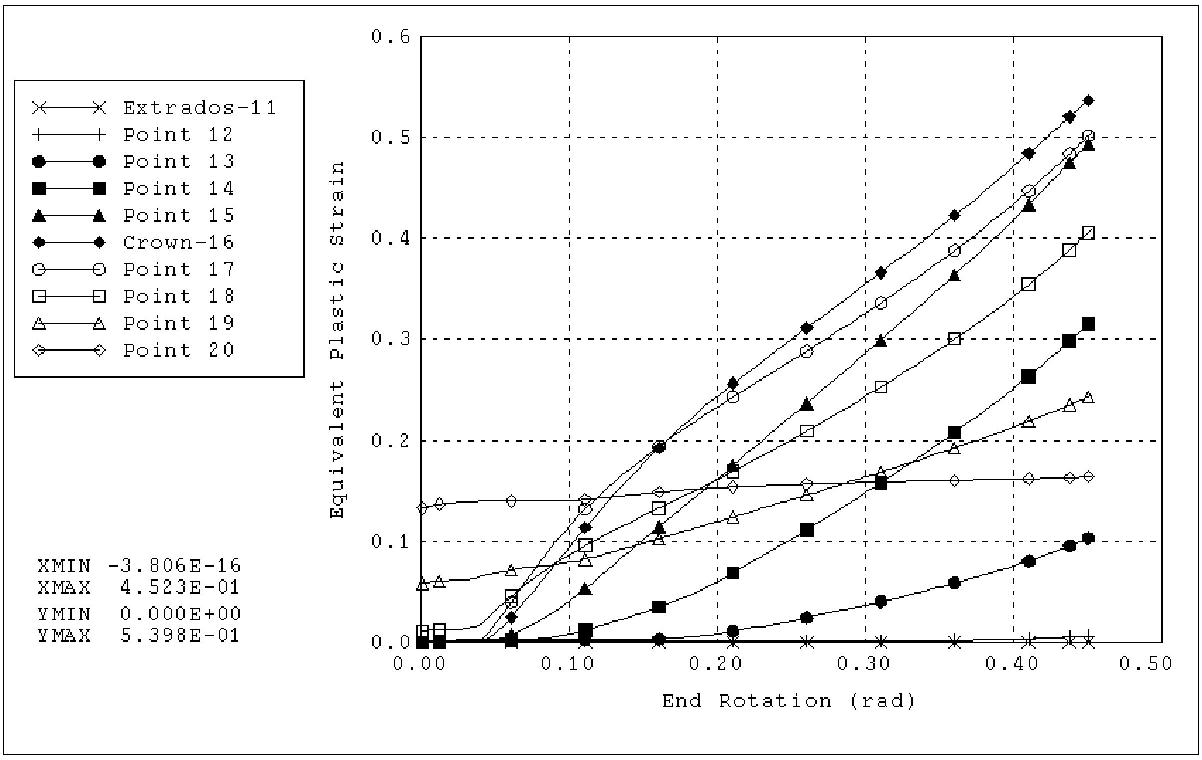

Fig. 3.5.25 Variation of the Equivalent Plastic Strain With End-rotation Around the Second Half of the Cross-Section, Mid-Wall - Internal Pressure: 2200 psi

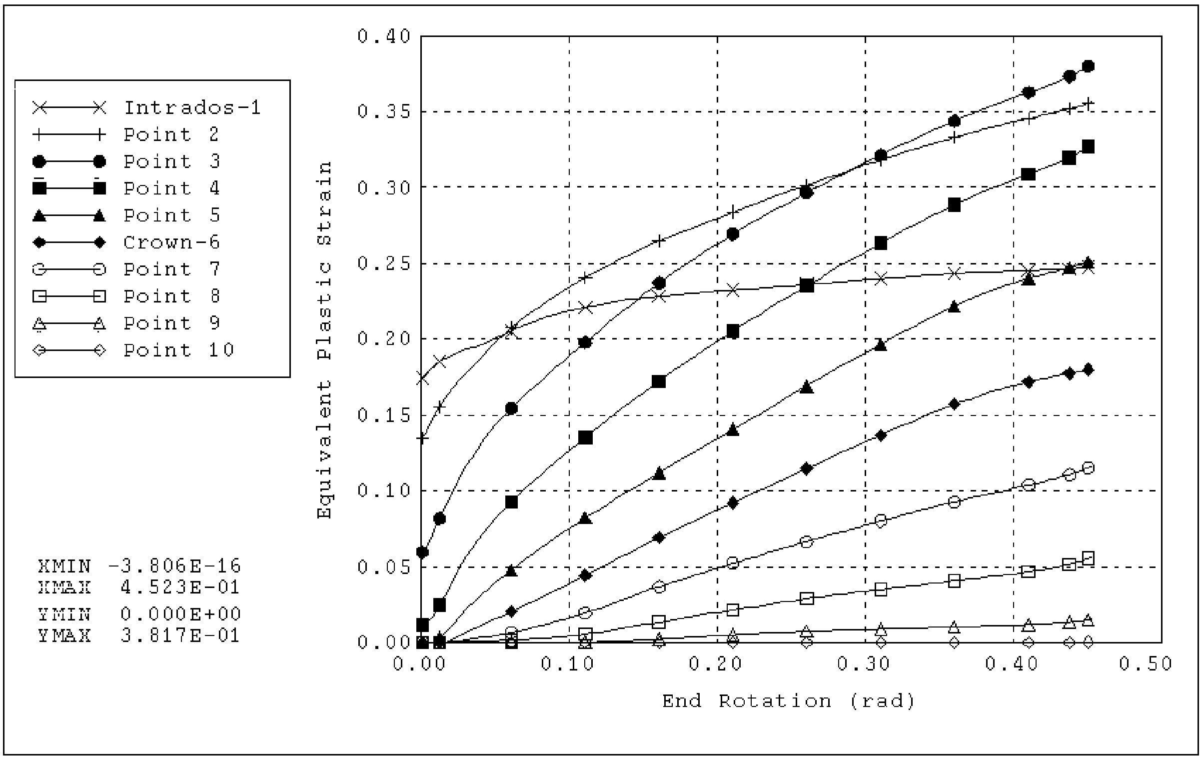

Fig. 3.5.26 Variation of the Equivalent Plastic Strain With End-rotation Around the First Half of the Cross-Section, Outside Wall - Internal Pressure: 2200 psi

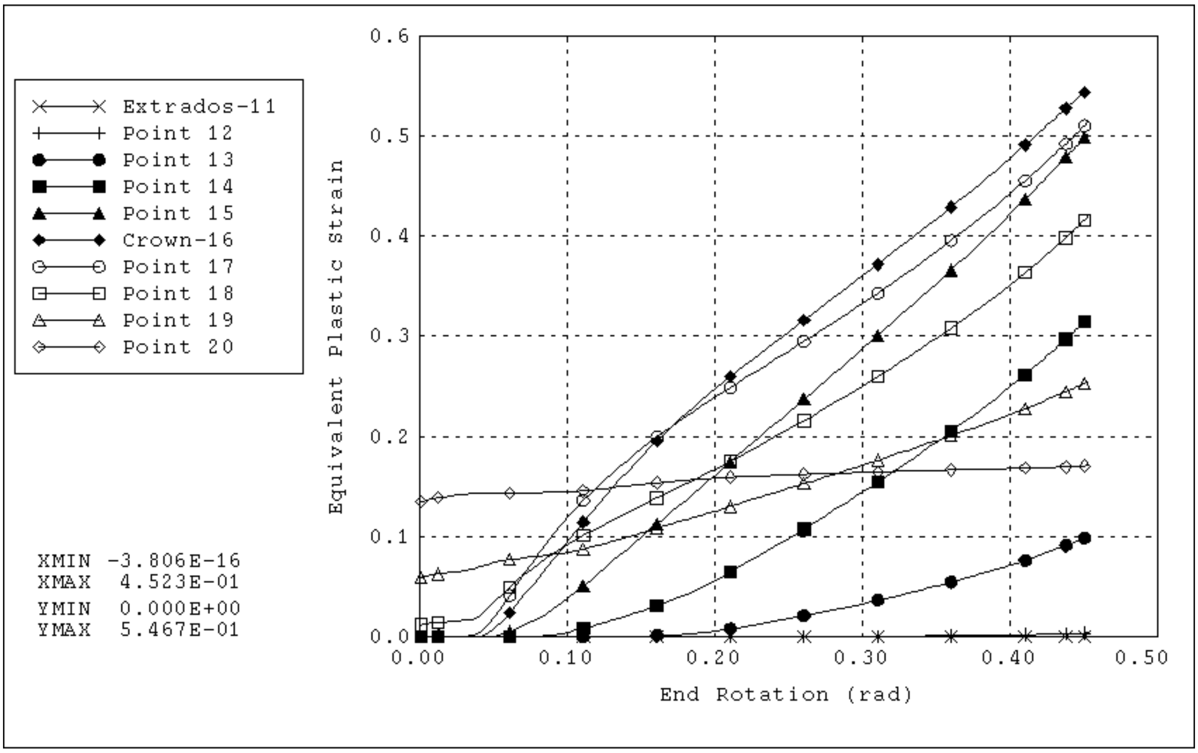

Fig. 3.5.27 Variation of the Equivalent Plastic Strain With End-rotation Around the Second Half of the Cross-Section, Outside Wall - Internal Pressure: 2200 psi

3.5.3 Progression of Yielding

In the previous section, the progression of yielding was studied at each point of the critical section of the model. Here, the model of the pipe elbow is treated as a whole, and the progression of yielding in the whole model is studied by marking, on the load-deflection curve, the point where yielding is initiated, and then the number of plastic hinges as they are being formed.

Whenever a point, belonging to any of the 24 sections of the model, transcends the elastic limit of the material, on the inside, outside and at mid-wall, it is considered to be a plastic hinge. Showing the number of plastic hinges on the load-deflection curve, at equal intervals of end-rotation, gives an indication of the rate of hinge formation.

3.5.3.1 Case without Internal Pressure

Figure 3.5.28 shows the load-deflection curve of the model with $h=0.1615$, for the load case that doesn't include any internal pressure effects. As can be seen from this figure, initiation of yielding occurs well before the load-deflection curve deviates from linearity, at a moment value of $M=4.1796\times10^{5}$ lb-in. and a corresponding end-rotation of $\theta=7.2001\times10^{-3}$ radians (~0.41°).

The first three plastic hinges are formed almost simultaneously; i.e. during the same increment, at a moment value of $M=9.5119\times10^{5}$ lb-in. and an end-rotation of $\theta=2.1602\times10^{-2}$ radians (~1.24°). Just before the model reaches instability, at a load of $M=1.1088\times10^{6}$ lb-in. and an end-rotation of $\theta=6.4847\times10^{-2}$ radians (~3.72°); 148 points, out of a total of 480, become plastic hinges.

3.5.3.2 Case with Internal Pressure of 1200 psi

Figure 3.5.29 shows the load-deflection curve of the pipe elbow, with an internal pressure of 1200 psi. The point of first yield, lies on the linear part of the curve, at a moment value of $M=4.7535\times10^{5}$ lb-in. and an end-rotation of $\theta=5.4008\times10^{-3}$ radians (~0.31°). This value of the moment is higher, and the value of end-rotation is lower than in the case without internal pressure; this is again due to the stiffening effect of pressure.

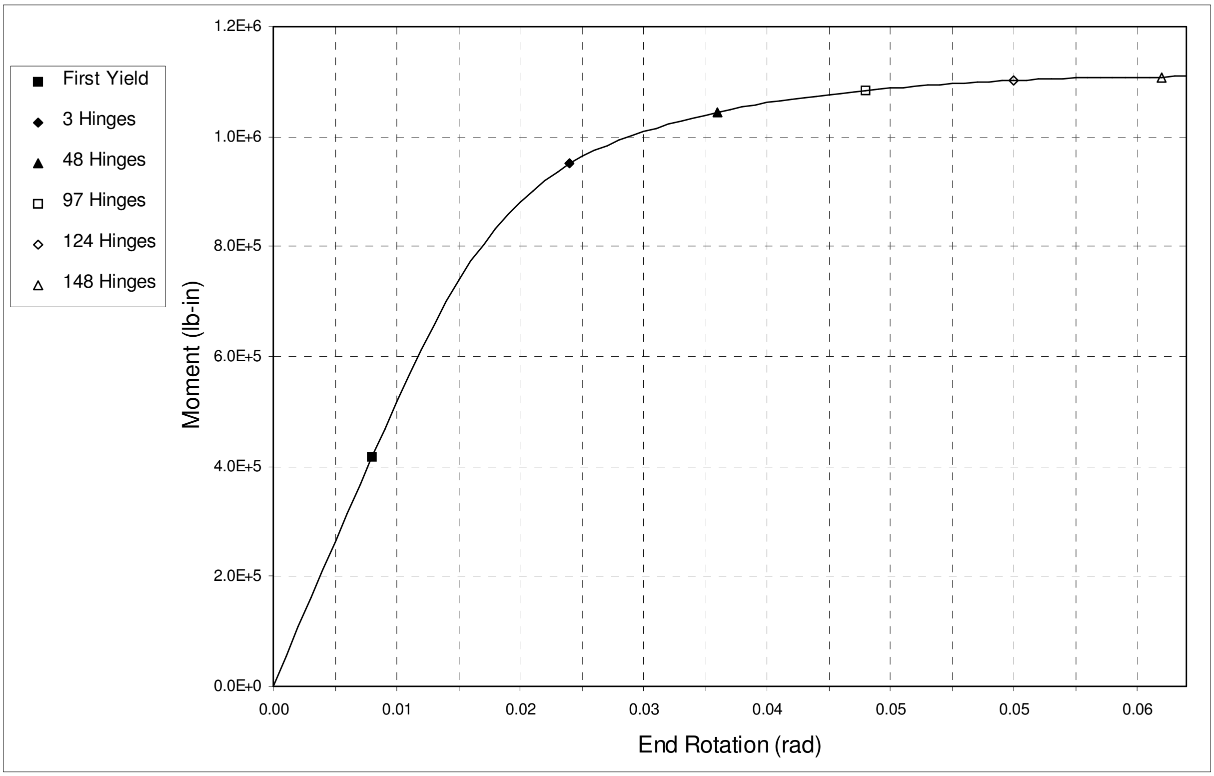

Fig. 3.5.28 Load-Deflection Curve for an Elbow With h=0.1615 - No Internal Pressure

The first four plastic hinges are formed at a load of M=1.1338×10^{6} lb-in. and an end-rotation of θ=1.4402×10^{-2} radians (~0.83°). And just before instability is reached, at a moment of M=2.6618×10^{6} lb-in. and a corresponding end-rotation of θ=8.6470×10^{-2} radians (~4.95°), 304 plastic hinges are present in the model. This shows that the presence of internal pressure not only has a stiffening effect, but also causes the pipe elbow to withstand much more plastification, before it reaches instability.

3.5.3.3 Case with Internal Pressure of 2200 psi

Unlike the previous two cases, the load-deflection curve of a model, subjected to an internal pressure of 2200 psi, as shown in Fig. 3.5.30, does not have a clearly linear part at start of loading. This is due to the fact that the elbow develops plastic hinges even before any moment loading is applied.

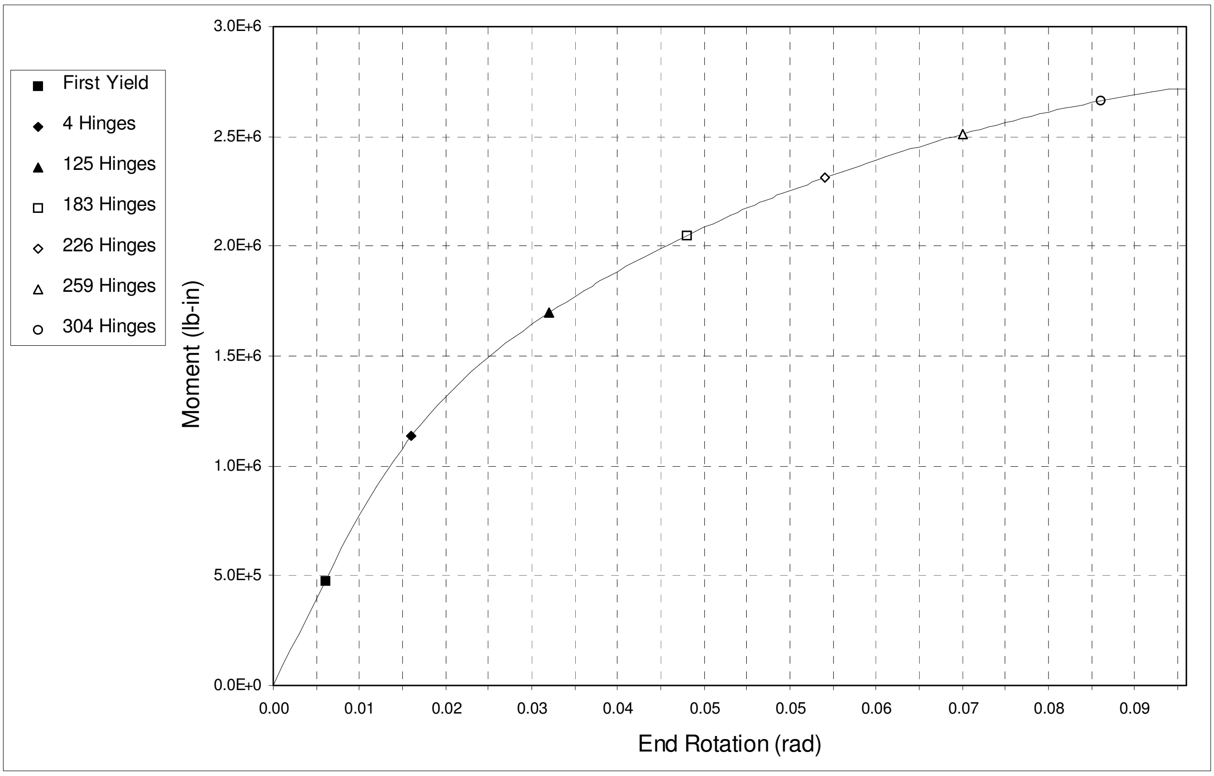

Fig. 3.5.29 Load-Deflection Curve for an Elbow With h=0.1615 - Internal Pressure: 1200 psi

In Fig. 3.5.30, the origin is marked as the point of "first yield"; however, this only means that the model is already actively yielding, at the start of load application. Furthermore, after the first increment of end-rotation ($M=1.0219\times10^5$ lb-in., $\theta=3.1253\times10^{-4}$ radians), 100 points have been found to have developed plastic hinges. Almost all points, 478 out of a total of 480, form plastic hinges, well before the model reaches instability.

For these reasons, and since an elbow could fail due to local material imperfections or manufacturing defects, and also because the end-rotation reached before instability is unrealistically large, these results are deemed questionable. It is important, therefore, to consider the results obtained at very high values of internal pressure, like in this case, with a lot of care.

3.5.4 Stress and Strain Distribution around the Cross-Section

In this section, the distribution of axial, hoop and equivalent stresses and strains, around the cross section is examined, once at initiation of yielding, and another time at instability. The same model used throughout the cross-section analysis, h=0.1615, is used here, excluding any effects of internal pressure. This analysis is repeated once with an intermediate value of internal pressure, namely 1200 psi, and again with the highest pressure that this model can sustain, 2200 psi.

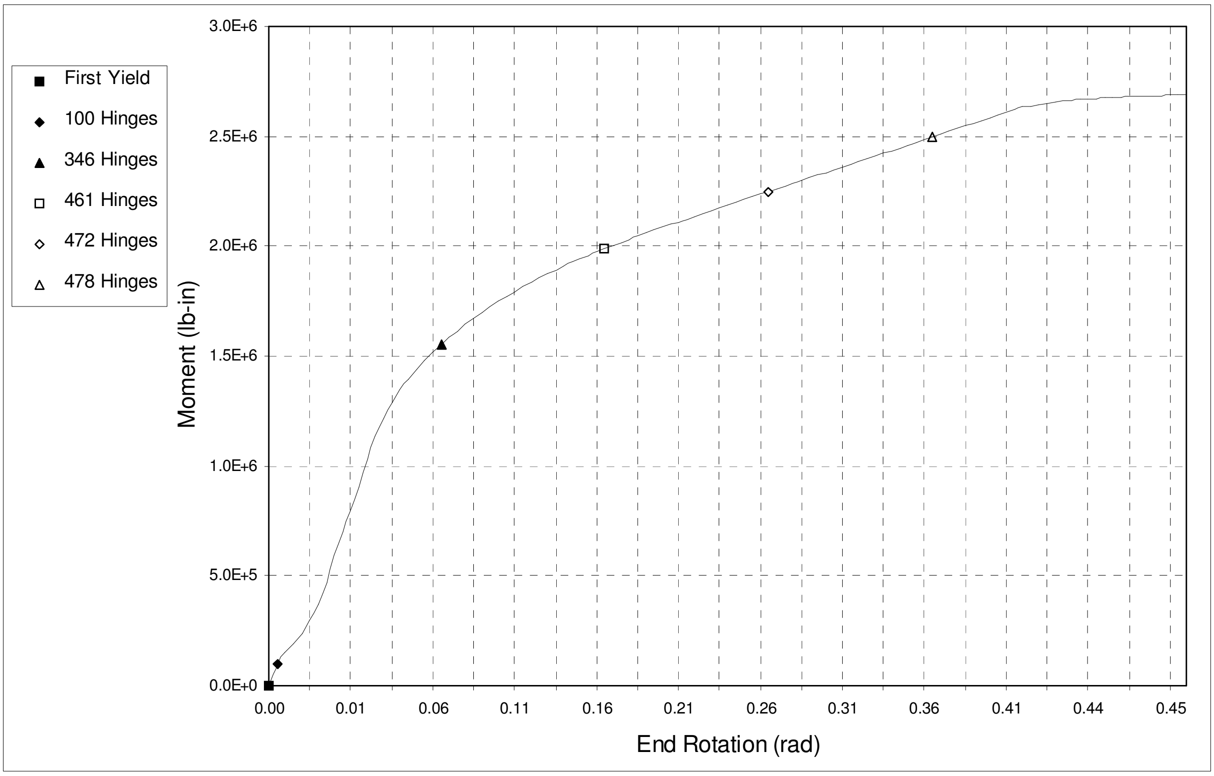

Fig. 3.5.30 Load-Deflection Curve for an Elbow With h=0.1615 - Internal Pressure: 2200 psi

This approach is helpful in getting a better understanding of the collapse behavior of the pipe bend, and of the effect of internal pressure on this behavior. Studying the axial and hoop components of stress and strain separately, gives a better and more detailed view of the loading condition, and of the state of stress and strain at the critical cross-section. The distribution of equivalent stress and strain is useful in evaluating the status of the section, with respect to the Mises yield criterion, and hence to understand how yielding is initiated, and how it progresses.

3.5.4.1 Case without Internal Pressure

3.5.4.1.a Start of Yielding

Figure 3.5.31 shows the distribution of axial stress, around the critical section at the onset of yielding ($M=4.1796\times10^5$ lb-in. ; $\theta=7.2001\times10^{-3}$ radians). The magnitude of axial stress, at mid-wall, is highest at the crowns and null at the intrados and extrados, and the stress is compressive at one crown and tensile at the other. This agrees to a great extent with the distribution that would be predicted by the simple beam bending theory, especially since the value of end-rotation is small at start of yielding, and since the critical section is very close to the loaded end, at which loading is almost in pure bending.

From the same figure, it can also be seen that the maximum value of tensile axial stress belongs to a point on the outside surface close to the left crown (point 16), and the maximum compressive stress occurs at a point close to the right crown (point 6), also on the outer side of the wall. The stress value is null at the intrados and the extrados at both the inside and the outside of the pipe wall.

Figure 3.5.32 shows the distribution, around the critical section, of the corresponding (axial) strain, also at start of yielding. The maximum compressive strain is on the outside surface at point 8, and the maximum tensile strain is on the outside surface at point 14. As expected, all axial strains have a zero value at the intrados and the extrados.

From Fig. 3.5.33, which shows the distribution of hoop stress around the section, it can be seen that the maximum value of compressive stress was at point 9, on the inside surface; and the maximum tensile stress was at point 13, also on the inner side of the pipe wall. Again, all values of stress were null at the intrados and extrados. It must be noted that this stress distribution could not be predicted by the simple beam bending theory, since these stresses are induced by the ovalization of the cross-section. It is also important to note that the hoop stresses are much greater than the axial stresses shown in Fig. 3.5.31.

The distribution of hoop strain, is shown in Fig. 3.5.34. As expected, the maximum hoop strains, are on the inside surface, and are compressive at point 9, and tensile at point 13. It is noted that the distributions of axial and hoop stresses and strains for the case without internal pressure, at start of yielding are anti-symmetric with respect to the neutral axis; this neutral axis being the straight line that passes through the intrados and the extrados. For example, the values of hoop strain, on the inside surface, at points 10 and 12, are equal in magnitude but opposite in sign.

Due to this fact, it is clear that the distribution of Mises stress, shown in Fig. 3.5.35, is very close to being symmetric with respect to the same neutral axis. If examined closely however, slight deviations from symmetry can be detected. The maximum values of Mises stress occur between points 8 and 9, and between points 13 and 14.

From Fig. 3.5.36, it can be seen that during the same finite increment of the numerical technique used, yielding was initiated on the inside surface at points 9 and 13, and on the outside surface at points 8 and 14. The increment used being reasonably small, it can be said that these points started yielding almost simultaneously; however, it can safely be assumed that first yielding took place on the inside surface at point 9, since this is the point that has the highest value of plastic equivalent strain at this early stage.

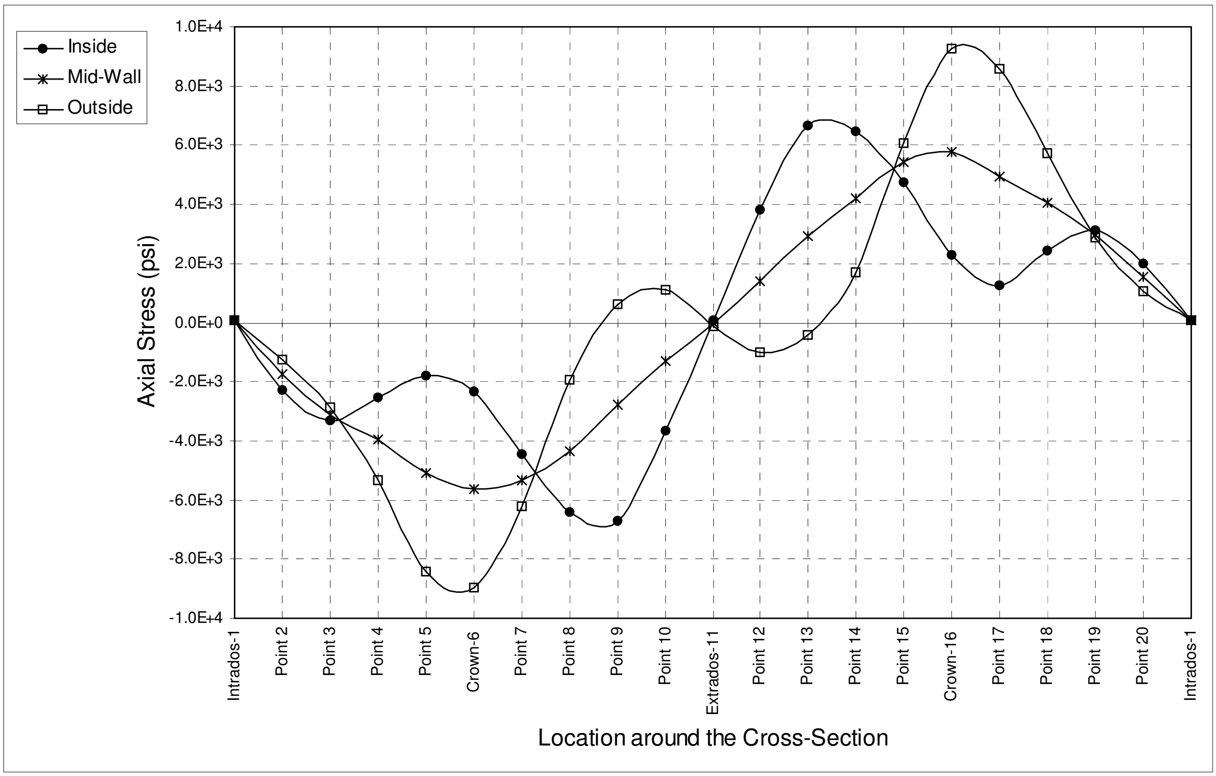

Fig. 3.5.31 Distribution of Axial Stress Around the Cross-Section at Start of Yielding - No Internal Pressure

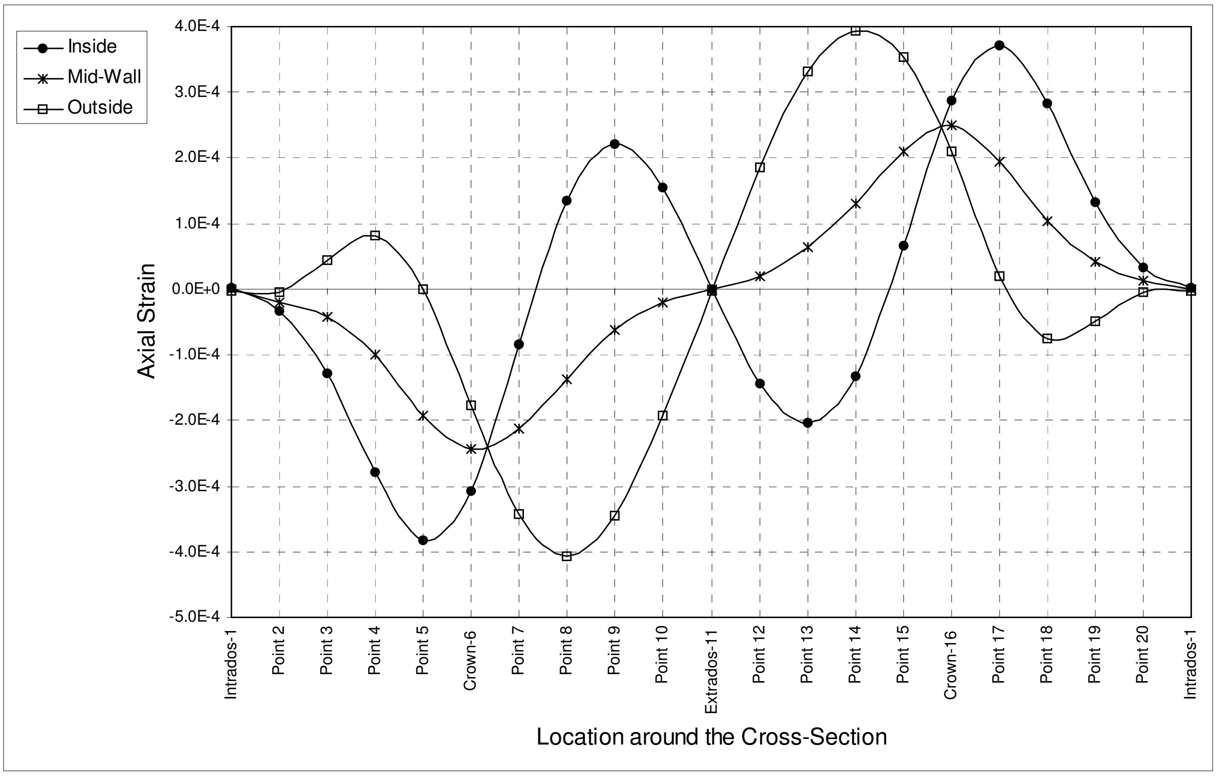

Fig. 3.5.32 Distribution of Axial Strain Around the Cross-Section at Start of Yielding - No Internal Pressure

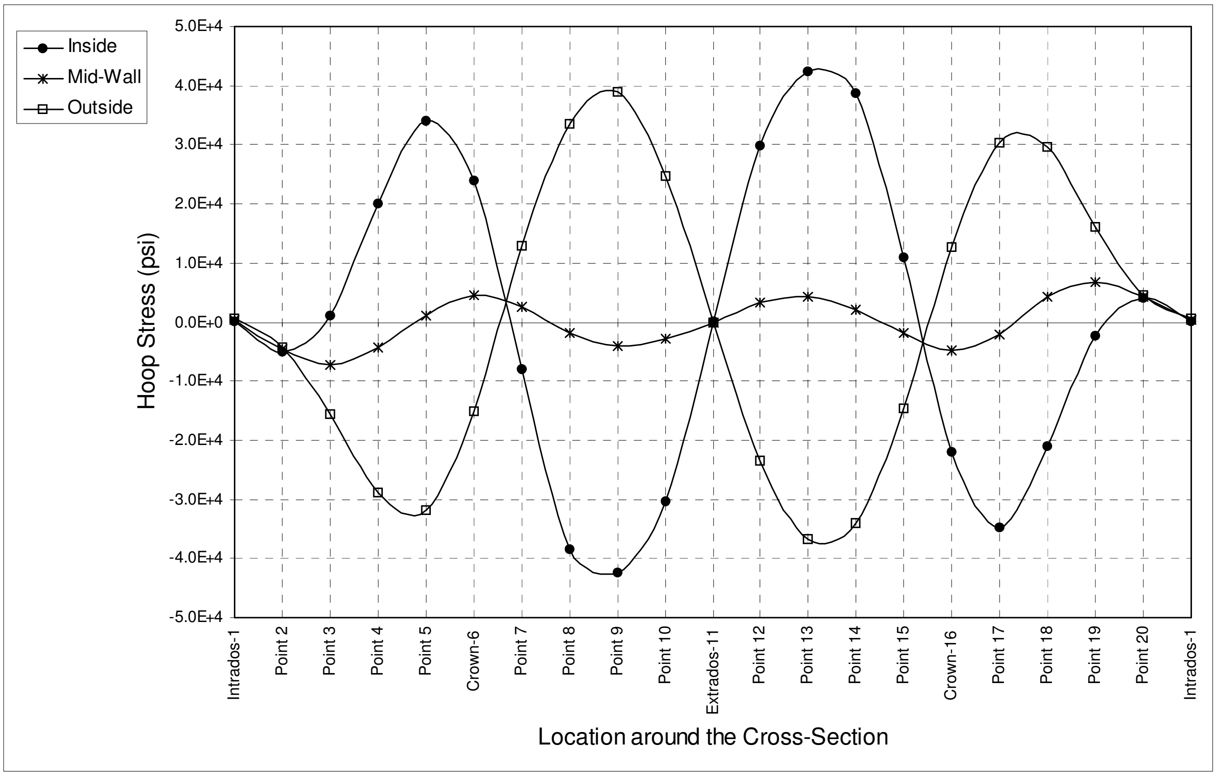

Fig. 3.5.33 Distribution of Hoop Stress Around the Cross-Section at Start of Yielding - No Internal Pressure

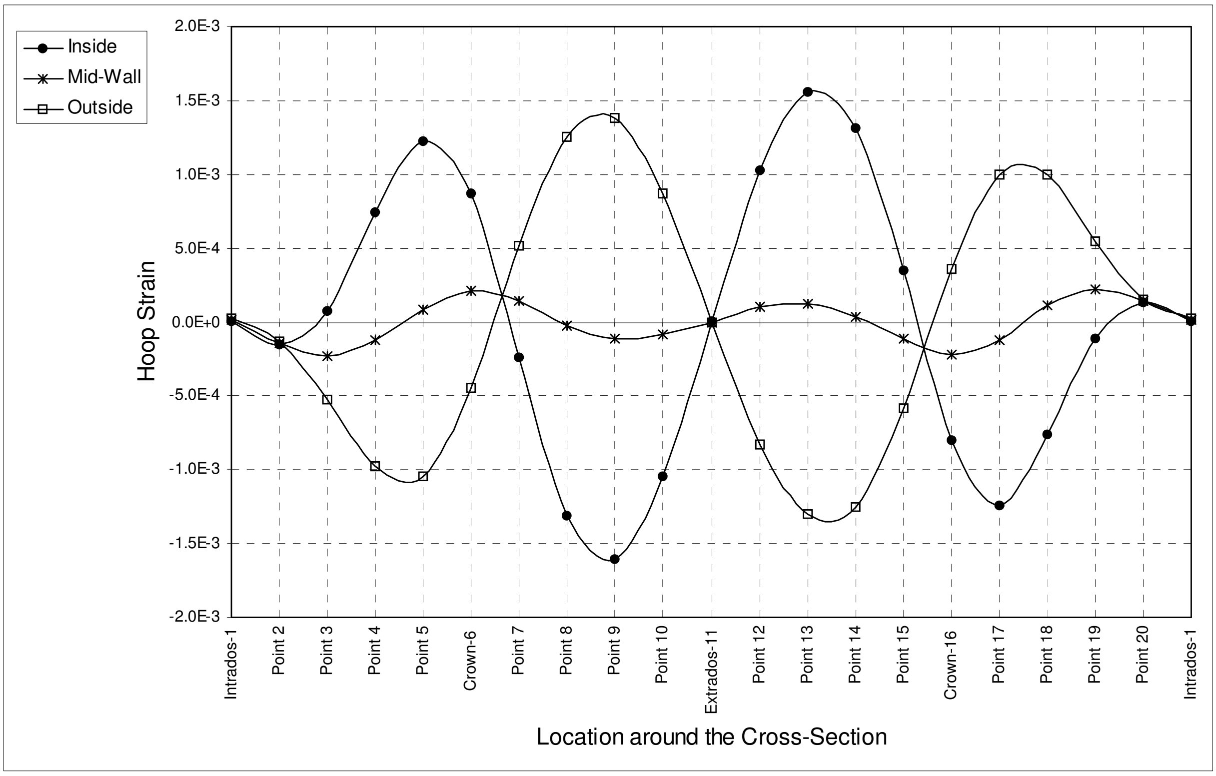

Fig. 3.5.34 Distribution of Hoop Strain Around the Cross-Section at Start of Yielding - No Internal Pressure

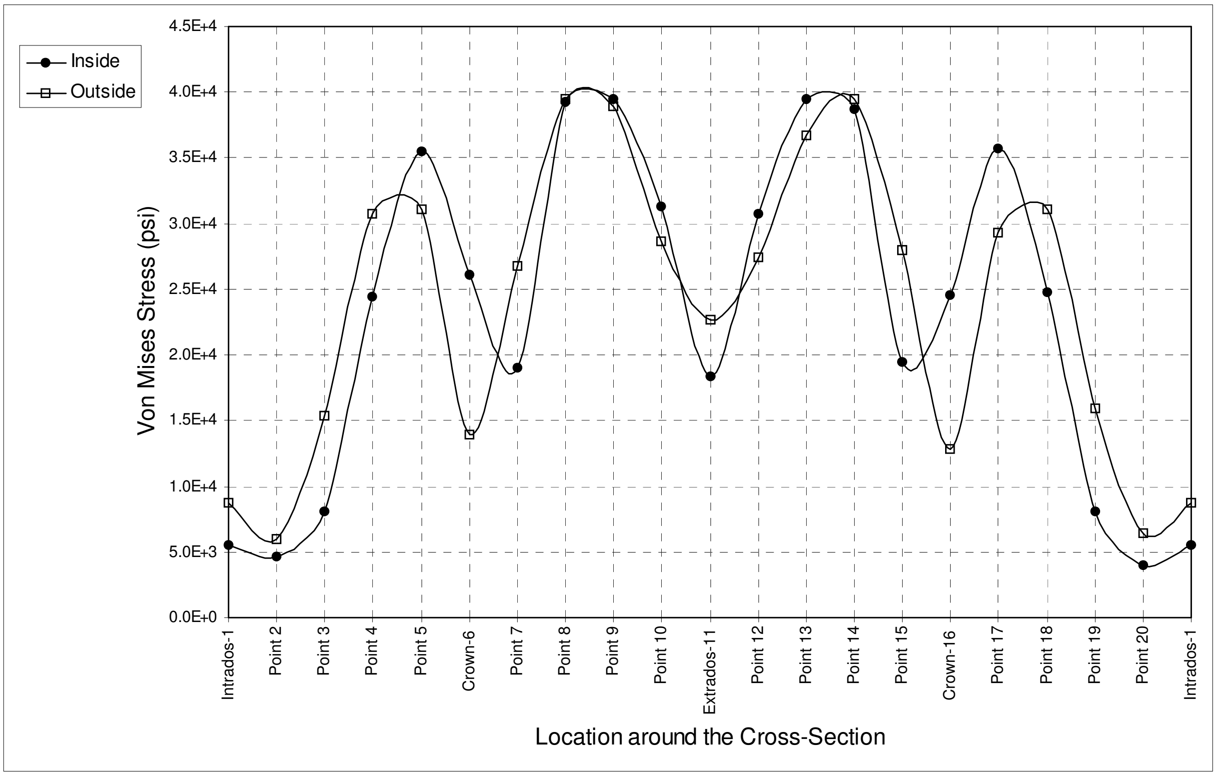

Fig. 3.5.35 Distribution of Mises Stress Around the Cross-Section at Start of Yielding - No Internal Pressure

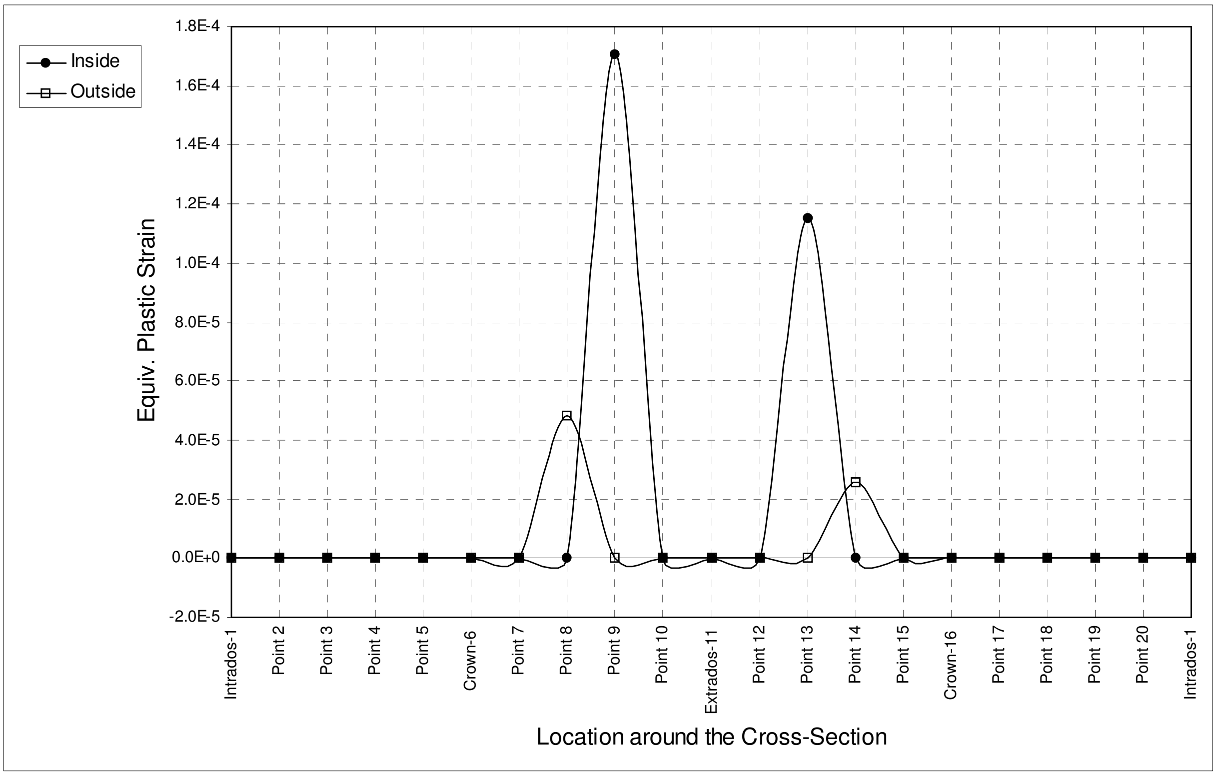

Fig. 3.5.36 Distribution of Equivalent Plastic Strain Around the Cross-Section at Start of Yielding - No Internal Pressure

3.5.4.1.b Instability

Figure 3.5.37 shows the distribution of axial strain around the critical cross-section, at the instant where the elbow reaches instability (M=1.1089×10^6 lb-in. ; θ=6.6651×10^{-2} radians). The maximum strain at this load level is compressive, and takes place on the outside surface near point 8. The highest strain on the inside surface is also compressive, and exists close to point 5. The strain values here are an order of magnitude higher than those at start of yielding.

It is also noted that the distribution is similar, to some extent, to the axial strain distribution at start of yielding, but of course the effect of geometric nonlinearity is more pronounced at instability. Therefore, the strain values at the intrados and extrados are no longer at zero level. Moreover, the anti-symmetry that existed at start of yielding is not complete here. For example, on the outer surface, points 8 and 14, which are symmetrically located with respect to the axis passing through the extrados and intrados, do have local maximum values of strain of opposite sign; however, the values are far from being equal in magnitude.

Figure 3.5.38 shows the distribution of hoop strain, around the cross-section, at instability. The inside surface at point 9 still has the maximum compressive hoop strain, and the maximum tensile strain remains on the inside surface at point 13, like they were at start of yielding. The values of strain however, are an order of magnitude greater than they were at the onset of yielding.

Figure 3.5.39 shows the distribution of equivalent plastic strain around the cross-section. By comparing this distribution to the one at start of yielding, shown in Fig. 3.5.36, it can be seen that points 9 and 13 still hold the maximum values of strain, on the inside wall. On the outside wall, however, the maximum value shifted from point 8 to point 9, and a local maximum appeared at point 5 with a higher strain value than the expected local maximum which exists at point 14.

Furthermore, by comparing Figs. 3.5.39 and 3.5.35, some resemblance is detected between the distribution of equivalent plastic strain at instability and the distribution of Mises stress at start of yielding.

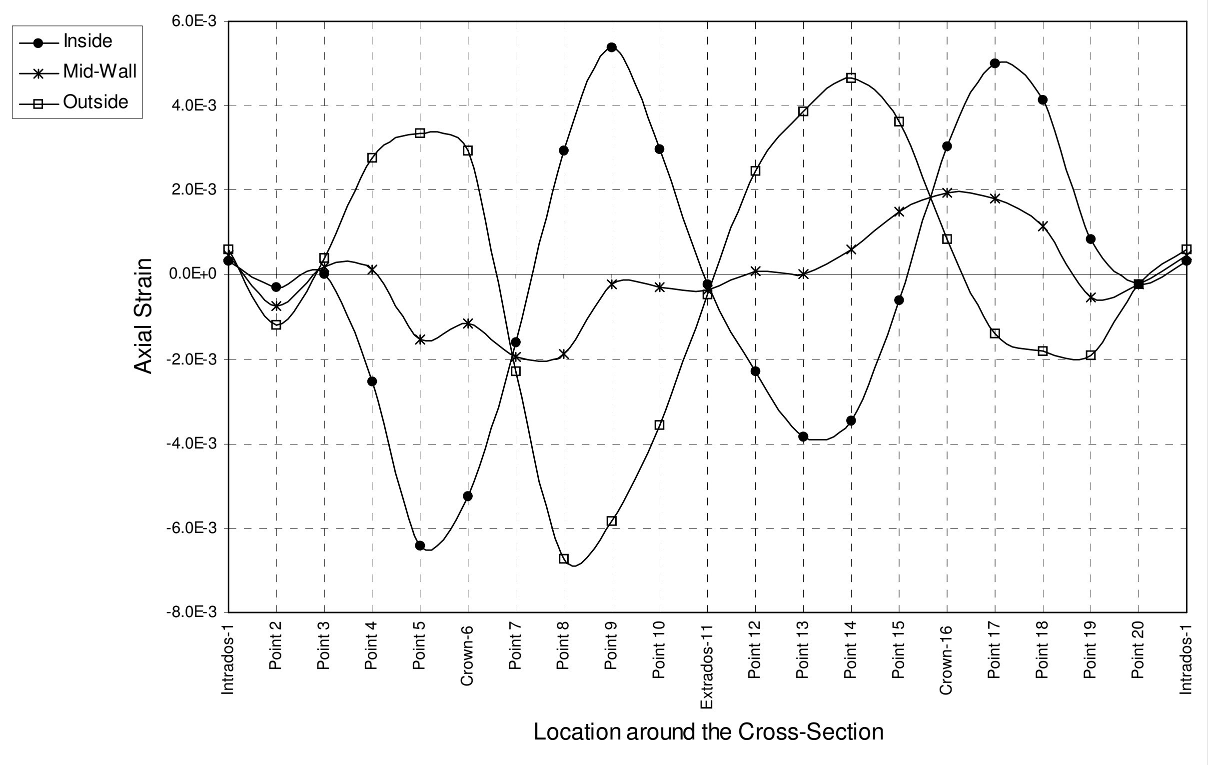

Fig. 3.5.37 Distribution of Axial Strain Around the Cross-Section at Instability - No Internal Pressure

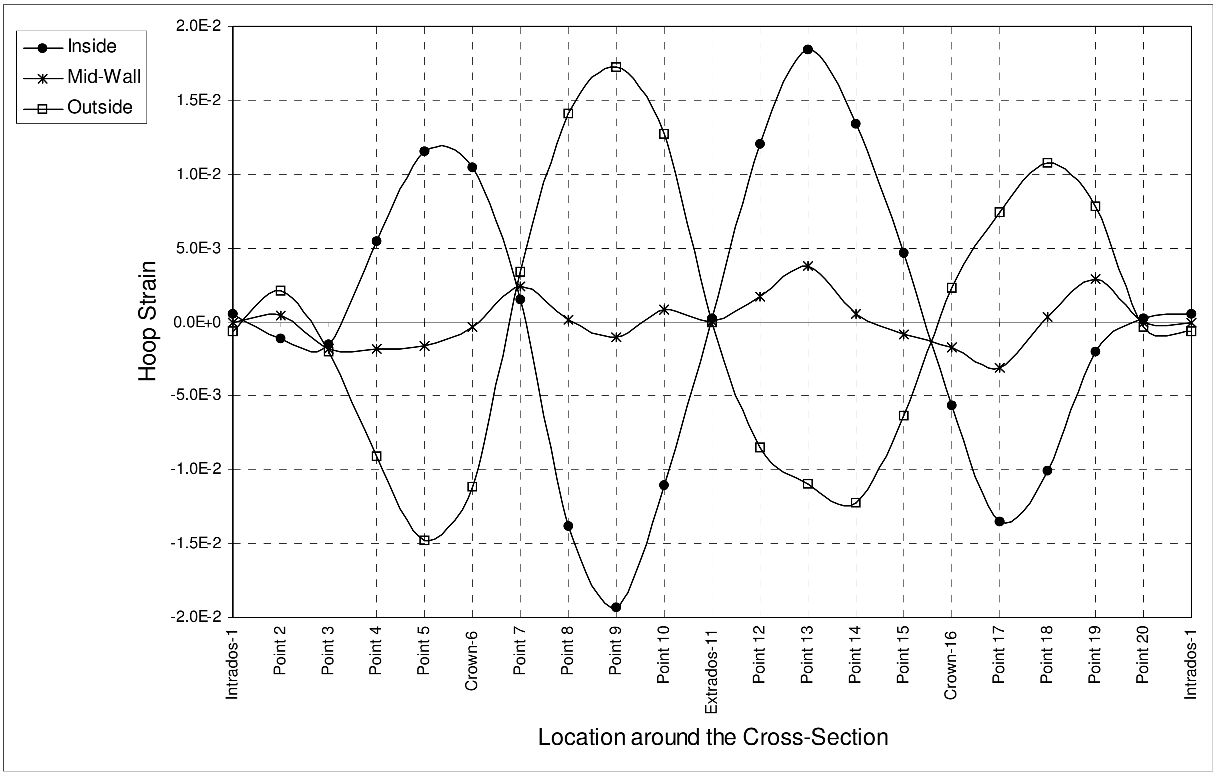

Fig. 3.5.38 Distribution of Hoop Strain Around the Cross-Section at Instability - No Internal Pressure

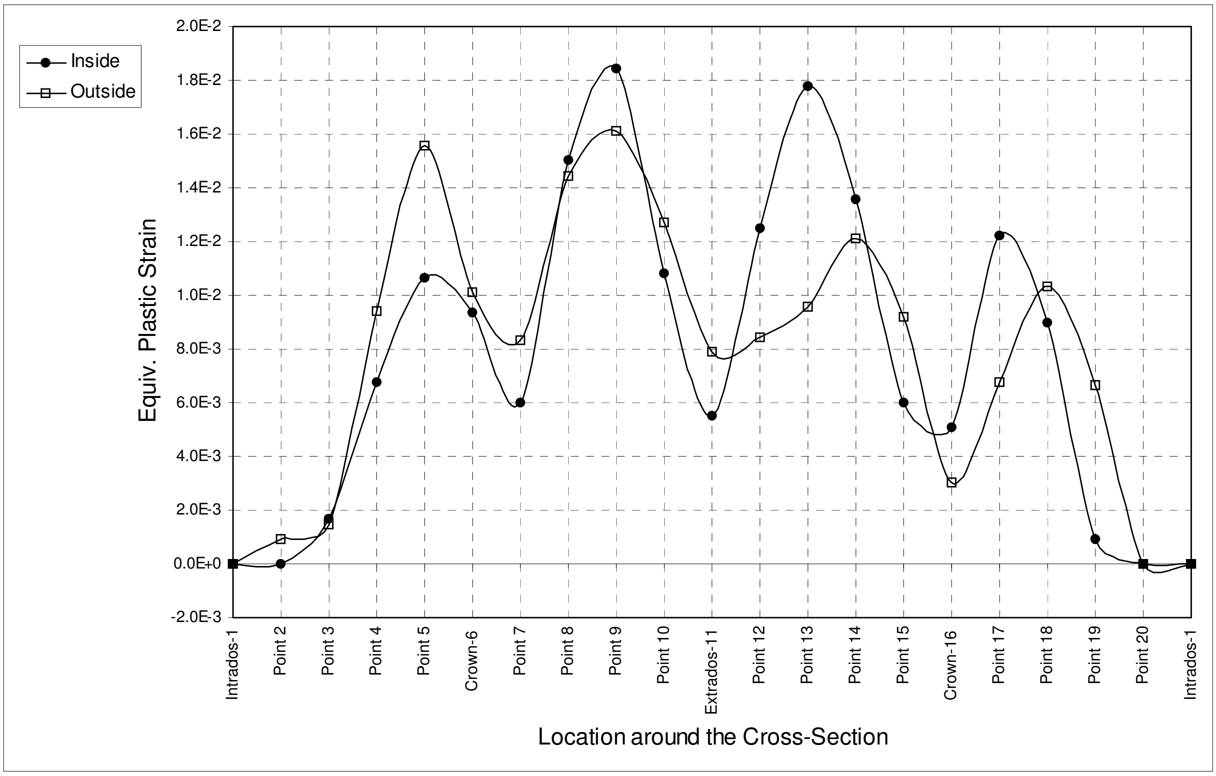

Fig. 3.5.39 Distribution of Equivalent Plastic Strain Around the Cross-Section at Instability - No Internal Pressure

3.5.4.2 Case with Internal Pressure of 1200 psi

3.5.4.2.a Start of Yielding

The distribution of axial stress around the critical section, at the onset of yielding ($M=4.7535\times10^5$ lb-in. ; $\theta=5.4008\times10^{-3}$ radians) is presented in Fig. 3.5.40. It can be seen that there is a close similarity between this case, and the case without internal pressure, shown in Fig. 3.5.31; the main difference being a superimposed tensile stress at all points of the section, mainly due to internal pressure. Therefore, all values of axial stress are positive (tensile) and as expected, the maximum value remains on the outer side of the pipe wall, at the left crown (point 16), and the minimum value remains on the outer side of the wall, at the right crown (point 6).

The same kind of similarity exists between the distribution of axial strain for this case, shown in Fig. 3.5.41, and the distribution of axial strain for the case without internal pressure that was shown in Fig. 3.5.32. However, the increase in strain, due to internal pressure, is not uniformly distributed on all points, as is obvious from the inequality of the values of strain at the intrados and extrados. The maximum tensile strain remains at point 14, on the outer surface; however, the maximum compressive strain is on the inner side of the pipe wall, at point 5, instead of the outer side at point 8.

Figure 3.5.42 shows the hoop stress distribution around the section. The maximum tensile stress is at point 13, on the inner surface of the pipe wall, and the maximum compressive stress exists at point 9, also on the inside surface. By comparing this figure to Fig. 3.5.33, which shows the hoop stress distribution for the case with no internal pressure, it can be seen that the two distributions are very similar and that the main difference is the superimposed tensile stress induced by the pressure. The same can be said about the corresponding hoop strain distribution, presented in Fig. 3.5.43, when compared to the strain distribution of the case without pressure.

The discussion above, and Figs. 3.5.40 through 3.5.43, suggest that internal pressure induces a nearly uniform distribution of axial and hoop stresses. It also suggests that under the sole effect of internal pressure, the region near the intrados, should have lower axial strain, and higher hoop stress and hoop strain, compared to the remaining regions of the cross-section. This is in complete agreement with what has been indicated in the literature (Shalaby, 1996) and confirmed by experimental investigation (Makhutov et al, 1991).

Figure 3.5.44 shows the Mises stress distribution, and Fig. 3.5.45 shows the equivalent plastic strain distribution around the section. From both of these figures, it can be seen that the first six points to yield, actually started yielding during the same numerical increment. These are points 5, 13 and 14 on the inside surface, and points 8, 9 and 18 on the outside surface; and although these points started to yield almost simultaneously, Fig. 3.5.45 shows that the inside surface at point 13 is where yield was initiated.

3.5.4.2.b Instability

Figure 3.5.46 shows the distribution of axial strain, around the cross-section, at instability (M= 2.7175×10^{6} lb-in. ; θ= 9.5496×10^{-2} radians). The maximum tensile strain is located on the outside wall at the left crown (point 16), and the maximum compressive strain is on the inside surface at point 4. From this figure, it is seen that at this value of the moment load, bending has more effect than pressure, since the first half of the cross-section is under compression, and the second half is clearly under tension.

By comparing Figs. 3.4.47 and 3.4.38, it can be seen that the distribution of hoop strain is shifted towards the tensile side of the scale, under the influence of internal pressure effects. Of course, there are major differences between both distributions besides this shift, because the stiffening effect of pressure lets instability occur at different values of out-of-plane moment and end-rotation, and thereby lets the section ovalize differently.

Similarly, the distribution of equivalent plastic strain in this case, shown in Fig. 3.5.48, is fundamentally different from the one belonging to the case without pressure, shown in Fig. 3.5.39. The maximum strain here, occurs on the inside wall at point 4, and its value is comparable to the maximum value of strain, which occurs on the inside wall at point 9, in the case where no pressure is applied.

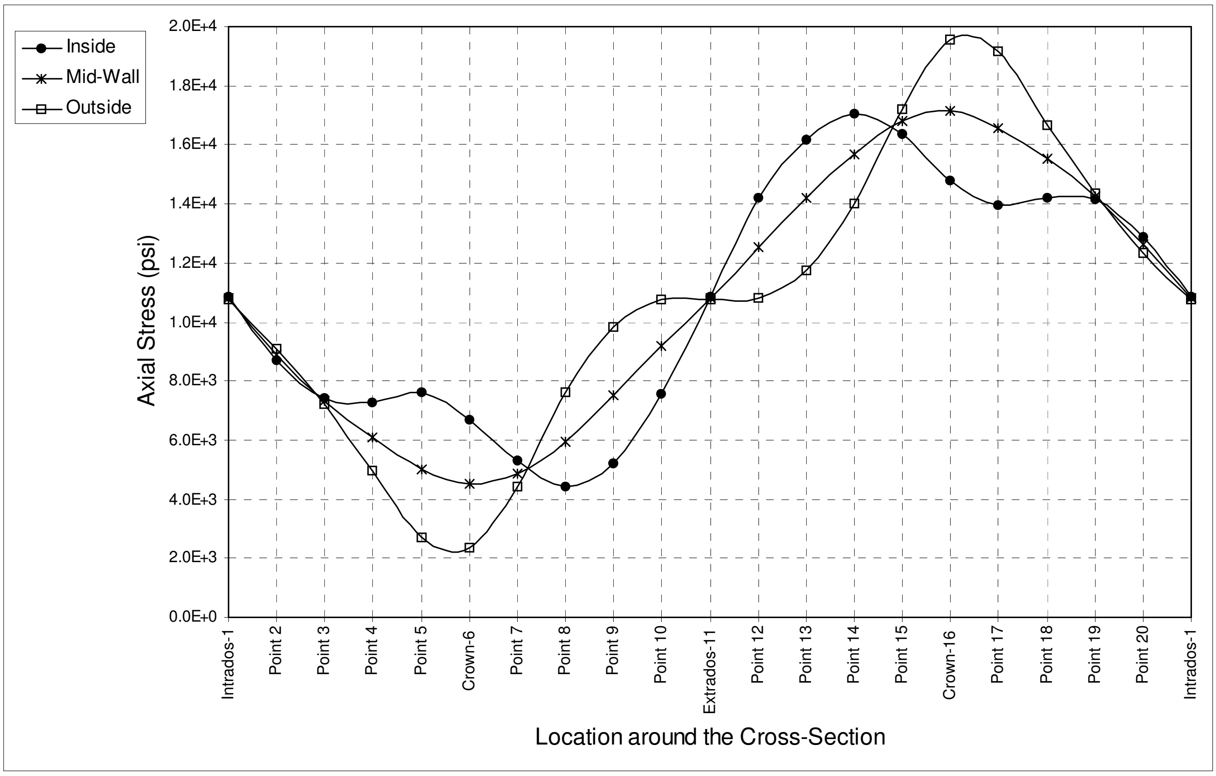

Fig. 3.5.40 Distribution of Axial Stress Around the Cross-Section at Start of Yielding - Internal Pressure: 1200 psi

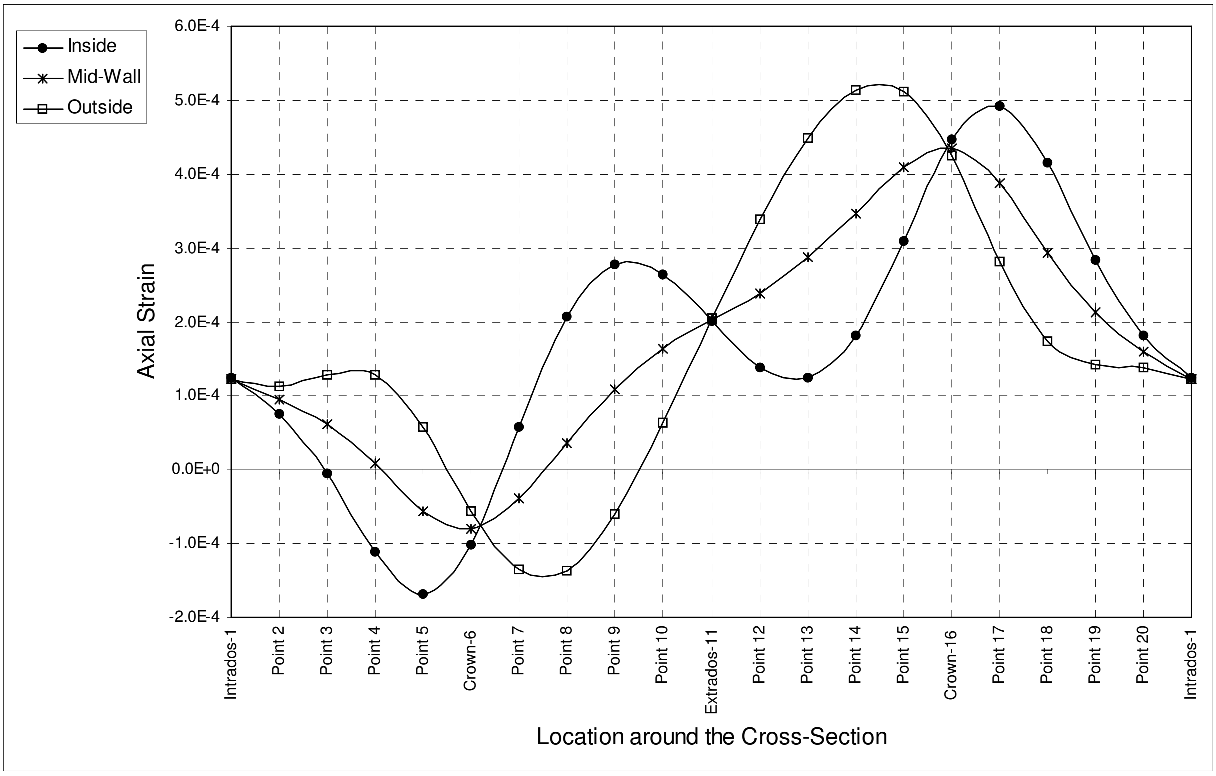

Fig. 3.5.41 Distribution of Axial Strain Around the Cross-Section at Start of Yielding - Internal Pressure: 1200 psi

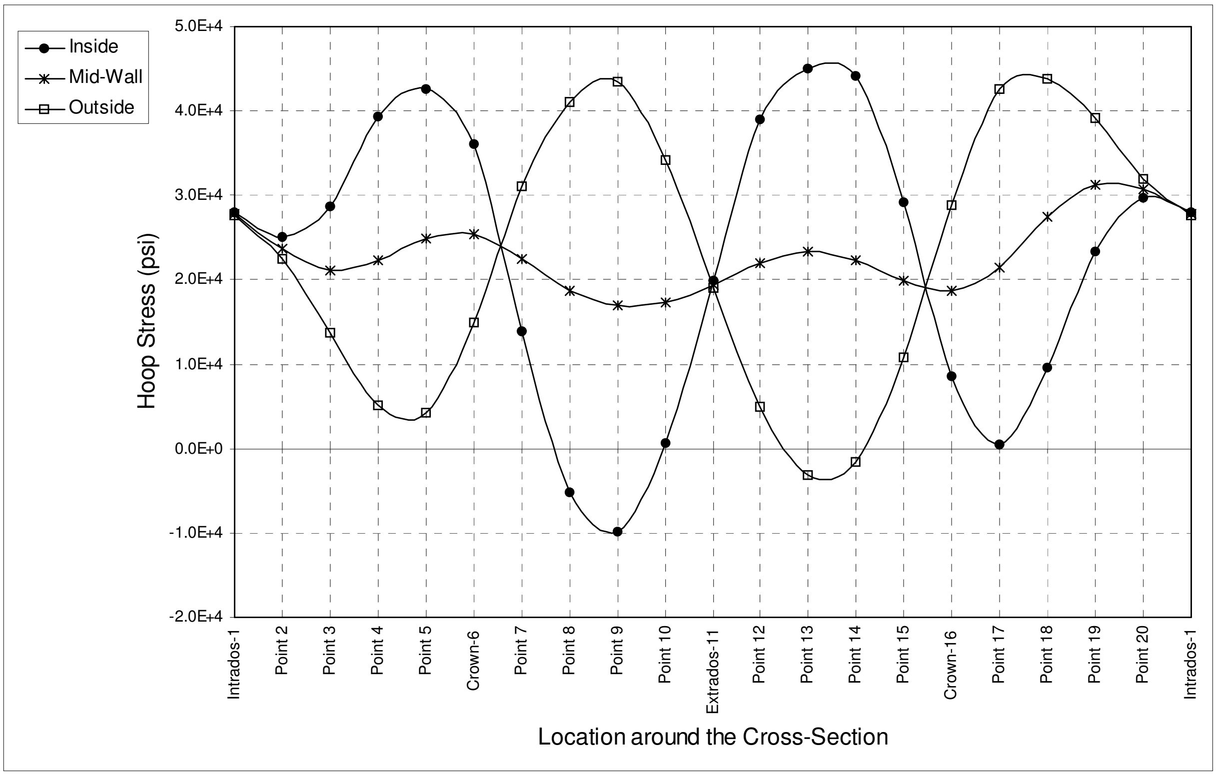

Fig. 3.5.42 Distribution of Hoop Stress Around the Cross-Section at Start of Yielding - Internal Pressure: 1200 psi

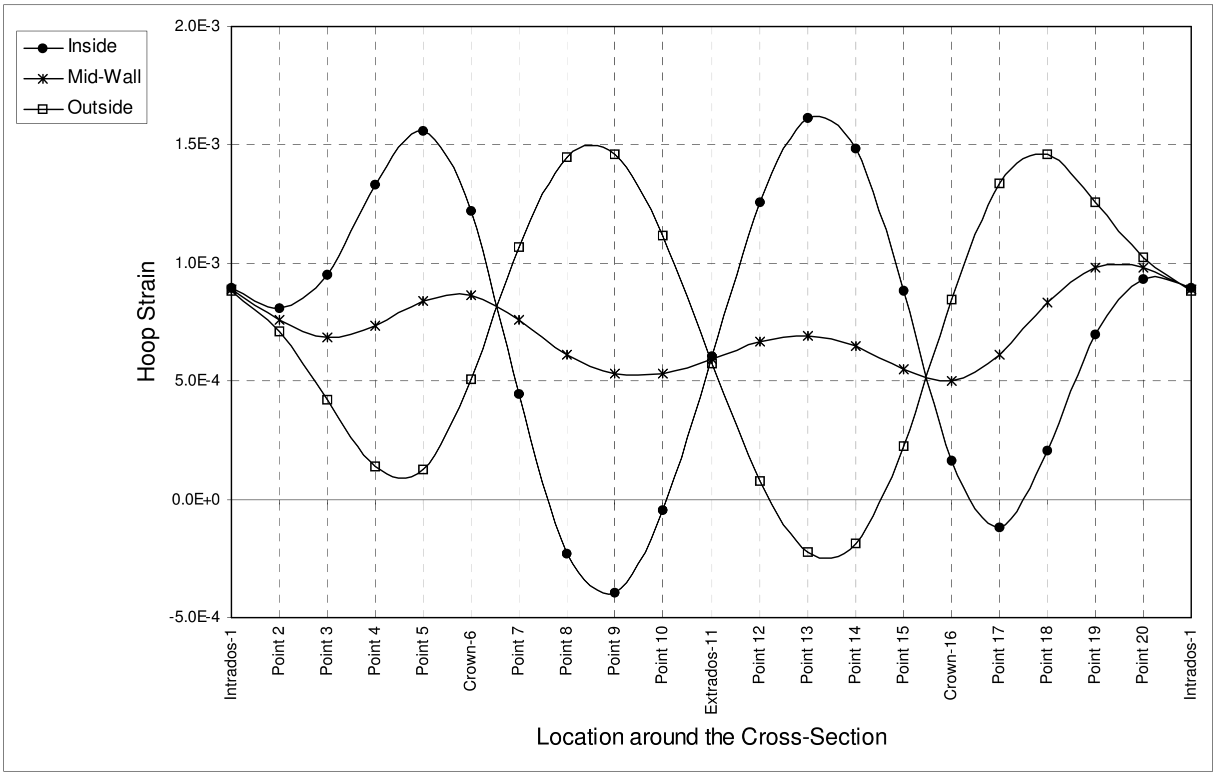

Fig. 3.5.43 Distribution of Hoop Strain Around the Cross-Section at Start of Yielding - Internal Pressure: 1200 psi

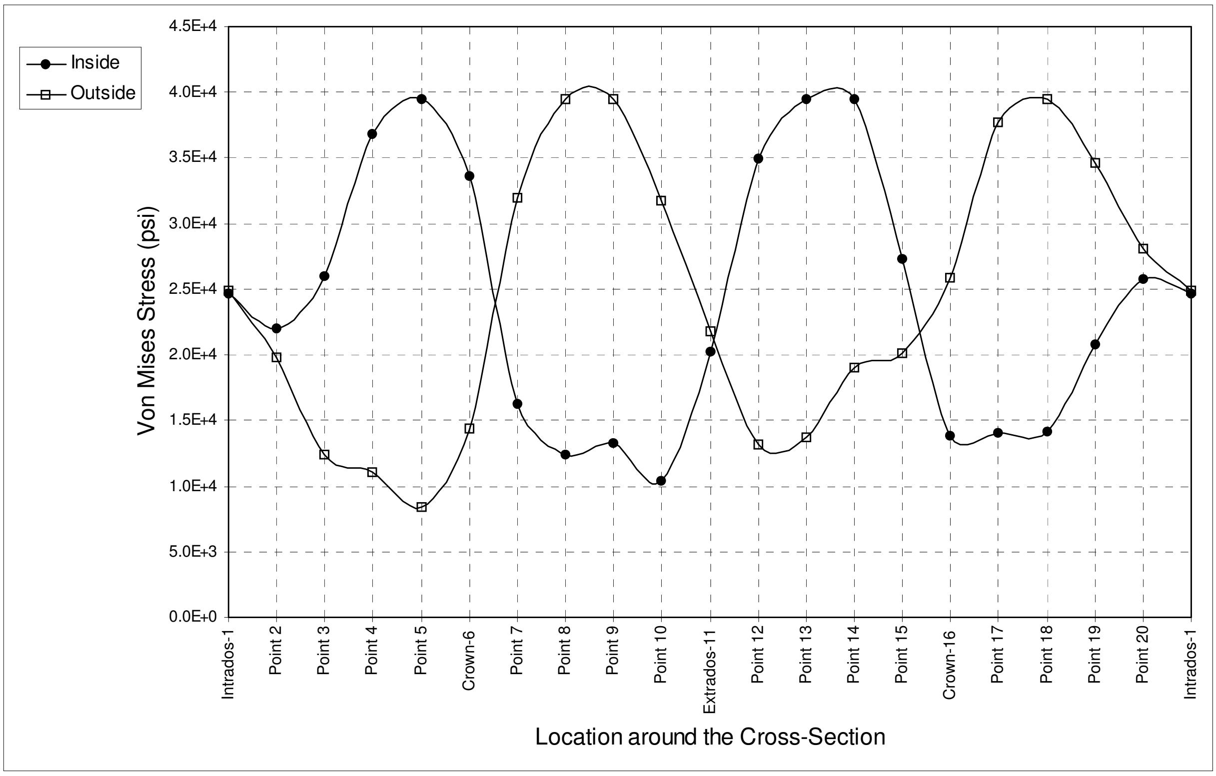

Fig. 3.5.44 Distribution of Mises Stress Around the Cross-Section at Start of Yielding - Internal Pressure: 1200 psi

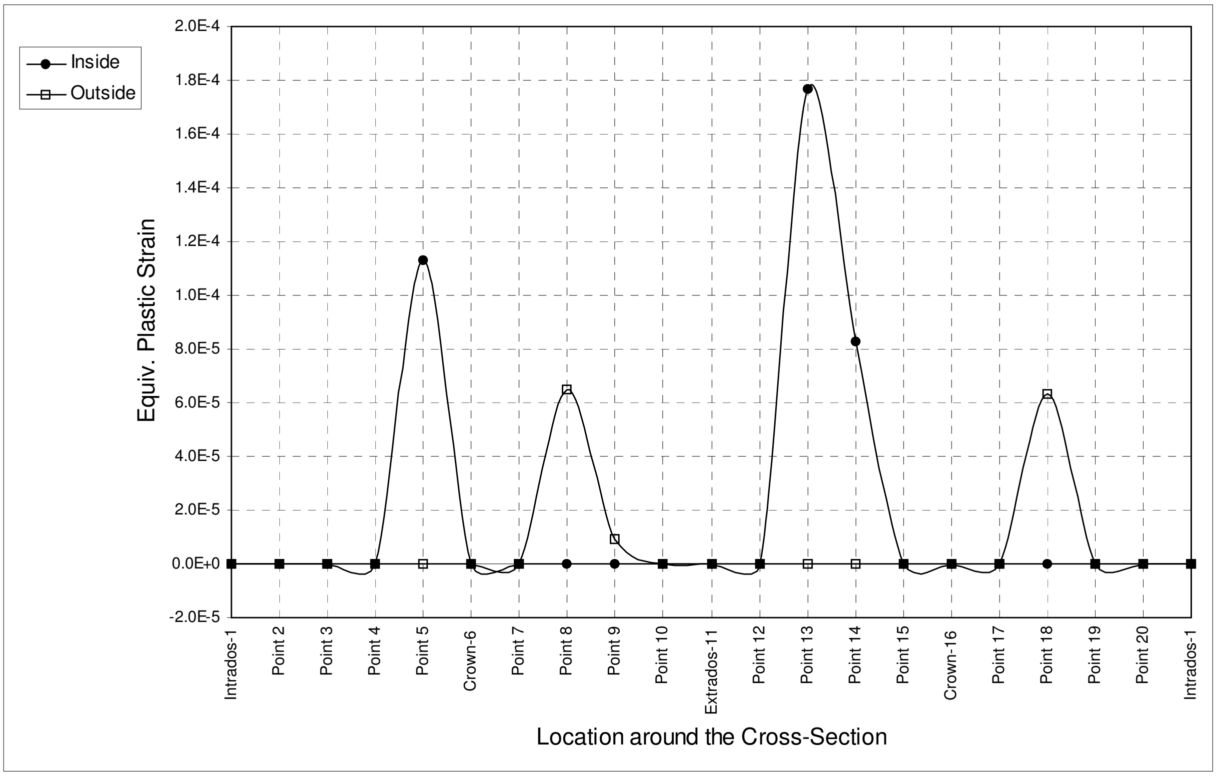

Fig. 3.5.45 Distribution of Equivalent Plastic Strain Around the Cross-Section at Start of Yielding - Internal Pressure: 1200 psi

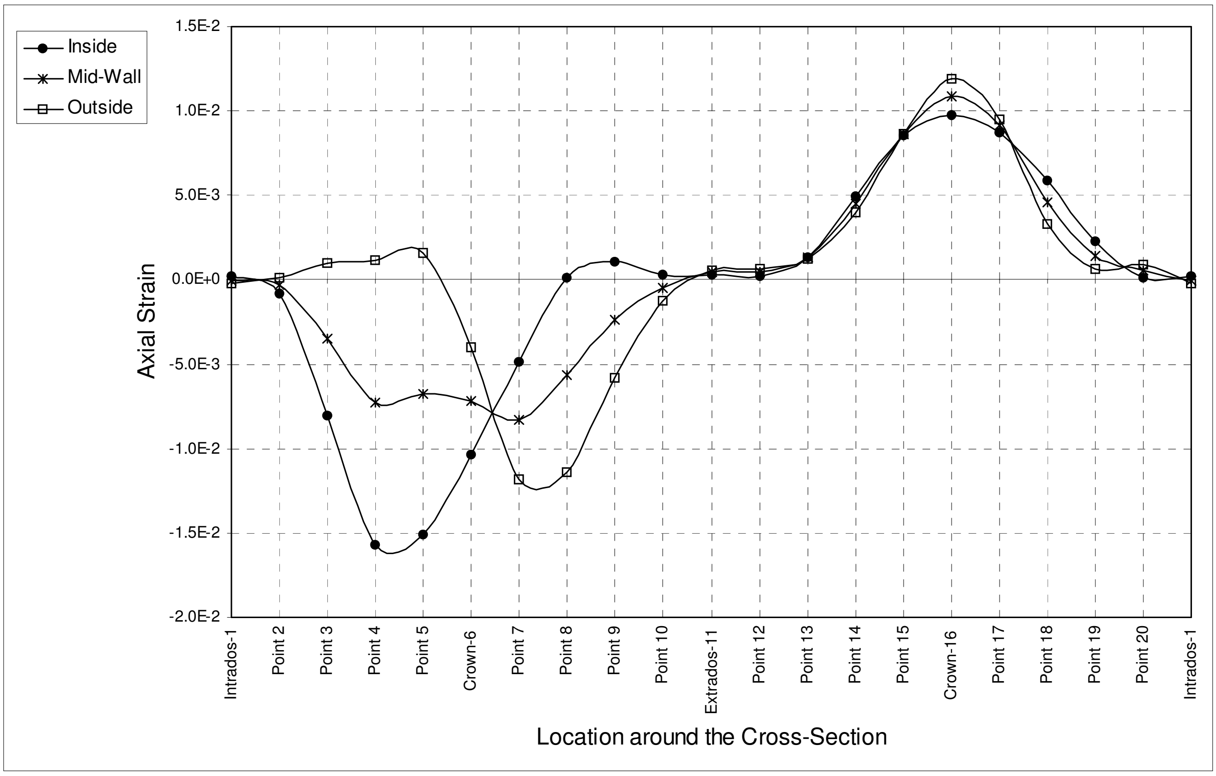

Fig. 3.5.46 **Distribution of Axial Strain Around the Cross-Section at Instability - Internal Pressure: 1200 psi**

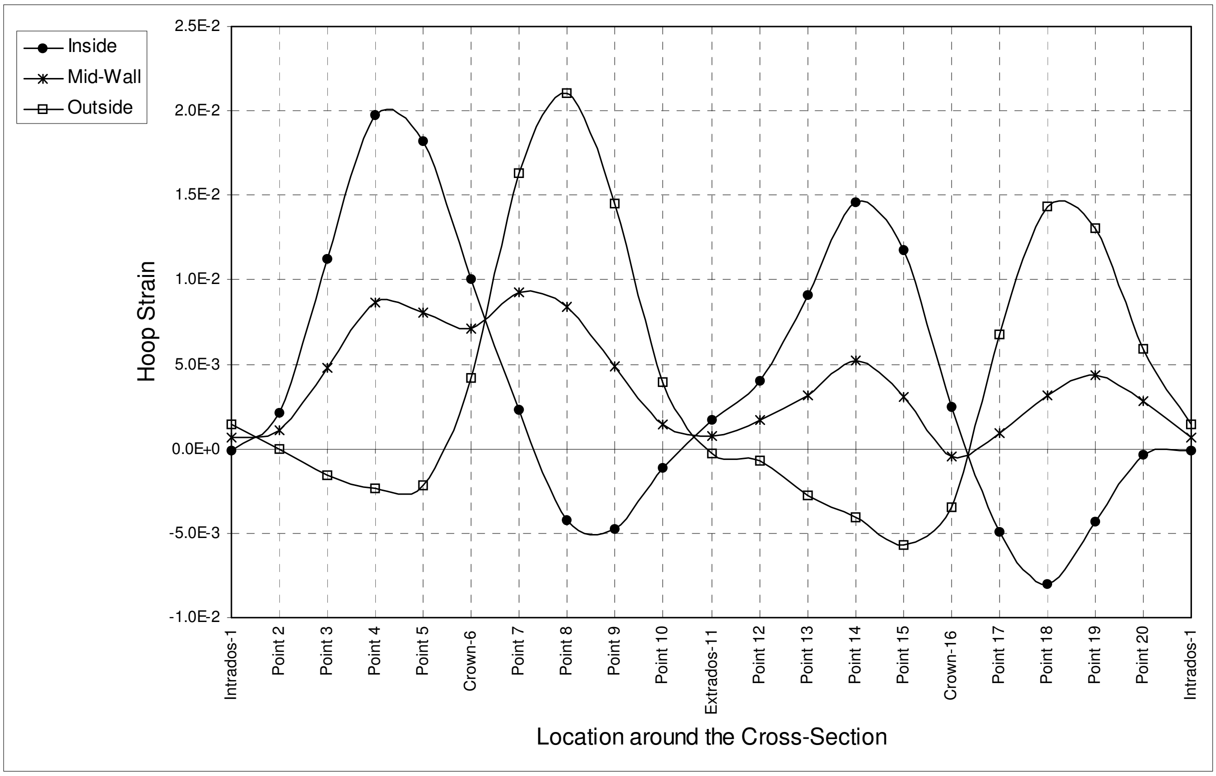

Fig. 3.5.47 **Distribution of Hoop Strain Around the Cross-Section at Instability - Internal Pressure: 1200 psi**

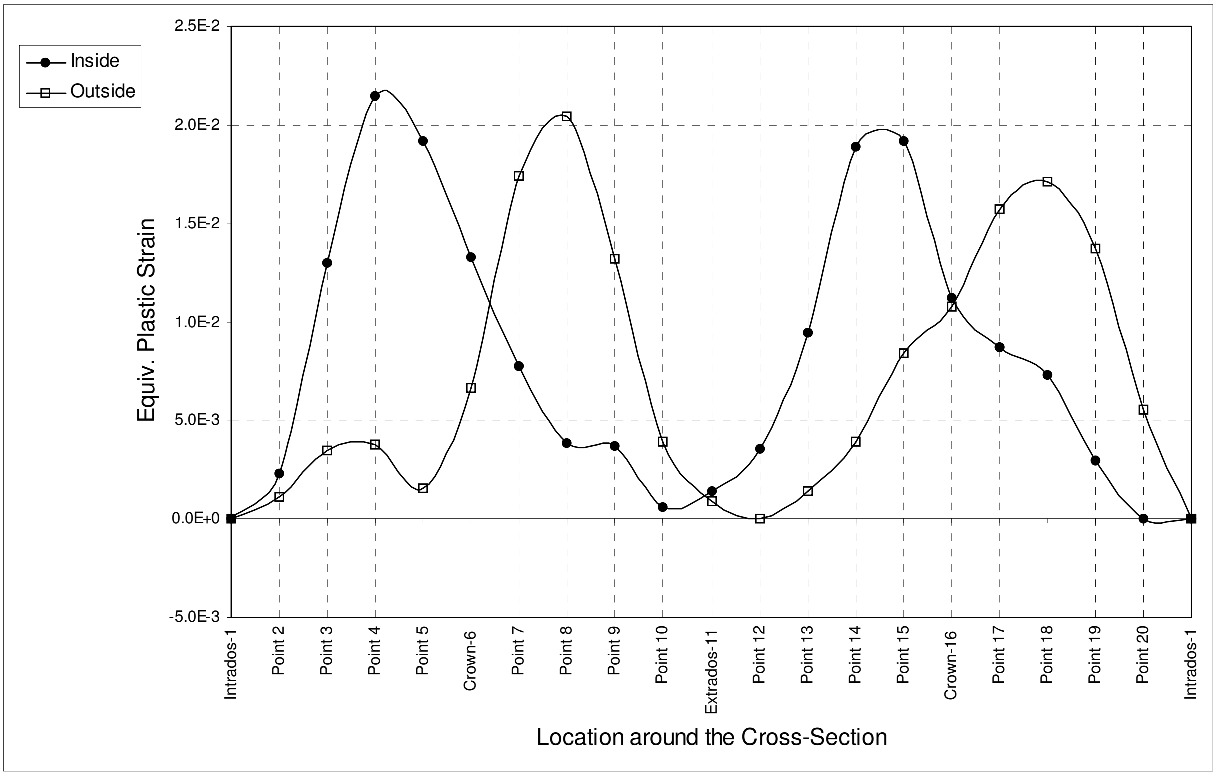

Fig. 3.5.48 Distribution of Equivalent Plastic Strain Around the Cross-Section at Instability - Internal Pressure: 1200 psi

3.5.4.3 Case with Internal Pressure of 2200 psi

3.5.4.3.a Start of Yielding

Figures. 3.5.49, 3.5.50, 3.5.51, 3.5.52, 3.5.53 and 3.5.54 present the distributions of axial stress, axial strain, hoop stress, hoop strain, Mises stress and equivalent plastic strain, respectively; after the first increment of moment loading has been applied (M= 1.0219×10^5 lb-in. ; θ= 3.1253×10^{-4} radians). This moment load is small, compared to the moment at which instability occurs, and can be considered negligible, especially since the pipe elbow studied here (h=0.1615) undergoes extensive plastification, even before any moment loading is applied, when subjected to a very high internal pressure of 2200 psi.

Therefore, at this load level, this case reduces to the case of a pipe bend under internal pressure loading only. Shalaby (1996) conducted a detailed study of the later case, for an elbow with the same bend factor, under approximately the same value of internal pressure, and the results presented herein are in very close agreement with his results.

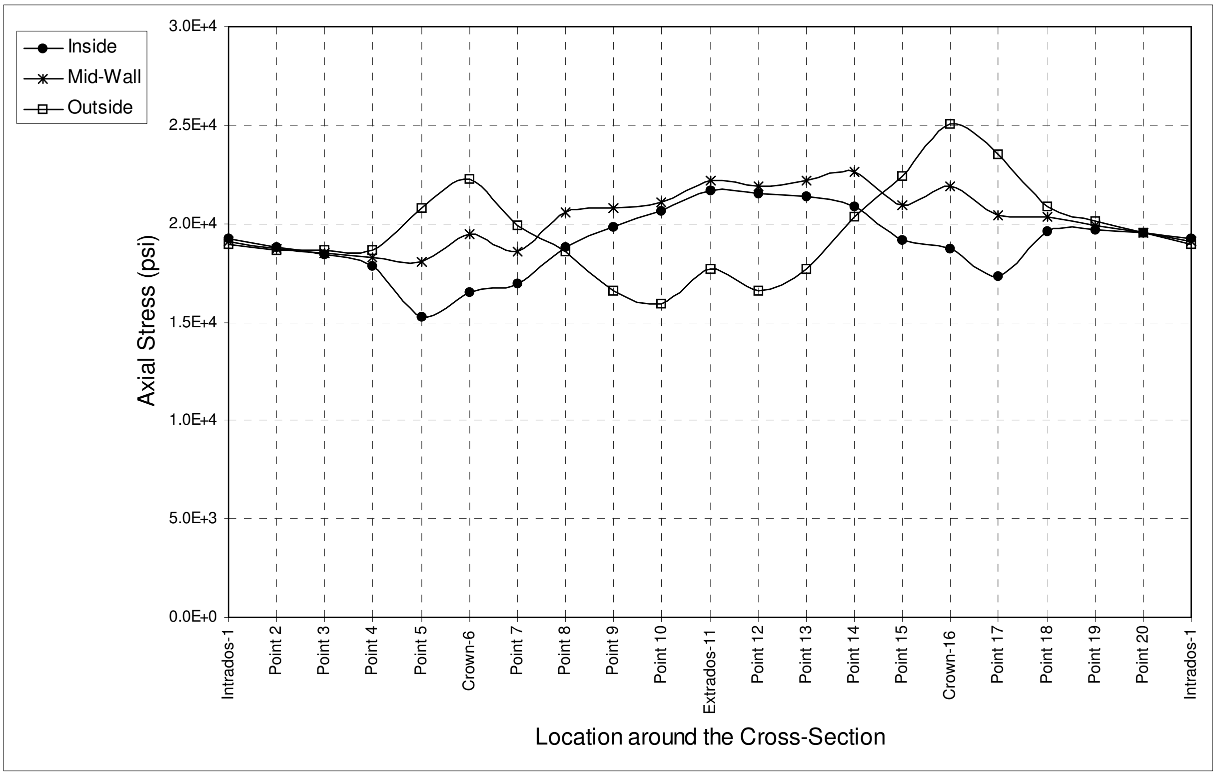

Fig. 3.5.49 Distribution of Axial Stress Around the Cross-Section at Start of Yielding - Internal Pressure: 2200 psi

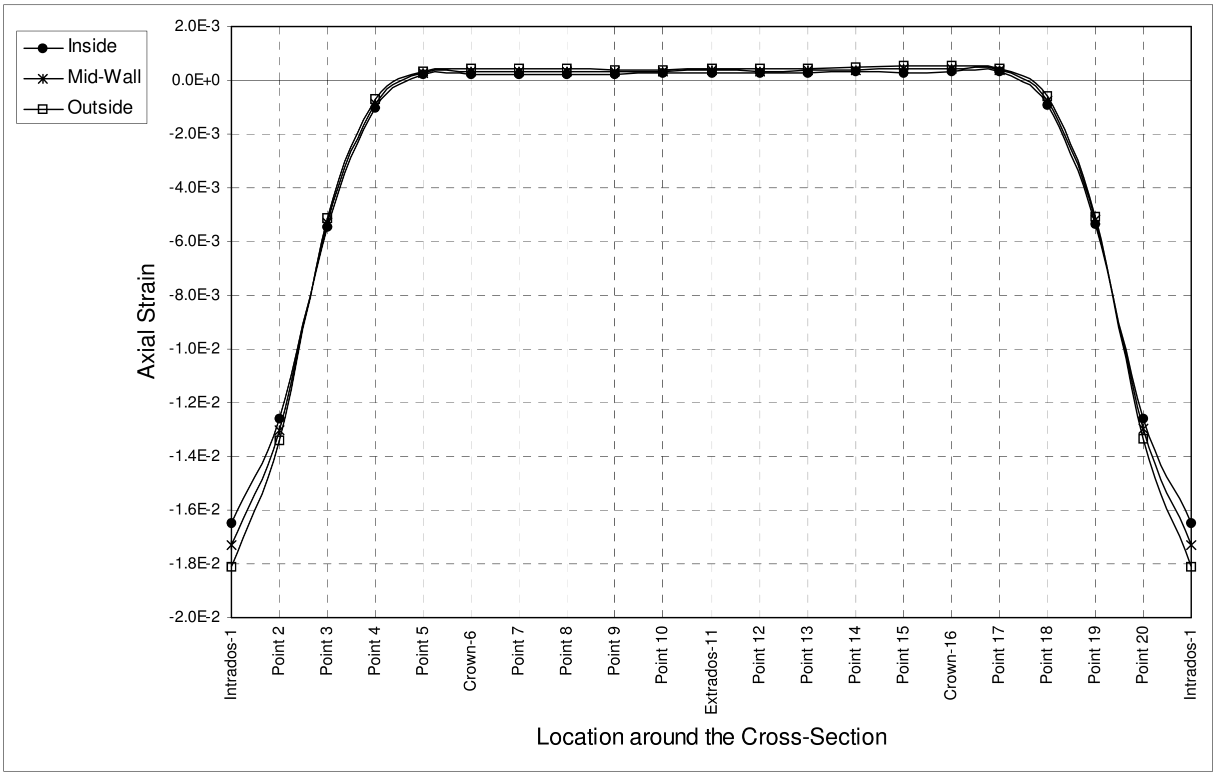

Fig. 3.5.50 Distribution of Axial Strain Around the Cross-Section at Start of Yielding - Internal Pressure: 2200 psi

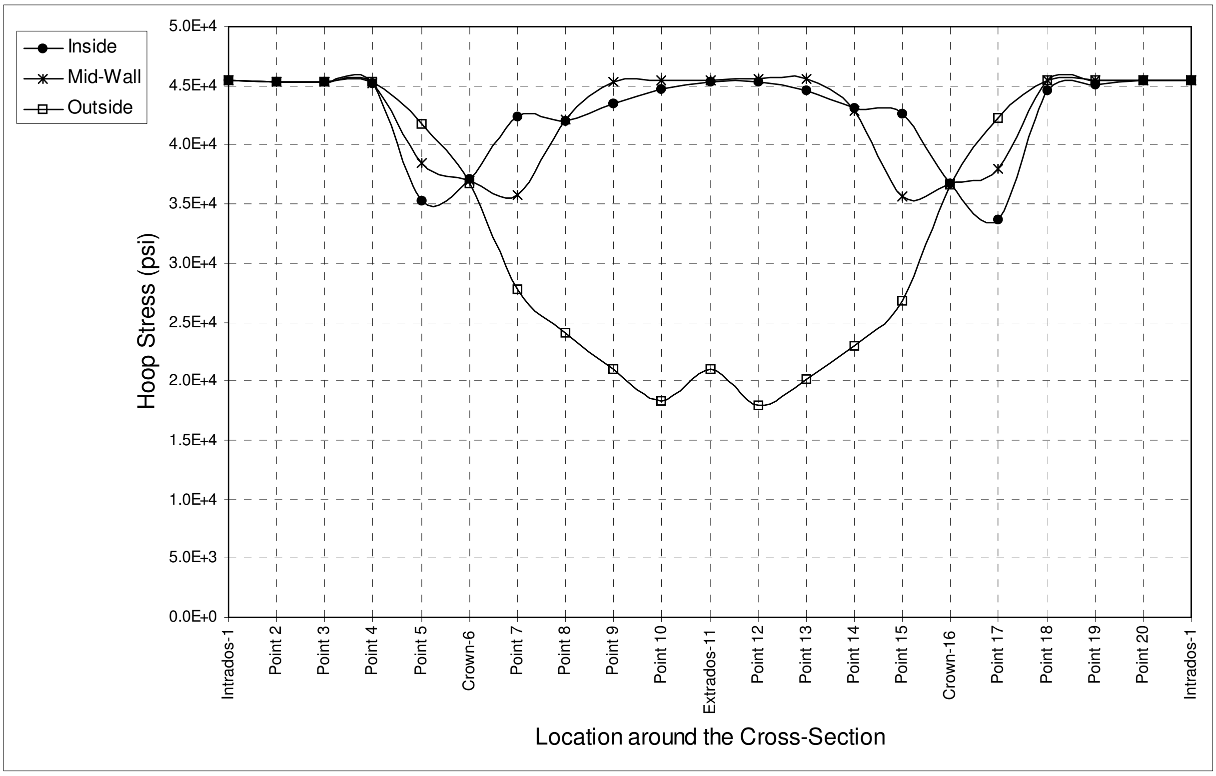

Fig. 3.5.51 Distribution of Hoop Stress Around the Cross-Section at Start of Yielding - Internal Pressure: 2200 psi

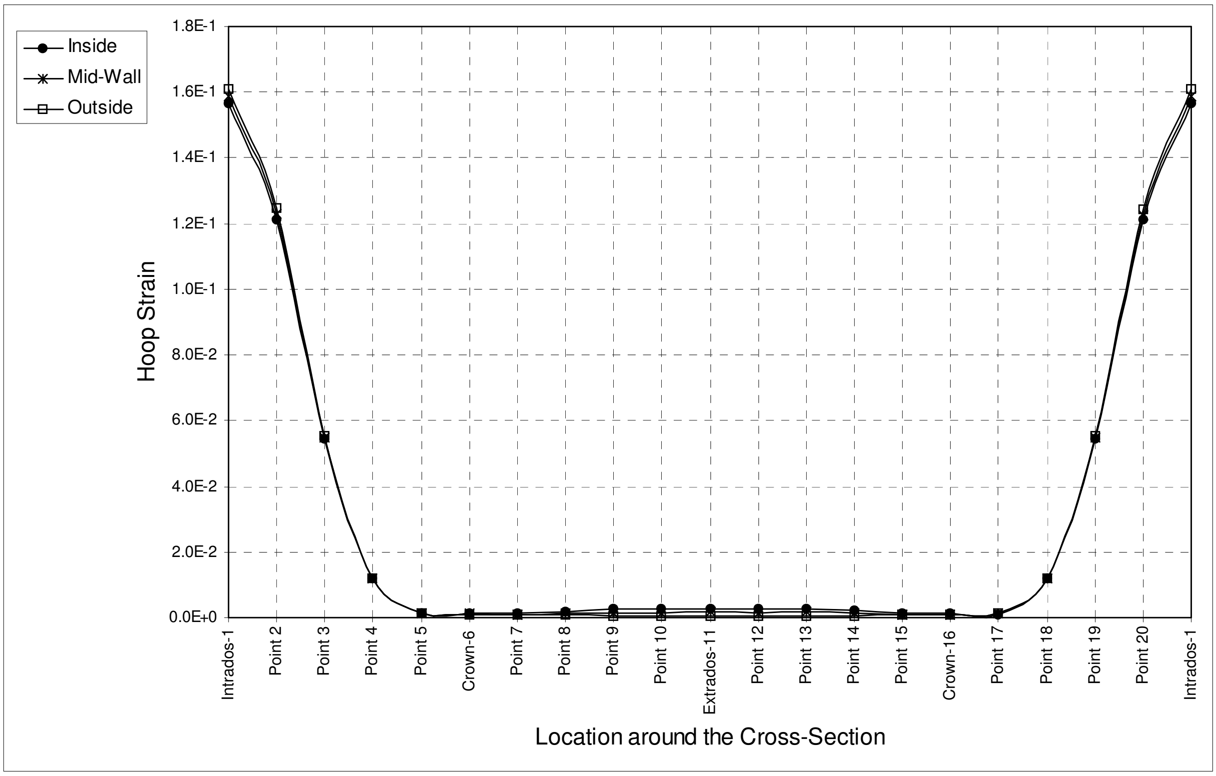

Fig. 3.5.52 Distribution of Hoop Strain Around the Cross-Section at Start of Yielding - Internal Pressure: 2200 psi

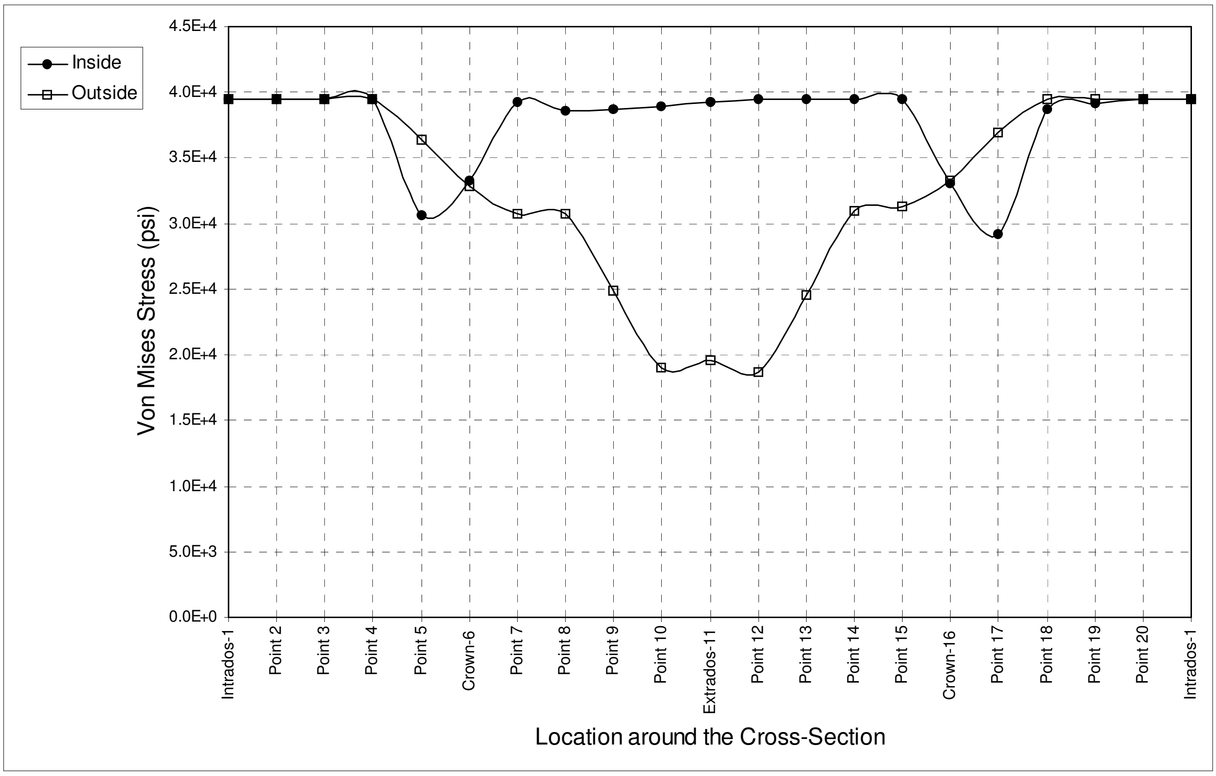

Fig. 3.5.53 **Distribution of Mises Stress Around the Cross-Section at Start of Yielding - Internal Pressure: 2200 psi**

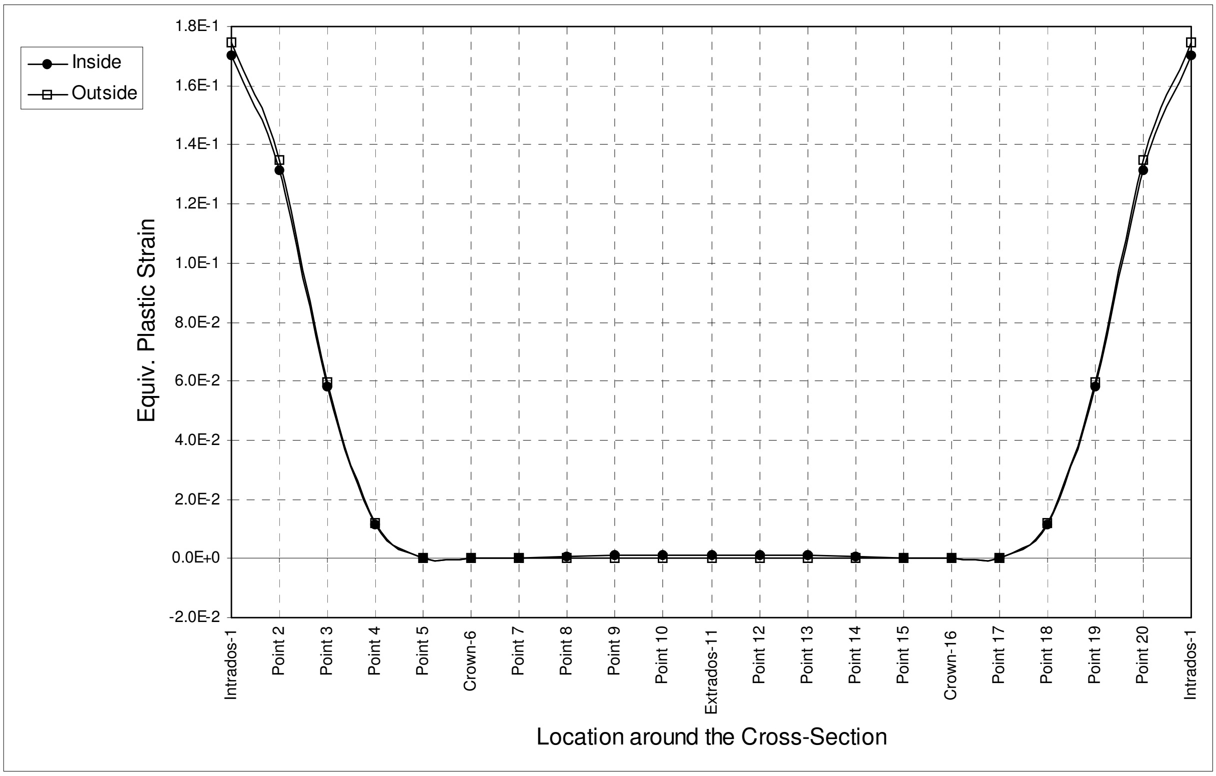

Fig. 3.5.54 **Distribution of Equivalent Plastic Strain Around the Cross-Section at Start of Yielding - Internal Pressure: 2200 psi**

3.5.4.3.b Instability

Figure 3.5.55 shows the distribution of axial strain, around the critical cross-section, at the point where the model reaches instability ($M=2.6872\times10^6$ lb-in. ; $\theta=0.4523$ radians). It is clear from this figure, that the right half of the cross-section is under compression, and the left half is under tension, due to the bending load. The point with maximum tensile strain is located on the outer surface of the left crown (point 16). The maximum compressive strain is located on the inside surface of point 4.

It is noted that the tensile strains are larger than the compressive ones, and this is due to the effect of pressure. It is also noted that the value of axial strain, at the intrados, is lower than at the extrados, as discussed before.

Figure 3.5.56 shows the distribution of hoop strain around the section. It can be seen from this figure that the maximum hoop strain exists at point 3. It is noted that the intrados has much higher hoop strain values than the extrados, as discussed before. Figure 3.5.57 shows the distribution of equivalent plastic strain. The maximum strain occurs on the outside wall, at the left crown, and has a value of $\varepsilon_{ep}=54.67$ percent.

It must be noted that Figs. 3.5.54 through 3.5.56 have exceedingly high values of strain, and hence the curves that they contain seem to coincide, although considerable differences do exist, at some points, between the strain values at the inner and the outer sides of the pipe wall. It is also important to note, that the results obtained at such high values of internal pressure should be treated with caution.

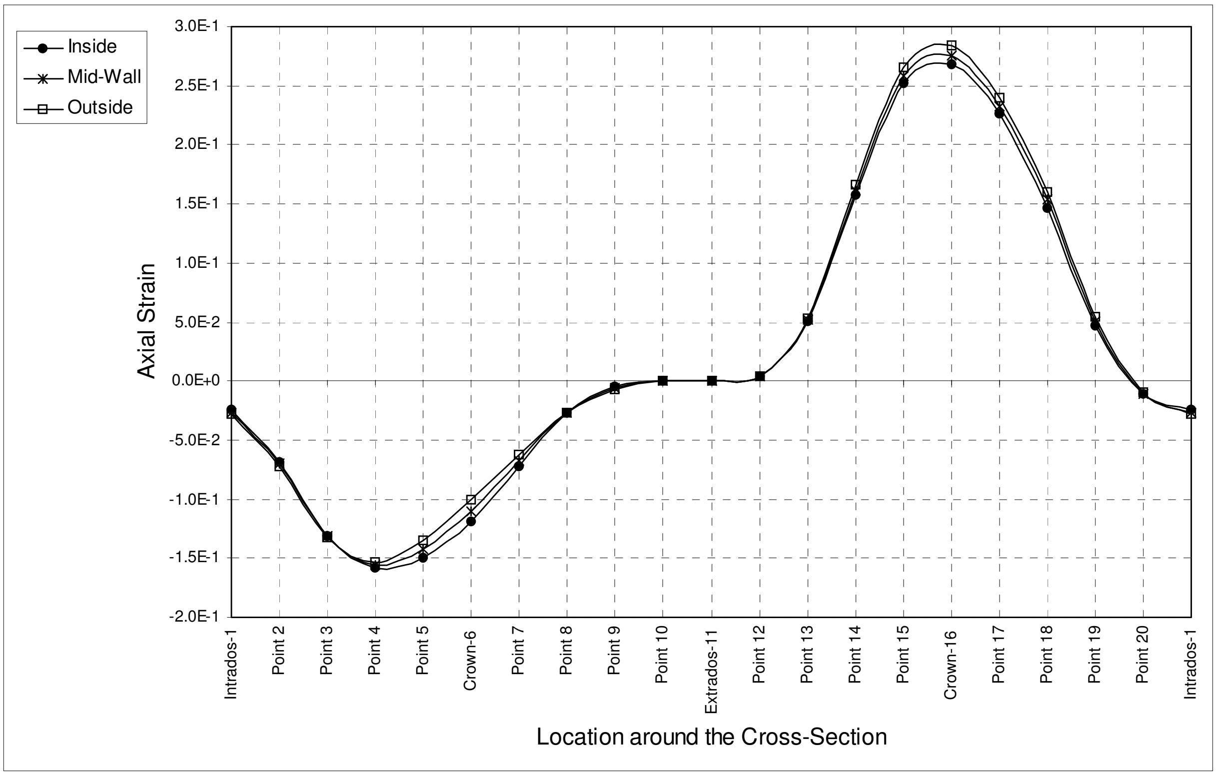

Fig. 3.5.55 Distribution of Axial Strain Around the Cross-Section at Instability - Internal Pressure: 2200 psi

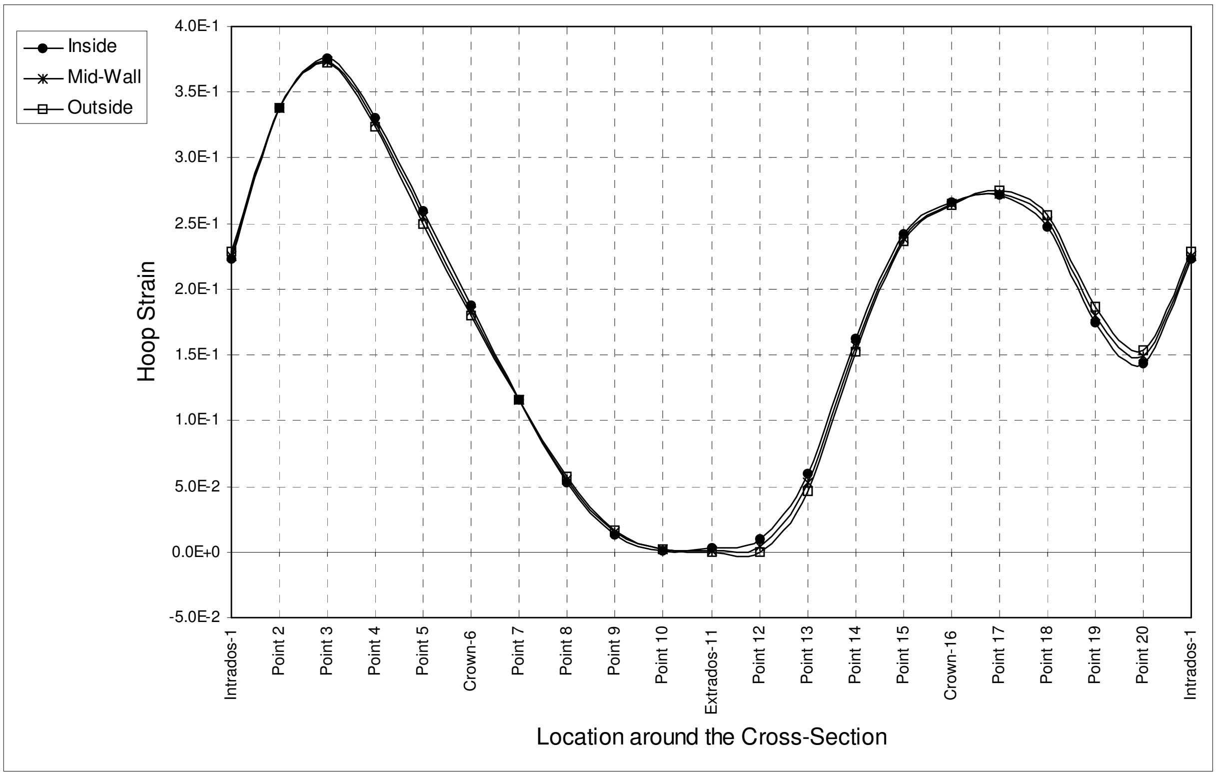

Fig. 3.5.56 Distribution of Hoop Strain Around the Cross-Section at Instability - Internal Pressure: 2200 psi

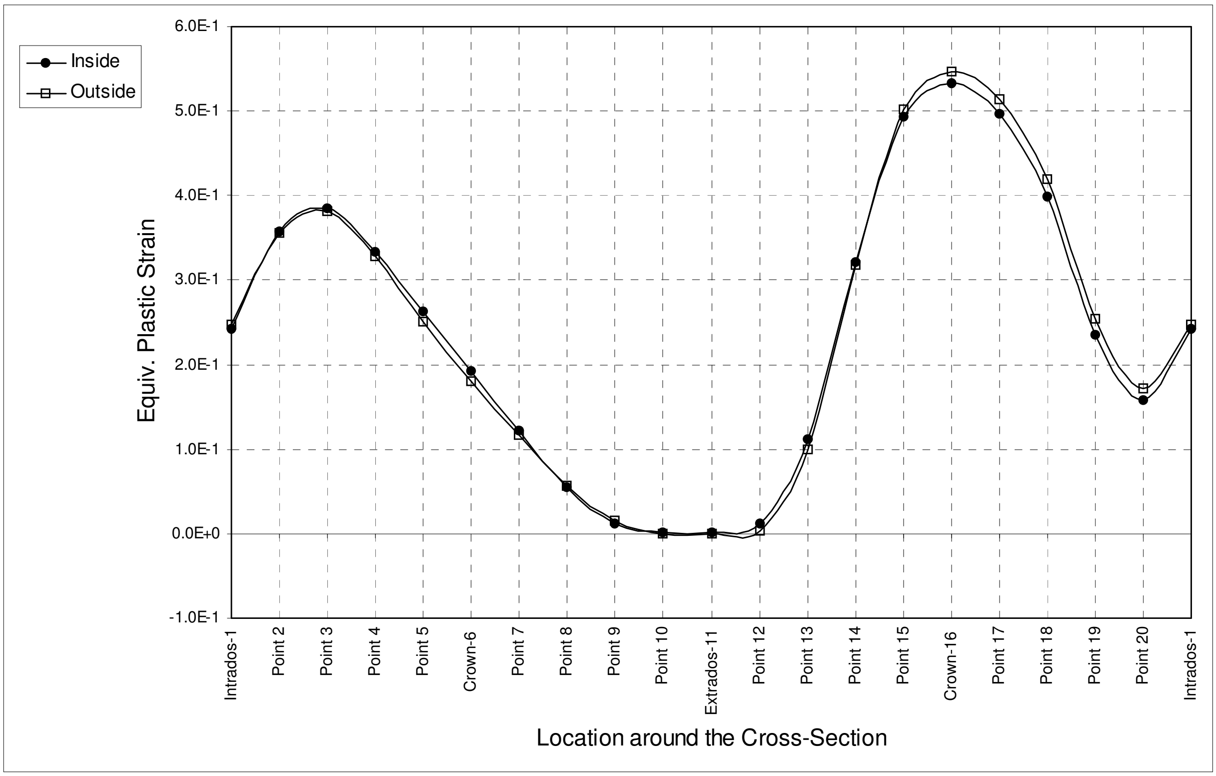

Fig. 3.5.57 Distribution of Equivalent Plastic Strain Around the Cross-Section at Instability - Internal Pressure: 2200 psi

3.5.5 Deformed Shapes

Figure 3.5.58 shows the original as well as the deformed shapes of the elbow with h=0.1615, at instability ($M=1.1089\times10^6$ lb-in. ; $\theta=6.6651\times10^{-2}$ radians), for the case where no internal pressure is applied to the model. This wireframe representation shows the 24 sections at which the finite element code performs numerical integration. It must be noted that the first and last sections shown are 1.585° away from the real ends of the model, in the non-deformed configuration.

The figure shows three orthogonal views of the model. It can be seen from this figure that the loaded end is the one that deforms the most. Cross-section ovalization is best shown by the side view, placed on the right side of the figure. It is noted that the way the section ovalizes agrees with what is described in the literature, as shown in Fig. 1.2.1. On the other hand, the warping of the cross-sections that are closest to the loaded end, is very clear in the top view, placed at the top left corner of the figure.

Figure 3.5.59 shows the elbow, at instability (M= 2.7175×10^6 lb-in. ; θ= 9.5496×10^{-2} radians), in the case where an internal pressure of 1200 psi is sustained throughout loading history. In this case, the end-rotation is greater than in the previous case, and the warping of the cross-section is limited, due to the stiffening effect of the pressure, and the tensile force that is applied at the loaded end, to simulate the closed end condition, as discussed before.

Figure 3.5.60 shows the same elbow, also at instability (M=2.6872×10^6 lb-in. ; θ=0.4523 radians), subject to an internal pressure value of 2200 psi. It is obvious that in this case the end-rotation is much greater than in the other two cases. The loaded end undergoes some in-plane rotation upwards, along with the out-of-plane rotation, under the influence of the Bourdon effect. In addition to the ovalization and warping of the end section, all 24 sections show a marked increase in diameter, due to extensive plastification and high pressure load.

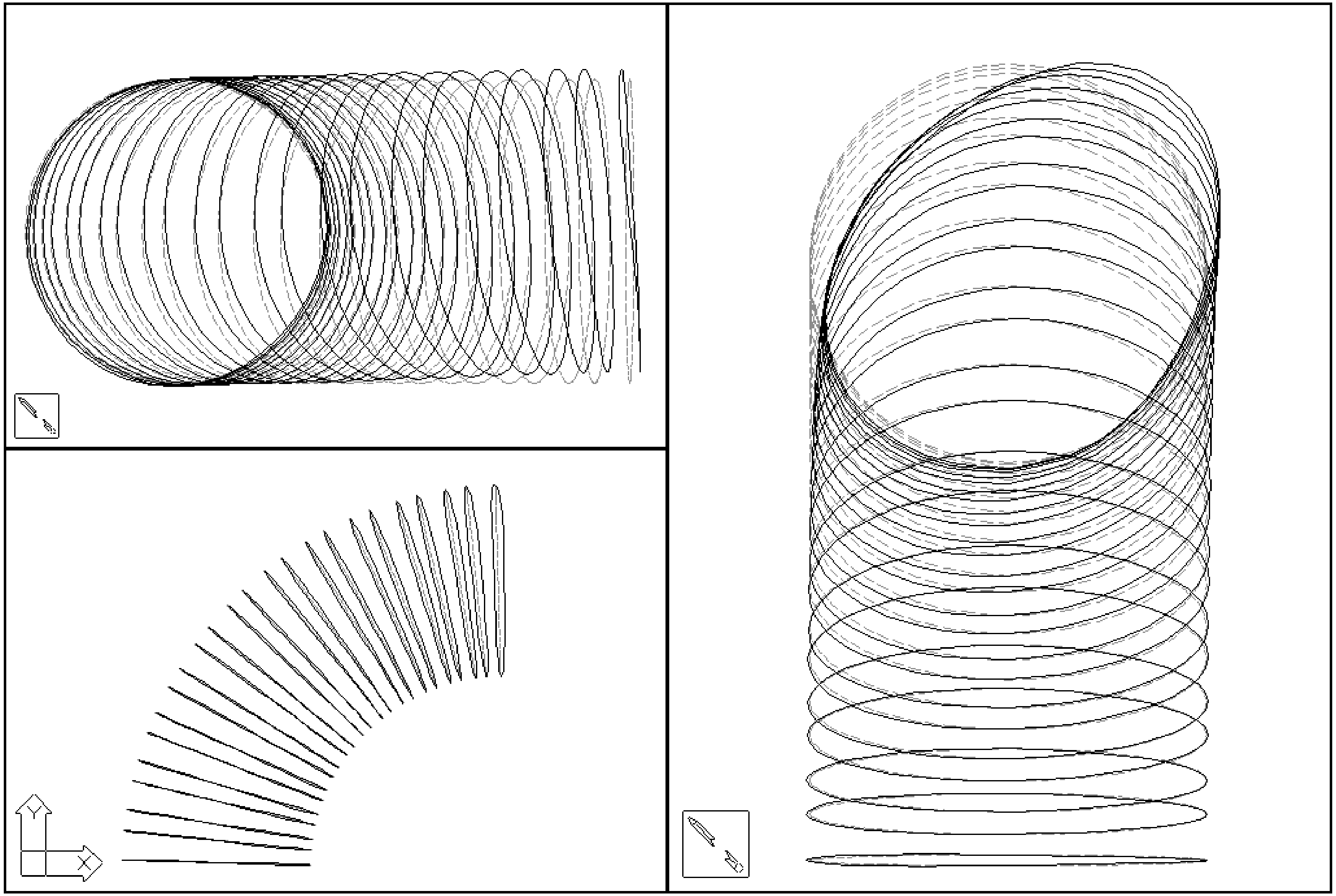

Fig. 3.5.58 Wireframe Representation of the Integration Sections of a Model With h=0.1615, Showing the Original and the Deformed Shapes of the Model, and the Cross-Sectional Deformation - No Internal Pressure

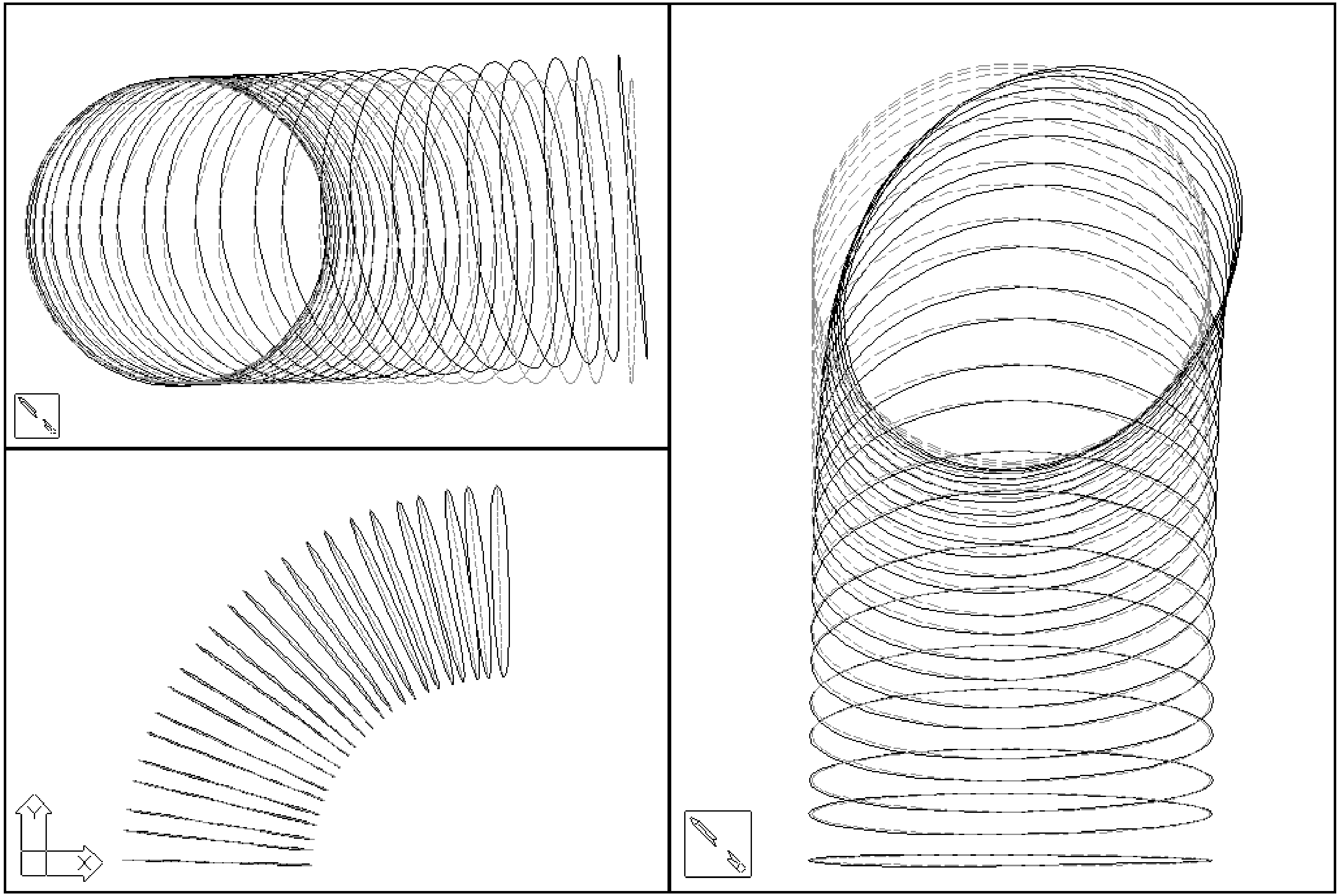

Fig. 3.5.59 Wireframe Representation of the Integration Stations of a Model With h=0.1615, Showing the Original and the Deformed Shapes of the Model and the Cross-Sectional Deformation - Internal Pressure: 1200 psi

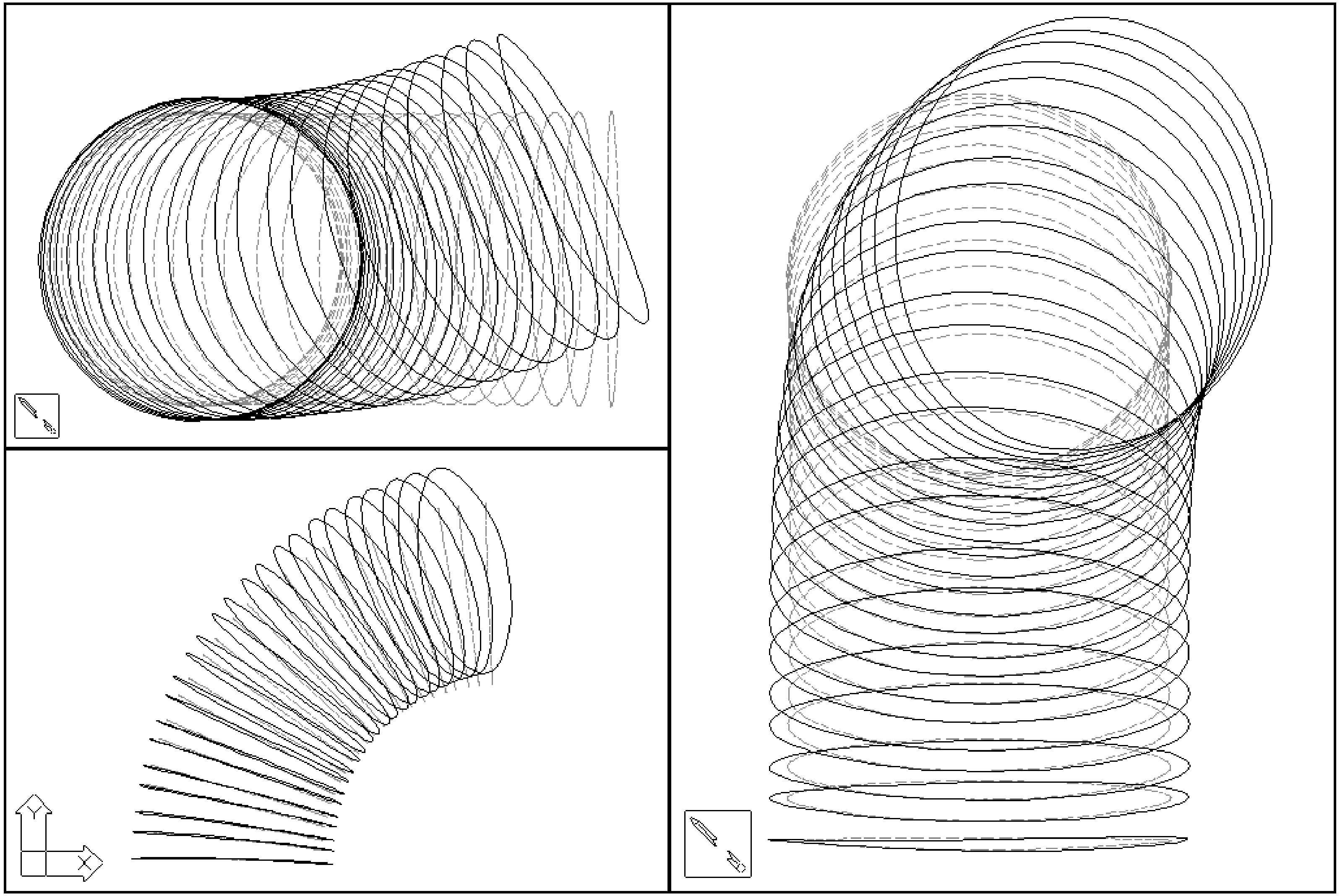

Fig. 3.5.60 Wireframe Representation of the Integration Stations of a Model With h=0.1615, Showing the Original and the Deformed Shapes of the Model and the Cross-Sectional Deformation - Internal Pressure: 2200 psi

Chapter Four

Conclusions

By examining the results of this investigation, discussed in the previous chapter, the following conclusions were attained:

Throughout this study, pipe bends were modeled assuming an elastic-perfectly-plastic material, and analyzed assuming large displacements. By studying the effects of geometric nonlinearity, it could be concluded that in the absence of internal pressure, large-displacement analyses give more conservative estimates of the limit moments, than small-displacement analyses using the same material model. It was also found that small-displacement analyses fail to predict the stiffening effect of pressure and give a continuously decaying limit load with increased pressure.

Material strain hardening was found to give higher (i.e. less conservative) limit load estimates than those obtained using perfectly-plastic material models. It also counteracts the weakening effect of high internal pressure. Therefore, in a large-displacement analysis with a strain-hardening material, collapse and instability moments level off as the pressure increases, and do not decline as in the case of a perfectly-plastic material. The load-deflection curve obtained from a small-displacement analysis with a perfectly-plastic material model, keeps a constant positive slope and never reaches a maximum, thus making it impossible to find a definitive instability load.

The load-deflection behavior of a standalone 90° elbow, subjected to an out-of-plane end-moment, remains linear at the beginning of loading history. Then, as the moment load is increased, the structure's overall stiffness starts decreasing gradually due to plastification and cross-sectional distortion. Finally, the pipe bend undergoes instability, which is represented by the peak point of the load-deflection curve.

Internal pressure has an obvious effect on this behavior, which is more significant in elbows with a smaller bend factor (i.e. smaller wall thickness). Internal pressure impedes cross-sectional ovalization and warping, and hence increases the stiffness of the elbow in the direction of moment loading. Higher values of pressure have a detrimental effect on the stiffness, due to the additional stresses induced by the pressure itself. Therefore, it was found that for each model, the collapse moment increases with the addition of pressure, and then starts declining again. The same trend is displayed by the moment at which the elbow starts to exhibit nonlinear response.

The instability moment follows a similar trend of variation, but tends to increase slightly near the high end of the pressure range. However, results obtained at very high values of pressure should be interpreted with caution, since they indicate that unrealistically large end-rotation can be reached by the models before instability. The effect of internal pressure on the value of end-rotation at instability, is displayed as an initial slight increase, followed by a significant decrease, and a final sharp increase, near the high end of the pressure range.

In the absence of internal pressure, the collapse and instability moments were found to have almost identical values. It was also found that the twice-elastic-slope method, gives an estimate of the collapse moment, which is generally smaller than the value of the instability moment, of the same model, at the same pressure. Increasing the bend factor, by increasing the pipe wall thickness, leads to an increase in the value of both collapse and instability moments. In addition, for a model with a higher bend factor, the peak values of both collapse and instability moments are achieved at higher values of internal pressure.

The axial distribution of Mises stress at start of yielding, and the axial distribution of equivalent plastic strain at instability, were studied for one selected elbow. Three cases were presented, one without internal pressure, another with P=1200 psi, and the last with P=2200 psi. The critical cross-section was found to be located at the loaded end of the elbow. The deformed shapes of the elbow show that this section is more severely distorted before reaching instability, than all other sections of the elbow.

This cross-sectional distortion causes through-the-wall bending effects. These are revealed by the presence of bending stresses, which are much greater in the hoop direction than membrane stresses. Hoop stresses were also found to be several times higher than the axial stresses present in the same section, which is also an indication of the importance of these through-the-wall bending effects.

Considerable plastification occurs, and hundreds of plastic hinges are formed in the structure of the elbow before reaching instability, especially in the presence of pressure. By examining the deformed shapes of the elbows, for the cases with and without pressure, the effect of pressure is clear in reducing cross-sectional distortion and in allowing a larger end-rotation to be achieved before instability.

The Von Mises stress distribution at the onset of yielding, is changed by the uniform axial and hoop stress components added by internal pressure. The distribution of equivalent plastic strain is also changed, because of the larger end-rotation made possible by the stiffening effect of pressure.

Maximum strain locations are shifted away from the elbow's crowns, due to its curved geometry, and form four high-strain locations around the critical cross-section. Internal pressure either promotes or impedes straining in some of these locations, and shifts them slightly.

In this work, estimates of the limit moments were found for the case where a 90° pipe bend is loaded out of its own plane. These results can be readily used by designers, in conjunction with the limit load estimates, given by Shalaby (1996) for the case of in-plane bending. In addition, the effect of internal pressure, and that of the pipe bend factor, were investigated. This data provides a basis, upon which design guidelines can be set or improved.

A detailed stress analysis of the pipe bend, especially of its critical section, in the out-of-plane loading case, is provided herein. Shalaby (1996) also presented a detailed stress analysis of pipe bends under in-plane bending. These results can be very useful, for designers as well as researchers, in gaining a deeper understanding of the structural behavior of pipe bends.

Of course, more work is needed to cover other aspects of the pipe bend problem, like variable and combined loading, and to investigate different effects, like end-constraints.

References

ABAQUS/Standard Ver. 5.8. "User's Manual," "Example Problems Manual," and "Theory Manual." Hibbit, Karlsson and Sorensen Inc., Providence, 1998.

Abo-Elkhier, M. "Analysis of Pipe Bends Using Pipe Elbow Element." *Computers and Structures*, 37(1), 1990: 9-15.

ASME Boiler and Pressure Vessel Code, Section III, Division 1. "Nuclear Power Plant Components." ASME, New York, 1992.

Bantlin, A. "Formänderung und Beanspruchung federnder Ausgleichröhre." *Zeitshrift des Vereines Deutscher Ingenieure*, 54, 1910: 43-49.

Barthélemy, J. "Étude de la Déformation et des Tensions Internes des Tuyaux à Ligne Moyenne Planne, Soumis à des Efforts Extérieurs et à une Pression Interne." *Bulletin de L'association Technique Maritime*, 1947.

Bathe, K. J. and C. A. Almeida. "A Simple and Effective Pipe Elbow Element - Linear Analysis." *Journal of Applied Mechanics*, 47, 1980: 93-100.

Bathe, K. J. and C. A. Almeida. "A Simple and Effective Pipe Elbow Element - Interaction Effects." *Journal of Applied Mechanics*, 49, 1982: 165-171.

Bathe, K. J. and C. A. Almeida. "A Simple and Effective Pipe Elbow Element - Pressure Stiffening Effects." *Journal of Applied Mechanics*, 49, 1982: 914-918.

Beskin, L. "Bending of Curved Thin Tubes." Trans. ASME, 67, 1945: A-1.

Bolt, S. E. and W. L. Greenstreet. "Experimental Determinations of Plastic Collapse Loads for Pipe Elbows." *Trans. ASME*, 71-PVP-37, 1971.

Cheng, D. H. and H. J. Thailer. "In-Plane Bending of Curved Circular Tubes." *Trans. ASME*, 68-PVP-12, 1968.

Clark, R.A. and E. Reissner. "Bending of Curved Tubes." *Advanced Applied Mechanics*, 2, 1951: 93-112.

Clark, R. A., T.I. Gilroy and E. Reissner. "Stresses and Deformations of Toroidal Shells of Elliptical Cross Section." *Journal of Applied Mechanics, Trans. ASME*, 74, 1952:37-48.

Dhalla, A. K. "Plastic Collapse of a Piping Elbow: Effects of Finite Element Convergence and Residual Stresses." *Proc. 4th International Conference on Pressure Vessel Technology, The Institution of Mechanical Engineers*, 11, London, 1980: 243-249.

Dhalla, A. K. "A Procedure to Evaluate Structural Adequacy of a Piping System in the Creep Range." *Benchmark Problem Studies and Piping Systems at Elevated Temperature*, PVP-66, ASME, 1982.

Dhalla, A. K. "Collapse Characteristics of a Thin-Walled Elbow: Validation of a an Analytical Procedure." Trans. ASME, 109, Nov. 1987: 394-401.

Dhalla, A. K. and S. Z. Newman. *Inelastic Analysis of Battelle-Columbus Piping Elbow Creep Test*. Westinghouse Advanced Reactors Division, Madison, 1978.

Dodge, W. G. and S. E. Moore. "Stress Indices and Flexibility Factors for Moment Loadings on Elbows and Curved Pipe." *Welding Research Council (WRC) Bulletin*, 179, 1972: 1-19.

Gerdeen, J. C. "A Critical Evaluation of Plastic Behavior Data and a Unified Definition of Plastic Collapse Loads for Pressure Components." *Welding Research Council (WRC) Bulletin*, 254, 1979: 3-64.

Greentsreet, W. L. *Experimental Study of Plastic Responses of Pipe Elbows*. ORNL/NUREG-24 Report, Contract No. W-7405-eng-26, 1978.

Gross, N. "Experiments on Short-Radius Pipe Bends." *Proc. Institution of Mechanical Engineers*, 1(B), 1952-1953: 465-479.

Gross, N. and H. Ford. "The Flexibility of Short-Radius Pipe Bends." *Proc. Institution of Mechanical Engineers*, 1B, 1952: 480.

Hibbit, H. D. "Special Structural Elements for Piping Analysis." *ASME special publication 'Pressure Vessels and Piping: Analysis and Computers'*, 1974: 1-10.

Hibbit, H. D. and E. K. Leung. "Verification and Application of an Inelastic Analysis Method for LMFBR Piping Systems." Welding Research Council (WRC) Bulletin, 308, 1985: 1-28.

Hilsenkopf, P. , B. Boneh, and P. Sollogoub. "Experimental Study of Behavior and Functional Capability of Ferritic Steel Elbows and Austenitic Stainless Steel Thin-Walled Elbows." *International Journal of Pressure Vessels and Piping*, 33, 1988: 111-128.

Kafka, P. G. and Dunn M. B. "Stiffness of Curved Circular Tubes with Internal Pressure." *Journal of Applied Mechanics*, *Trans. ASME*, 78, 1956: 247-254.

Kitching, R. , K. Zarrabi, and M. A. Moore. "Limit Moment for a Smooth Pipe Bend Under In-Plane Bending." *International Journal of Mechanical Science*, 21, 1979: 731-738.

Kussmaul, K. , H. Diem, and D. Blind. "Investigations of the Plastic Behavious of Pipe Bends." *ASME PVPD*, 127, 1987:55-66.

Makhutov, N. A., S. V. Serikov and A. G. Kotousov. "Increasing the Design Strength of Piping Fittings." *Strength of Materials*, 23(4), 1991: 468-472. (Based on a paper that appeared in Russian, *Problemy Prochnosti*, 4, April 1991: 77-80.)

Marcal, P. V. "Elastic-Plastic Behaviour of Pipe Bends with In-Plane Bending." *Journal of Strain Analysis*, 2(1), 1967: 84.

Marcal, P. V. and C. E. Turner. "Elastic Solution in the Limit Analysis of Shells of Revolution with Special Reference to Expansion Bellows." *Journal of Mechanical Engineering Science*, 3(3), 1961: 252-257.

McAfee, W. J. ed. "Compilation of Piping Benchmark Problems - Cooperative International Effort." *IWGFR/27*, June 1979.

Mello, R. M. and D. S. Griffin. "Plastic Collapse Loads for Pipe Elbows Using Inelastic Analysis." *Trans. ASME*, 96(J), 1974: 177-183.

Ohtsubo, H. and O. Watanabe. "Flexibility and Stress Factors of Pipe Bends - An Analysis by the Finite Ring Method."*, Trans. ASME*, 76-PVP-40, 1976: 1-10.

Ohtsubo, H. and O. Watanabe. "Stress Analysis of Pipe Bends by Ring Elements." *Journal of Pressure Vessel Technology*, 100, 1978: 112-122. (Based on a paper that appeared in Japanese, *Trans. Japan Society of Mechanical Engineers*, 42(362), 1976: 30-37.)

Pardue, T. E. and I. Vigness. "Properties of Thin Walled Curved Tubes of Short Bend Radius." *Trans. ASME*, 73, 1951: 77-84.

Reissner, E. "On Bending of Curved Thin-Walled Tubes." *Proc. National Academy of Science*, USA, 35, 1949: 204-208.

Rodabaugh, E. C. "Interpretive Report on Limit Analysis and Plastic Behavior of Piping Products." *Welding Research Council (WRC) Bulletin*, 254, 1979: 65-82.

Rodabaugh, E. C. and H. H. George. "Effect of Internal Pressure on Flexibility and Stress-Intensification Factors of Curved Pipe or Welding Elbows." *Trans. ASME*, 79, 1957: 939-948.

Shalaby, M. A. *Elastic-Plastic Behavior and Limit-Load Analysis of Pipe Elbows under In-Plane Bending and Internal Pressure*. M. Sc. Thesis, American University in Cairo, 1996.

Smith, R. T. "Theoretical Analysis of the Stresses in Pipe Bends Subjected to Out-of-Plane Bending." *Journal of Mechanical Engineering Science*, 9(2), 1967: 115-123.

Smith, R. T. and H. Ford. "Experimental Study of the Flexibility of a Full-Scale Two-Dimensional Steam Pipeline." Journal of Mechanical Engineering Science, 4(3), 1962: 270.

Smith, R. T. and H. Ford. "Experiments on Pipe Lines and Pipe Bends Subjected to Three-Dimensional Loading." *Journal of Mechanical Engineering Science*, 9(2), 1967: 124-137.

Sobel, L. H. and S. Z. Newman. "Instability Analysis of Elbows in the Plastic Range." *Proc. 4th Structural Mechanics in Reactor Technology (SMiRT) Conference*, L3(2), San Francisco, 1977: 1-11.

Sobel, L. H. and S. Z. Newman. "Elastic-Plastic In-Plane Bending and Buckling of an Elbow: Comparison of Experimental and Simplified Analysis Results." Westinghouse Advanced Reactors Division, Report WARD-HT-94000-2, 1979.

Sobel, L. H. and S. Z. Newman. "Comparison of Experimental and Simplified Analytical Results for the In-Plane Plastic Bending and Buckling of an Elbow." *Journal of Pressure Vessel Technology*, 102, 1980: 400-409.

Sobel, L. H. and S. Z. Newman. "The Southwell Method for Predicting Plastic Buckling Loads for Elbows." *Journal of Pressure Vessel Technology*, 105, 1983: 2-8.

Sobel, L. H. and S. Z. Newman. "Simplified, Detailed, and Isochronous Analysis and Test Results for the In-Plane Elastic-Plastic and Creep Behavior of an Elbow." *Journal of Pressure Vessel Technology*, *Trans. ASME*, 108, 1986:297-304.

Spence, J. "An Upper Bound Analysis for the Deformation of Smooth Pipe Bends in Creep." *2nd International Union of Theoretical and Applied Mechanics Symposium 'Creep in Structures'*, 1970. Ed. Hult , Springer-Verlag, Berlin, 1972: 234:246.

Spence, J. "Creep Analysis of Smooth Curved Pipes under In-Plane Bending." *Journal of Mechanical Engineering Science*, 1973.

Spence, J. and G. E. Findlay. "Limit Loads for Pipe Bends under In-Plane Bending." *Proc. 2nd International Conference on Pressure Vessel Technology*, I-28, ASME, New York, 1973.

Takeda et al. "A New Finite Element for Structural Analysis of Piping Systems." *Proc. 5th Structural Mechanics in Reactor Technology (SMiRT) Conference*, M5(5), Berlin, 1979.

Tueda, M. "Bourdon Tubes and Bending of Thin Curved Tubes." *Memoirs*, Kyoto Imperial University, February 1936.

Turner, C. E. and H. Ford. "Examination of the Theories for Calculating the Stresses in Pipe Bends Subjected to In-Plane Bending." *Proc. Institution of Mechanical Engineers*, 171, 1957: 513-515.

Vigness, I. "Elastic Properties of Curved Tubes." *Trans. ASME*, 65, 1943: 105-120.

Von Kármán, Th. "Über die Formänderung dünnwandiger Röhre, insbesondere federnder Ausgleichröhre." *Zeitshrift des Vereines Deutscher Ingenieure*, 55, 1911: 1889-1895.

Whatham, J. F. "In-Plane Bending of Flanged Pipe Elbows." *Trans. Metal Structures Conference*, 1978.

Whatham, J. F. and J. J. Thompson. "The Bending and Pressurizing of Pipe Bends with Flanged Tangents." *Nuclear Engineering and Design*, 54, 1979: 17-28.